THE EFFECTS OF CONCENTRATION, INTERACTION, SIZE DISTRIBUTION AND SHAPE ANISOTROPY ON RHEOLOGY OF COLLOIDAL MIXTURES

BY

TIANYING JIANG

DISSERTATION

Submitted in partial fulfillment of the requirements
for the degree of Doctor of Philosophy in Chemical Engineering
in the Graduate College of the
University of Illinois at Urbana-Champaign, 2013

Urbana, Illinois

Doctoral Committee:

Professor Charles F. Zukoski, Chair
Professor Kenneth S. Schweizer
Professor Jonathan J. L. Higdon
Assistant Professor Charles M. Schroeder

ABSTRACT

This dissertation studies the rheological properties of dense colloidal mixtures. Particular interest is focused on the role of volume fraction and strength of interactions that lead to glass or gel formation. Variables studied include particle concentration, strength of attraction, particle size distribution, and particle shape, which have effects on dynamic arrest transitions, jamming conditions and steady flow properties of dense suspensions. A special attention is paid to changes in properties at volume fractions exceeding the dynamic arrest transitions and approaching maximum packing fractions. For mixtures of particles, dynamic state diagrams are constructed as functions of large particle volume fraction ratio and total particle volume fraction as particle interactions are varied.

The main effort is focused on the system composed of spherical silica particles with different sizes (100nm-1μm) dispersed in low molecular weight polyethylene glycol (PEG) melts with molecular weight 400 and 2000. For this system we explore the impact of the polymer molecular weight on the dynamic arrest transition, linear elasticity, shear thickening, and yielding for both monomodal and bimodal particle size distributions. Data is reported showing a varied dynamic arrest transition volume fraction, weakened shear thickening behavior and augmented shear elasticity in higher molecular weight polymer melt (PEG2000) for single-component system and denoting a stronger particle-particle attraction in higher molecular weight polymer which cannot be a consequence of adsorbed polymer layer entanglement. For bimodal mixtures in PEG400, particles interact with excluded volume potentials and the dynamic arrest transition volume fraction is a non-monotonic function of large particle volume fraction ratio. The dynamic arrest volume fraction is strongly correlated with the maximum packing fraction for each mixture. The data show that rheological properties of dynamic arrested states diverge in a consistent way when approaching

maximum packing fractions. When dispersed in PEG2000 where particles are attractive, the dynamic arrest volume fraction is a monotonic function of large particle volume fraction ratio, which is not correlated with maximum packing fraction. Flow properties at this condition are dominated by attractions.

In a further study, the flow properties of suspensions of large (diameter~1μm) and small (diameter~300nm) polystyrene particles suspended in an aqueous electrolyte were investigated. Here two types of large particles were investigated: spheres and dumbbell shaped particles. Weak shape anisotropy of the large particles delays the dynamic arrest transition and decreases the viscoelasticity at fixed volume fractions in single-component systems, but enhances the dynamic arrests and alters the jamming conditions in binary mixtures compared to sphere mixtures with bimodal size distributions. A consistent understanding of rheology in dense suspensions is built up based on particle localization effects.

ACKNOWLEDGEMENTS

I would like to thank my graduate research advisor, Dr. Charles F. Zukoski for his patient guidance, great enthusiasm and reasonable expectations throughout my graduate study, who always encourages me to make efficient progress no matter what difficulties I have met in the last five years. In my opinion, he is the best advisor one graduate student could expect for. I would also thank all my colleagues in Zukoski group, both the previous and current group members, for their help and discussion about the research. They make it a great pleasure to work in the lab and their friendship brings a lot of fun to my life in Urbana. Thanks also go to my parents who have been consistently supporting me no matter what difficulties I encountered in life or in work.

This material is based on work supported by the U.S. Department of Energy, Division of Materials Science under Award No.DE-FG02-07ER46471, through the Frederick Seitz Materials Research Laboratory at the University of Illinois Urbana-Champaign. Research in this work was carried out in part in the Frederick Seitz Materials Research Laboratory Central Facilities, University of Illinois University, which are partially supported by the U.S. Department of Energy under grants DE-FG02-07ER46453 and DE-FG02-07ER46471.

Table of Contents

Chapter 1. Introduction

1.1 Overview

Colloidal dispersions with particle size ranged from 10nm to 10μm have been used widely in industrial processing where large surface areas and high solid concentrations are required, including paints, ceramics, food and electronics. With the ability to tune particle interactions, concentration, size and shape, the physical properties of colloidal dispersions can be easily designed and improved thus making the application of this group of materials ubiquitous.[1-4]

There are different strategies to vary the parameters of colloidal suspensions in order to control processing. Particle shape can be manipulated by different manufacturing techniques.[5, 6] Particle size can also be varied in a wide range within 10nm-10μm, particle interaction can be tuned by varying temperature, the chemistry of the particle surface and the colloid materials, surface chemistry and dispersion medium, while the particle concentration can also be manipulated over in a wide range to achieve different state behaviors.[7] Despite knowing that these parameters can be used to vary suspension properties, designing and engineering colloidal dispersions with desired mechanical, optical or electrical properties, requires a deeper fundamental understanding of the effects of particle shape, size, interaction and concentration which all influence the state behaviors and rheology of the suspension in a cooperative way. Many studies have been carried out to study the phase behaviors and the rheology of dense suspensions composed of single-component colloids with concentrations and interactions varied, involving dynamic arrest transitions (glass transition and gelation) and the flow properties of repulsive glasses, attractive glasses and gels.[8]

When the size polydispersity is large enough or the suspension is concentrated with sufficient rapidity, the suspension reaches a jammed state at random close packing where the dispersion shows no long-range ordered structure as seen in crystals. As show in Figure 1.1, which is a schematic state diagram of single-component spherical hard-core colloidal dispersion, when the particle-particle interaction energy at contact ε/k_BT=0, the resulting interactions are purely volume exclusion in nature and the system is referred to as being composed of hard spheres. At low volume fractions, the suspension is a liquid with very low elasticity. As volume fraction increases towards random close packing (~0.64) the suspension viscosity increases rapidly and elasticity become apparent. Depending on the method used to characterize the suspension's relaxation rate, hard sphere suspensions are said to undergo a glass transition for ϕ_c~0.58 in experimental reports. At this point density fluctuations are said to not relax in a time period of 10 seconds.[9] The exact volume fraction defining the glass transition depends on the method which is used to characterize relaxation processes. As ϕ_c is increased, particles are trapped in cages formed by nearest neighbors for increasing long periods of time resulting in increasing time for long-range diffusion and reduced relaxation rates. The glass transition is ultimately seen as a dynamic process where the system is a liquid for observations of duration longer than the relaxation time and a solid for observations of duration shorter than the relaxation time. Hard spheres show glassy dynamics characterized by rapid diffusion within cages and slow diffusion for large distances, at volume fractions above 0.5. The period of observation required to see liquid-like behavior diverges as random close packing is approached. The volume fraction characterizing the onset of glassy behavior or the volume fraction where particles become

localized by cages of nearest neighbors is defined as ϕ_x and is said to demark the dynamic arrest transition. The prediction of the value of ϕ_x depends on the details of the theory used and varies between 0.52 for idealized mode coupling theory (MCT)[10] to 0.432 for naïve mode coupling theory (nMCT)[11]. Both MCT and nMCT are designed to predict when collective interactions result in the localization of particles by entropic forces produced by nearest neighbors. In its idealized form, MCT predicts that long-range diffusion ceases for $\phi_c>\phi_x$. Many observations demonstrate that above ϕ_x, suspensions are able to relax when exposed to stress and zero-shear viscosities are observed.

This theory was advanced with the introduction of dynamic localization theory where the cross-over volume fraction ϕ_x is set to be the point where there is an inflection in a dynamic potential. This potential is used to describe the motion of particles due to collective particle motions in the suspensions. The dynamic potential results from force correlations and does not alter the suspension's microstructure and is a theoretical construct used to capture the fluctuating forces acting on the particles. The dynamic potential thus only alters the dynamics of particle motion which is associated with time dependent force correlations and predicts that the onset of glassy behavior does not occur as an abrupt transition but is observed as a smooth transition in zero shear rate viscosity and diffusivity where the rate of change of these parameters occurs more rapidly for $\phi_c>\phi_x$. For $\phi_c<\phi_x$, the dynamic potential drives particles to diffuse randomly throughout the suspension volume. For $\phi_c>\phi_x$, the dynamic potential develops a local minimum at r_L and a barrier at r_L. Long range particle diffusion requires activated motion out of the dynamic potential. This occurs with a characteristic hopping time. As volume fraction is raised the local minimum in the dynamic potential grows in depth, the barrier over which

the particles must diffuse increases in height and the hopping time becomes longer as shown in Figure 1.2(A). In this model, long range diffusion does not cease until the suspension hits the maximum packing fraction which is ~0.64 for hard spheres.[12] With increasing strength of particle attractions, the dynamical ϕ_x can be changed. With weak attractive energy at contact (ε/k_BT~2), theoretical studies predict re-entrant behavior with ϕ_x slightly increased above the hard sphere value.[13, 14] The existence of re-entrant glasses formation has also been confirmed experimentally and the prediction of this phenomena is one of the major achievements of MCT.[15] With stronger attraction introduced, dynamic arrest occurs at lower volume fraction, than what is seen in hard sphere suspensions. These systems are called gels. For all these systems the maximum packing fraction ϕ_m is controlled only by the particle hard core geometry, and thus cannot be varied due to tuning interactions.

As the volume fraction of suspensions is raised, their flow properties often show very similar properties where, with increased stress a low shear rate viscosity is followed by a shear thinning region leading to a high-shear viscosity plateau which is interrupted by shear thickening at high enough volume fraction. According to dynamic localization theory, when shear stress is increased on suspensions with $\phi_c>\phi_x$, the barrier over which the particles must diffuse decreases in height. At the absolute yield stress, the local minimum and barrier in dynamic potential disappear with a saddle point developing at the inflection point (Figure 1.2 (B)). These universal features are of course modified by suspension parameters of volume fraction, particle size, shape, and interaction potential. Here dynamic localization theory is used to explore the consequences of particle localization in complex media where pair potentials are poorly understood and the

maximum packing fraction can be varied. Of particular interest is developing methods to characterize the dynamic arrest transition ϕ_x and to explore changes in flow properties when approaching the maximum packing volume fraction ϕ_m. To do this I purposely study colloidal dispersions with bimodal size distribution and tunable particle-particle interaction by controlling the suspension medium. Here ϕ_m is controlled by varying particle geometry and particle size distribution. ϕ_x is controlled by both packing and varying particle interactions.

1.2 Binary Mixtures

It is important to understand the effect of polydispersity in colloidal suspension not only for wide existence of multimodal colloidal mixture but also for optimizing the properties of colloidal dispersions. There are many examples of colloidal mixtures in the nature such as the proteins in eye lens protein mixtures formed by γ- and α-crystallins where phase separation occurs on decreasing temperature.[16] Complexity is expected in the properties when increase the degrees of freedom in colloidal suspensions by adding a different species of particle as shown in experimental systems.[17, 18] In addition, theoretical studies have predicted that novel dynamics and structures can be produced by heterogeneity in size, shape and interaction of colloids.[19-21]

In colloid-polymer composite systems colloid-colloid interactions can be controlled precisely by changing the colloid-polymer segment interaction and the thickness of the adsorbed polymer layer. Few studies have explored the effect of size disparity when particles of mixed size are incorporated into the composite. One especially important question lies in understanding how the rheology in dense polymer composite melts. Detailed studies show that particle interactions are systematically varied with increasing

polymer radius of gyration. Here the effects of increasing particle size are explored for two polymer molecular weights under the entanglement molecular weight. In addition, the effects of introducing bimodality of particle size into polymer composite melts are explored.

Complexity in colloidal suspensions can also be introduced by changing particle shape. Most detailed studies have been carried out on suspensions composed of spheres. Recently studies have established that particles with weak shape anisotropy but hard interactions share universal rheological behavior of spheres if ϕ_m is recognized as changing with particle shape. The effects are explored if we introduce shape anisotropy to bimodal mixtures of colloidal particles.

Therefore, in the following chapters, suspension flow properties are characterized of two carefully designed experimental systems: silica particles dispersed in polyethylene glycol (PEG) in Chapter 2-4 and polystyrene particles in aqueous phase in Chapter 5. In Chapter 2, silica particles with four different sizes in PEG are studied as a function of polymer molecular weight leading to an understanding of the effects of polymer molecule weight and particle size on flow properties. In Chapter 3, binary mixtures of colloids in low molecular weight PEG are studied, where interaction is volume exclusion and glasses form at high volume fractions. In Chapter 4, the polymer-induced attraction on the rheology of binary colloidal dispersions is investigated. In Chapter 5, polystyrene particles are designed to incorporate shape anisotropy in binary mixtures to help us develop further understanding about the glass transition in dense suspension. In Chapter 6, rheology of different systems are understood in the frame of nMCT and dynamic localization theory based on the studying the entropic barrier height and external shear

induced hopping. In Chapter 7, the results are summarized and main conclusions are given.

1.3 Tables and Figures

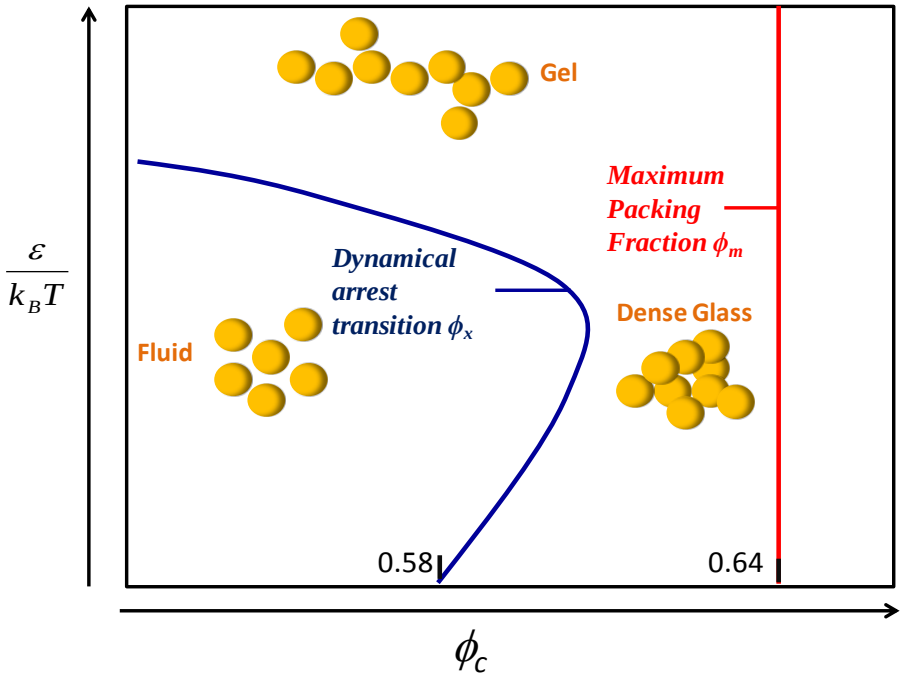

Figure 1.1 Schematic state diagram of single-component spherical particle.

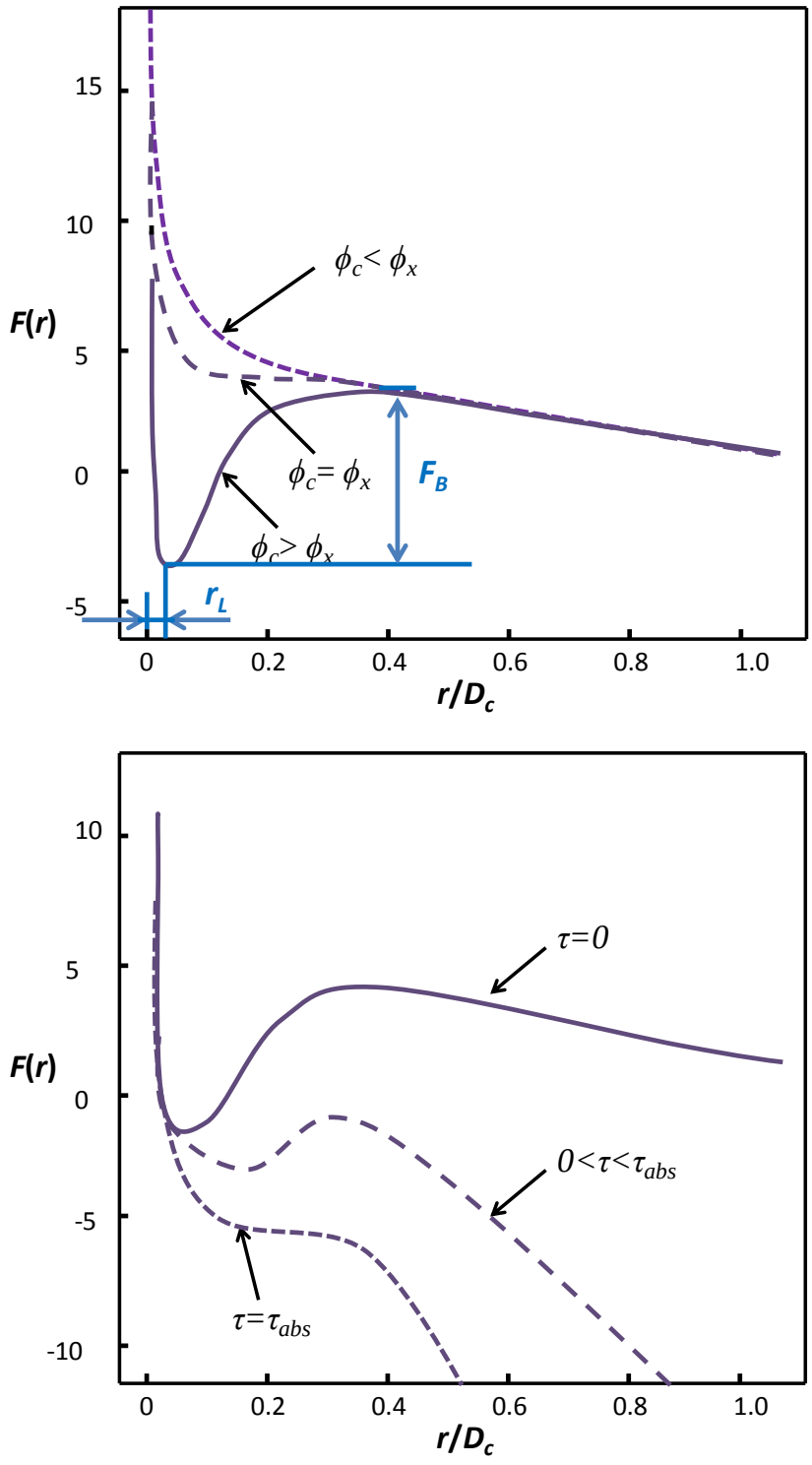

Figure 1.2 Schematic dynamic potential as a function of particle displacement for (A) zero shear condition denoting transition from delocalization to localization with r_L and F_B labeled for $\phi_c > \phi_x$, and for (B) suspension with $\phi_c > \phi_x$ when exposed to different shear.

1.4 References

1. L. N. Lewis, *Journal of the American Chemical Society*, 1990, **112**, 5998-6004.
2. C. G. Li, T. Y. Bai, F. F. Li, L. Wang, X. F. Wu, L. Yuan, Z. Shi and S. H. Feng, *Crystengcomm*, 2013, **15**, 597-603.
3. W. K. Bae, J. Joo, L. A. Padilha, J. Won, D. C. Lee, Q. L. Lin, W. K. Koh, H. M. Luo, V. I. Klimov and J. M. Pietryga, *Journal of the American Chemical Society*, 2012, **134**, 20160-20168.
4. G. B. McKenna, T. Narita and F. Lequeux, *Journal of Rheology*, 2009, **53**, 489-516.
5. W. K. Kegel, D. Breed, M. Elsesser and D. J. Pine, *Langmuir*, 2006, **22**, 7135-7136.
6. K. E. Sung, S. A. Vanapalli, D. Mukhija, H. A. McKay, J. M. Millunchick, M. A. Burns and M. J. Solomon, *Journal of the American Chemical Society*, 2008, **130**, 1335-1340.
7. Z. Cheng, P. M. Chaikin, W. B. Russel, W. V. Meyer, J. Zhu, R. B. Rogers and R. H. Ottewill, *Materials & Design*, 2001, **22**, 529-534.
8. E. Zaccarelli, *Journal of Physics-Condensed Matter*, 2007, **19**, 323101.
9. W. Vanmegen and S. M. Underwood, *Physical Review Letters*, 1993, **70**, 2766-2769.
10. W. Gotze, *Journal of Physics-Condensed Matter*, 1999, **11**, A1-A45.
11. E. J. Saltzman and K. S. Schweizer, *Journal of Chemical Physics*, 2003, **119**, 1197-1203.
12. C. G. Dekruif, E. M. F. Vanlersel, A. Vrij and W. B. Russel, *Journal of Chemical Physics*, 1985, **83**, 4717-4725.
13. K. Dawson, G. Foffi, M. Fuchs, W. Gotze, F. Sciortino, M. Sperl, P. Tartaglia, T. Voigtmann and E. Zaccarelli, *Physical Review E*, 2001, **63**, 17.
14. M. Tripathy and K. S. Schweizer, *Physical Review E*, 2011, **83**, 041406.
15. R. C. Kramb, R. Zhang, K. S. Schweizer and C. F. Zukoski, *Journal of Chemical Physics*, 2011, **134**, 014503.
16. N. Dorsaz, G. M. Thurston, A. Stradner, P. Schurtenberger and G. Foffi, *Soft Matter*, 2011, **7**, 1763-1776.
17. A. Mohraz, E. R. Weeks and J. A. Lewis, *Physical Review E*, 2008, **77**, 060403.
18. W. J. Hunt and C. F. Zukoski, *Langmuir*, 1996, **12**, 6257-6262.
19. W. Gotze and T. Voigtmann, *Physical Review E*, 2003, **67**, 021502
20. R. Jadrich and K. S. Schweizer, *Journal of Chemical Physics*, 2011, **135**, 234902.
21. D. C. Viehman and K. S. Schweizer, *Physical Review E*, 2008, **78**, 051404.

Chapter 2. Role of Particle Size and Polymer Length in Rheology of Colloid-Polymer Composites [1]

2.1 Introduction

The mechanical properties of polymers are often enhanced by addition of sub-micron colloidal particles.[1] Such particle filled polymer melts are referred to as nanocomposite when the particle size is below ~100nm in diameter. Particles can enhance elasticity, push the composite glass transition temperature up or down and can increase or decrease the viscosity of the composite melt.[2, 3] Previous studies that focused on the rheology of unentangled polymer nanocomposite melts demonstrated that in miscible systems, the rheology of the composite melt is well described as effective hard spheres suspended in a Newtonian continuous phase up to a high packing fractions.[2, 4] On the other hand, for the same polymer-particle systems, at fixed particle size when the polymer molecular weight is increased to a value near where the polymer chains entangle, detailed studies of composite microstructure demonstrate the inappropriateness of treating polymer melts as structure-less continuum even when the ratio of polymer radius of gyration to the particle diameter, R_g/D_c, is only 0.02.[2]

Here we investigate changes in flow properties in composites of unentangled polyethylene glycol (PEG) with a focus on the effects of silica particle size and high rates of deformation. We are interested in uncovering the effects of particle size and polymer molecular weight on the reinforcing properties of highly filled composites while exploring melt flow properties at shear rates where these composites thicken. In these systems, PEG adsorbs to the particle surface, giving rise to particle and polymer

[1] Reproduced with permission from *Macromolecules* DOI 10.1021/ma301184t. Copyright 2012 American Chemical Society

miscibility. The particle's index of refraction is nearly matched to that of the polymer and charges at the particle surface are eliminated by the low dielectric constant of the polymer melt such that direct inter-particle interactions are limited to very weak van der Waals attractions. At low particle volume fractions these systems are thus expected to have rheological behavior similar to that of polymer coated particles in a Newtonian continuous phase.

When macroscopic surfaces are driven together in a polymer melt where the polymer adsorbs to the particle surface, soft repulsions begin to appear when the surfaces are separated at a distance of less than ~5-6R_g, with a hard repulsion developing for separations of 2-3R_g.[5, 6] In colloid filled polymer melts, the hard particle surfaces alter polymer configurations. These zones of altered configuration begin to interact as the particle volume fraction is raised. As with macroscopic surfaces, when the average surface separation between two particles, h, in units of D_c is estimated as: $\frac{h}{D_c} = \left(\frac{\phi_m}{\phi_c}\right)^{1/3} - 1$, adsorbed polymer layers begin to interact at h/R_g<3.6 for unentangled polymer and h/R_g<6 for entangled polymer. Here ϕ_c is the volume fraction and ϕ_m is the maximum packing fraction (~0.64 for spheres). As a result, in addition to chemical details of segment-particle surface interactions, the potential of mean force between particles is expected to be a function of D_c, R_g and volume fraction just as charge stabilized particles, the interaction between which is a function of D_c, $1/\kappa$ (Debye length) and ϕ_c.[7, 8]

For particles suspended in polymer melts to experience soft repulsions mediated by the adsorbed polymer layer, the appropriate attraction strength between polymer

segments and particle surface must be achieved. Weak attractions result in depletion attractions that drive the particles to aggregate. Thus to produce a stable dispersion of particles in a melt, the polymers must experience a net attraction to the particle surface.[9] The Polymer Reference Site Interaction Model (PRISM) of Schweizer and coworkers has been developed to predict microstructures of polymer and particles in nanocomposite melts.[10] Comparisons of polymer and particle microstructure for low molecular weight unentangled polymer with PRISM predictions show near quantitative agreement.[11, 12] PRISM predicts weak changes to composite microstructure and adsorbed layer thickness with increasing polymer molecular weight.

Contrast matching neutron scattering[13] and rheological studies[14] demonstrate that the adsorbed polymer layer grows in thickness with increasing molecular weight. Indeed Anderson et al show that when working with 44 nm silica particles suspended in polyethylene glycol melts with molecular weights of 400-20,000, the particle's intrinsic viscosity increased in a manner consistent with an effective hard core diameter of $D_c(1+2.8R_g/D_c)$.[14] Anderson et al reported that this increase in effective particle size with molecular weight is accompanied by a decrease in colloidal stability indicative of a weakening of repulsions or the introduction of weak inter-particle attractions. However for low molecular weight (MW<1000), the effective hard sphere model captures the linear viscoelastic rheology until particles are brought to a volume fraction where $h/D_c \sim 3.6R_g/D_c$. Increases in adsorbed polymer layer thickness are associated with greater structure in colloidal suspensions. There is thus some confusion as to success of PRISM for low molecular weight polymer composites as well as the failure of PRISM at higher molecular weights based on the nature of the absorbed polymer layer and how it

influences the potential of mean force felt by the particles. These observations of silica in PEG melts augment earlier studies of polybutylene melts filled with polystyrene spheres[15] and suggest that nonequilibrium polymer configurations become increasingly dominant as polymer molecular weight grows.

Here nonequilibrium configurations are associated with the inability of adsorbed polymer segments to rapidly exchange with those in the bulk such that polymer configurations near the particle surface cannot relax into an equilibrium state over reasonable time scales. The increased segment residence time at the particle surface alters particle and polymer microstructures.[13] In studies of composites made of 44 nm silica in PEG for molecular weights above 3000, the proximity of the surfaces was found to introduce greater entanglement at volume fractions where $h/D_c<6R_g/D_c$. The interaction of the adsorbed polymer layers at these average surface spacing does not lead to particle aggregation, but increasing polymer MW does result in kinetic arrest of the particles at ϕ_c~0.30 and the composites displaying brittle fracture. The gel transition observed in these systems is not well described as a glass transition of effective hard spheres.

A variety of previous studies have explored the role of soft repulsions on linear and nonlinear suspension rheology. For example, the effects of particle size and polymer induced interaction potentials on rheological properties and microstructure of charged polymer colloids (with varying ionic strength, particles with grafted polymers (fixed graft size and variable particle size[16]) as well as microgel systems and particles with the core-shell microstructures have been extensively reported.[17-20] Often, these studies analyze experimental observations starting models where the adsorbed or grafted polymers starts

define an effective hard core volume fraction that accounts for the increased excluded volume introduced by the adsorbed or grafted polymer layers.

Consistently, as volume fraction is raised, there is a transition from a state where a zero shear rate viscosity can be measured to a state the suspensions shear thinned in all measurable shear rates, $\dot{\gamma}$. Often volume fractions are reached where the suspensions show a dynamic yield stress where the stress is very weakly dependent on $\dot{\gamma}$ followed at high shear rates by the approach of a high shear rate terminal viscosity. At effective volume fractions where the yield stress plateau develops, the linear elastic storage modulus, *G'*, displays a high frequency plateau while the linear loss modulus, *G"*, develops a minimum indicating a separation of relaxation time scales. These features are consistent with the onset of glassy behavior as predicted by mode coupling theory (MCT) .[17] However at effective volume fractions where absorbed polymer layers begin to interact, the deformability of adsorbed or grafted layers dominate the flow,[20] demonstrating the need for care in interpreting the flow properties at high volume fraction and high stresses.

Working with a range of particle sizes enables us to explore a broad range of shear rates. The particles are Brownian and for the Newtonian polymer melts studied here, the diffusivity can be written as $D_0=k_BT/3\pi\eta_pD_c$. Here η_p is the viscosity of solvent and k_BT is product of the Boltzmann parameter and absolute temperature. Typically shear thickening is associated with high applied stresses where hydrodynamic interactions dominate the suspension microstructure. This occurs where the rate of shear is larger than the rate of diffusion. This ratio of rates is characterized by the Peclet number, $Pe = 3\pi\eta_p\dot{\gamma}D_c^3 / 4k_BT$ and thickening is typically observed when Pe>10.[21] Thickening

becomes noticeable as the volume fraction increases and, initially is observed as a logarithmic increase viscosity with shear rate. As the volume fraction approaches close packing the viscosity undergoes a discontinuous increase as shear rate is increased.

If thermally active particles are suspended in a Newtonian continuum and experience only hard core interactions, dimensional analysis suggests that for a given volume fraction, shear thickening will be observed at a universal value of *Pe*.[21] As a result, the absolute shear stress at the onset of shear thickening satisfies $\tau_c \propto D_c^{-3}$. When interactions other than those of volume exclusion are operational, the size dependence of τ_c will change. For example, for particles experiencing short range, screened electrostatic repulsions satisfy $\tau_c \propto D_c^{-2}$.[7] Similar results have been observed with particles experiencing soft repulsions that demonstrate the sensitivity of shear thickening to the hydrodynamic permeability of polymer coat.[16, 22] Attractions are known to delay thickening to larger stresses[23] while soft polymer layers are known to weaken the onset of thickening.[22] Little has been reported for shear thickening in nanocomposite melts where, as discussed above the effects of particle size, interactions of absorbed polymer layers and changes to the potential of mean force due to nonequilibirum polymer configurations become important.

Here we focus on four different colloid-polymer composites composed of two different silica particle sizes (D_c=127nm referred to as small particles and D_c=612nm referred to as large particles) and two different polymer molecular weights (polyethylene glycol with molecular weight equaling to 400 and 2000 where the molecular weight for entanglement is ~4000).[14] Below in Section 2.2 we discuss how we create our

composites and characterize composite rheology under steady shear and in linear and nonlinear oscillatory rheometry.

In Section 2.3 we discuss our results with careful attention to the magnitudes moduli, to volume fraction dependencies of characteristic frequencies extracted from linear elastic studies and yielding behavior with a particular focus on flow curves and the stress at the onset of thickening. We show that there are three effects altering composite mechanics at high volume fractions with increasing polymer molecular weight and increasing particle size. First we show that the potential of mean force experienced by the particles suspended in polymer melts is altered by particle size and this effect is enhanced in high MW polymer melts. Secondly, as polymer molecular weight grows- even below the entanglement molecular weight, particles experience weak attractions that extend beyond the extent of bound polymer layers. We attribute these attractions to very slow exchange of absorbed polymer segments with those in the bulk. This gives rise to the effective particle surface becoming chemically similar to the bulk such that the enthalpy of exchange of a segment from bulk to the effective particle surface drops, resulting in a depletion attraction. Thirdly, as the volume fraction is raised such that h/R_g is of order unity, interactions of the polymer layers begin to dominate flow properties. Finally we report that in the composites formed of the low molecular weight polymer, hard sphere scaling is not observed at shear thickening and that shear thickening is considerably weakened as polymer molecular weight is increased.

2.2 Experimental Methods

2.2.1 Sample Preparation

Monodisperse silica particles are synthesized by method that is developed by Stober[24] and extended by Bogush et al.[25] Two different sizes are prepared with D_l=612±20nm (referred to as large particles) and D_s=127±7nm (referred to as small particles) which will be mainly discussed below. In addition, two more particle sizes are included in shear thickening behavior study for low molecular weight which are (730±8) nm and (213±9) nm particles. The product particles are suspended in ethanol solution containing water and ammonia hydroxide. The resulting suspension is concentrated to a mass fraction ~0.20 by heating up the suspension to evaporate the solvent and drive off the ammonia. Following previous studies,[2] we chose to work with polyethylene glycol with MW~400 (MW: 380~420, PEG400, low molecular polymer) at T=25°C and MW~2000 (MW: 1900~2200, PEG2000, high molecular polymer) at T=75°C as the polymer melts. PEG400 is a Newtonian fluid with viscosity ~0.10 Pa s at T=25°C. PEG2000 is also a Newtonian fluid at the condition we study with viscosity ~0.10Pa s at T=75°C.

Concentrated silica particle suspensions are mixed with PEG and the resulting suspensions are placed into a vacuum oven with temperature kept above T_m of PEG to remove ethanol. Below we refer to the four different sets of composites separately as SCSP (small colloid in short polymer), LCSP (large colloid in short polymer), SCLP (small colloid in long polymer) and LCLP (large colloid in long polymer). To determine the volume fraction ϕ_c of particle with mass fraction X_c<0.50, the equation $\phi_c=(\rho_T/\rho_c)X_c$ is used, where ρ_T and ρ_c are the density of the filled composites and pure polymer melts. The composite density, ρ_T, is determined using a Mettler/KEM DA-100 density meter for

low molecular weight polymer (PEG400). The particle density was measured in previous studies to be ρ_c=1.6g/cm^3.[2] The results are quite consistent for large and small particles for the same mass fraction samples. For X_c>0.50, the composite viscosity was too high to be measured in the density meter and volume fraction were determined by extrapolating the plot in the ϕ_c-X_c panel. Previous study has confirmed a similar density of composites independent of polymer molecular weight,[14] so we would use the same volume fraction here for SCLP and LCLP at same mass fractions.

2.2.2 Rheology

Rheology experiment is carried out at C-VOR Bolin rheometer where a cone and plate geometry is used. The cone diameter is 20mm with a 4° angle. Here the temperature is kept at 25°C for PEG400 and 75°C for PEG2000 to keep the similar matrix viscosity high enough (η_p=0.10Pa s) to make sure of studying in a high dimensionless frequency range ($\omega^* = 3\pi\eta_p\omega D_c^3 / k_B T$) and high dimensionless shear rate range ($Pe = 3\pi\eta_p\dot{\gamma}D_c^3 / 4k_B T$) to observe shear thickening in the measurement window which will be discussed below.

Oscillatory stress is used to measure elastic modulus *G'* and viscous modulus *G"* as a function of frequency ω in the frequency sweep experiment with strain γ=0.01 held constant to make sure of searching in a linear region, and *G'* and *G"* are measured by varying shear stress/strain at fixed frequency ω=0.1Hz to study the nonlinear rheology and yielding behavior. Moreover continuous stress is applied in the viscometry measurement to study the viscosity as a function of applied shear stress or shear rate to understand the shear thickening behavior. Pre-shear has been applied and 1 min recovery time has been allowed before each measurement. We found that the samples recovered

their properties within the time frame of switching shear stresses. The measurements were found to be reproducible with the samples showing no thixotropy and flow properties being independent of shear-history.

2.3 Results and Discussions

2.3.1 Low Concentration Viscosity

In Figure 2.1, the relative zero shear viscosity $\eta_{r,0} = \eta_0/\eta_p$ is plotted as a function of silica particle volume fraction, where η_0 is the viscosity in the low shear rate region and η_p is the polymer matrix viscosity (η_p=0.10Pa s for PEG400 at T=25°C and for PEG2000 at T=75°C), and the resulting low volume fraction data is fit to:

$$\eta_{r,0} = 1 + 2.5k\phi_c + H(k\phi_c)^2 \qquad (2.1)$$

Here $k=\phi_{eff}/\phi_c$ with ϕ_{eff} standing for the effective hard sphere volume fraction and H is interaction coefficient which should be 5.9 for hard sphere interaction.[26] The fitting results are also included in Table 2.1.

Within experimental uncertainty, when suspended in PEG 400, both large and small particles behave essentially like hard spheres with single particles dissipating energy as if they have a slightly larger core size. An effective particle size can be calculated from k assuming that single particles dissipate energy under shear as if they were composed with a hard core surrounded by an immobilized polymer layer with thickness δ at the outer edge of which the non-slip boundary condition holds. Under these conditions, $k=\phi_{eff}/\phi_c=(D_{eff}/D_c)^3=(1+2\delta/D_c)^3$. We tabulate the values of δ in Table 2.1. For PEG2000, k is larger than for PEG400 showing that the steric layer thickness is independent of the particle size, but increases proportionally with the square root of the polymer polymerization degree in agreement with previous work, where steric layer thickness is

found to be proportional to R_g ($R_g \propto \sqrt{N}$ with N representing the polymerization degree) for PEG with MW in the range of 400-20000.[14] The values in Table 2.1 are smaller than the values reported for 44 nm diameter silica particles reported previously,[14] which may reflect the effects of surface curvature. Also for PEG2000, *H* is increased slightly for both large and small particles further away from 5.9, denoting enhanced pair interactions. However, *H* lies close to the hard sphere value of 5.9 showing that the interaction is small for both PEG400 and PEG2000.

2.3.2 Linear Rheology

At elevated volume fractions, the linear elastic properties of these composites vary dramatically with particle size and polymer molecular weight. In Figure 2.2, we present the linear elastic moduli and viscous moduli as a function of frequency for representative volume fractions of the four sets of composites. Here the dimensionless parameters are obtained as following: $G'^* = G' D_c^{\,3} / k_B T$, $G''^* = G'' D_c^{\,3} / k_B T$ and $\omega^* = \omega D_c^{\,2} / D_0$, where *G'*, *G''*, ω are the elastic modulus, viscous modulus and angular frequency ($\omega = 2\pi f$ with *f* representing frequency in unit of Hz), and D_0 is the dilute particle diffusion coefficient.

At low frequencies the composites enter a low frequency terminal region where both *G'** and *G''** increase as power law functions of ω* with exponents of 2 and 1, respectively, below a crossing point ω_{x1}^*, where $G'^* = G''^* = G_{x1}^*$.[27] For the data shown in Figure 2.2, the terminal region is only observed with LCSP while, for the other three sets of data, the terminal region is entered at frequencies lower than could be probed. At even higher frequencies, there is a second crossing point at ω_{x2}^*, where $G''^* > G'^*$. As the volume fraction increases, a minimum develops in *G''* at ω_m and *G'* develops a "rubbery" plateau, $G_p' = G'(\omega_m)$.

In the terminal region at low frequencies, the viscous nature of the composite is probed with composite's zero shear rate viscosity given by G''/ω. The cross over frequency ω_{x1}*, characterizes the rate particles can diffuse out of nearest neighbor cages such that the inverse of ω_{x1}* is comparable to the α-relaxation time of colloidal glasses.[28, 29] At frequencies between ω_{x1}* and ω_{x2}*, the sample is deformed at rates where particles cannot exchange nearest neighbors but at rates slower than the time it takes particles to explore the nearest neighbor cage. For frequencies greater than ω_{x2}*, the deformation rate becomes larger than the short time rate of particle diffusion within their cage, particle motion is increasingly frozen and the suspension responds with a high frequency viscosity.[27]

As shown in Figure 2.2, due to fixed instrumental frequency range and a substantial change in particle volume, the range of dimensionless frequencies covered by the experiments for large and small particles are substantially different. A consequence is that we cannot probe the low frequency region for large particle composites and we cannot probe deeply into the high frequency region for small particle composites. In addition we note that the range of dimensionless moduli measured is substantially larger for the large particles than for the small particles. Despite the large dimensionless moduli reported, the absolute moduli for the large particles are small and thus we can only report reliable measurements at the largest volume fractions studied.

As mentioned above, values of the $1/\omega_{x1}$ (or the frequency at the maximum in G'') are often taken as characterizing the α-relaxation time for particles diffusing out of nearest neighbor cages[4, 28] For near hard sphere interactions, the α-relaxation frequency decreases with increasing volume fraction as $(\phi_g - \phi_c)^{-\alpha}$ with ϕ_g~0.58 up to a critical volume

fraction above which this critical scaling is no longer observed and the α-relaxation time increases more slowly with volume fraction.[4] The deviation from the critical scaling is taken as an indication that the system has entered an activated relaxation zone where relaxation times will diverge only at random close packing. In the activated glassy transport model of Schweizer and coworkers, the magnitude of relaxation time in the activated region is set by the height of a dynamical potential which is determined in a self-consistent manner from the equilibrium microstructure and D_0 while the magnitude of the elastic modulus is set by the curvature of the dynamical potential at its minimum.

We note that $\omega_{x1}^* < 10^{-3}$ for SCSP and for LCSP $10^{-1} < \omega_{x1}^* < 10^{0}$ for similar range of volume fractions and that there is a greater characteristic frequency as determined by ω_{x1}^* and ω_m^* for the small particles than the large particles. Interpreted in terms of the activated transport model, this suggests that, at the same volume fraction, the confining potential for the large particles has a lower barrier across which the particles must diffuse to exchange nearest neighbors than is experienced by the small particles. Moving to higher MW we see that ω_{x1}^* for SCLP is less than 5×10^{-4} for all volume fractions greater than 0.39 indicating greatly reduced rates of long range diffusion are created by suspending the small particles in higher molecular weight melts. On the other hand, ω_{x1} for LCLP are of the same order as LCSP showing that the barrier to diffusion is approximately the same at low and high molecular weights clearly indicating that effects of absorbing polymer are enhanced as the average spacing between the particles shrinks relative to the polymer's radius of gyration.

In the frequency range between ω_{x1}^* and ω_{x2}^*, the particles remain diffusive but cannot exchange nearest neighbors. The separation of time scales for long range and short

range diffusion are classic indicators of glass or gel formation. All the composites studied here show this state transition. In Figure 2.3, we present volume fraction dependencies of ω_m*,and G_p'* along with the prediction of Kobelev et al for hard sphere glasses.[30] The horizontal lines in Figure 2.3(A) are dimensionless frequency ω* for f=0.1Hz for the four different sets of composites where we ran stress sweep experiments discussed in the following subsection.

The frequency at the minimum in G'', ω_m, is often taken as a surrogate for the beta relaxation time- the time it takes particles to explore nearest neighbor cages.[4] With this interpretation in mind we see in Figure 2.3(A) that the large particles have considerable greater short time diffusivities than small particles when suspended in both low and high molecular weight polymers. We note that we have chosen temperatures such that the viscosity of the PEG400 melt is the same as the PEG2000 such that the shifts in ω_m* can be made at fixed matrix viscosity η_p. In this case, the self-diffusivity of the particles in the two molecular weight melts is expected to be similar. We note that ω_m* appears to be a weak function of polymer molecular weight once particle size is fixed. This suggests that despite evidence of greater attractions between particles with increased molecular weights, particle mobility within cages set by nearest neighbors is weakly dependent on polymer molecular weight.

While the changes in ω_{x1} and ω_m are associated with changes to the dynamical potential barrier to diffusion,[31] changes in G_p'* are associated with probing the curvature of the dynamical potential barrier and its minimum and are argued to have a form: $\frac{G' D_c^{\,3}}{k_B T} = 0.58\phi \frac{D_c^{\,2}}{r_{loc}^{\,2}}$,[32] where r_{loc} is the localization length or a measure of the range of

local particle motion when trapped within nearest neighbor cages. When particle-particle attractions are increased, r_{loc} is decreased, resulting in larger elasticity.

In Figure 2.3(B), $G_p'^*$ is essentially the same for SCSP and LCSP with volume fraction dependence captured well by the volume fraction dependence of predicted zero stress dimensionless elastic modulus G'^*: $G'^* = (1.6\times10^{-4})e^{26\phi}$ for hard spheres.[30] These results are consistent with the low volume fraction viscosity measures suggesting nearly hard sphere behavior for low molecular weight suspending media [4] and suggest that r_{loc}/D_c is similar for small and large particles in PEG400. We note substantial differences in ω_{x1}^* values for these samples suggesting that the barrier height for activated diffusion is larger for the small particles. We note that theoretical studies suggest that for hard particles, there is a tight linkage between the barrier height, F_B and the localization length with $F_B \sim r_{loc}^{-1}$,[31] suggesting that elasticities and diffusion times should be inversely correlated. We expect the diffusion times to scale as $\exp(F_B/k_BT)$ such that an increase in modulus will track a rapid drop in ω_{x1}^*. That we do not observe this coupling as we change particle size suggests we are not working with volume exclusion potentials of mean force.

The limiting high frequency behavior of the elastic modulus of colloidal suspensions has been explored by Lionberger and Russel who show that, at high frequencies for no slip boundary conditions $G'^* \sim \omega^{*1/2}$ while for slip boundary conditions G'^* is independent of strain frequency.[33] We note a tendency toward slip boundary conditions as particle size decreases for PEG400.

When polymer MW is increased to 2000, $G_p'^*$ increases tremendously for both large particles and small particles. For SCLP, samples become solid-like when ϕ_c is as low as

0.37, where h/R_g=13. Due to this average particle separation being approximately twice that where we expect adsorbed polymer layers interact, we conclude that the jump in modulus cannot be explained by repulsive interactions and that these systems form colloidal gels due to attractions. This effect is also seen in the increase of $G_p'^*$ for large particles in moving from small polymer to large polymer melts.

The volume fractions of the large particle composites studied here are well above that where small hard particles display glassy behavior. However, these systems show limited separation at time scales in frequency sweeps and, as discussed below, have a very weak dynamic yield stress plateau in continuous shear studies. This may be attributed to these particles experiencing a weak attraction such that the system lies in a re-entrant glassy region where attractions melt the glass.

These results indicate that particles feel stronger attractions in PEG2000 than in PEG400. Independent of molecular weight PEG adsorbs strongly to the particle surface.[13] Thus these attractions are between polymer coated surfaces. Within the context of a PRISM framework, the primary variable controlling composite microstructure and mechanics is the exchange enthalpy of moving a polymer segment from the bulk to the particle surface, ε_{pc}. If ε_{pc} is small, polymer does not adsorb and depletion attractions develop. Only when ε_{pc} is sufficiently large will thermodynamically stable layers form and the particles and polymer become miscible.[34] Here we have a system where the polymer adsorbs and generates miscible composites. However, the particles are also seen to experience attractions. We believe this is due to non-equilibrium adsorption of polymers arising from increasing number of absorbed polymer segments per chain as polymer molecular weight increases. The increased number of binding segments per

chain will reduce the ability of the adsorbed polymers to reach equilibrium with polymer segments in the bulk. As a result, from the perspective of a polymer segment in the bulk, the surface will look as it is composed of PEG segments resulting in a decrease in effective ε_{pc}. Thus while the exchange enthalpy is sufficient to create a stable polymer layer at each particle surface, because polymers cannot exchange freely with those in the bulk, a weak depletion attraction develops as a result of a drop in the effective ε_{pc}.

From the studies of the linear rheology of these composite melts, we draw two conclusions: (1) as ϕ_c increases gels or glasses are formed. The high volume fractions where the separation of time scales occurs (for all but SCLP) suggests the systems experience volume exclusion and weak attractions. (2) The differences in ω_m* for SCSP and LCSP denotes that composite dynamics are controlled by details of interactions while the magnitudes and volume fraction dependencies of G_p* for these two samples suggest hard sphere behavior. When increasing the MW of polymer, the jump in G_p* indicates that attractions are introduced.

Having established general features of the polymer induced particle interactions, below we explore the effects of polymer induced attractions on the nonlinear rheology of the composites and changes to the flow properties when the composites are subjected to continuous shear.

2.3.3 Nonlinear Rheology and Yielding Behavior

In many reports of suspension dynamics, yielding is investigated by subjecting suspensions to a fixed strain frequency and an increasing maximum strain. At high volume fractions the G'* is seen to decay while G''* passes through a maximum and crosses G'* at a specific strain and stress amplitude. These strains and stresses are

typically taken as characterizing yield stress and strain of the suspension. As discussed above and shown in Figure 2.2, as ω^* is increased above ~10^1-10^2, ω_{x2}^* is approached. At these frequencies, for all strains- even in the linear response region $G''^*>G'^*$ and this standard method of characterizing yield stresses becomes difficult to interpret. This is of particular concern in studies where particle size is varied as increasing D_c, increase ω^* rapidly driving the sample characterization towards ω_{x2}^* and making it difficult to compare flow properties between materials at the same volume fraction containing particles of different sizes. Here we propose to use a frequency near ω_m^* for amplitude sweeps as a means of characterizing yielding behavior as particle size is varied.

As shown in Figure 2.3(A), f=0.1Hz is near the frequency ω_m where the minimum of G''^* is detected and rubbery plateau of G'^* is observed. We use this frequency to investigate yielding. By choosing a frequency near ω_m^*, we are looking at yielding at strain frequencies where the particles are trapped in cages. Therefore we are thus characterizing the nonlinear deformation behavior by increasing the maximum strain at a frequency within a range that exceeds the rate the particles can exchange nearest neighbors and below a frequency where the particles do not respond to flow. As a result, particles have insufficient time to escape from the dynamical arrest state at low strain magnitude, but ample time to explore nearest neighbor cages during a strain cycle.

Results of these amplitude sweeps are shown in Figure 2.4 where in large strain limit, for the 127 nm particles in both polymers, the moduli decrease $G'^* \propto \gamma^{-2}$, $G''^* \propto \gamma^{-0.6}$ ($\phi_c \geq 0.534$ for SCSP and $\phi_c \geq 0.398$ for SCLP). For the 612 nm particles in the low molecular weight polymer, $G'^* \propto \gamma^{-1}$ ($\phi_c \geq 0.580$). When suspended in PEG2000 the large particles have moduli that decay as $G'^* \propto \gamma^{-1.6}$ ($0.504 \leq \phi_c \leq 0.592$) in the large amplitude

limit. Here γ is the shear strain. For LCSP (Figure 2.4(B)) and LCLP (Figure 2.4(D)), the large strain behavior of G''^* is complicated by the onset of strain thickening, where the G''^* is decreased first and then increased in the large γ magnitude limit. To understand this phenomenon better, continuous shear is applied which will be discussed in the next subsection. All these modulus behaviors at large shear strain are summarized in Table 2.2.

Kobelev and Schweizer extended the activated transport model to predict an absolute yield stress where the applied stress eliminates thermodynamical barrier limiting diffusional exchange of nearest neighbors. In previous studies this has been associated with the stress (strain) in amplitude sweeps where $G'^*=G''^*=G_x^*$.[30] In Figure 2.5 we present τ_x^*($\tau_x^* = \tau_x D_c^3 / k_B T$), G_x^* and γ_x which represent a measure of the absolute yield stress, the elasticity at the yield stress and the strain at the yield stress, respectively.

The trends with change in particle size and molecular weight observed in G_p^* are duplicated in Figure 2.5(A) and (B) for τ_x^* and G_x^*. For both large particles and small particles, increasing polymer MW results in increases in stress τ_x^* and elasticity G_x^* at yield point, consistent with the presence of attractions. We note that G_x^* are larger for LCSP than SCSP. We attribute this to the larger dimensionless frequency of deformation which pushes G''^* closer to G'^*.

2.3.4 Flow Curves and Shear Thickening

The response of the composite melts to continuous shear is presented in Figure 2.6, where we present the dimensionless stress τ^* as a function of Pe, where $\tau^*=\tau D_c^3/8k_BT$ (where τ is the stress). These composite melts show general flow features expected for concentrated colloidal suspensions: i) at low Pe and low volume fractions, a terminal

region can be observed where in this double logarithmic plot, the slope of the curve $d\log_{10}(\tau)/d\log_{10}(\dot{\gamma})$ has a value of unity, and the composite melts show a zero shear rate viscosity. ii) As volume fraction increases the composite melts shear thin at a volume fraction dependent value of $Pe = Pe_1$. As the volume fraction increases the stress begins to develop a plateau where $p = d\log_{10}(\tau)/d\log_{10}(\dot{\gamma})$ takes on a value <<1 for an extended *Pe* region. For the SCLP composites, at the highest volume fractions studied, *p* approaches zero indicating the composite melt is showing a dynamic yield stress. iii) Above a second characteristic volume fraction dependent value of $Pe = Pe_2$, a high shear rate terminal behavior is approached where *p* again approaches unity, iv) Pe_2 is weakly dependent on volume fraction while Pe_1 decreases with increasing volume fraction as the dynamic yield stress plateau becomes more prominent. v) At sufficiently high volume fractions shear thickening occurs at Pe_3 above which the slope $p>1$. While Pe_3 is a function of volume fraction, the stress at thickening, τ_c^*, is a weak function of volume fraction. We note that these features are those expected of dense suspensions of stable particles suspended in low molecular weight solvents.[16] One thing to note here is that for the highest ϕ_c samples of LCSP and LCLP, a double yielding phenomenon is observed for LCSP. This first continuous thickening with smooth change of slope p is explained as a result of hydrocluster formation as other samples, the second discontinuous thickening with sharp change of slope p is attributed to jamming which is only observed at very high ϕ_c. This phenomenon has also been reported previously with polymer stabilized large particles in low MW solvent.[35] We report viscosities based on average shear stress and shear rate. If there are flow instabilities or shear banding, we did not observe them.

Shear thinning in dilute colloidal suspensions occurs as hydrodynamic forces alter suspension microstructure. These effects have been extensively studied with calculations of changes to microstructure with stress predicted and measured.[36] As volume fraction is raised the suspension develops a glassy response where *G"* develops a minimum. This behavior manifests itself in continuous shear as the slope *p* for the dynamic stress plateau decreasing rapidly as volume fraction is raised. The shear rate at which hydrodynamic forces dominate over thermodynamic forces is a weak function of volume fraction (i.e., Pe_2 shows a weak volume fraction dependence), and the range of shear rates where shear thinning is observed increases. These ideas have been developed for particles suspended in low molecular weight solvents but apply equally to the composite systems at hand.

The dynamic glass transition theory postulates that above a cross over volume fraction, ϕ_x, corporative motion is increasingly required for particles to exchange nearest neighbors. For $\phi_c/\phi_x<1$, increases in shear stress result in continuous changes of suspension microstructure and shear thinning occurs by smooth and rapid diffusion. As ϕ_c/ϕ_x grows above unity, particles become increasingly localized, the barrier to diffusion increases rapidly and the rate of diffusion decreases rapidly resulting in a rapidly increasing zero shear rate viscosity. For $Pe_1<Pe<Pe_2$, if the dynamical energy barrier height were independent of the applied stress, the result would be a dynamic yield stress plateau where the stress is independent of *Pe* ($\tau^* \sim Pe^p$ where $p \sim 0$).[37] In this region particles are trapped by nearest neighbors for a substantial period of time before the imposed microstructural deformation forces particles to rearrange their microstructure and energy is dissipated in rapid particle jumps at a rate that controlled by the thermodynamic forces acting on the particles and thus is independent of the applied shear

rate.[37] If the applied stress is sufficient to alter suspension microstructure such that the energy dissipated in each particle jump decreases with increased shear rate, a weaker yield stress plateau will be observed ($p>0$). The more strongly localized are the particles due to crowding or due to inter-particle forces, the less the rate of deformation is controlled by smooth deformation and the larger the fraction of energy in the sheared system will be dissipated by rapid jumps between localized positions. The high shear rate terminal regime is entered at Pe_2 where the rate of deformation becomes comparable to the rate of diffusion over the dynamical barrier. For larger shear rates, a high shear rate plateau viscosity is achieved and hydrodynamic interactions control stress transfer and the suspension microstructure.[38] These hydrodynamic stresses ultimately drive particles to form hydroclusters and at Pe_3, shear thickening is observed.

This idealized picture is altered by details of particle interactions as seen for the four sets of data shown in Figure 2.7 where we compare flow curves at the same volume fraction for the two particle sizes suspended each in the two polymer melts. The growth of p (i.e., the weakening of the dynamic yield stress plateau) and an increase in Pe_1 are associated with a decrease in R_g/D_c. At this volume fraction, the high shear rate viscosity is similar for all but the SCLP. This system displays a very slow approach to high shear rate terminal viscosity dominated purely by hydrodynamic interactions. If the particles behaved as hard spheres, the flow curves in Figure 2.7 would superimpose. This is seen for SCSP and LCSP samples over the range of Pe where we could gather overlapping data suggesting the samples interact weakly. However, consistent with the linear and nonlinear viscoelastic data shown in previous sections increasing polymer molecular

weight alters particle interactions at low shear rates indicating that the increased molecular weight alters the potentials of mean force experienced by the particles. .

Here to explore the shear thinning behavior, we use the slope p at the inflection point Pe_d where $\frac{d^2 \log_{10}(\tau^*)}{d \log_{10}(Pe)^2} = 0$ (or the stress plateau region where the slope $p = d\log_{10}(\tau^*)/d\log_{10}(Pe)$ is constant). p decreases with increasing volume fraction as expected, with the detailed information of p supplied in supporting information. We did not present the values of p for LCSP as we are not able to get to measure stresses at sufficiently small values of Pe to track the inflection point. Based on other comparisons, similar behaviors between SCSP and LCSP are expected for the slope at the inflection point. Of particular significance is that at fixed ϕ_c ~0.505 (as shown in Figure 2.7), p increases as R_g/D_c decreases indicating that the development of a well-defined yield stress plateau is sensitive to soft interactions that are 1% or less of the particle diameter. This can be imagined as indicating that particles are more highly constrained by nearest neighbors and that the barrier to flow is less readily degraded as the extent of the adsorbed polymer layer relative to the particle size increases. And when changing to PEG2000, p decreases sharply especially for SCLP.

As pointed by de Kruif et al.[36], the viscosity of hard-sphere systems at shear-thinning region correlates empirically with

$$\frac{\eta_r - \eta_{r,\infty}}{\eta_{r,0} - \eta_{r,\infty}} = \frac{1}{1 + \left(\tau^* / \tau_d\right)^m} \tag{2.2}$$

Here $\eta_{r,0}$ is the relative zero shear viscosity of the suspension, $\eta_{r,\infty}$ is the relative high shear rate viscosity of the suspension, τ_d is the critical dimensionless shear stress which

can be treated as the inflection point of the stress plateau and is a function of volume fraction, and m is a fitting parameter. This correlation works well up to ϕ_c~0.50 for hard sphere systems with $1.4<m<1.8$. At elevated volume fraction where $\eta_{r,\infty} << \eta_{r,0}$, $p=2/(2+m)$ yielding for volume exclusion and weakly attractive systems below the gel point [2, 39-41] $0.53<p<0.59$. By assuming that this correlation characterizes the ability of shear to alter microstructure and stress transfer at volume fractions where the particles are not localized, we are able to define a glass or gel volume fraction as that point where $p<0.56$. Using this definition we see that the gel or glass transition occurs at volume fractions of 0.511, 0.330 and 0.549 for SCSP, SCLP and LCLP respectively. We note that p changes in a continuous manner as volume fraction is raised and that this definition of kinetic arrest is somewhat arbitrary. On the other hand, the volume fractions of kinetic arrest defined by this method are close to those where ω_m is first observed: corresponding to 0.533, 0.369 and 0.570 for SCSP, SCLP and LCLP, respectively indicating a variety of measures capture the onset of rapid slowing of relaxation times with increasing volume fraction.

Shear thickening is associated with hydrodynamic stresses forcing particle together and the build-up of clusters held together by shear forces. At high volume fraction these clusters span the shear gap and result in positive normal stresses and discontinuous jumps in viscosity as shear rate is increased. Shear thickening is delayed by strong interparticle forces-attractions or repulsions. The larger the repulsion is, the higher the shear rate is required to establish the correct hydrodynamic conditions to drive cluster formation. As shown in Figure 2.6, SCSP, LCLP and LCLP all reach hydrodynamically controlled stress transfer and shear thickening is observed. For the SCLP case, the inter-particle

forces remain sufficiently strong that, over the shear stress range probed, hydrodynamic forces cannot overcome inter-particle forces and thickening is not observed. The dimensionless stresses at the onset of thickening are shown in Figure 2.8(A) with detailed values shown in Supporting Information. While hydrodynamic forces must dominate stress transfer to observe shear thickening, short range inter-particle forces also are known to have a strong impact on the shear rate at the onset and the degree of shear thickening. For particles only experiencing excluded volume interactions, due to the no flux boundary condition at the particle-fluid interface, Brownian forces gives rise to large gradients in particle number density at the particle surface. The pair distribution function relates hydrodynamic and Brownian forces through the conservation equation and equation governing particle motion. The gradient of pair distribution function is a measure of the effect of magnitude of the thermodynamic force required to balance hydrodynamic force and ensure the no-flux boundary condition. For hard spheres the critical stress at thickening scales as D_c^{-3}. As discussed below, the composites studied here do not display this size scaling and we are forced to recognize that even for the low molecular weight polymer, the details of the potential of mean force near contact are important in establishing the onset and magnitude of the thickening.[8]

We observe that the stress at thickening is a weakly increasing function of volume fraction. We associate this with the average inter-particle spacing such that as the particles approach contact, the stress required for them to thicken will diverge. The equilibrium surface separation, h, can be expressed as:

$$h / D_c = (\phi_m / \phi_c)^{1/3} - 1 \qquad (2.3)$$

As the adsorbed polymer layer soft interaction is important, proved already in dilute suspension, here we would incorporate a simplified surface interaction potential in the following form:[16]

$$U(r) = Ah^{-B} \tag{2.4}$$

where A and B are fitting parameters determined by polymer size and particle size. Here we base our discussion on the assumption of force balance where hydrodynamic force equals potential of mean force at the equilibrium surface separation.

$$\frac{3\pi\tau_c D_c^3}{16h} = -k_B T \frac{\partial(U/k_B T)}{\partial r} \tag{2.5}$$

From these expressions we postulate that inter-particle forces influence the stress scale but not the volume fraction dependency of this divergence and write the dimensionless stress at thickening as:

$$\tau_c^* = C\left[\left(\frac{\phi_m}{\phi_c}\right)^{1/3} - 1\right]^{-B} \tag{2.6}$$

where ϕ_m is a maximum packing fraction (set here to be 0.64 consistent with previous experimental studies[36]). We anticipate C will be independent of volume fraction and carry information about particle size and pair potential while B will be a universal constant. Shown in Figures 2.8(A) and (B) are plots of τ_c* fit with Equation (2.6). We tabulate best fits for our data in Table 2.3 where we note our expectation of a constant value of the exponent B within experimental uncertainty. Our experimental results of critical shear stresses for small particles in PEG400 and large particles in PEG400 and PEG2000 are summarized in Supporting Information and presented in Figure 2.8(A) along with a comparison of a previous correlation of experimental data for hard spheres:[8]

$$\frac{\tau_c D_c^3}{8k_B T} = 0.1e^{\phi/0.153} \tag{2.7}$$

The proposed scaling captures the data well with B a weak function of D_c or R_g, and the coefficient C dependent on D_c. Here C increases with D_c in PEG400, showing a scaling $\tau_c \propto D_c^{-\alpha}$ where α is smaller than 3. The change in modulus with polymer molecular weight is associated with an increase in attraction which is expected to delay thickening. This expectation is confirmed with magnitude of τ_c* being slightly larger for LCLP than LCSP.[13] Previous studies with silica particles dispersed in silicon oil have shown that medium viscosity has no effect on critical shear thickening stresses. In these studies a universal shear response is observed when hard sphere scaling and effective volume fractions are used. As a result, we can conclude that deviations from this universal behavior result from variations in particle interactions.[42] Similarly in our study where the viscosity kept constant with temperature increasing for LCLP, we do not attribute the slight increasing observed in τ_c* to the temperature change which affects the dimensionless scaling, but to an increased attractive interaction that results from increasing polymer MW. This conclusion is confirmed by the disappearance of shear thickening when moving from SCSP to SCLP.

To confirm the particle size scaling of thickening in PEG400 melts, we gathered thickening data on two more particle size (D_c=213nm and D_c=730nm). The critical stresses at the onset of thickening are shown Figure 2.8(B) with the results of fitting the data summarized in Table 2.3, In Figure 2.9, we show how the characteristic critical stress for thickening varies as a function of D_c/R_g, where R_g is held constant and D_c is varied. C increases from near zero for small D_c/R_g according to a linear manner and

approaches a constant value at large D_c/R_g, which can be explained as a consequence of reduced particle softness when increasing D_c considering the thickness of polymer layer is constant. For these systems we expect the adsorbed polymer to reach equilibrium with polymer in the bulk and to result in a polymer layer of thickness ~1 nm.[2] The particles are thermodynamically stable and the potential of mean force is short range and monotonically repulsive. The results in Figure 2.9 indicate that only for D_c/R_g>600 with the influence of that soft repulsion begin to have minimal influence on the onset of thickening. Therefore, under conditions of small D_c (D_c/R_g<600), the soft interactions of the adsorbed layers drive the critical stress to scale as $\tau_c \propto D_c^{-2}$ instead of $\tau_c \propto D_c^{-3}$, even though hard sphere behavior is seen in the low shear rate viscosity under dilute conditions. This may be explained as a consequence of adsorbed polymer layer deformation when applying high shear. A similar mechanism has been applied to explain the shear thinning behavior for smaller particles.[43] In addition, we note that the ω dependence of *G'* at high frequencies also reflects the deformation of polymer layers. As the particles are thermodynamically dispersed in polymer melts, no irreversible aggregation is observed in the high shear response. However, we note that with increased molecular weight, the attractions produced by having the polymer adsorb in a non-equilibrium manner increase the critical stress for thickening.

2.3.5 The Role of Polymer Induced Particle-Particle Interaction in Controlling Viscoelasticity of Composites

Four different sets of colloid-polymer composites are designed purposely here to understand the role of polymer induced particle-particle interaction in controlling composite viscoelasticity. Specifically, particles are suspended in PEG400 and PEG2000.

These polymers molecular weights are chosen as they remain under the entanglement limit but are sufficiently different to alter pair interaction potentials. Two different particle sizes are chosen, where D_c=612nm for large particles and D_c =127nm for small particles, to provide a measure of the effects of changes in particle size on characteristic shear stresses, shear rates and strain frequencies.

From linear rheology where we investigate the samples at a strain frequency in the elastic modulus plateau and flow curves where we investigate properties at shear rates in the dynamic stress plateau, we conclude that by changing the suspended medium from PEG400 to PEG2000 attractive interactions are introduced. Our studies suggest that with increasing volume fraction, the SCLP enters dynamical arrest state. This occurs at a value of ϕ_c, suggesting formation of strongly bonded gel. The LCLP system shows a much higher dynamical arrest transition volume fraction lying close to the value of LCSP. Considering all these effects, we propose a state diagram showing dynamical arrest transition boundaries in Figure 2.10 (A) in the panel of polymer *MW*-ϕ_c. In low MW polymers (PEG400), particles experience basically volume exclusive interaction and both particles form dense glasses at large ϕ_c. For high MW polymers (PEG2000), the inter-particle attractions are introduced with strength and range independent of particle size. For LCLP, attractive dense glasses are formed showing dynamical arrest transition volume fraction close to that seen with the LCSP system. This is attributed to re-entrant behavior.[44] For SCLP, the relative attractive range (scaled with particle size) is larger, this re-entrant behavior is suppressed, and a gel is formed at low ϕ_c. This suppression of re-entrant behavior due to attraction range enlarge has been predicted.[45]

To understand the polymer-induced soft interaction in PEG400, it is necessary to apply high shear rate and study shear thickening phenomenon. In Figure 2.10 (B), we propose a state diagram of shear thickening in the panel of τ^*-ϕ_c. For a fixed particle size, at for τ^* just below τ_c^*, shear thinning occurs. When crossing the boundary of τ_c^*, hydroclusters are formed with shear thickening observed. τ_c^* is a weak function of ϕ_c, but increases sharply when approaching maximum packing fraction ϕ_m, where jamming conditions can be achieved. This shear thickening transition boundary is moved to larger stresses by increasing D_c as a result of reducing the relative softness of the pair potential as characterized by a reduction of R_g/D_c, and saturation in reduced softness is observed for $D_c/R_g>600$ as suggested in Figure 2.8 (B).

2.4 Conclusion

These studies uncover a surprisingly complex set of phenomena associated with suspending particles in polymer melts. The system chosen has seen extensive study where we know the polymer segments have a strong affinity for the particle surface and that to high volume fractions the polymer remains adsorbed to the particle surface with a layer thickness growing approximately as R_g. This type of absorption is not predicted from equilibrium theories which are, however able to capture polymer and particle microstructure at the lowest molecular weight, suggesting nonequilibrium absorption for higher molecular weight polymers. We associate this nonequilibrium absorption with an increase in inter-particle attraction and suggest this is due to a depletion effect where polymer segments in the bulk observe a particle surface that appears as if it is composed of polymer segments instead of the bare silica as experienced when the polymer segments can easily equilibrate with those in the bulk.

The consequences of these polymer particle interactions are seen in dense suspension rheology where for low molecular weight (PEG400), the particles appear to interact as expected for particles experiencing short range repulsive interactions. The composites undergo glass transitions with a cross over volume fraction near 0.5 where a separation of relaxation times becomes apparent indicating the onset of caging. The softness of the repulsive interaction is, however, important at high stresses where the onset of thickening is delayed to higher stresses as D_c/R_g increases with an apparent saturation for D_c/R_g>600.

In the high molecular weight polymer we see evidence of attractions. For the small particles, the attractions are sufficient to produce a gel at volume fractions above 0.3 while for the large particles the attractions effect is not large enough to shift the suspensions to gelation. The attractions are of sufficient magnitude that thickening is not observed for small particles.

One surprising result of this study is the substantial rheological consequences in moving from a polymer with degree of polymerization of 9 to a polymer with degree of polymerization of 45. Both degrees of polymerization are below the entanglement value of ~100-150. Thus the adsorption of the polymer to the particle surface induces interactions that are not at equilibrium well below the point where the polymers entangle and these nonequilibrium effects have substantial rheological consequences. Particles are often added to polymer melts to enhance composite elasticity. Often this is attributed to particle induced polymer interactions (e.g., the particles alter polymer relaxation times by creating effective cross link points). Here we show that substantial alterations to

composite properties can arise where the particles are, on average, spaced at many times the polymer radius of gyration due to polymer induced changes to particle interactions.

2.5 Tables and Figures

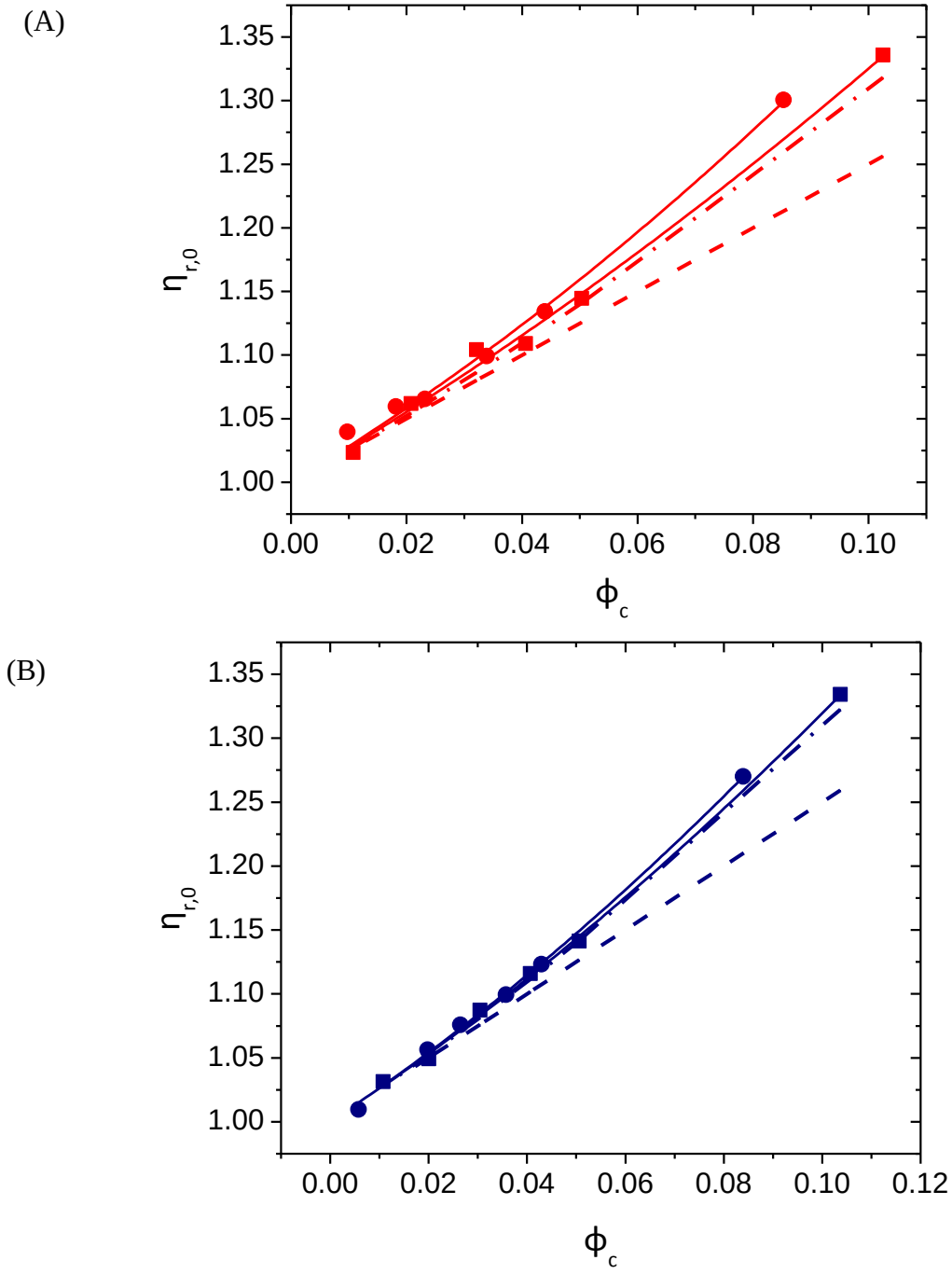

Figure 2.1 Measurement of the zero shear viscosity of PEG400 (square) and PEG2000(circle) as a function of ϕ_c for (A) small particles and (B) large particles, with Einstein's equation (dashed line) and Einstein's equation with 2nd term (dot-dash line) included, and fitting curve to Equation(2.1) (solid line).

Table 2.1 Fitting parameter for zero shear viscosity at low concentration

	D_c=127nm			
	k	H	δ(nm)	R_g/D_c
PEG 400 (R_g=0.8nm)	1.06±0.08	5.4±2.0	1.2	$6x10^{-3}$
PEG2000 (R_g=1.9nm)	1.09±0.08	7.6±1.1	1.9	$1.5x10^{-2}$
	D_c=612nm			
	k	H	δ(nm)	R_g/D_c
PEG 400 (R_g=0.8nm)	1.01±0.04	6.5±1.0	1.0	$1.3x10^{-3}$
PEG2000 (R_g=1.9nm)	1.02±0.04	7.6±1.3	2.0	$3.1x10^{-3}$

(A)

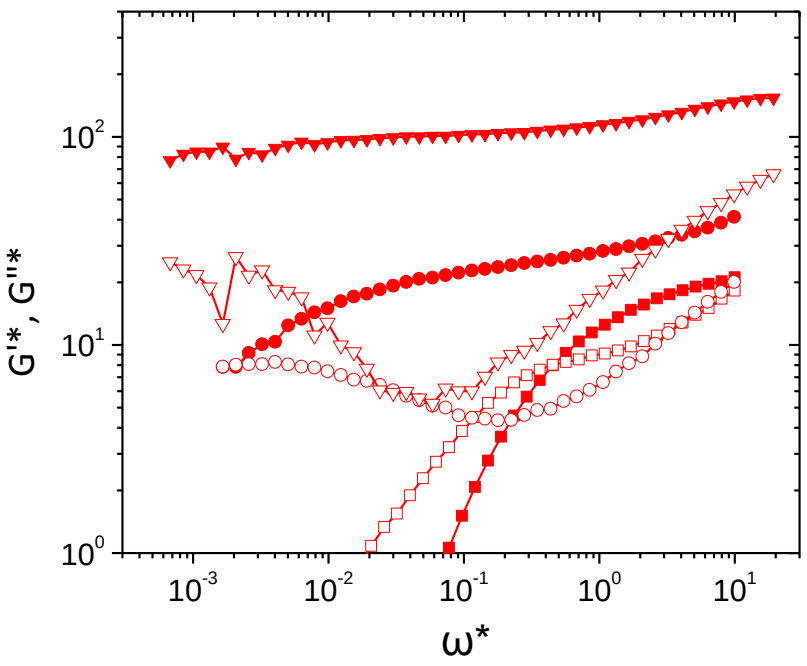

(B)

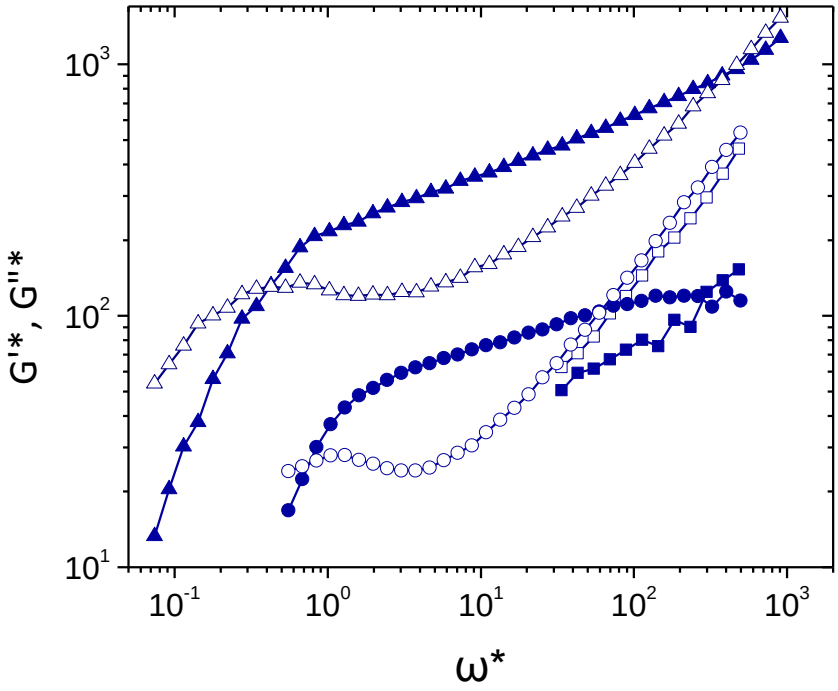

Figure 2.2 (continued on next page)

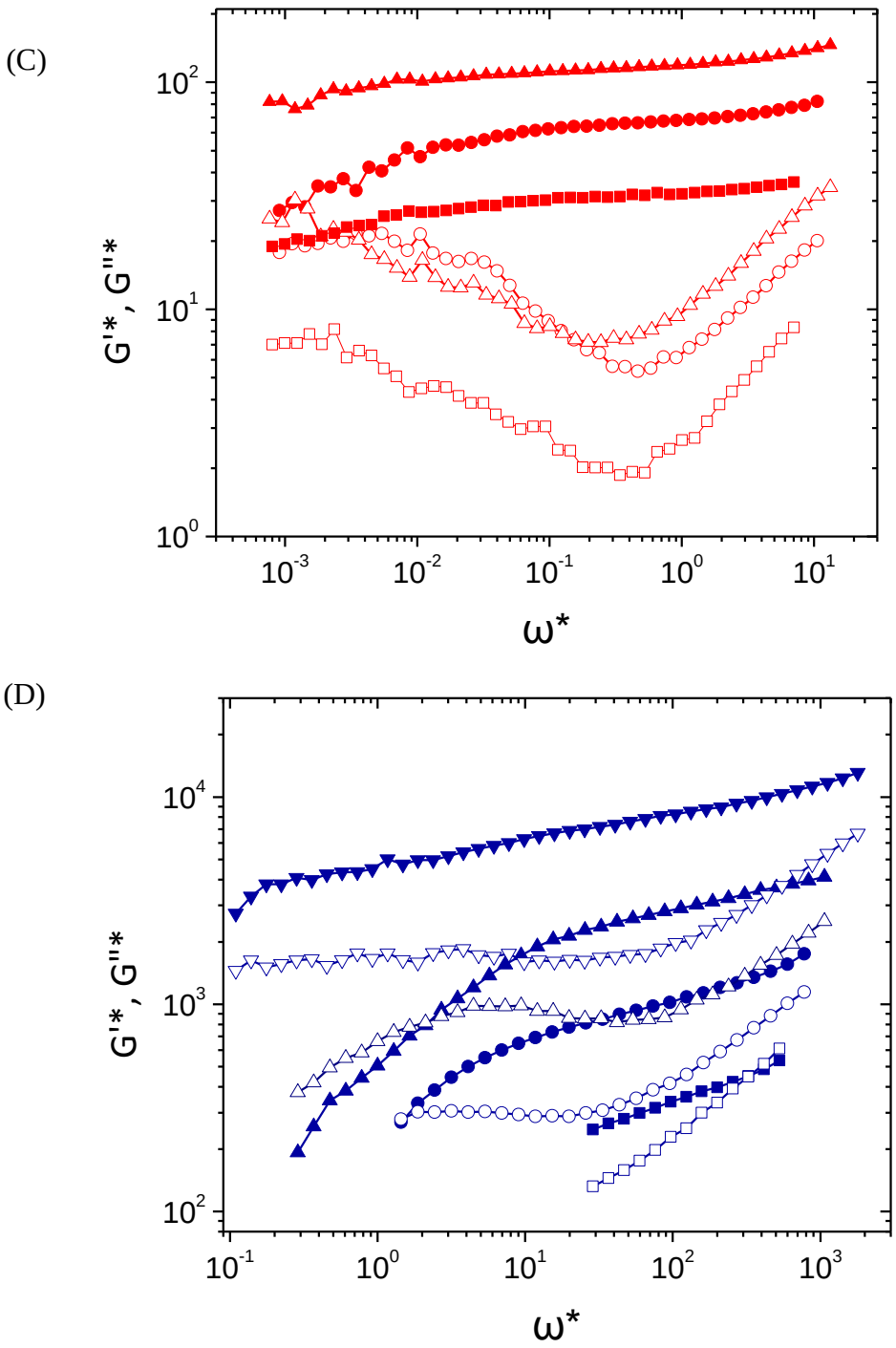

Figure 2.2 Linear *G'** (Close symbols) and *G"** (Open symbols) for (A) SCSP at ϕ_c=0.511(■, □), 0.534 (●,○) and 0.604 (▼, ▽); (B) LCSP at ϕ_c=0.580(■, □), 0.604 (●,○) and 0.629 (▲,△); (C) SCLP at ϕ_c=0.369(■, □), 0.438 (●,○) and 0.479 (▲,△); (D) LCLP at ϕ_c=0.549(■, □), 0.570 (●,○), 0.592 (▲,△) and 0.615 (▼, ▽).

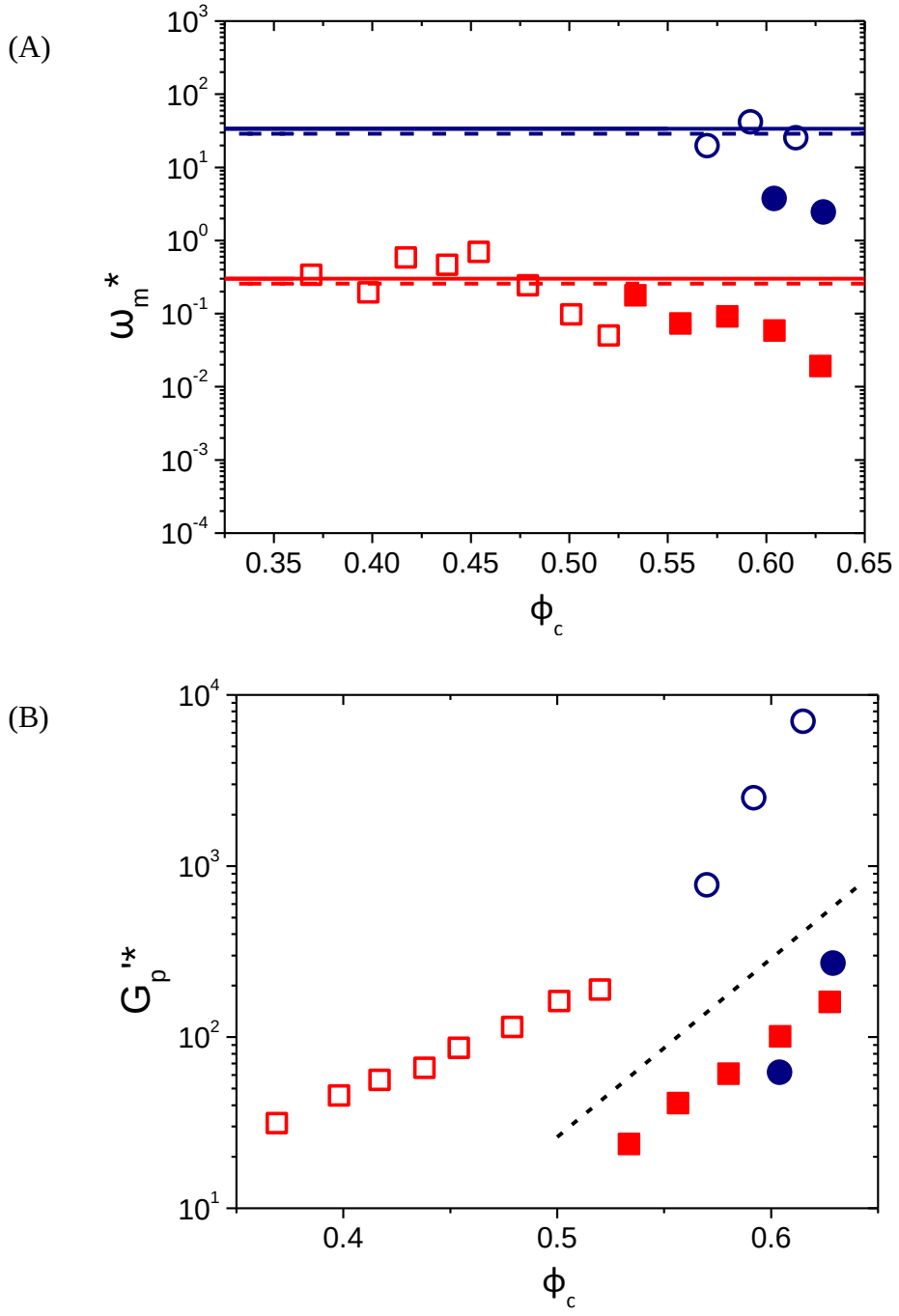

Figure 2.3 Dimensionless frequency ω_m*(A), dimensionless elastic moduli G_p'*(B) at the local minimum of *G"** point plot with volume fraction for SCSP(■), LCSP(●), SCLP(□) and LCLP(○). The solid line (red for SCSP, blue for LCSP) and dashed line (red for SCLP, blue for LCLP) in (A) is dimensionless frequencies for *f*=0.1Hz. The dashed line in (B) is prediction of Kobelev et al[30].

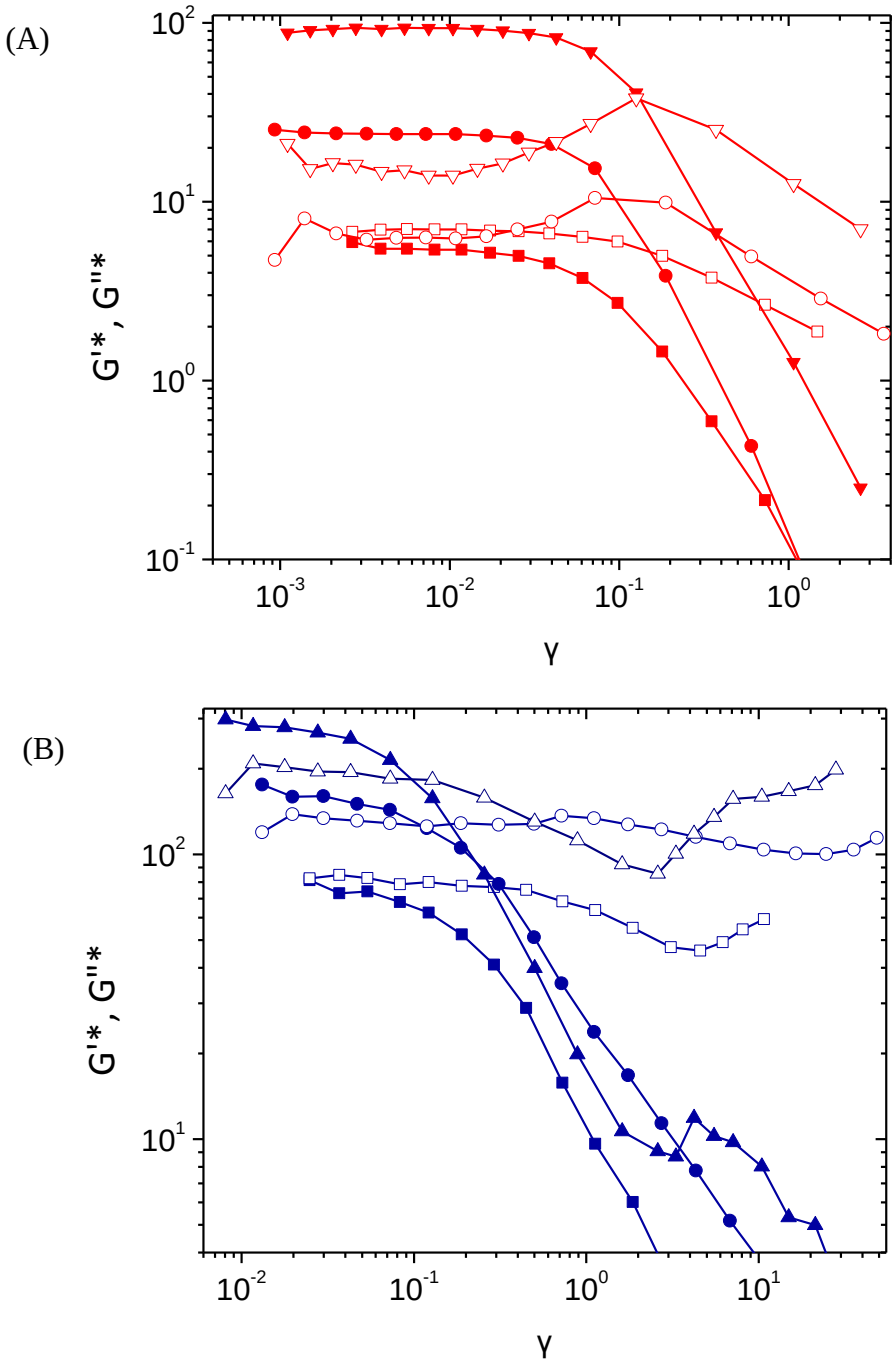

Figure 2.4 (continued on next page)

(C)

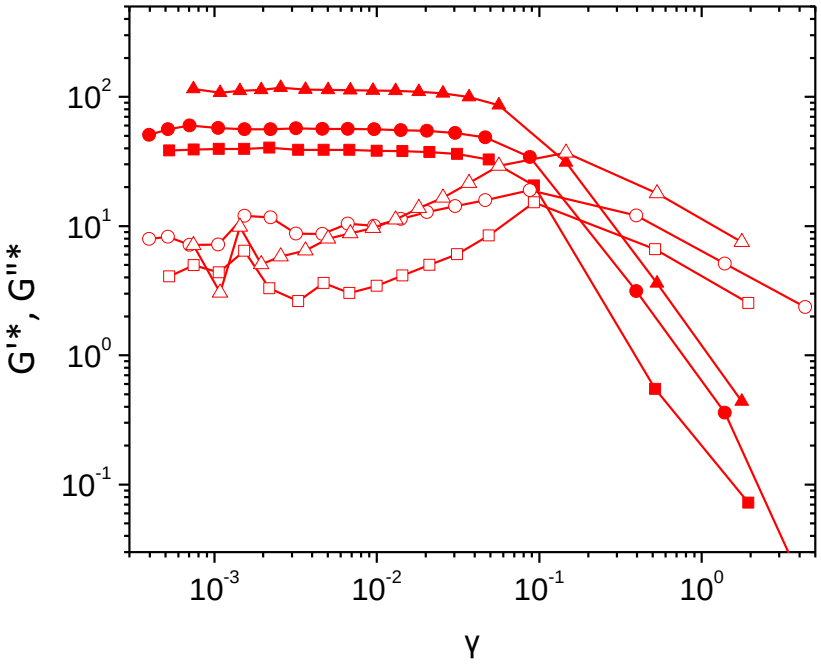

(D)

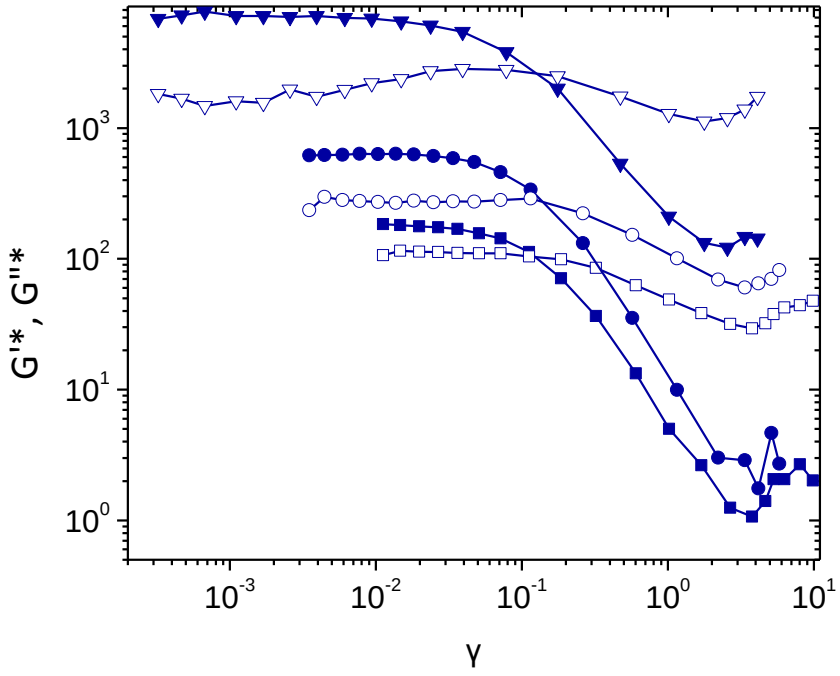

Figure 2.4 Stress sweep experiment results for *f*=0.1Hz with *G'*** (Close symbols) and *G''*** (Open symbols) plot with strain for (A) SCSP at ϕ_c=0.511(■, □), 0.534 (●,○) and 0.604 (▼, ▽); (B) LCSP at ϕ_c=0.580(■, □), 0.604 (●,○) and 0.629 (▲,△); (C) SCLP at ϕ_c=0.398(■, □), 0.438 (●,○) and 0.479 (▲,△); (D) LCLP at ϕ_c=0.549(■, □), 0.570 (● ,○) and 0.615 (▼, ▽).

Table 2.2 Summary of modulus behavior at large shear strain

	SCSP	LCSP	SCLP	LCLP
ϕ_c range	$\phi_c \geq 0.534$	$\phi_c \geq 0.580$	$\phi_c \geq 0.398$	$0.504 \leq \phi_c \leq 0.592$
G'^*	$G'^* \propto \gamma^{-2}$	$G'^* \propto \gamma^{-1}$	$G'^* \propto \gamma^{-2}$	$G'^* \propto \gamma^{-1.6}$
G''^*	$G''^* \propto \gamma^{-0.6}$	Thickening	$G''^* \propto \gamma^{-0.6}$	Thickening

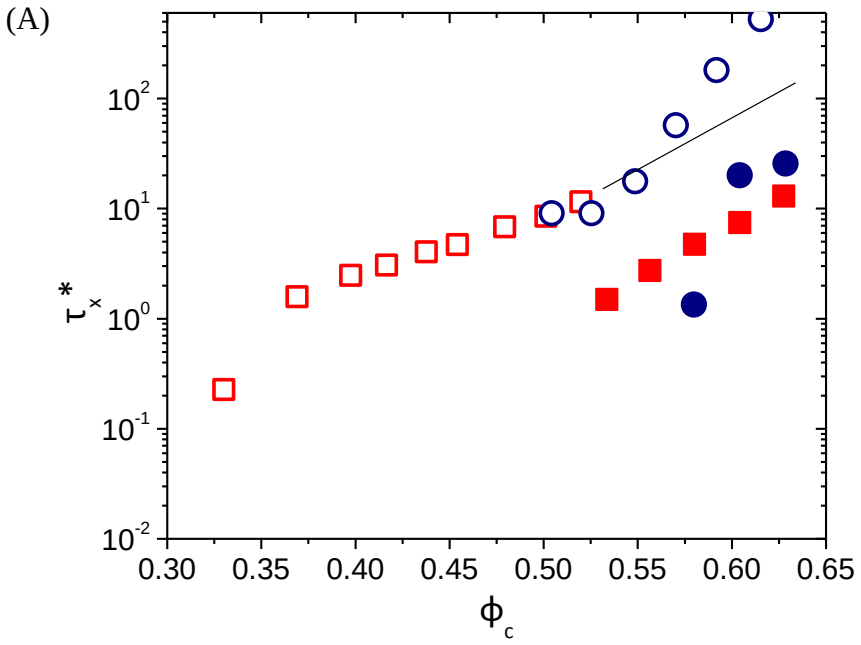

Figure 2.5 (continued on next page)

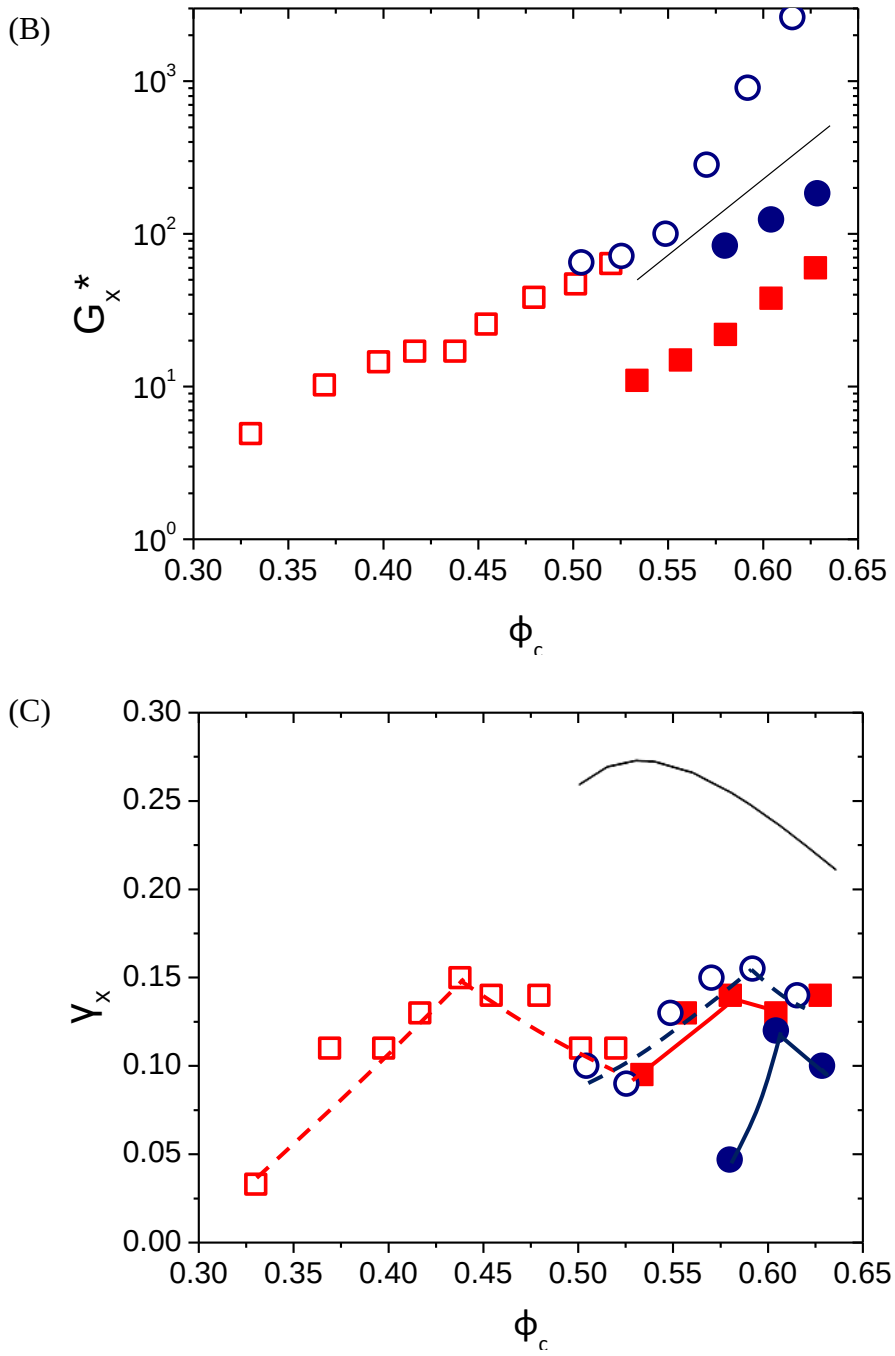

Figure 2.5 (A) The dimensionless stress τ_x^* (B) dimensionless elasticity G_x^* (C) strain γ_x at the cross point where $G'^*=G''^*=G_x^*$ plot with volume fraction for SCSP(■), LCSP(●), SCLP(□) and LCLP(○).The curves (red solid for SCSP, blue solid for LCSP, red dashed for SCLP and blue dashed for LCLP) in Figure (C) are used to guide eyes for the peak in γ_x. And the black solid lines are predictions by Kobelev et al.[30]

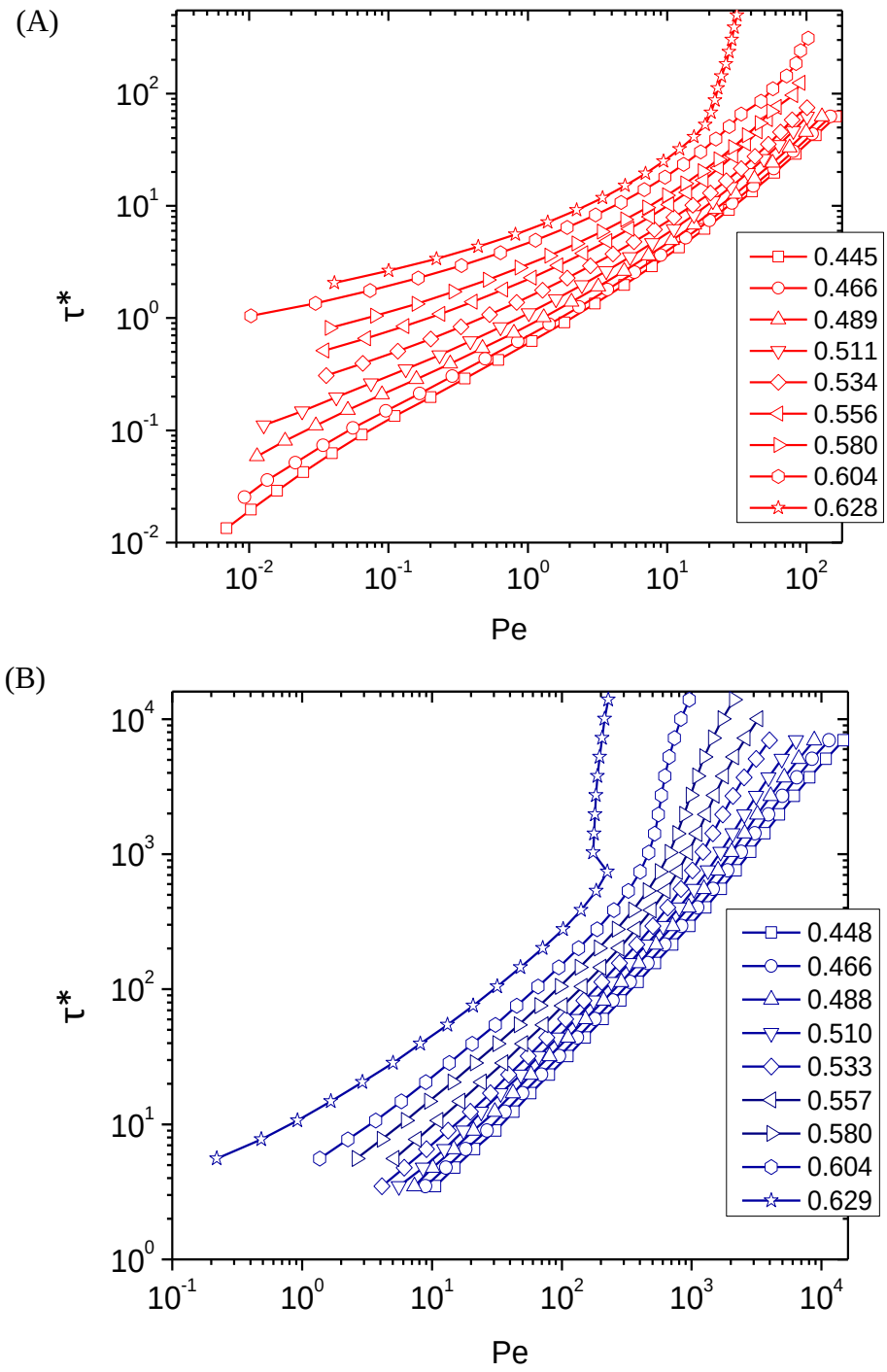

Figure 2.6 (continued on next page)

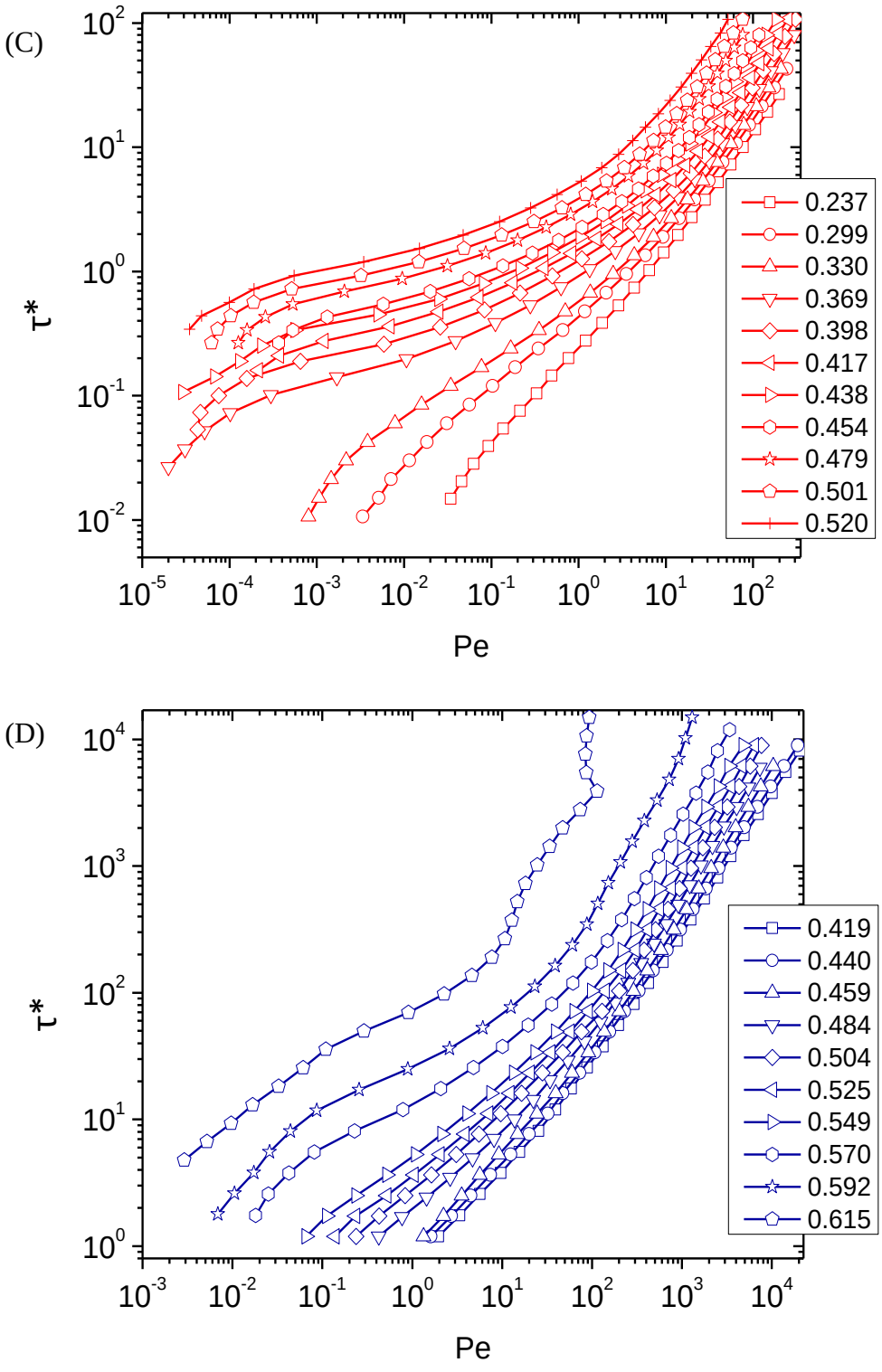

Figure 2.6 Flow curves for (A) SCSP (B) LCSP (C) SCLP (D) LCLP.

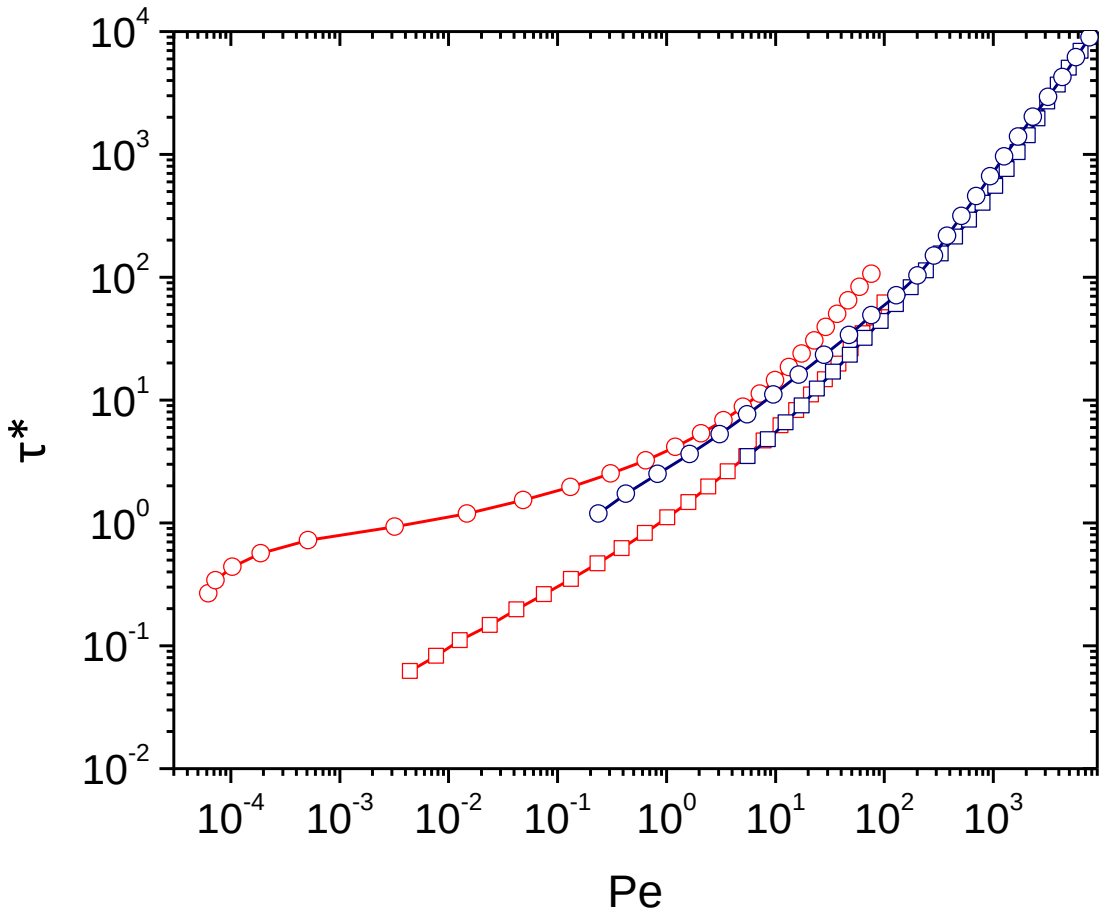

Figure 2.7 Flow curves for small particles (red) and large particles (blue) suspended in PEG 400 (square) and PEG 2000 (circle) at ϕ_c~0.505 (SCSP: 0.511, LCSP: 0.510, SCLP: 0.501 and LCLP: 0.504).

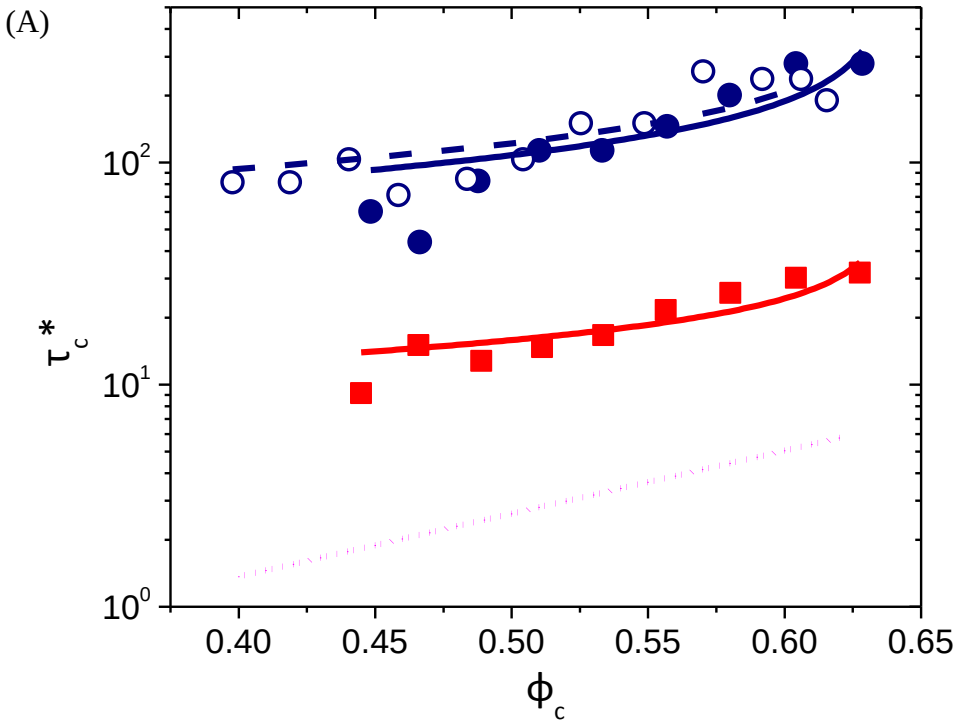

Figure 2.8 (continued on next page)

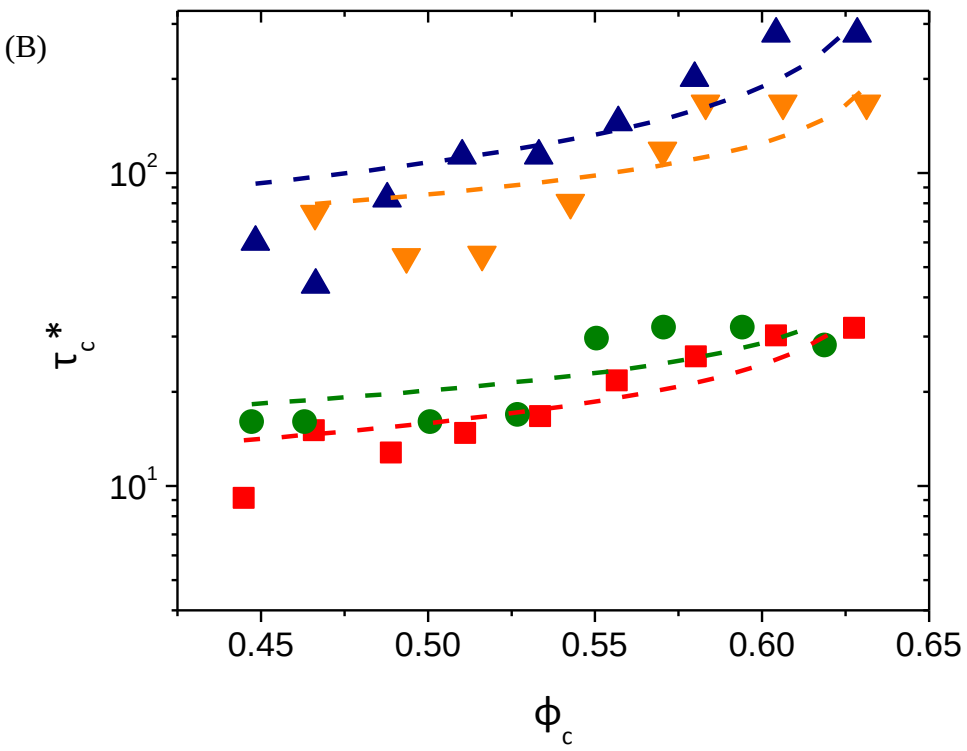

Figure 2.8 (A) The dimensionless shear stress for onset thickening for SCSP(■), LCSP (●), and LCLP (○) plot as a function of volume fraction. The solid line (red for SCSP, blue for LCSP) and dashed line (LCLP) are fitting curves in form of Equation (2.6). The dotted line is the correlation of hard sphere experiment experiencing Brownian force reported before.[16] (B) The dimensionless shear stress for onset thickening for particles in PEG400 D_c=127nm(■), D_c=213nm (●), D_c=612nm (▲) and D_c=730nm (▼)plot as a function of volume fraction. The dashed line is fitting curve in form of Equation (2.6).

Table 2.3 Fitting parameters of Equation (2.6) for particles suspended in PEG400 and LCLP

Particle size D_c (nm)	D_c/R_g	B	C
127 (PEG400)	158	0.31 ± 0.06	7.3 ± 1.6
213 (PEG400)	266	0.26 ± 0.10	10.8 ± 3.8
612 (PEG400)	765	0.41 ± 0.08	39.8 ± 13.6
730 (PEG400)	912	0.28 ± 0.09	43.5 ± 16.3
612 (PEG2000)	322	0.39 ± 0.09	46.7 ± 15.2

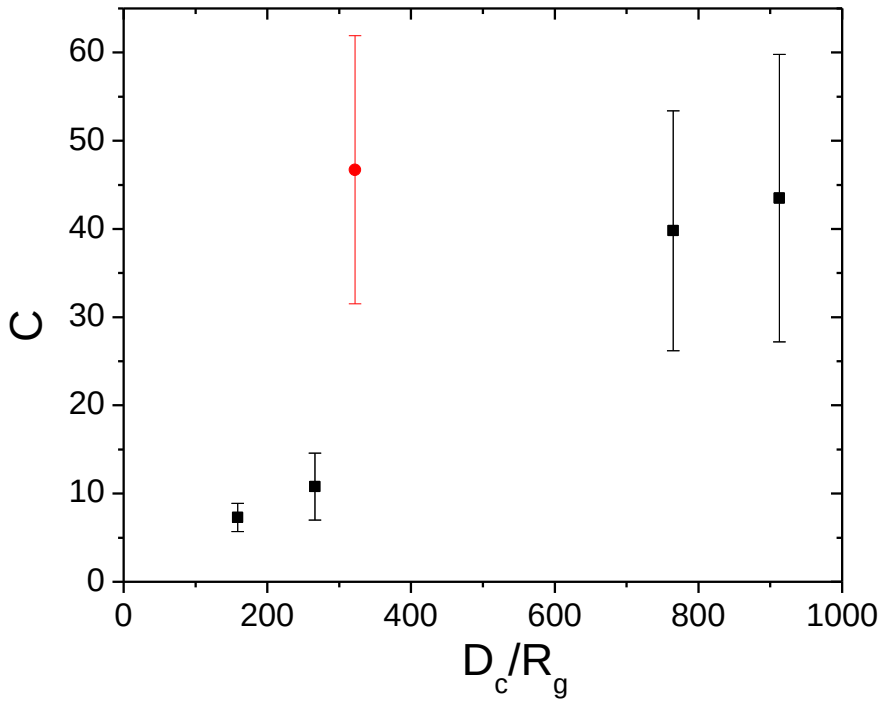

Figure 2.9 Coefficient of Equation (2.6) C as a function of D_c/R_g for particles dispersed in PEG 400 (■) and in PEG 2000 (●).

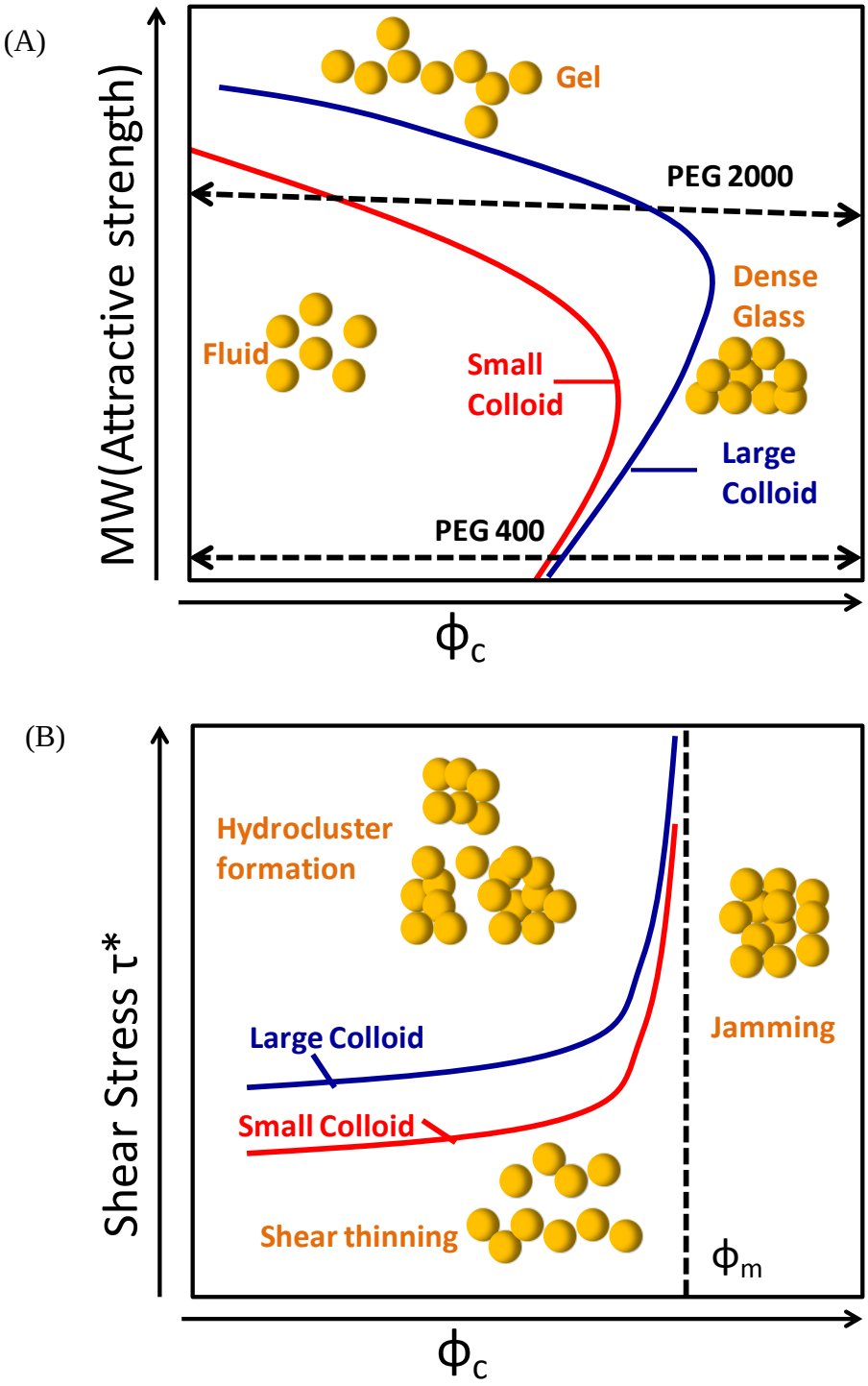

Figure 2.10 (A) Schematic dynamical arrest transition boundaries in the panel of polymer *MW*-ϕ_c for different particle sizes. (B) Schematic shear thickening boundaries in the panel of τ^*-ϕ_c for different particle sizes in PEG400.

2.6 References

1. J. H. Koo, *polymer nanocomposites: processing, characterization, and applications*, McGraw-Hill, New York, 2006.
2. B. J. Anderson and C. F. Zukoski, *Macromolecules*, 2008, **41**, 9326-9334.
3. A. Tuteja, M. E. Mackay, S. Narayanan, S. Asokan and M. S. Wong, *Nano Letters*, 2007, **7**, 1276-1281.
4. B. J. Anderson and C. F. Zukoski, *Journal of Physics-Condensed Matter*, 2009, **21**, 285102.
5. S. Granick and H. W. Hu, *Langmuir*, 1994, **10**, 3857-3866.
6. H. W. Hu and S. Granick, *Science*, 1992, **258**, 1339-1342.
7. B. J. Maranzano and N. J. Wagner, *Journal of Chemical Physics*, 2001, **114**, 10514-10527.
8. B. J. Maranzano and N. J. Wagner, *Journal of Rheology*, 2001, **45**, 1205-1222.
9. B. J. Anderson and C. F. Zukoski, *Langmuir*, 2010, **26**, 8709-8720.
10. K. S. Schweizer and J. G. Curro, *Atomistic Modeling of Physical Properties*, 1994, **116**, 319-377.
11. L. M. Hall, B. J. Anderson, C. F. Zukoski and K. S. Shweizer, *Macromolecules*, 2009, **42**, 8435-8442.
12. S. Y. Kim, L. M. Hall, K. S. Schweizer and C. F. Zukoski, *Macromolecules*, 2010, **43**, 10123-10131.
13. S. Y. Kim, University of Illinois Urbana-Champaign, 2011.
14. B. J. Anderson and C. F. Zukoski, *Macromolecules*, 2009, **42**, 8370-8384.
15. R. Buscall and R. Ettelaie, *Industrial & Engineering Chemistry Research*, 2006, **45**, 6915-6922.
16. L. N. Krishnamurthy, N. J. Wagner and J. Mewis, *Journal of Rheology*, 2005, **49**, 1347-1360.
17. M. Siebenburger, M. Fuchs, H. H. Winter and M. Ballauff, *Journal of Rheology*, 2009, **53**, 707-726.
18. Y. Lu and M. Ballauff, *Progress in Polymer Science*, 2011, **36**, 767-792.
19. N. Dingenouts, C. Norhausen and M. Ballauff, *Macromolecules*, 1998, **31**, 8912-8917.
20. H. Senff, W. Richtering, C. Norhausen, A. Weiss and M. Ballauff, *Langmuir*, 1999, **15**, 102-106.
21. R. G. Larson, in *Topics in Chemical Engineering*, ed. K. Gubbins, Oxford University, New York, Editon edn., 1999, pp. 342-353.
22. N. J. Wagner and J. F. Brady, *Physics Today*, 2009, **62**, 27-32.
23. V. Gopalakrishnan and C. F. Zukoski, *Journal of Rheology*, 2004, **48**, 1321-1344.
24. W. Stober, A. Fink and E. Bohn, *Journal of Colloid and Interface Science*, 1968, **26**, 62-69.
25. G. H. Bogush, M. A. Tracy and C. F. Zukoski, *Journal of Non-Crystalline Solids*, 1988, **104**, 95-106.
26. G. K. Batchelor, *Journal of Fluid Mechanics*, 1977, **83**, 97-117.
27. J. Mewis and N. J. Wagner, *Colloidal Suspension Rheology*, Cambridge University Press, Cambridge, United Kingdom, 2012.

28. M. E. Helgeson, N. J. Wagner and D. Vlassopoulos, *Journal of Rheology*, 2007, **51**, 297-316.
29. T. G. Mason and D. A. Weitz, *Physical Review Letters*, 1995, **75**, 2770-2773.
30. V. Kobelev and K. S. Schweizer, *Physical Review E*, 2005, **71**, 021401.
31. K. S. Schweizer and G. Yatsenko, *Journal of Chemical Physics*, 2007, **127**, 164505.
32. Y. L. Chen and K. S. Schweizer, *Journal of Chemical Physics*, 2004, **120**, 7212-7222.
33. R. A. Lionberger and W. B. Russel, *Journal of Rheology*, 1994, **38**, 1885-1908.
34. J. B. Hooper and K. S. Schweizer, *Macromolecules*, 2006, **39**, 5133-5142.
35. R. J. Larsen, J. W. Kim, C. F. Zukoski and D. A. Weitz, *Physical Review E*, 2010, **81**, 011502.
36. C. G. Dekruif, E. M. F. Vanlersel, A. Vrij and W. B. Russel, *Journal of Chemical Physics*, 1985, **83**, 4717-4725.
37. R. T. Bonnecaze and J. F. Brady, *Journal of Rheology*, 1992, **36**, 73-115.
38. W. B. Russel, D. A. Saville and W. R. Schowalter, *Colloidal Dispersions*, Cambridge University Press, Cambridge, 1989.
39. B. E. Rodriguez, E. W. Kaler and M. S. Wolfe, *Langmuir*, 1992, **8**, 2382-2389.
40. J. Mewis, W. J. Frith, T. A. Strivens and W. B. Russel, *Aiche Journal*, 1989, **35**, 415-422.
41. C. J. Rueb and C. F. Zukoski, *Journal of Rheology*, 1998, **42**, 1451-1476.
42. S. S. Shenoy and N. J. Wagner, *Rheologica Acta*, 2005, **44**, 360-371.
43. A. S. Sarvestani, *Nanoscale Research Letters*, 2010, **5**, 791-794.
44. K. Dawson, G. Foffi, M. Fuchs, W. Gotze, F. Sciortino, M. Sperl, P. Tartaglia, T. Voigtmann and E. Zaccarelli, *Physical Review E*, 2001, **63**, 17.
45. M. Tripathy and K. S. Schweizer, Physical Review E, 2011, **83**,041406.

Chapter 3. Rheology of High Density Glass of Binary Colloidal Mixtures in Unentangled Polymer Melts[2]

3.1 Introduction

Flow properties and state behaviors of particles suspended in polymer melts are complicated by the sensitivity of particle's potential of mean force to particle-polymer segment interactions.[1] Miscible systems are formed when polymer absorbs to form a thermodynamically stable layer. We explore the flow properties of binary mixtures of miscible polymer-particles systems, where we pay particular attention to suspension relaxation rates which are brought on by altering the relative contributions of the large and small particles as the total volume fraction exceeds dynamical arrest transitions and approaches jamming conditions.

The state behaviors of dense suspensions containing particles of a single size have been studied as a function of particle interaction strength to predict and understand the kinetic arrest transition when moving from a liquid to a glass or gel.[2] Mode coupling theory (MCT) and its recent extensions to incorporate activated processes were developed to describe the collective dynamics where nearest neighbor cages block long range diffusion.[3] This model and its extensions have been shown to be robust in predicting the onset of slowed dynamics and activated processes as volume fraction or strength of attraction is increased.[4] Well above this dynamical arrest transition, there is a random close packing volume fraction where particle diffusion ceases.

Suspension viscosity increases rapidly as the volume fraction approaches close packing. This is exemplified by the classic Krieger-Dougherty equation for the relative

[2] This work is reproduced from *Soft Matter* DOI: 10.1039/c3sm27874c. Copyright 2012 Royal Society of Chemistry.

viscosity of suspensions with volume fractions ϕ_c which can be written: $\eta_r = (1-\phi_c/\phi_m)^{-[\eta]\phi_m}$ where, for hard spheres, $[\eta] = 2.5$. The maximum packing volume fraction is ϕ_m and is often reported to be ~ 0.64 for suspensions of hard spheres.[5-7]

The dynamical arrest volume fraction is expected to lie well below maximum packing (at volume fractions near 0.50 as predicted by MCT, with experimental results higher than the theoretical prediction).[8-10] In its original form, MCT predicted that when particles are localized by nearest neighbors, the long-range diffusion ceases and the relaxation time diverges.[11] As there is a great deal of evidence suggesting that suspensions in glassy states retain well defined zero shear rate viscosities,[6, 7, 12, 13] Schweizer and co-workers developed the dynamic arrest theory.[14] This theory defines a cross-over volume fraction ϕ_x which demarks the onset of particle localization. Above ϕ_x, the particles experience a dynamical potential, the depth of which grows with volume fraction. The relaxation time is determined by the rate of diffusion out of the dynamical potential well. The theory predicts a smooth change in relaxation times as volume fraction exceeds ϕ_x with the rate of long range diffusion vanishing only at close packing. As a result, the experimental glass transition is tied to an experimentally chosen relaxation time. When the observation time is longer than the time for particles to diffuse out of the dynamical potential well, the material is liquid-like. While the observation time is shorter, the particles are localized in nearest neighbor cages and the material is solid-like. Thus for volume fractions above ϕ_x, there is an experimental deformation frequency above which the material is a solid and below which the material is a liquid. The experimental result for this glass transition is usually higher than the theoretical prediction as stated above. The links between the divergence in extrapolated viscosity

associated with approaching to a maximum packing fraction and the changes in viscosity typically associated with the glass transition remain poorly understood. Here we use high density glasses of binary colloidal mixtures in low molecular weight polymer melts to systematically investigate this high concentration behavior.

Mixing hard spheres of different sizes is known to increase ϕ_m. Previous studies of binary mixtures demonstrate that hard sphere mixtures will display fluid-fluid phase separation when the size ratio d_l/d_s (where d_i is particle diameter with $i=l$ indicating large and $i=s$ indicating small) is larger than ~5. Experimental systems have been explored to build phase diagrams where equilibrium phase separation has been observed.[15, 16] Theoretical work has been carried out to study hard sphere demixing by a virial approach for size ratio ~6 and ~3 in the ϕ_s-ϕ_l panel where spinodals and binodals are shifted to a higher volume fraction when the size disparity incresaes.[17]

These studies focus on equilibrium phase boundaries. Recent studies relying on MCT demonstrate that a binary mixture of hard-core particles with a size ratio $\delta=d_l/d_s=5$ will undergo a dynamic arrest transition without competition with liquid-liquid phase separation.[18] These studies show that when $\delta\leq 8$, glasses and gels are formed upon increasing volume fraction and for $\delta\geq 8$ liquid/liquid phase separations will occur before the nonergodic state boundary line is crossed.[19, 20] For systems where equilibrium glasses are formed, it is found that when $\delta\geq 1.54$, adding small particles into a dense suspension of large particles or large particle to a dense suspension of small particles will result in faster relaxations such that the overall volume fraction required for a glass-fluid transition will increase. However, when $\delta\leq 1.25$, increases in overall volume fraction by adding the second component to a glass of the first component can result in slower relaxations.[21, 22]

Recent MCT studies have also predicted multiple distinct glassy states by considering whether small particles are mobile when δ>3.[23] Here we study the rheology of binary mixtures of near hard spheres with a size ratio δ=4.8. This size ratio is small enough to obtain nonergodic transitions while avoiding liquid/liquid phase separations and large enough to give rise to re-entrant glass transitions.

Previous experimental studies on the viscosity of binary hard sphere mixtures explored mixing effects on ϕ_m, with little focus on exploration of dynamical arrested transitions.[5, 7, 24] At a fixed size ratio when the volume fraction ratio is varied, a non-monotonic change in maximum packing fraction is used to explain variations in suspension rheology.[5] In agreement with theoretical predictions, the peak in maximum volume fraction is shifted to the higher larger particle fractions, $R=\phi_l/(\phi_s+\phi_l)$, with increasing δ.[7] This behavior results in re-entrant glass formation when the second component is added to a glass of the first.[21, 22] The effects of shifting ϕ_m with changes in R are also reflected in mixtures displaying weaker shear-thickening than single-component suspensions at the same volume fraction.[25] These results suggest that the transport properties of mixtures can be expressed in terms of distance from the maximum packing fraction.

In this work, to minimize the van der Waals attraction and electrostatic repulsion, we use silica particles suspended in melts of polyethylene glycol with a molecular weight of 400, PEG 400. Previous studies using 44nm particles demonstrated that polymer-particle interactions are sufficiently strong to produce thermodynamically stable polymer layers at the particle surfaces. This layer increases the effective particle diameter at low volume fractions such that the particles can be considered as effective hard spheres up to a glass

transition volume fraction. Above this transition volume fraction, steric layer interactions will increasingly dominate composite mechanical properties.[26] Despite behaving rheologically as hard spheres with sizes increased by the thickness of the absorbed layer, the suspension microstructures observed with small angle X-ray scattering are poorly described as being composed of hard spheres when fitting with hard sphere model at the volume fractions above 0.10. Instead, the microstructures of both the particle and polymer segments of these low molecular weight composites are well predicted by the particle reference site interaction models (PRISM) of Schweizer and coworkers.[1, 27] This theory indicates that the particles experience a monotonically decaying potential of mean force with a decay length on the order of polymer segment diameter.[28]

Therefore, although the absorbed layer is a small fraction of a particle diameter, the dense composite microstructure is not well described by that for hard spheres even when suspended in polymers of molecular weight as low as 400.[26] For higher molecular weights, there is experimental evidence that working at volume fractions where the average particle separation is less than ~6R_g, the particle surfaces force changes of polymer configuration and this can dramatically alter the potential of mean force experienced by the particles and give rise to dramatic changes to composite mechanical properties.[29] Further evidence suggesting that composites cannot be considered as one-component systems comes from comparing experimental yielding behaviour observed in nonlinear oscillatory shear response[26] with the yielding behaviour predicted by Schweizer and coworkers.[30] These results suggest that even for the degree of polymerization as low as 9, the internal degree of freedom associated with the polymer gives rise to a rich diversity of behaviors when particles are forced into close proximity.[4, 30]

In a previous study, we have explored the dynamical arrest transition and continuous shear-thickening behavior of two different submicron sized colloids (d_l=612nm and d_s=127nm) in PEG400.[31] The similarity of state behaviors and diverging properties of stress at shear-thickening when approaching jamming conditions indicates that the particles with relatively thin adsorbed polymer layers experience close to purely volume exclusive potentials of mean force, suggesting that the adsorbed polymer layers that give rise to colloidal stability at equilibrium are of limited importance in controlling packing and processability at high stresses.[31] These studies again suggest that the mechanical properties of miscible nanocomposites are controlled by the approach to a maximum packing fraction. By working with binary mixtures, we are able to alter this maximum packing fraction and explore this hypothesis.

We extend our previous study of the silica particles of d_s=127nm and d_l=612nm in PEG400 to binary mixtures of these particles where we characterize the steady shear and frequency dependent behavior as a function of R and $\phi_{c.}$ We analyze our results under a pseudo one-component model where flow properties are characterized in terms of the product of two functions: one that characterizes the distance of the total volume fraction and the close packing and the second that is independent of volume fraction and depends on R.

We introduce the sample preparation procedure and the measurement technique in Section 3.2. Results and discussions are presented in Section 3.3 with cross-over volume fraction characterized through changes in shear-thinning behaviour followed by an analysis of relaxation times, elasticities, yielding behaviours and finally how these composites shear thickened. A summary of the results and conclusions are given in

Section 3.4.

3.2 Experimental Methods

3.2.1 Sample Preparation

Monodispersed silica particles are synthesized by method that is developed by Stöber[32] and extended by Bogush et al.[33] Two different sizes are prepared with d_l=612±20nm (referred to as large particles) and d_s=127±7nm (referred to as small particles) with which binary mixtures will be made. The product particles are suspended in ethanol solution containing water and ammonia hydroxide. The resulting suspension is concentrated to a mass fraction ~0.20 by heating up the suspension to evaporate the solvent and drive off the ammonia. Following previous studies,[31] we chose to work with polyethylene glycol with MW~400 (PEG400, Sigma-Aldrich) at T=25℃ as the polymer melts. PEG400 is a Newtonian fluid at the condition where we study with viscosity of 0.10 Pa s at T=25℃. The two concentrated silica particle suspensions with a fixed mass fraction ratio are mixed with PEG (with eventual large particle volume fraction ratio R=0, 0.29, 0.5, 0.71, 1) and the resulting suspension is placed into vacuum oven with temperature kept above T_m of PEG to remove ethanol.[31]

3.2.2 Rheology

Flow measurements were carried out on a C-VOR Bolin rheometer with a cone and plate geometry. The cone diameter was 20mm with a 4° angle. The temperature was kept at 25℃ where the PEG400 has a viscosity of η_p=0.10Pa s which is large enough to ensure that measurements are made in the high dimensionless frequency range and in the high dimensionless shear rate range enabling the observation of shear-thickening as discussed below.

Continuous stresses are applied to study the viscosity as a function of applied shear stress. Oscillatory stresses are applied to measure elastic modulus *G'* and viscous modulus *G"* as functions of frequency ω in the frequency sweep experiments. In this work, the maximum strain was held as $\gamma \leq 0.01$ to ensure that only linear properties are reported. The samples are well behaved showing no thixotropy and the properties reported are independent of shear-history.

We have previously shown that at low concentrations both large and small particles interact weakly and are well described with $\eta_{r,0} = 1 + 2.5k\phi_c + H(k\phi_c)^2$ where k=1.06±0.08, H=5.4±2.0 for the small particles and k=1.01±0.04, H=6.5±1.0 for the large particles.[31] Hard sphere pair potentials occur when H=5.9, suggesting that adsorbed layers increase the effective hard sphere volume fraction ($k=\phi_{eff}/\phi_c$) by 6% and 1% for the small and large spheres respectively. These results suggest that the particles are interacting weakly as volume fraction is raised.

To compare the magnitudes of the mixture properties, below we choose a particle length scale as an average diameter $<D>$. This approach characterizes the mixture as a pseudo one-component system.[34] We assume that systems composed of binary mixtures behave similarly as a monodisperse system with diameter $<D>$ with same number density ($\rho_l+\rho_s$) and same total volume fraction. So that we have:

$$<D>^3 (\rho_l + \rho_s) = \rho_l d_l^3 + \rho_s d_s^3 \qquad (3.1)$$

which results in:

$$<D> = \left(\frac{R}{d_l^3} + \frac{1-R}{d_s^3}\right)^{-1/3} \qquad (3.2)$$

The values of $<D>$ for the five different sets of suspensions are summarized in Table 3.1.

3.3 Results and Discussions

3.3.1 Dense suspension Rheology and Glass Transitions

In this section, we explore the flow properties of composites when exposed to a continuous stress. In Figure 3.1(A)-(E), for different values of R, the steady relative viscosity $\eta_r=\eta/\eta_p$ is plotted as a function of applied dimensionless shear stress $\tau^*=\tau\langle D\rangle^3/8k_BT$, where η_p is the viscosity of polymer melt and k_B is Boltzmann constant.

These data sets are similar. At low shear stresses and low concentrations, a zero shear viscosity plateau is observed. With increasing shear stress, shear-thinning occurs where the viscosity decreases with increasing the shear stress. When the shear stress is increased to a critical value, a high shear stress plateau viscosity is achieved. By increasing the shear stress further, continuous shear-thickening is detected.

As the volume fraction is increased, the zero shear viscosity plateau is no longer probed at the lowest stress measurements. The larger particles have a smaller diffusivity resulting in longer absolute relaxation times required to observe the zero shear viscosity once the suspension enters a state of kinetic arrest. Experimentally we set the lower limit of shear rate at $10^{-2}s^{-1}$ limiting our ability to probe this long-relaxation time regime. For a fixed volume fraction, and dimensionless stress, the viscosity is a non-monotonic function of R with the lowest viscosities achieved for R=0.71.

As discussed in more detail below, these particles do not show hard sphere scaling such that the characteristic stresses and shear rates at a fixed volume fraction do not scale on $\langle D\rangle^3$. In combination with the absolute changes in the relaxation rates and the range of relaxation rates probed experimentally, determining the location of the localization volume fraction is difficult with oscillatory shear experiments as is commonly done.[26, 35]

Here we seek an alternative method based on empirical correlations developed for shear-thinning suspensions containing Brownian fluids below the localization volume fraction. This approach is based on the observation that for low volume fractions $d\log_{10}(\tau)/d\log_{10}(\dot{\gamma})=1$ while in the kinetically arrested low shear rate region, $d\log_{10}(\tau)/d\log_{10}(\dot{\gamma})$ approaches zero, suggesting there is a cross-over in shear-thinning behaviour with $d\log_{10}(\tau)/d\log_{10}(\dot{\gamma})$~0.5. This approach can be linked to many experiments for suspensions of Brownian particles experiencing a variety of pair potentials shear thin from a zero shear rate viscosity η_0 to a high shear rate viscosity of η_∞ as:

$$\frac{\eta-\eta_\infty}{\eta_0-\eta_\infty}=\frac{1}{1+\left(\tau/\tau_d\right)^d} \tag{3.3}$$

where τ is the applied stress and τ_d is the stress where the viscosity drops to half way between η_0 and η_∞, and 1.4<d<1.8.[5, 36] This expression correlates shear-thinning for hard spheres when ϕ_c<0.5 and for attractive and repulsive particles below localization or disorder/order phase transition volume fractions.[37] We choose to characterize shear-thinning through a shear-thinning exponent, p, which is defined to be the slope of the flow curvein log-log coordinates of τ^* vs. Peclet Number, Pe, as evaluated at the reflection point of the flow curve (so $p=d\log_{10}(\tau^*)/d\log_{10}(Pe)$ when $d^2\log_{10}(\tau^*)/d\log_{10}(Pe)^2=0$). Here Pectlet number is defined as $Pe=3\pi\eta_p\dot{\gamma}<D>^3/4k_BT$ with $\dot{\gamma}$ being the shear rate. In Figure 3.1 (F), flow curves for elevated ϕ_c (R=0.29) are plotted corresponding to the plot for same samples as shown in Figure 3.1 (B) to show the characteristic shear-thinning behaviors in flow curves, with p being a decreasing function of ϕ_c. This tendency is also observed for other values of R. As the localization transition is approached, η_0/η_∞>>1, resulting in p=2/(2+d). From the empirically derived values of d,

we find that for non-localized suspensions $0.53<p<0.59$.

At higher volume fractions the suspensions develop a dynamic yield stress plateau where p approaches zero. We choose a way to locate ϕ_x as the volume fraction where $p<0.56$.[31] We choose this method to characterize the localization volume fraction as we expect it to be robust against changes in particle size, size distribution or pair potential.

This method of characterizing the onset of localization demarks the onset of a dynamic yield stress plateau-a characteristic of all gelled or glassy suspensions. The dynamic yield stress plateau is associated with a large separation in relaxation times. At low stresses the suspensions will be liquids with a viscosity η_0. Above a shear rate, Pe_1 which characterizes a shear rate which equals to the rate of equilibrium diffusion out of nearest neighbor cages, shear-thinning takes place. At higher shear rates, hydrodynamic forces dominate suspension microstructure and stress transfer mechanisms thus the suspension takes on the high shear rate viscosity. The transition from shear-thinning to constant viscosity takes place at a shear rate Pe_2. At elevated volume fractions, Pe_1 and Pe_2 are more widely separated and p approaches zero. The empirical correlations indicate that as long as particles are not localized, (for hard spheres, this means $\phi_c<0.5$), p is greater than or equal to ~0.56; while for localized suspensions (or for hard spheres when $\phi_c>0.5$), p decreases towards zero. We associate the volume fraction where p decreases with the onset of caging and the growth of the dynamical potential. For the small particles studied here this transition occurs at $\phi_x=0.511$.

For composites of uniform spheres, we seek an estimate of the kinetic arrest volume fraction in a similar manner. To do this we assume that the binary mixture can be treated as a pseudo single-component system that will have properties modified by an R

dependent maximum packing fraction, ϕ_m, and an effective average size that depends on the rheological property studied.

As a result, we seek to correlate properties in terms of functions that have a form of $F(R)F_2(\phi,\phi_m,\phi_x)$. We start by knowing that the cross-over volume fraction demarking the onset of dynamic localization occurs for R=0 at ϕ_x=0.511, which is close to the prediction of MCT for the critical glass transition volume fraction of single-component system 0.516.[21] We then argue that for our pseudo one-component systems where R>0, we will see similar flow curves. As we are interested in flow behavior dominated by equilibrium forces, we focus our attention on stresses smaller than those characterizing shear-thickening. We locate ϕ_x for R>0 by seeking volume fractions for other sets of composites where the flow curves superimpose with the R=0 flow curve at ϕ_x=0.511. The result is shown in Figure 3.2.

Excellent superposition of the data is found for these five flow curves in the shear-thinning region (dynamical yield stress plateau). Therefore we have ϕ_x=0.511, 0.557, 0.603, 0.605 and 0.510 for R=1, R=0.29, R=0.5, R=0.71 and R=1, respectively. As expected, the onset of non-ergodic behavior is the same for R=0 and R=1 and passes through a maximum between R=0.5 and R=0.71. Above these volume fractions, we expect the long range particle diffusion to become increasingly sluggish with Pe_2/Pe_1 growing rapidly with the volume fraction. The validity of defining the dynamic arrest volume fraction using this transition of shear-thinning exponent p is proved in inset of Figure 3.2, where universal decreasing tendency is observed when plotting p as a function of ϕ_c/ϕ_x for R=0, 0.29 and 0.5.

3.3.2 Linear Rheology

To explore composite properties above ϕ_x, we investigate their frequency dependent response in the linear deformation region. In Figure 3.3, we present the dimensionless linear elastic modulus G'^* and dimensionless linear viscous modulus G''^* as a function of dimensionless strain frequency ω^*. The dimensionless parameters are calculated as following: $G'^* = G' < D >^3 / k_B T$, $G''^* = G'' < D >^3 / k_B T$ and $\omega^* = \omega < D >^2 / D_0$, where G', G'', ω are the elastic modulus, viscous modulus and angular frequency ($\omega = 2\pi f$, where f is the deformation frequency in units of Hz), and D_0 is the dilute particle diffusion coefficient in expression of $D_0 = k_B T / 3\pi\eta_p < D >$.

All these five sets of composites display the expected characteristics of suspensions entering a state of dynamical arrest as volume fraction is increased. At low frequencies the composites approach a terminal behavior where G'' approaches $\eta_0\omega$ with η_0 being the zero shear rate viscosity. With increasing deformation frequency, there is a cross-over frequency, ω_{x1}^*, where $G'^*=G''^*=G_{x1}^*$ which denotes the inverse of the characteristic time for particles to escape the cage formed by nearest neighbors. For many of the systems studied we are unable to probe this cross-over region. With increasing volume fraction, a minimum develops in G''^* and a plateau develops in G'^*, showing that there is a separation of time scales associated with long-time and short-time diffusions.[26, 35] At high frequencies, G''^* has a stronger dependency on ω^* than G'^*, resulting in a second cross-over frequency at ω_{x2}^* where $G'^*=G''^*=G_{x2}^*$. For larger frequencies, $G'^*<G''^*$ denoting that rate of particle diffusion is increasingly negligible relative to the imposed rate of deformation.

These universal features indicate that all of the mixtures studied enter a state of

dynamical arrest at large volume fractions. Details of this transition depend on R. First, the frequency at the minimum in G''^*, ω_m^*, is an increasing function of R. If the particles were true hard spheres we expect ω_m^* to be equal for R=0 and R=1. Secondly, between ω_{x1}^* and ω_{x2}^*, G'^* increases as $\sim\omega^{*a}$ where for R=0, a~0 while for R=1, a~1/3. This change in slope can be attributed to a change in the particle-polymer boundary condition where it has been shown that in the high frequency limit a=0 is indicative of a slip boundary condition and a=1/2 is a no-slip boundary condition.[38] These different values of a suggest that as $\langle D \rangle$ decreases, the polymer-surface interactions become increasingly distinct from those commonly expected in low molecular weight solvents. Thirdly, the first volume fraction where we observe a minimum in G''^* changes in a non-monotonic manner as R is increased.

A second estimate of the cross-over volume fraction where particles become caged can be derived from the volume fraction where a minimum in G''^* is first observed, ϕ_{cr}, where from the data in Figure 3.3 we find: ϕ_{cr}= 0.523, 0.568, 0.642, 0.641 and 0.592 for R=0, 0.29, 0.5, 0.71 and 1, respectively, with the uncertainty about 0.012. The maximum in ϕ_{cr} for intermediate values of R indicates a delay in reaching the kinetically arrested state which suggests greater fluidity and a greater distance from a maximum packing fraction for particles experiencing volume exclusion interactions.

We note in passing that for R=0.5 and 0.7 the mixtures were readily processed and handled at total volume fractions of 0.7, an impossibly high value for suspensions of single-sized hard core particles. We also conclude that at deformation rates intermediate between ω_{x1}^* and ω_{x2}^*, the slip boundary condition giving rise to a<0.5 is enhanced as R is reduced from unity. ϕ_{cr} is influenced by hydrodynamic interaction at high frequency

which is varied by particle size. As a result, we use values of ϕ_x to characterize the cross-over volume fraction.

To further study the effect of mixing on dynamical arrest in these systems, the dimensionless characteristic frequencies ω_m*, ω_{x2}* and G_p'*, the dimensionless plateau elasticity defined as $G'^*(\omega_m^*)$, are plotted as a function of volume fraction ϕ_c in Figure 3.4 (A) (B). A comparison of these five different binary mixtures at ϕ_c=0.63 is made in Figure 3.5 to demonstrate the effects of changing R at fixed total solids loading.

The frequency at the minimum in G''^*, ω_m*, is a weakly decreasing function of ϕ_c while ω_{x2}* is an increasing function of ϕ_c. As shown in Figure 3.4(B), for different R, G_p'* is plotted as a function of ϕ_c, and is well represented as an exponential function of volume fraction of $G_p'^* = A\exp(b\phi_c)$ with b~26. This dependence is predicted by Kobelev and Schweizer for hard spheres.[30] By scaling according to this functional dependence for different R, the pre-exponential parameter A is a non-monotonic function of R with a minimum between R=0.5 and R=0.71, as shown in the inset of Figure 3.4(B). In Figure 3.4(B), we also show the elastic modulus of hard sphere glass at $\omega^*\approx 0.5$ reported by Koumakis et al,[39] which is substantially larger than our single-component system at high concentration (R=0 and R=1), reflecting a difference divergence behavior at ϕ_m.

The prediction of Kobelev and Schweizer is based on a Percus-Yevick solution for the structure of hard sphere suspensions which is known to fail at volume fractions approaching close packing. Under these predictions we expect G_p'* to diverge. More recent studies suggest that at very high volume fractions $G_p'^* \propto g(D)^2$, where $g(D)$ is the radial distribution function at contact which is expected to diverge as $1/(\phi_m - \phi_c)^\gamma$ where there are predictions with γ= 1 or γ=2.[3] Kramb et al found that for their near hard sphere

suspensions, $G_p'^*$ diverges as $1/(\phi_m - \phi_c)^4$ indicating that for some classes of particles γ=2.[40] A weaker divergence is expected for polymer suspensions with free volume or Doolittle model is applied to explain the suspension viscosity.[41]

In Figure 3.5, we compare the frequency dependent properties of five composites at the same total volume fraction of 0.63. We note again the non-monotonic dependence of G'^* on R with minimum values being reached between R=0.5 and R=0.71 where a plateau modulus between ω_{x1} and ω_{x2} is not established showing that at this volume fraction these suspensions retain some liquid-like properties. These features suggest that the maximum packing fraction is more distant from 0.63 for intermediate values.

As a first step in characterizing the approach to close packing we first obtain ϕ_m for these five different sets of composites by extracting the high frequency viscosity through fitting the linear loss modulus to a simplified model of G'' as following:[42]

$$G''(\omega) = \frac{G_p'(\tau_0\omega)}{(\tau_0\omega)^2 + 1} + \eta_\infty'\omega \tag{3.4}$$

where τ_0 is the long-range relaxation time, η_∞' is the high frequency viscosity, and G_p' is the elastic modulus at the plateau which is set as the valued at ω_m.

With this model and assuming $\omega_m >> 1/\tau_0$, we find $\eta_\infty' = G_p'/\omega_m$, so $\eta_{r,\infty}' = \eta_\infty'/\eta_p = G_p'/(\omega_m\eta_p)$.

To explore this phenomenon we correlate $\eta_{r,\infty}'$ with volume fraction. We expect the high frequency viscosity to diverge at close packing and make the an assumption that $\eta_{r,\infty}' \propto (\phi_m - \phi_c)^{-1}$ when ϕ_c approaching ϕ_m.[43] By defining dimensionless volume fraction $\phi^* = (\phi_m - \phi_x)/(\phi_m - \phi_c)$ where ϕ_x is taken as known and we seek

$$\eta_{r,\infty}'/\eta_{r,\infty}'(R,\phi_x) = \phi^* \tag{3.5}$$

Here $\eta_{r,\infty}'(R, \phi_x)$ is the relative high frequency viscosity of the suspension at ϕ_x. The value of $\eta_{r,\infty}'(R, \phi_x)$ is found as a vertical shift to collapse the data onto a single curve and represents the value of $\eta_{r,\infty}'$ at the cross-over volume fraction. For a given value of R, ϕ_m is fixed and ϕ_x is known. Shown in Figure 3.6(A) are the results of this treatment, where ϕ_m=0.631, 0.661, 0.713, 0.719 and 0.632 for R=0, R=0.29, R=0.5, R=0.71 and R=1 respectively. The uncertainty in determining ϕ_m is estimated about 0.005.

Good superposition of data is observed as shown in Figure 3.6(A) suggesting the viscosity diverges linearly with ϕ^* which is in keeping with the expectation that for near volume exclusion interactions $\eta_\infty' \propto 1/D_s^0(\phi) \propto g(D) \propto (\phi_m - \phi_c)^{-1}$,[43] where $D_s^0(\phi)$ is the self diffusivity and $g(D)$ is the radial distribution function at contact with ϕ_m~0.63 for both R=0 and R=1. The relative high frequency viscosity at the cross-over volume fraction, $\eta_{r,\infty}'(R, \phi_x)$ is a monotonic function of R, displaying a sharp decrease from R=0.71 and R=1, as shown in the inset panel of Figure 3.6(A). We suggest that this phenomenon results from the change in the stress transfer boundary condition at the polymer melt-solid surface. As we observed for R=1 and R=0, the small particles display a slip boundary condition while the large particles show no-slip boundary. For completeness we note that this scaling suggests that ω_m^* must also scale on ϕ^* and this is shown in Figure 3.6 (B).

Table 3.2 summarizes our results of ϕ_m and ϕ_x which are obtained from flow curve superposition above. The complete state diagram is presented in Figure 3.7, where the calculation results of Ouchiyama et al.'s prediction are also presented.[44] While our system is not composed of hard spheres, the values extracted from the divergence of $\eta_{r,\infty}'$ are very close to these predictions.

From Table 3.2 and Figure 3.7, we find that the ratio ϕ_m/ϕ_x is nearly constant with ϕ_m/ϕ_x=1.21±0.03. Previous results with MCT for binary mixtures have shown that the ratio of ϕ_x and ϕ_m is also constant.[45] This close connection between ϕ_m and ϕ_x is also observed in experimental results using shape anisotropic particles,[46] and suggests that $\eta_{r,\infty}'$ diverges as ϕ^*.

In Figure 3.8, we plot the plateau modulus $G_p'^*$ scaled with $G_p'^*(R, \phi_x)$ as a function of ϕ^*, showing that $G_p'^*$ diverges at jamming condition according to a power law $G_p'^*/G_p'^*(R,\phi_x) = \phi^{*0.7}$. The weak dependence on ϕ^* is an indication of the weak dependence of the localization length of the particle cage on volume fraction. This suggests that for particles to achieve these maximum packing fractions, polymer will be displaced from the particle surfaces. Also we show in the inset of Figure 3.8 plots of $G_p'^*/G_p'^*(R, \phi_x)$ as a function of ϕ_c/ϕ_x-1. Yatsenko and Schweizer predict that for hard spheres, the elastic modulus increases as a function of ϕ_c/ϕ_x-1 with the results correlated with an exponential function as $G_p'^*/G_p'^*(\phi_x) = e^{10.45(\phi_c/\phi_x - 1)}$.[47] This behavior has been confirmed experimentally.[40] We emphasize here that the correlations of $G_p'^*$ with ϕ^* and with ϕ_c/ϕ_x-1 are carried out without adjusting ϕ_m or ϕ_x from the values shown in Table 3.2. These correlations give us confidence that these values represent good estimates of the cross-over volume fraction and the volume fraction where diffusion ceases.

The divergence of $G_p'^*$ indicates that even though the polymer in which the particles are suspended is well below the entanglement molecular weight and even though the adsorbed layer thickness at the particle surface is less than 1% of a particle diameter, the particles in suspensions are not interacting as hard spheres. This is indeed confirmed by detailed studies of particle and polymer microstructure and is expected from the

predictions of polymer nanocomposite theories.[27]

An alternative approach to extract information about the jamming volume fraction can be found in the properties of ω_{x2}*. For ω*<ω_{x2}*, particles diffuse faster than the suspension deformation rate. When ω*>ω_{x2}^{*}, particles diffuse shorter distances per cycle of deformation such that at high frequencies particle motion is frozen and the suspension responds like a fluid with viscosity $\eta_{r,\infty}'$. As a result, we use 1/ω_{x2}* as a surrogate for the characteristic time for a particle to explore a cage of nearest neighbors. Unlike the strategy developed from $\eta_{r,\infty}'$, the dependence of both G'* and G''* on the stress boundary condition at the polymer melt/solid interface will be similar suggesting ω_{x2} will be a useful parameter to gauge how mechanical properties diverge as close packing is approached. By assuming that 1/ω_{x2} characterizes the time required for a particle to explore its localization volume, we write:

$$1/\omega_{x2} = r_{loc}^2 / D_s(\phi) \tag{3.6}$$

where r_{loc} is the localization distance which characterizes the size of a nearest neighbor cage. $D_s(\phi)$ is the short-range diffusivity and $D_s(\phi) = D_0 / g(D)$.[48] For hard spheres $r_{loc} \propto 1/g(D)$.[43] We thus anticipate:

$$\omega_{x2}^{*} / \omega_{x2}^{*}(R, \phi_x) = \phi^{*z} \tag{3.7}$$

From our previous analysis, we expect that z=1 if all the assumptions above are valid. Shown in Figure 3.9 is a plot of ω_{x2}*/ω_{x2}*(R, ϕ_x) as a function of ϕ* showing the collapse of the data using ϕ_m in Table 3.2. The trend line has a slope of unity.

3.3.3 Nonlinear Rheology

Yielding in colloidal suspensions is often assessed by investigating the nonlinear response of the suspension when deformed at a fixed frequency and is associated with a

decrease of G' with increasing maximum stress or strain. Under these conditions at low stresses, $G'>G''$ and as the magnitude of the applied stress is increased, G' rolls off and drops below G''. Within the context of the dynamical arrest theories for the colloidal glass transition, this roll-off is associated with how the applied stress lowers the barrier for diffusion out of a nearest neighbor cage. When the barrier is low enough, in the time frame of the deformation, particles can exchange nearest neighbors, and the suspension's elastic modulus decreases. At the point where the barrier is driven to zero, the material will flow like a liquid. Yielding in colloidal glasses and gels at a particular deformation frequency is often associated with the stress required to make $G'=G''$.[26, 49, 50]

As shown in Figure 3.3, if the stress sweep is made at $\omega^*<\omega_{x1}^*$ or $\omega>\omega_{x2}^*$, $G'<G''$ in the linear region. As a result, yielding as described above will only be observed at intermediate deformation frequencies. From a dynamical arrest perspective, this result follows from particle localization and a separation of time scales for diffusion within a cage and out of a cage of nearest neighbors. When $\omega^*<\omega_{x1}^*$, the deformation is so slow that particles can exchange nearest neighbors by diffusion in the time period of the deformation, whereas for $\omega^*>\omega_{x2}^*$, the particles cannot diffuse the localization distance in the time frame of the deformation and the suspension deforms in an affine manner. In our exploration of yielding we chose to study deformation at a fixed frequency of 0.1Hz which lies between ω_{x2} and ω_{x1} and lies near ω_m for many of the suspensions. We show our typical stress sweep experiment data in Figure 3.10(A) for our mixture representatives for ϕ_c=0.63 at f= 0.1Hz.

Here we note that as the maximum stress ($\tau^*=\tau<D>^3/k_BT$) to which the suspension is exposed is increased, G'^* rolls off its plateau value while G''^* passes through a

maximum. We associate the yield stress with the stress τ_x* where G'*=G''*= G_x*. In Figures 3.10(B) and (C) we see that τ_x* and G_x* can be characterized as exponential functions of the volume fraction, passing through a minimum at R=0.71 while the strain shown in Figure 3.10(D) at τ_x*, γ_x, passes through a maximum when increasing volume fraction, the magnitude of which diminishes at values of R intermediate between 0 and 1. The maximum of γ_x when increasing ϕ_c is also observed in previously reported hard sphere glasses by Koumakis et al.[39] This non-monotonic yield strain behavior with increasing ϕ_c can be explained as a combined effects of changes in τ_x* which reflects the entropic barrier height of the dynamic potential and changes in G_x* which reflects the minimum in the curvature of dynamical potential. With both parameters subtly altered by changes in ϕ_c, the ϕ_c dependence of γ_x is achieved. These have been predicted by Kobelev et al. theoretically, with the results also presented in Figure 3.10 (B)-(D).[30] We explain the diminishing of peak in γ_x between R=0 and R=1 as resulting from details of the heterogeneous environments experienced by localized particles of different sizes.

In Figure 3.11(A) we plot scaled τ_x* as a function of ϕ*, where we use ϕ_m as defined above. By adjusting the magnitude of $T_x(R)$ which is a function used to normalize τ_x* at ϕ_x, we force the data to collapse into the power law $\tau_x^*/T_x(R)=\phi^{*t}$, where we find out that t~1.

In Figure 3.11(B), we plot scaled G_x* as a function of ϕ*. By adjusting the magnitude of $J_x(R)$ which is a function used to normalize G_x* at ϕ_x, we seek the best data collapse into the power law $G_x^*/J_x(R)=\phi^{*j}$, where we find that j~0.7. While G_x* has the same dependence on ϕ* as G_p'*, we note that this is a weaker dependence that seen for τ_x*.

Extended from this nonlinear oscillatory rheology, large amplitude oscillatory shear

(LAOS) strain analyses have been applied to study the full nonlinear responses of suspensions.[51-54] These developed studies have suggested that at high amplitude strain in nonlinear oscillatory shear sweep experiment where the stress is not perfectly sinusoidal, commonly experimental results of commercial rheometer are the first-harmonic Fourier moduli G_1' and G_1''. However, other harmonics have also been determined from the whole nonlinear response which contributes significantly in fully understanding of yielding. Therefore, using the current definition of dynamic moduli G' and G'' at large amplitude strain renders the main points in yielding of this unexplored composite system, while detailed analysis of the strain curves of our samples may provide a rich area of further investigation.

3.3.4 Shear-Thickening

In Figure 3.2 we show that there is a great similarity in the shear-thinning behavior of samples near the glass transition showing that the approach to the dynamic stress plateau is dominated by thermodymanic (or caging interactions). However, as shown in Figure 3.1, at higher stresses the onset of thickening is dependent on *R*. In Figure 3.1 (A), we denote the method in determining τ_c* for the highest volume fraction. Shear-thickening is sensitive to pair potentials. This shows up in the size dependencies of the stress at the onset of thickening, τ_c*. For steric polymeric repulsions[31] or electrostatic repulsions,[55] $\tau_c \propto D_c^{-2}$. For pure hard sphere repulsions, $\tau_c \propto D_c^{-3}$. These previous studies suggest τ_c* is a weak function of volume fraction, but size variations can change the stress at the onset of thickening. For our samples we find that τ_c* is a weak function of volume fraction with a tendency to diverge at a maximum packing fraction as shown in Figure 3.12. In Figure 3.12, we also include the correlated experimental results for hard spheres

experiencing Brownian forces in low molecular weight solvent reported before.[56] This denotes again that we cannot simply treat the systems in polymer melts as volume exclusive spheres dispersed in continuum medium when applying high shear stress.

To understand the divergent behavior of τ_c* and how this varies with R, in Figure 3.13 we present scaled τ_c*/τ_c*(R, ϕ_x) as a function of ϕ*, together with fitting to a power law $\tau_c^*/\tau_c^*(R,\phi_x)=\phi^{*c}$, where τ_c*(R, ϕ_x) is an estimate of τ_c* at the cross-over point. We find that the stress at thickening diverges weakly with c~0.35 and τ_c*(R, ϕ_x) is a non-monotonic function of R with a sharp increase between R=0.71 and R=1 as shown in the inset panel of Figure 3.13. By looking at the data in detail, we can find that there is tendency to diverge as ϕ_m is approached but for volume fractions below ϕ_x (ϕ*<1), the data does not collapse well into the power law function of ϕ*.

Previous studies for single-component system suggest τ_c* is a weak function of volume fraction.[31] For our samples we find that τ_c* shows a weak volume fraction dependency with a tendency to diverge at a maximum packing fraction. By assuming dominance of soft interaction and applying force balance with details discussed in previous work,[31] the data can be fitted to the form

$$\tau_c^* = C\left[\left(\frac{\phi_m}{\phi_c}\right)^{1/3} - 1\right]^{-B} \tag{3.8}$$

We find that B is weakly dependent on particle size which reflects the softness of adsorbed polymer layer, while the characteristic stress, C, is sensitive to particle size. For suspensions of uniform spheres at R=0 and R=1, we find out that B=0.31 and B=0.41 respectively, with the average being 0.36, which can be well simplified with the power law in Figure 3.13 within a narrow volume fraction range.

From the collapse of the data when scaled to the distance to close packing, we conclude that thickening of these composites is well described by a model where volume fraction dependencies are determined by the distance from a maximum packing fraction. On the other hand, the magnitude of high frequency viscosity $\eta_{r,\infty}'(R, \phi_x)$, plateau elasticity $G_p'^*(R, \phi_x)$, the characteristic short-range diffusion rate $\omega_{x2}^*(R, \phi_x)$ and inverse of critical shear stress $1/\tau_c^*(R, \phi_x)$ are all functions of R (below $F(R, \phi_x)$ is used to denote these flow properties). These functions scaled by the values at R=0 ($F(0, \phi_x)$=2327, 30.9, 28.2 and 0.0782 for $\eta_{r,\infty}'(R, \phi_x)$, $G_p'^*(R, \phi_x)$, $\omega_{x2}^*(R, \phi_x)$ and $1/\tau_c^*(R, \phi_x)$ respectively) are plotted in Figure 3.14, where we observe that they all show a sharp change from R=0.71 to R=1. The largest changes are seen for $\eta_{r,\infty}'(R, \phi_x)$ and $1/\tau_c^*(R, \phi_x)$ which characterize the high frequency and high shear rate response respectively. We attribute this observation to the loss of the no-slip boundary condition for the effective particles when a small fraction of small particles is added to a suspension of large particles. We note that at R=0.71 the large particles represent only 2% of the total number of particles in the mixture. As a result, there will be an enormous change in the properties which are sensitive to the surface properties of the large particles as R increases from 0.71 to 1.

3.4 Conclusion

We investigate the phase diagram and rheology of a binary colloidal mixtures dispersed in unentangled polymer melts. Previous studies confirmed that glasses are formed by single component systems in this colloid-polymer composite. Here we show that despite the limited degree of polymerization of the melt and despite the absorbed polymer layer being less than 1% of the particle diameter, the composites cannot be treated as hard spheres suspended in viscous continuous phase.

Of particular interest is the link between the cross-over volume fraction which demarks the onset of collective motion and the maximum packing fraction. Building on knowledge that mixtures of hard particles of different size will have an R dependent maximum packing fraction, we hypothesize that the mechanical properties of suspensions of these particles will be dependent on the proximity to a maximum packing fraction and to diverge in a critical manner. We find that the divergence of the elastic modulus, the high frequency viscosity, the yield stress, and the rate of short time self-diffusion are captured by a single set of R dependent maximum packing fractions. In addition we find that the ratio of the cross-over volume fraction and the maximum packing fraction is a constant as R is varied from 0 to 1. Finally we find the stress at thickening is a weak function of volume fraction and has a very weak divergence as maximum packing fraction is reached.

The potential of mean force between these particles is monotonically repulsive and short-ranged. However, dense suspension microstructure is poorly described with an effective hard sphere diameter where the diameter is independent of volume fraction indicating that the internal degrees of freedom of the polymer and the way in which it absorbs to the particle surface are significant in controlling composite microstructure and dynamics.[36] Nevertheless, we conclude that the reduction in free volume for long-range and short-range diffusion produced by increasing the total solid volume fraction dominates suspension dynamics while the polymers play an indirect role. The polymer studied here is unentangled and is known to reach equilibrium configurations in the composite. If these conditions are not met, polymer relaxation processes may become important in controlling composite dynamics and stress transfer properties.

3.5 Tables and Figures

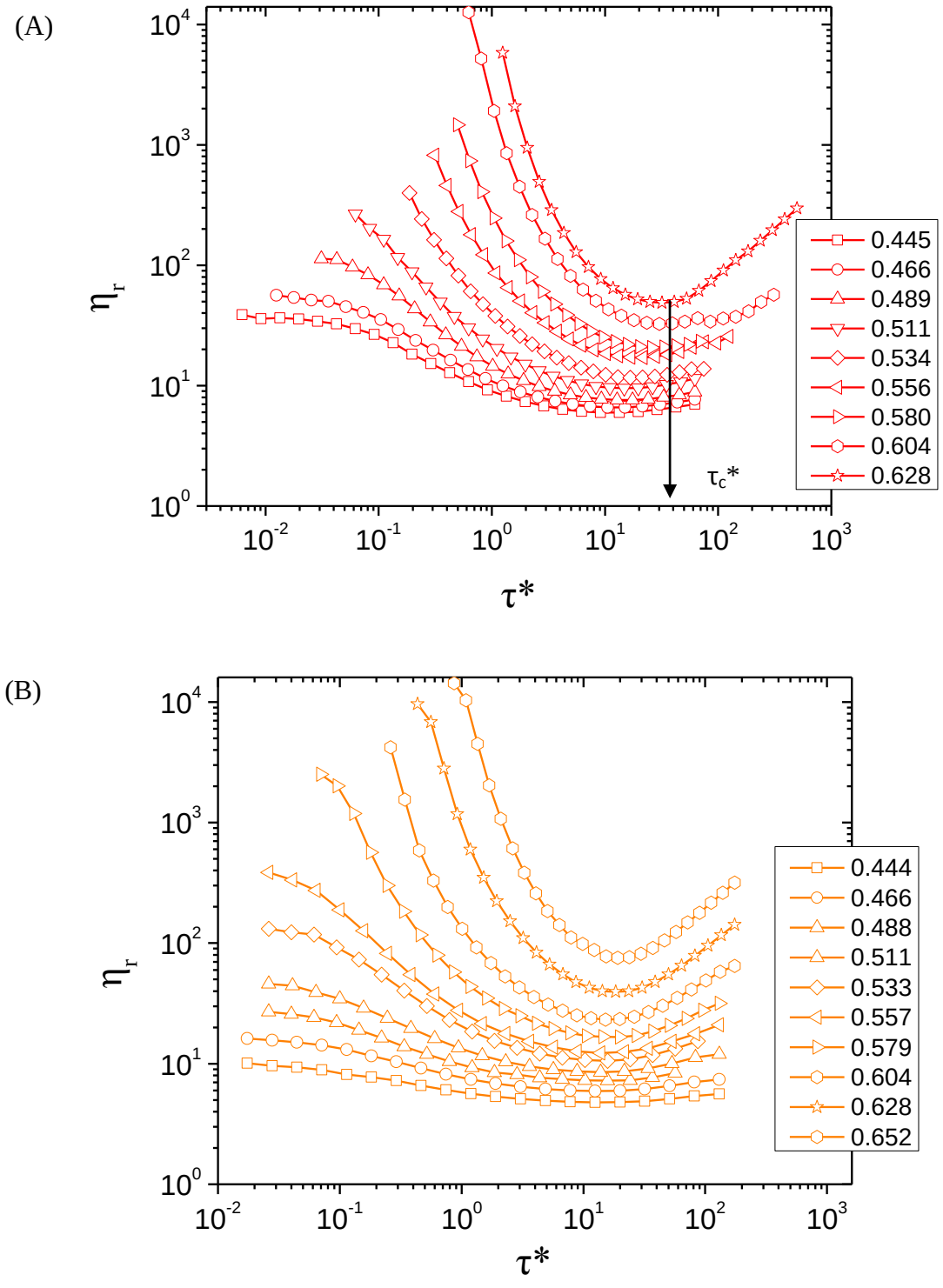

Figure 3.1 (continued on next page)

(C)

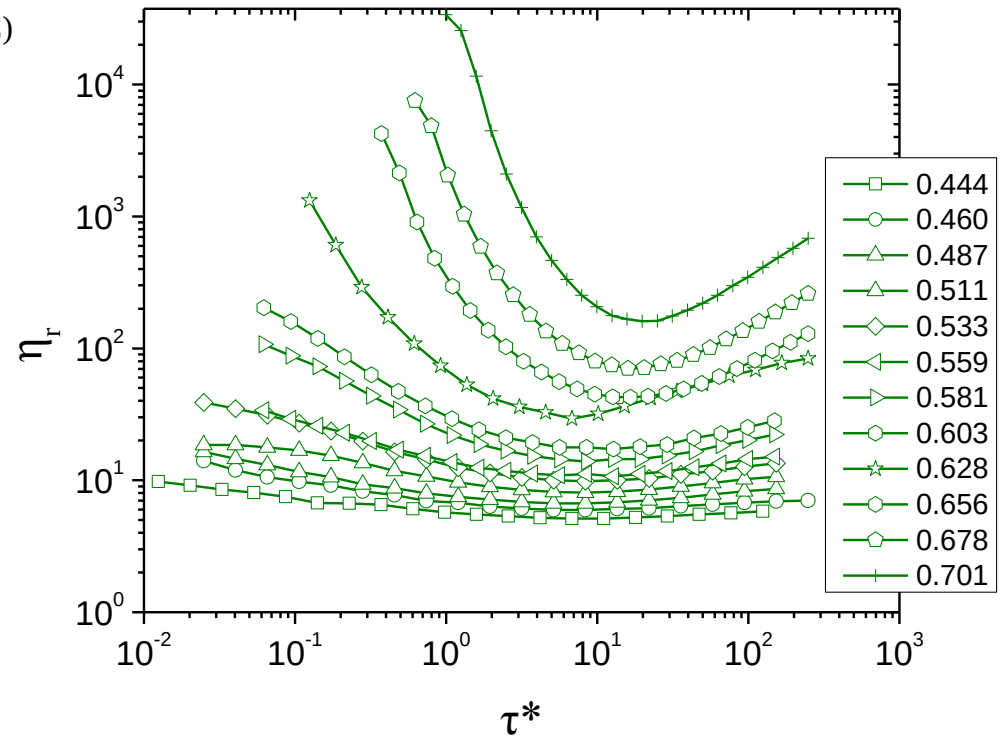

(D)

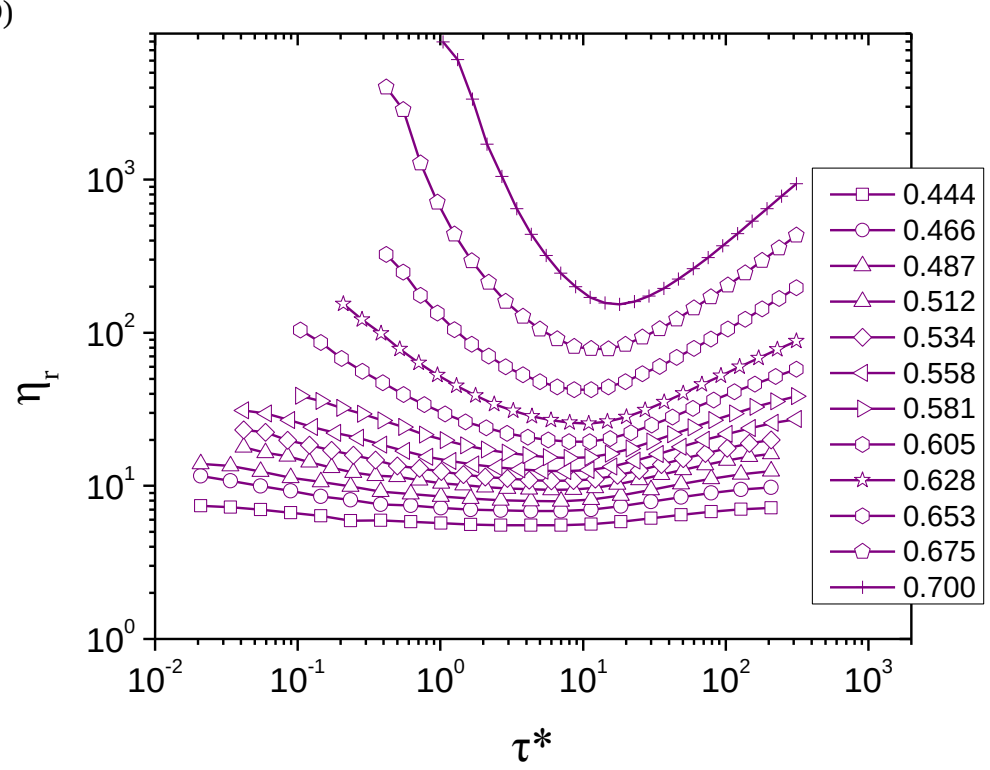

Figure 3.1 (continued on next page)

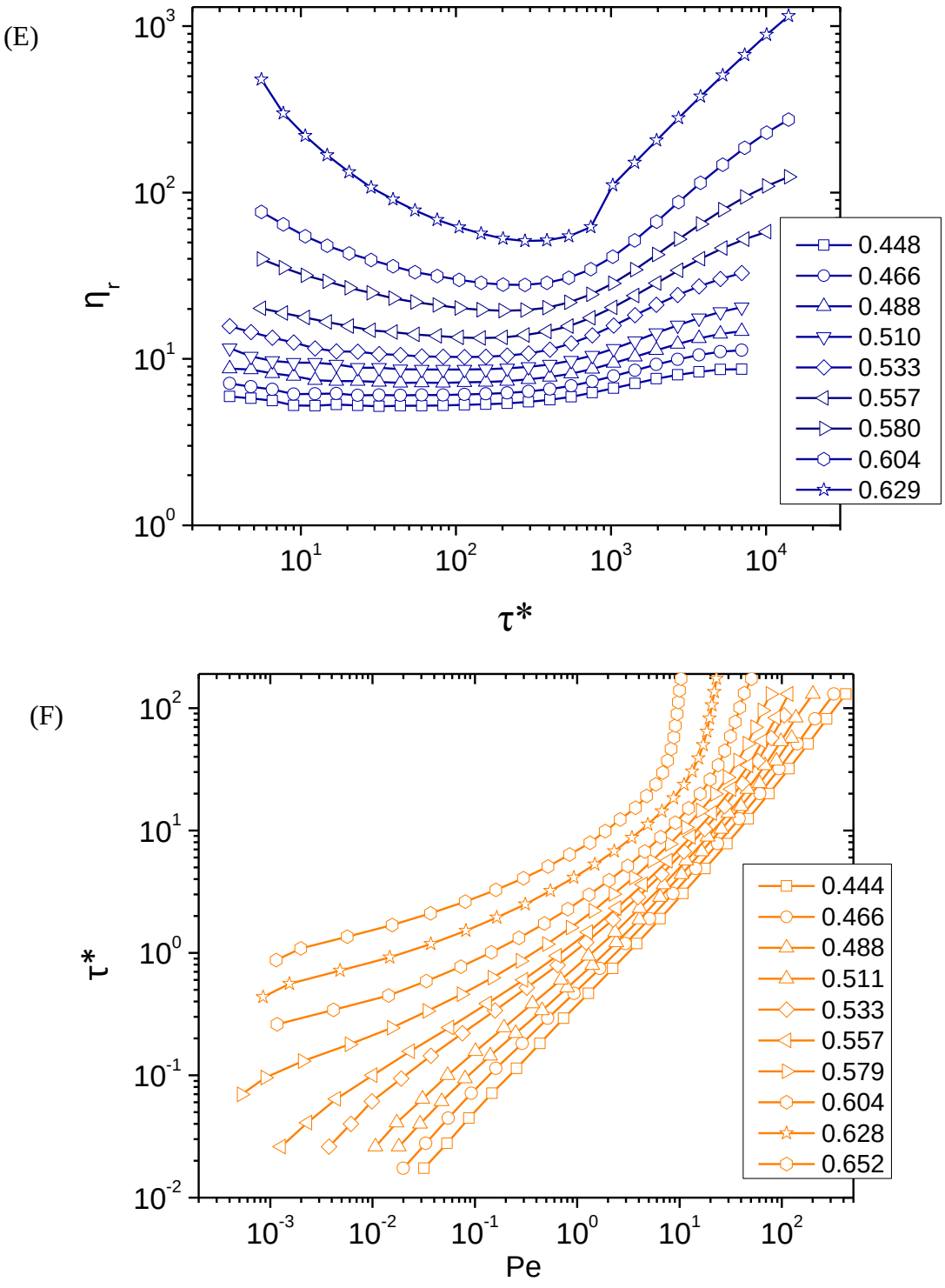

Figure 3.1 η_r as a function of τ^* for elevated ϕ_c at (A) R=0, (B) R=0.29, (C) R=0.5, (D) R=0.71 and (E) R=1. (F) Flow curves for elevated ϕ_c at R=0.29. The arrow in (A) shows the method of determining τ_c^*.

Table 3.1 Summary of volume average diameter <*D*>

R	0	0.29	0.5	0.71	1
<*D*>/nm	127	142	160	190	612

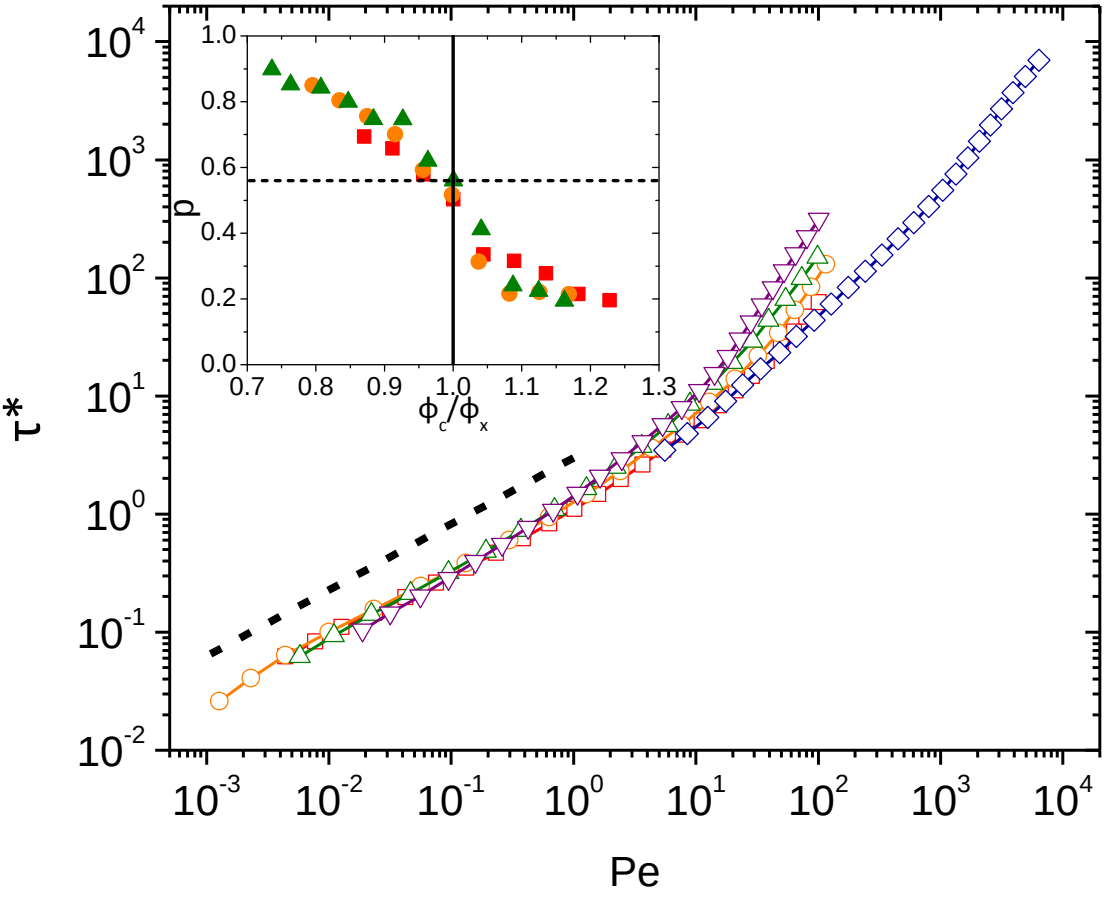

Figure 3.2 Flow curves of R=0 at ϕ_c=0.511(□), R=0.29 at ϕ_c =0.557(○), R=0.5 at ϕ_c =0.603(△), R=0.71 at ϕ_c=0.605(▽) and R=1 at ϕ_c =0.510(◇). The dashed line has a slope of 0.56. Inset shows p as a function of ϕ_c/ϕ_x for R=0 (■), 0.29(●) and 0.5 (▲), with the solid line denoting ϕ_c/ϕ_x=1 and dashed line denoting p=0.56.

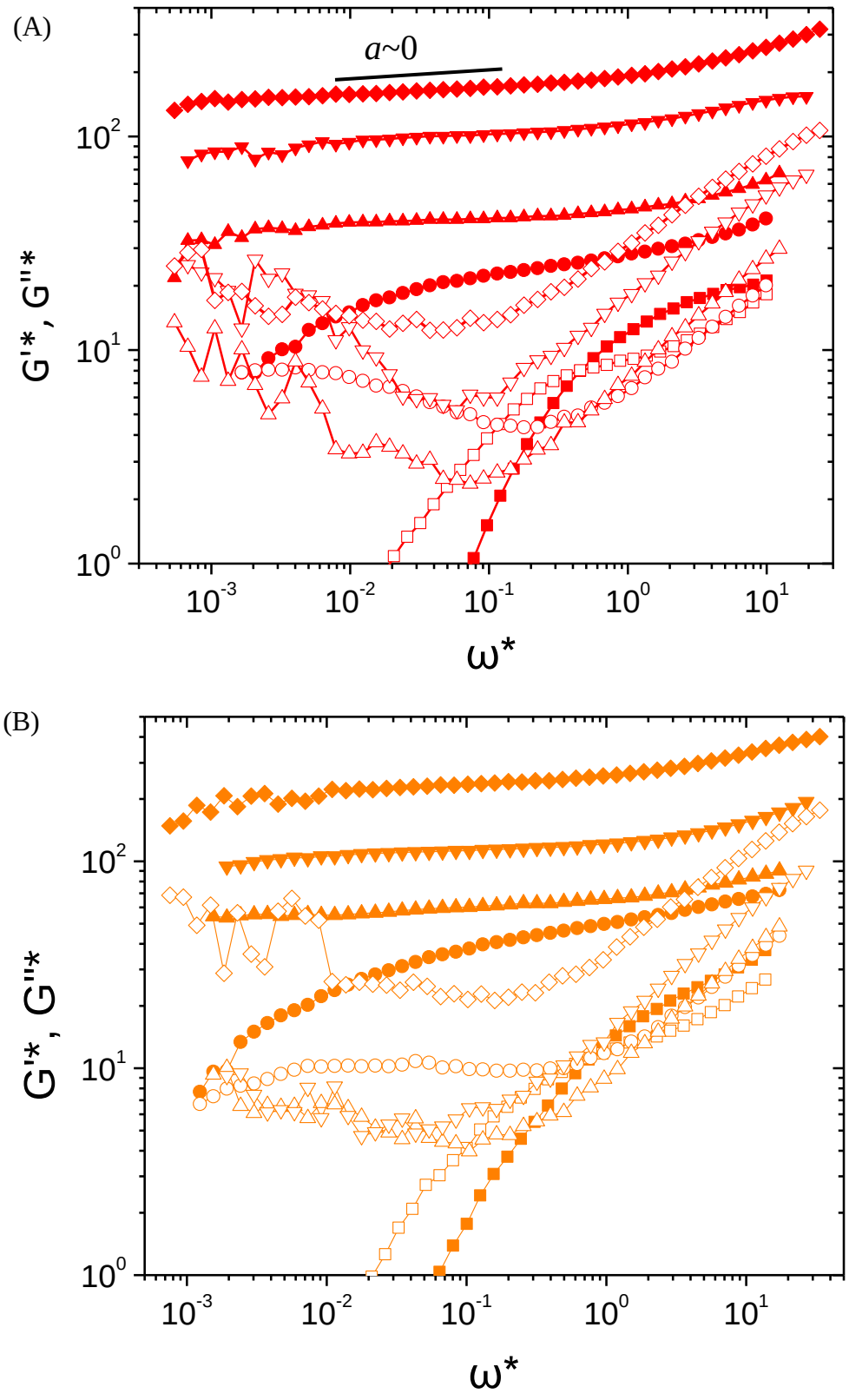

Figure 3.3 (continued on next page)

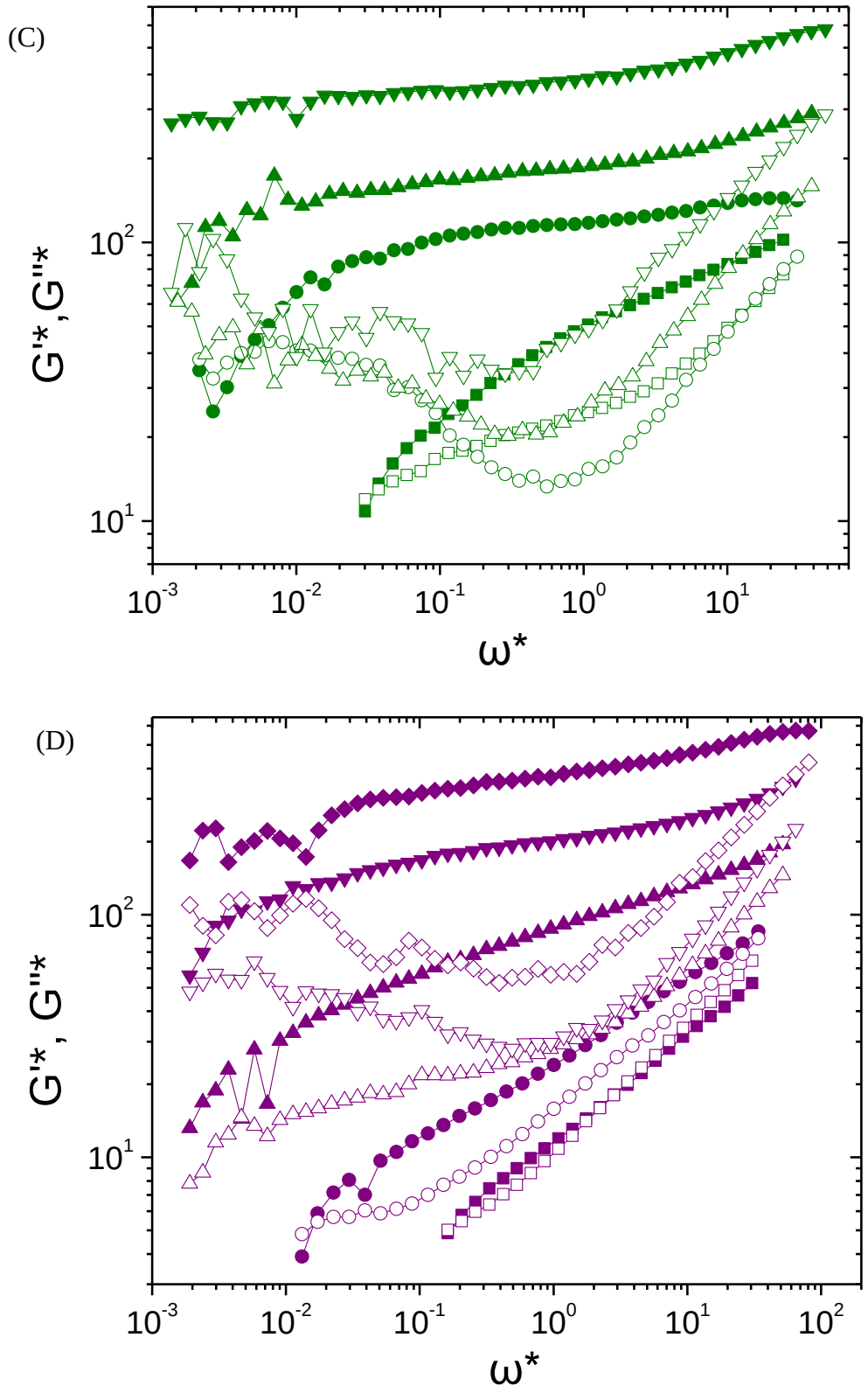

Figure 3.3 (continued on next page)

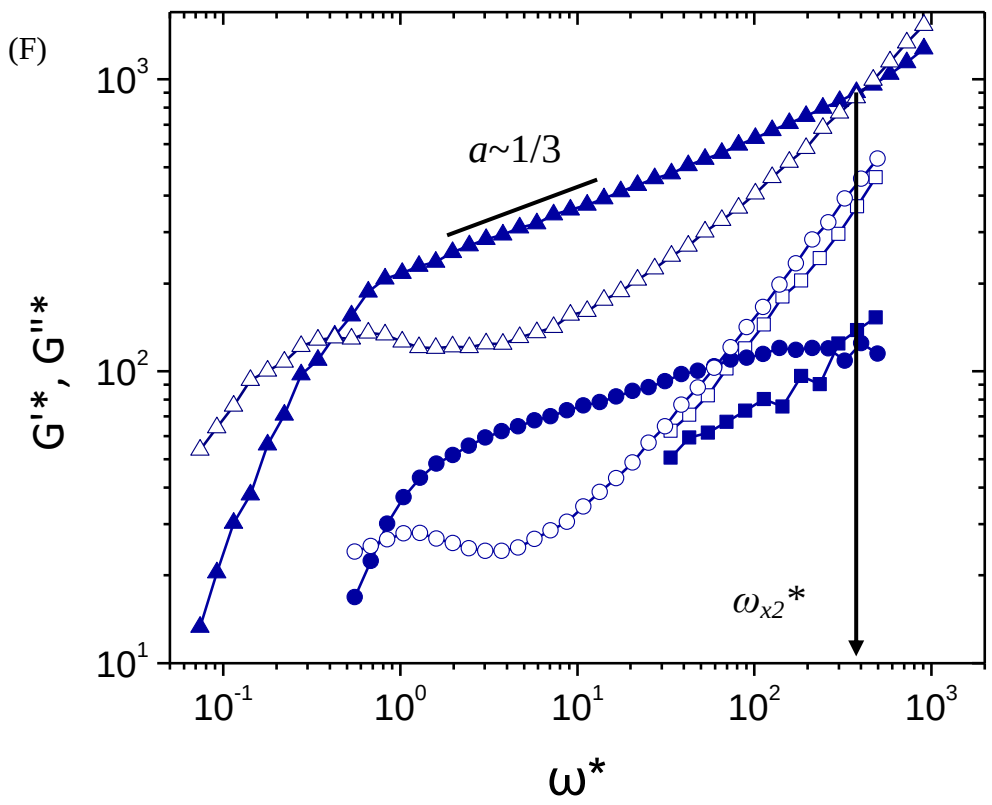

Figure 3.3 Linear *G'*** (Close symbols) and *G''*** (Open symbols) for (A) *R*=0 at ϕ_c=0.511(■, □), 0.534 (●,○) 0.557 (▲,△), 0.604 (▼,▽) and 0.628 (◆,◇); (B) *R*=0.29 at ϕ_c=0.557(■, □), 0.579 (●, ○) 0.604 (▲,△), 0.628 (▼, ▽) and 0.652 (◆,◇); (C)*R*=0.5 at ϕ_c=0.628(■, □), 0.656 (●,○) 0.678(▲,△) and 0.701(▼, ▽); (D)*R*=0.71 at ϕ_c=0.605(■, □), 0.628 (●,○) 0.653 (▲,△), 0.675 (▼, ▽) and 0.700 (◆,◇); (E) *R*=1 at ϕ_c=0.580(■, □), 0.604 (●,○) and 0.629 (▲,△). The solid lines in (A) and (E) show the slope *a* at the plateau. The arrow in (E) illustrates methods of determining ω_{x2}*.

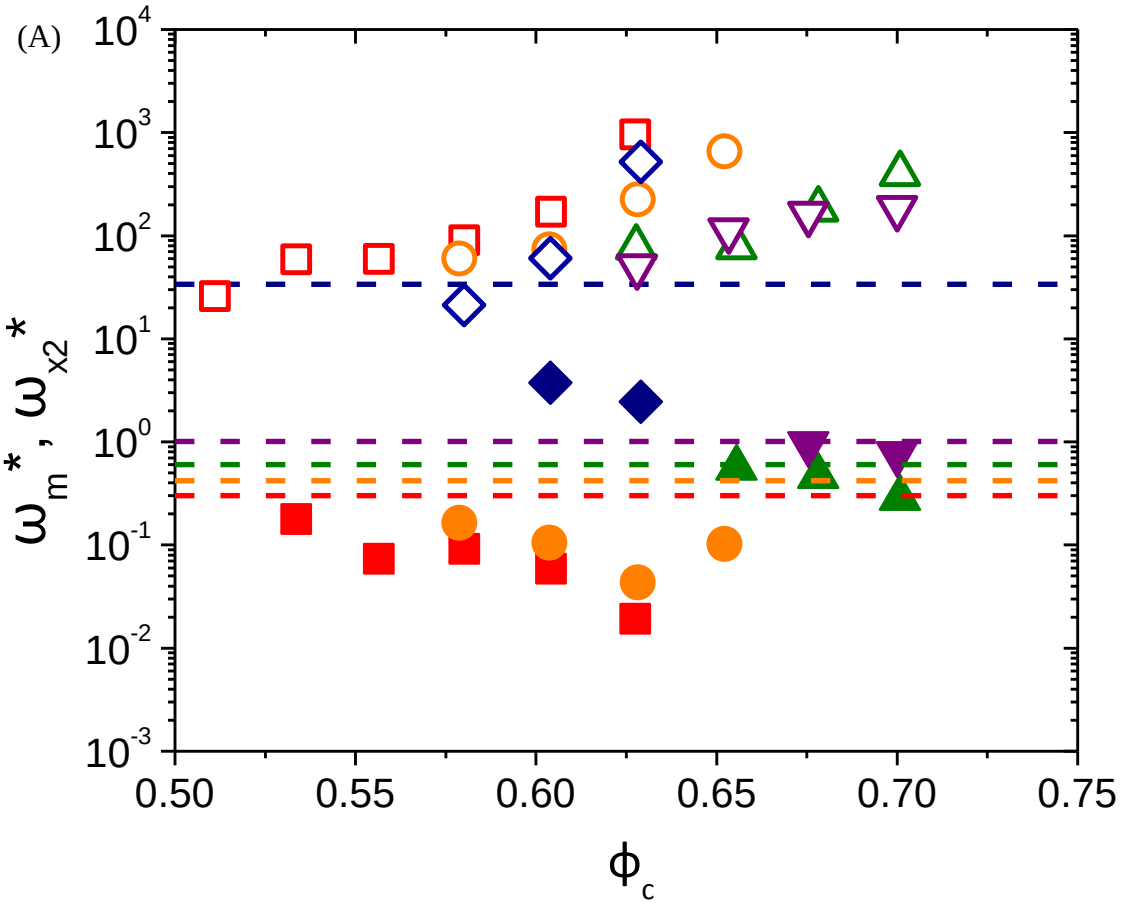

Figure 3.4 (continued on next page)

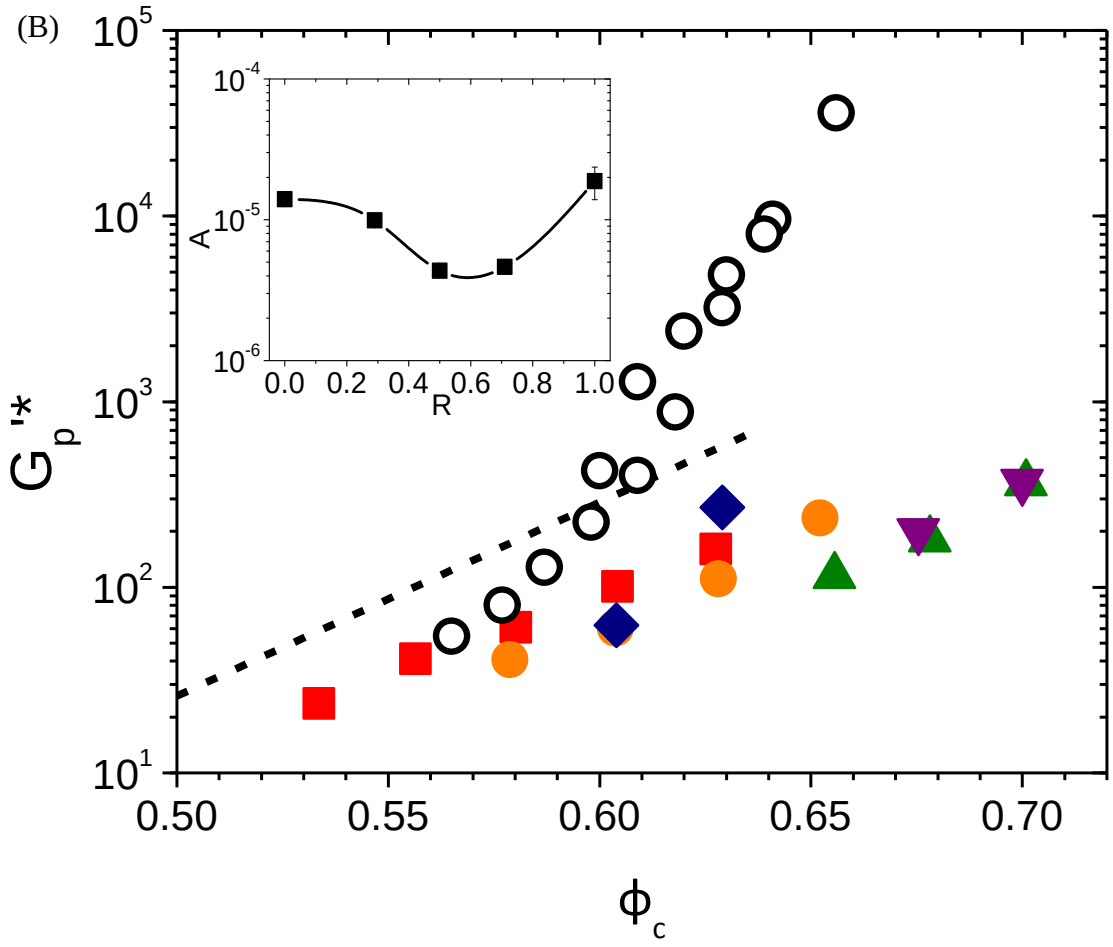

Figure 3.4 (A)ω_m*(close symbols), ω_{x2}* (open symbols) as a function of ϕ_c for R=0(■,□), R=0.29(●,○), R=0.5(▲,△), R=0.71(▼,▽) and R=1(◆,◇); (B) main panel: G_p'* as function of ϕ_c for R=0(■), R=0.29(●), R=0.5(▲), R=0.71 (▼) and R=1(◆), inset: A as a function of R. The dashed lines (red for R=0, orange for R=0.29, green for R=0.5, purple for R=0.71 and blue for R=1) in (A) are dimensionless frequencies for f=0.1Hz. The black dashed line in (B) main panel is prediction of Kobelev et al[30] for hard spheres. The Open circles in (B) are experimental results of hard sphere glass reported by Koumakis et al.[39] The solid curve in (B) inset is used to guide eyes.

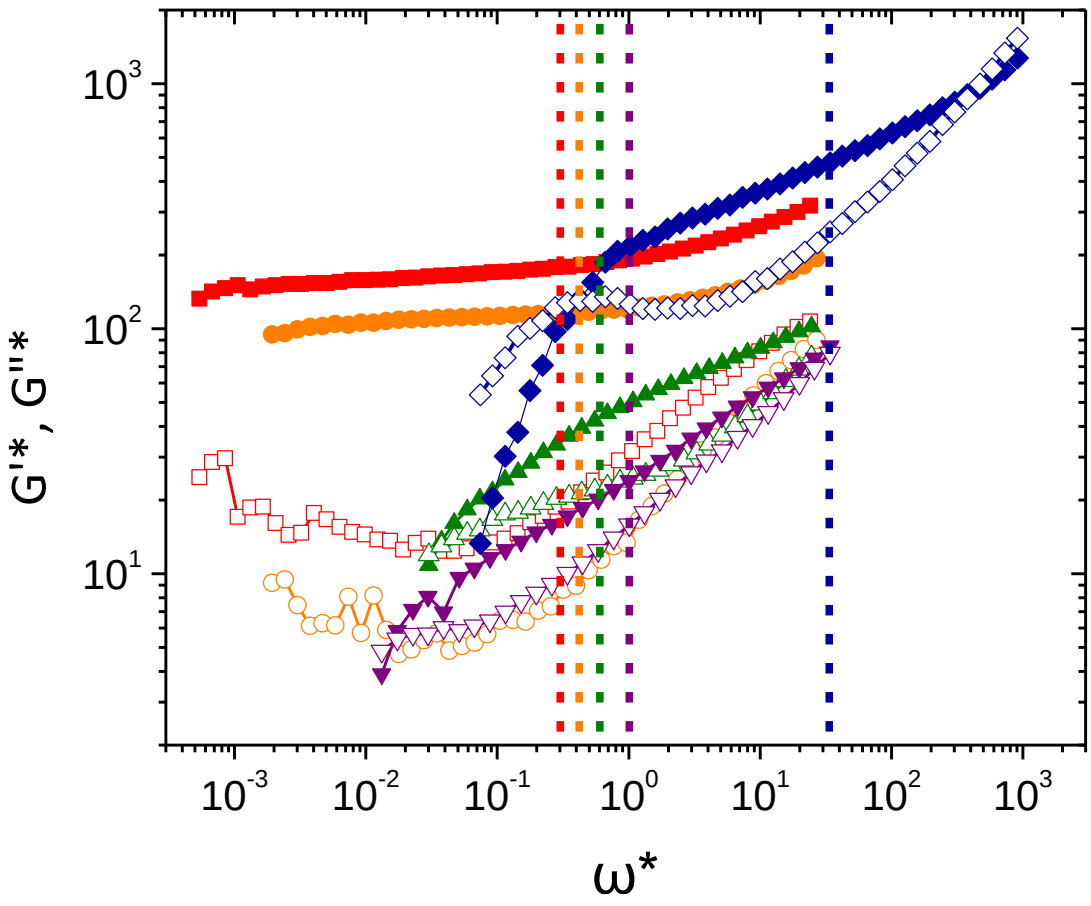

Figure 3.5 Frequency sweep experiment at ϕ_c=0.63 (C) for R=0(■, □), R=0.29(●, ○), R=0.5(▲, △), R=0.71 (▼,▽) and R=1(◆,◇) with close symbols for G'^* and open symbols for G''^*. The dashed lines (red for R=0, orange for R=0.29, green for R=0.5, purple for R=0.71 and blue for R=1) are dimensionless frequencies for f=0.1Hz.

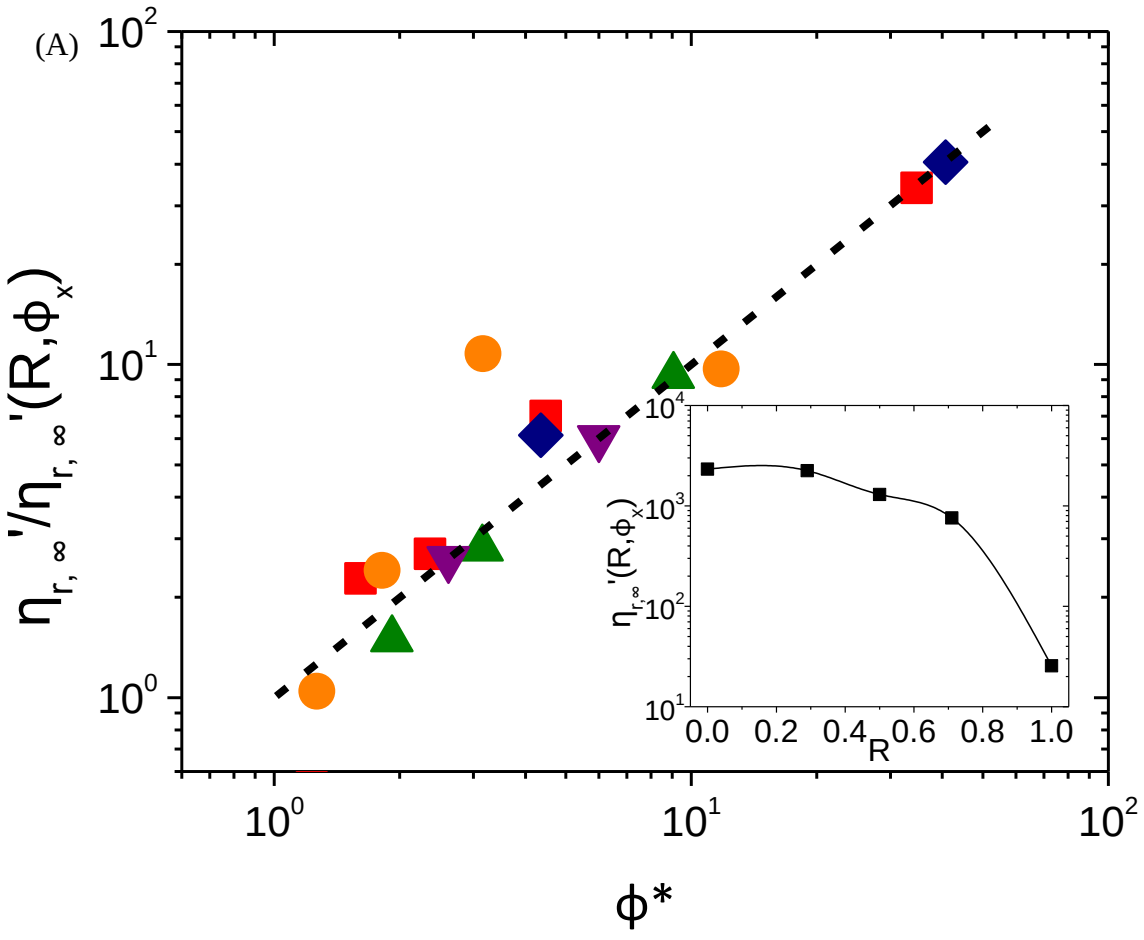

Figure 3.6 (continued on next page)

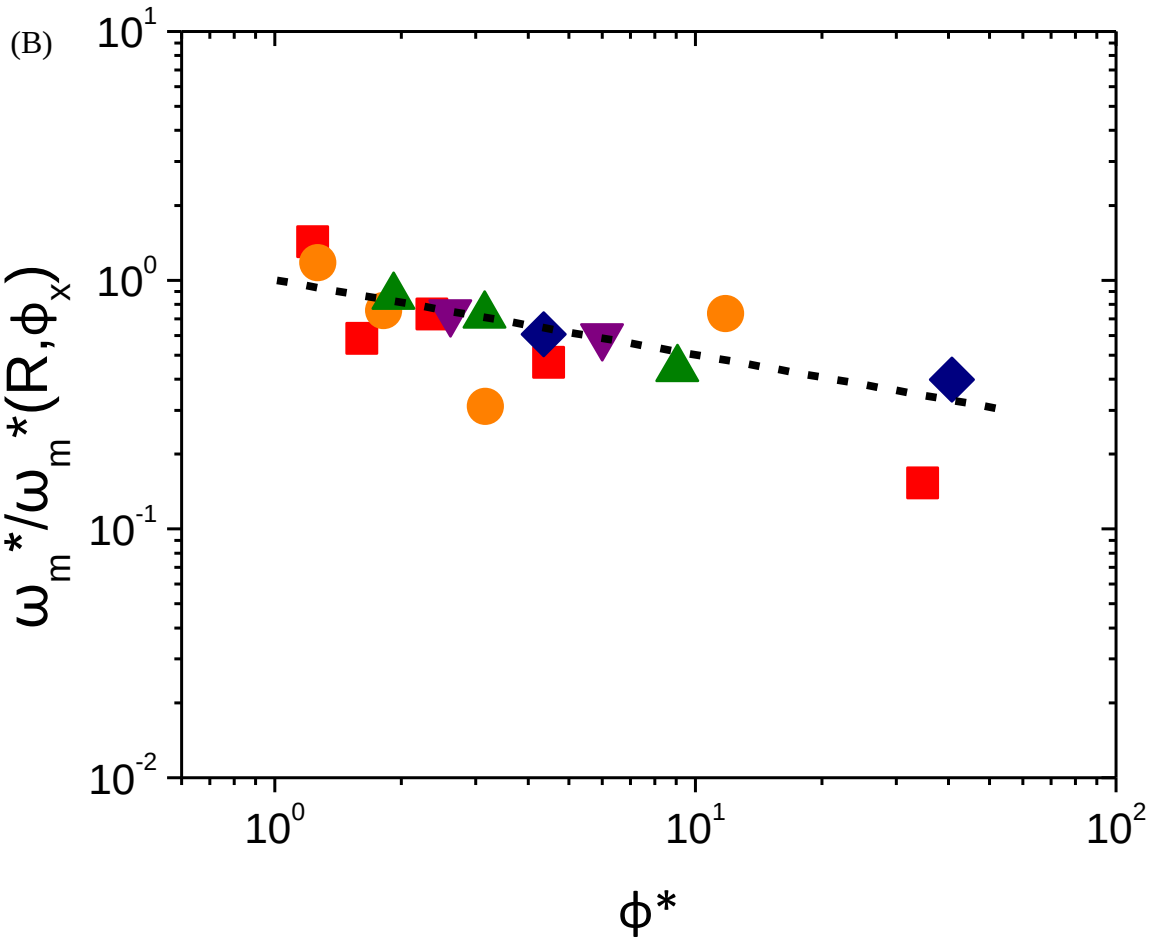

Figure 3.6 (A) Scaled high frequency viscosity $\eta_{r,\infty}'/\eta_{r,\infty}'(R, \phi_x)$ and (B) scaled dimensionless frequency ω_m^*/ω_m^* (R, ϕ_x) as a function of ϕ^* for R=0(■), R=0.29(●), R=0.5(▲), R=0.71 (▼) and R=1(◆).The dashed line in (A) is fitting of Equation (3.5), and the dashed line in (B) is fitting of power law $\omega_m^*/\omega_m^*(R,\phi_x)=\phi^{*-0.3}$. Inset of (A): $\eta_{r,\infty}'$ (R, ϕ_x) is plotted as a function of R with the solid curve used to guide eyes.

Table 3.2 Summary of ϕ_x, ϕ_m and ϕ_m/ϕ_x for different R

R	ϕ_x	ϕ_m	ϕ_m/ϕ_x
0	0.511	0.631	1.23
0.29	0.557	0.661	1.19
0.5	0.603	0.713	1.18
0.71	0.605	0.719	1.19
1	0.51	0.632	1.24

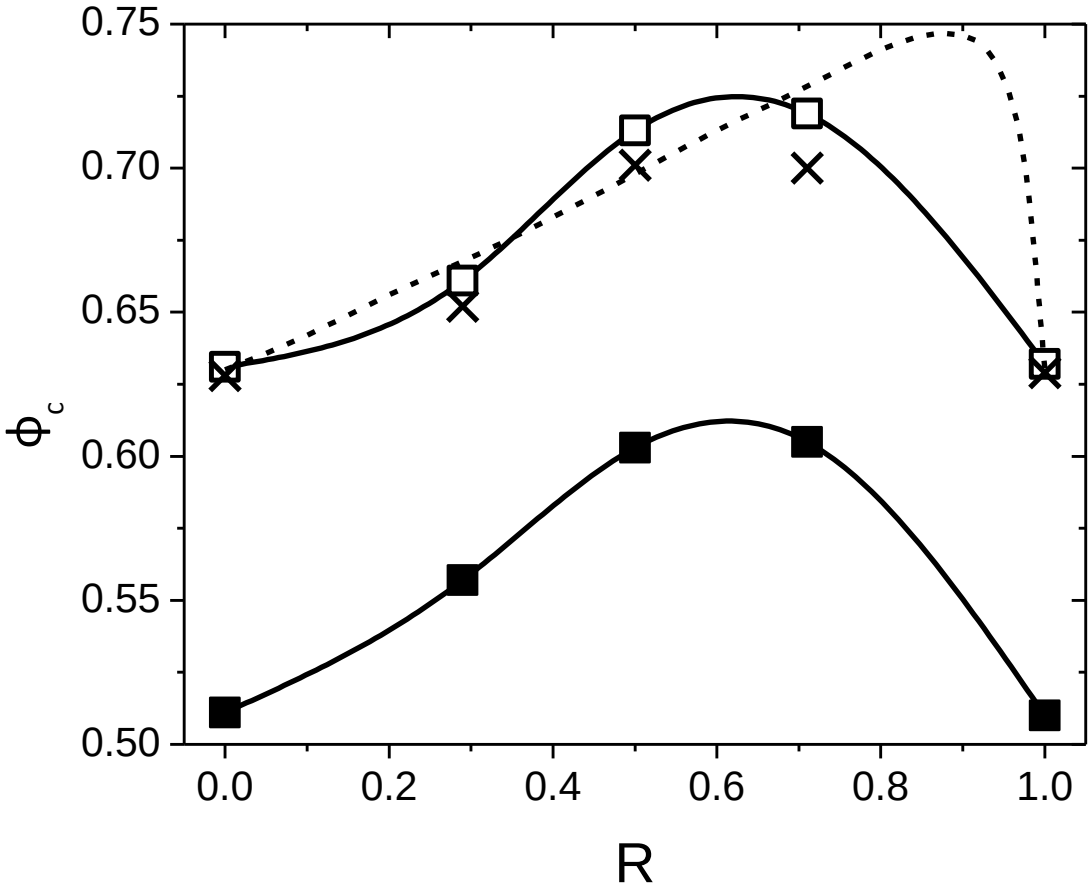

Figure 3.7 Phase diagram of the binary mixture with close squares for ϕ_x, open squares for ϕ_m. Solid curves are used to guide eyes. Cross symbols stand for the highest volume fraction samples investigated here. The dashed curve is the calculation result of Ouchiyama et al.'s equation.[44]

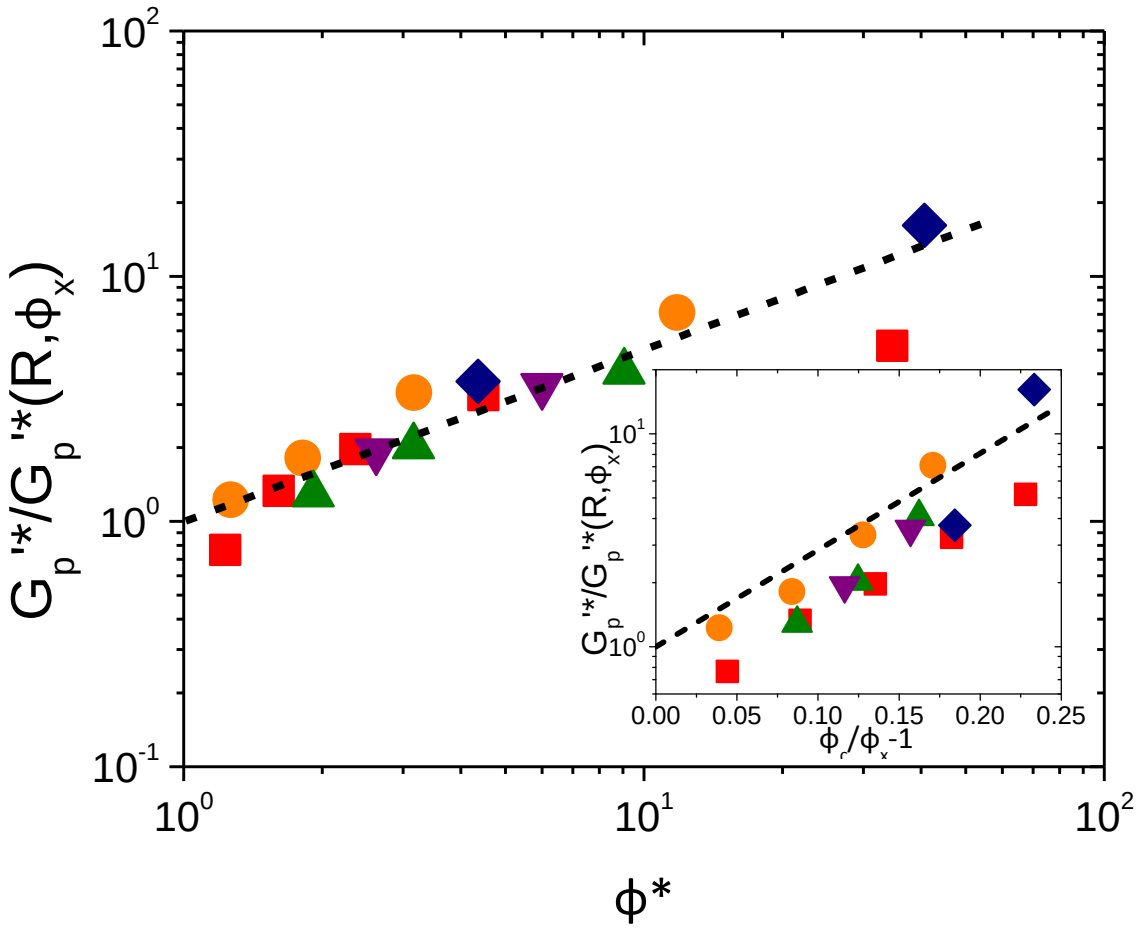

Figure 3.8 Scaled dimensionless elasticity $G_p'^*/G_p'^*(R, \phi_x)$ as a function of ϕ_* (Main Panel) and scaled dimensionless elasticity $G_p'^*/G_p'^*(R, \phi_x)$ as a function of ϕ_c/ϕ_x-1(Inset) for R=0(■), R=0.29(●), R=0.5(▲), R=0.71(▼) and R=1(◆).The dashed line in main panel is fitting of power law $G_p'^*/G_p'^*(R,\phi_x) = \phi^{*0.7}$. The dashed line in inset is correlation result of Yatsenko et al. for hard spheres.[47]

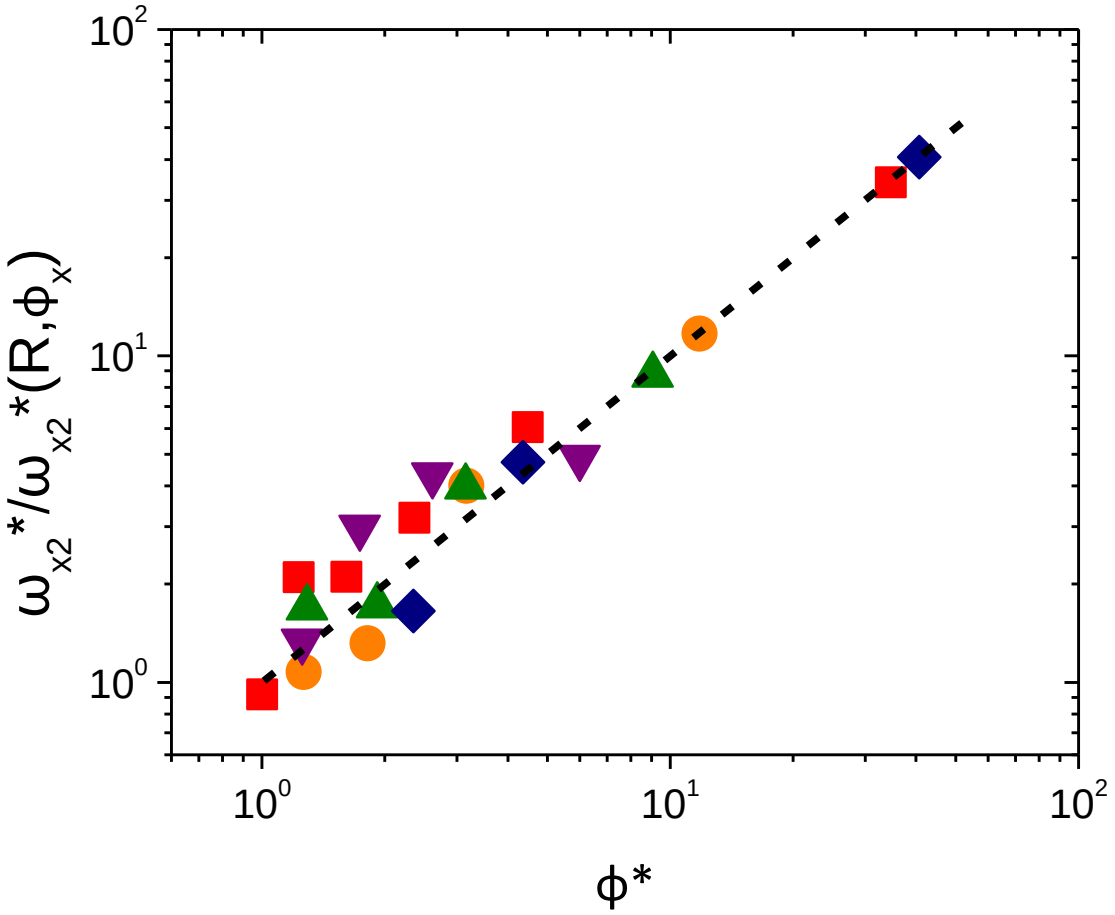

Figure 3.9 Scaled dimensionless frequency $\omega_{x2}*/\omega_{x2}*(R, \phi_x)$ as a function of $\phi*$ for R=0(■), R=0.29(●), R=0.5(▲), R=0.71 (▼) and R=1(◆). The dashed line is fitting of power law $\omega_{x2} * / \omega_{x2} * (R, \phi_x) = \phi *$.

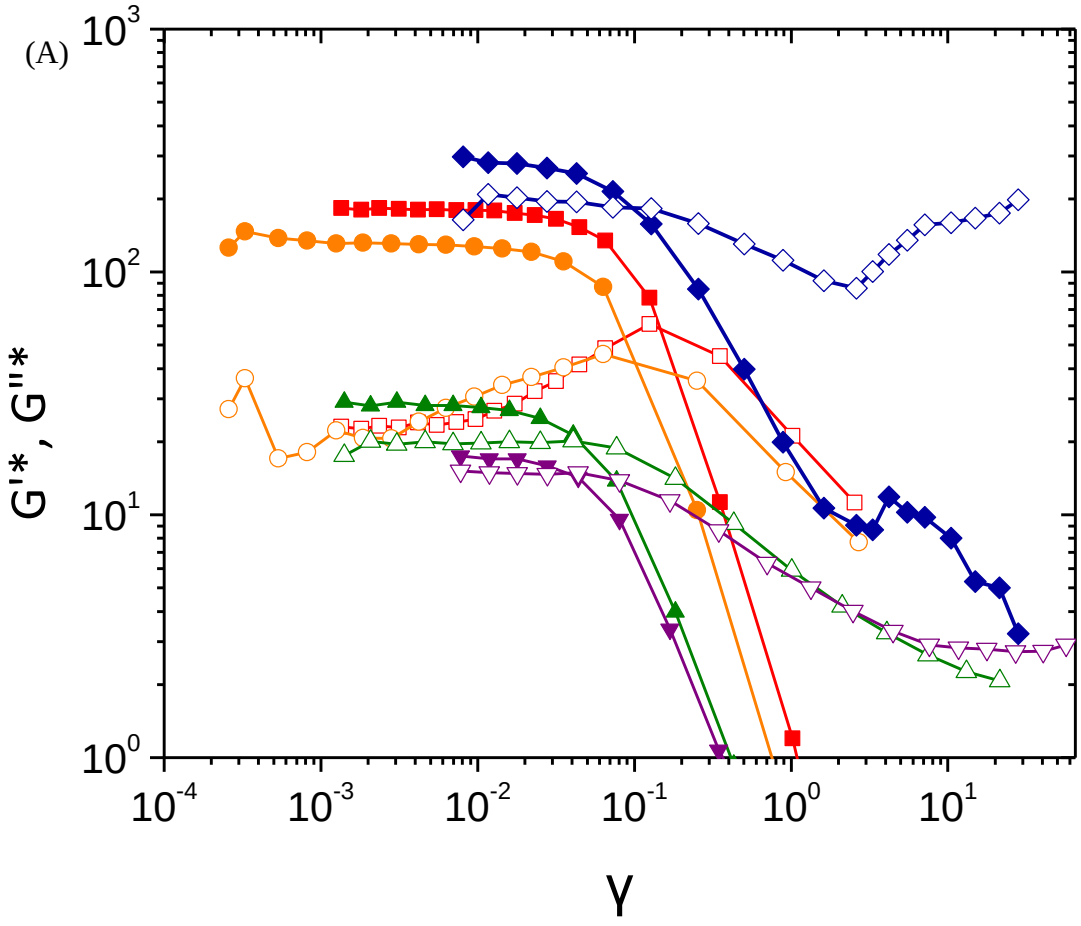

Figure 3.10 (continued on next page)

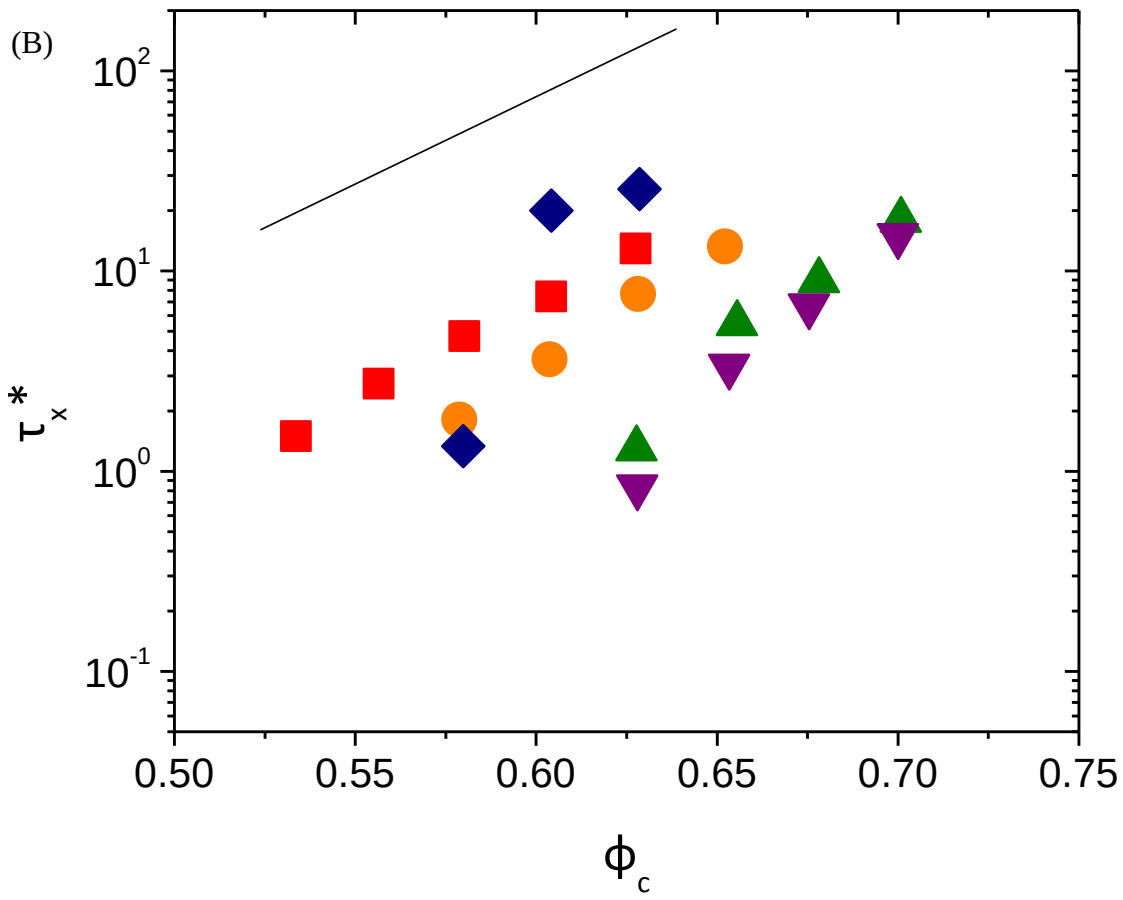

Figure 3.10 (continued on next page)

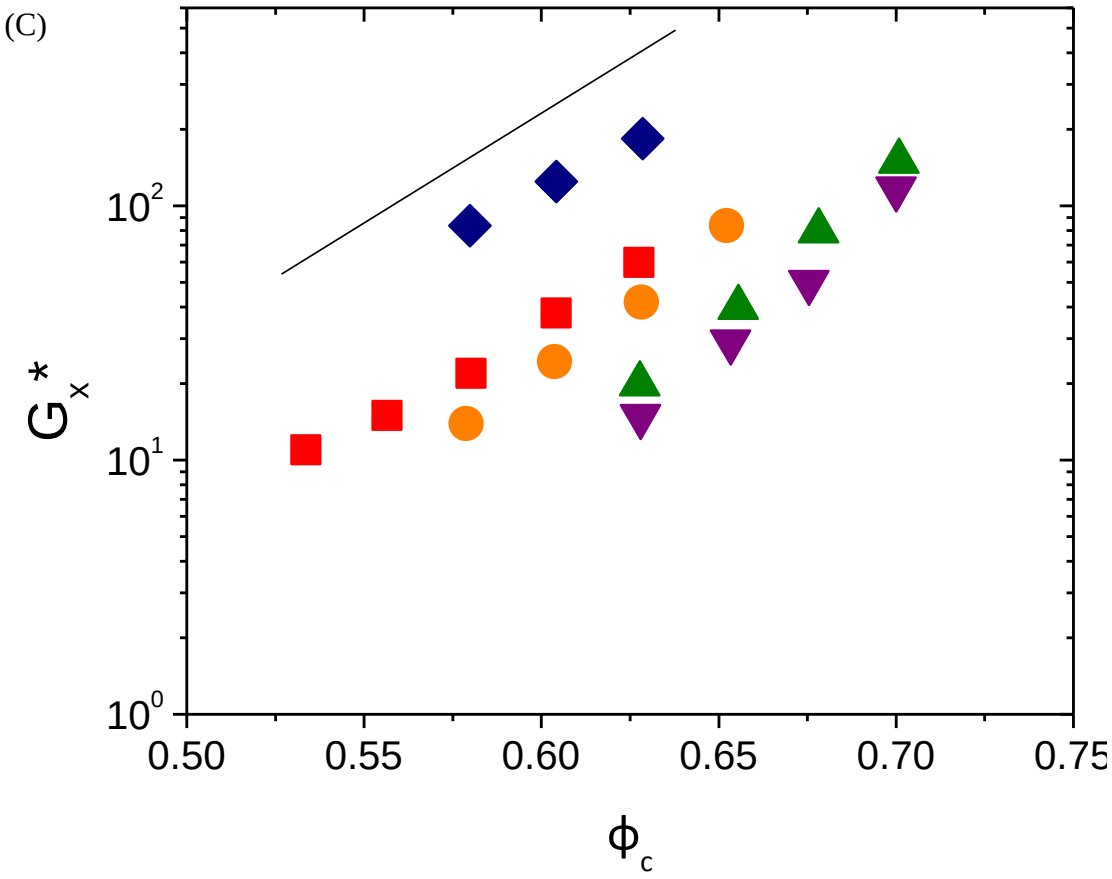

Figure 3.10 (continued on next page)

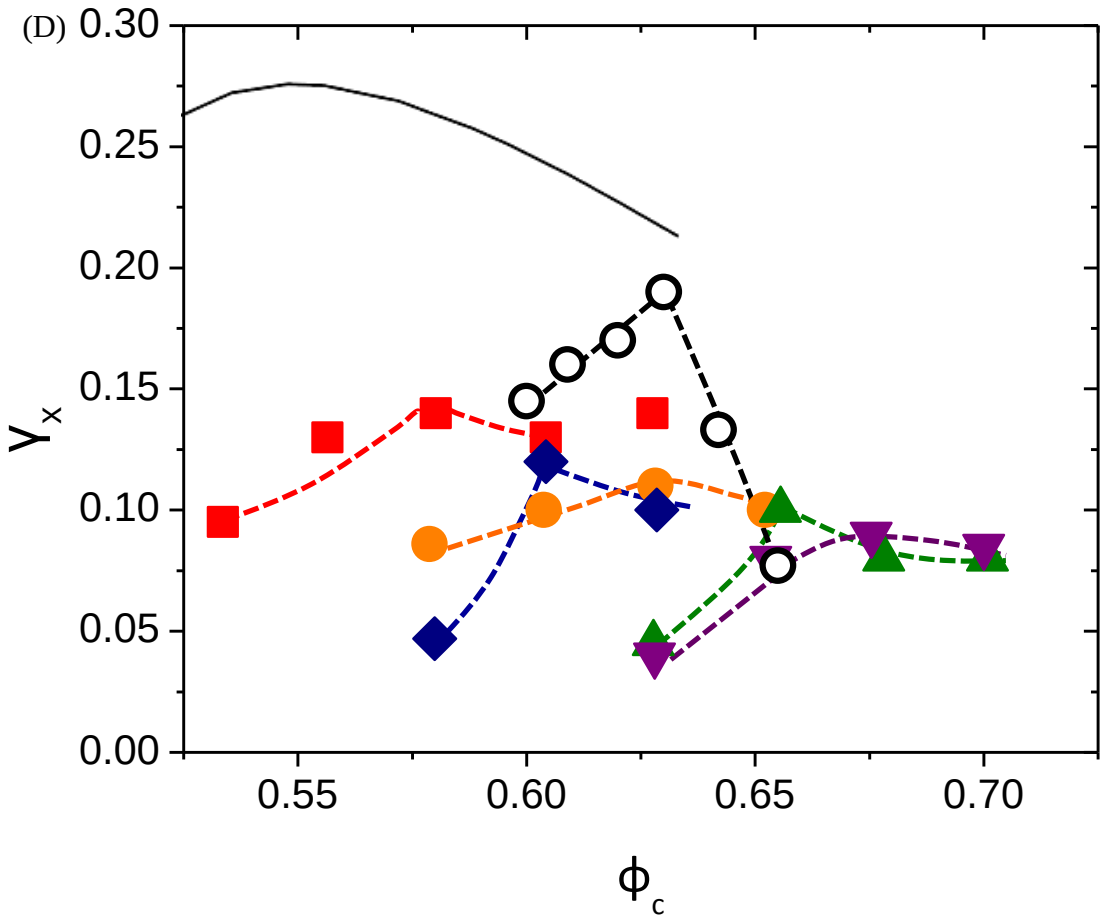

Figure 3.10 (A) Stress sweep experiment at f=0.1Hz at ϕ_c=0.63 for R=0(■, □), R=0.29(●,○), R=0.5(▲,△), R=0.71 (▼,▽) and R=1(◆,◇) with close symbols for G'^* and open symbols for G''^*. (B) τ_x^*, (C) G_x^* and strain (D) γ_x at the cross point where $G'^*=G''^*=G_x^*$ plot with ϕ_c for R=0(■), R=0.29(●), R=0.5(▲), R=0.71 (▼) and R=1(◆).The Open circles in (D) are experimental results of hard sphere glass reported by Koumakis et al.[39] The dashed curves in (D) are used to guide eyes for the peak in γ_x. The black lines in (B)-(D) are predictions by Kobelev et al.[30]

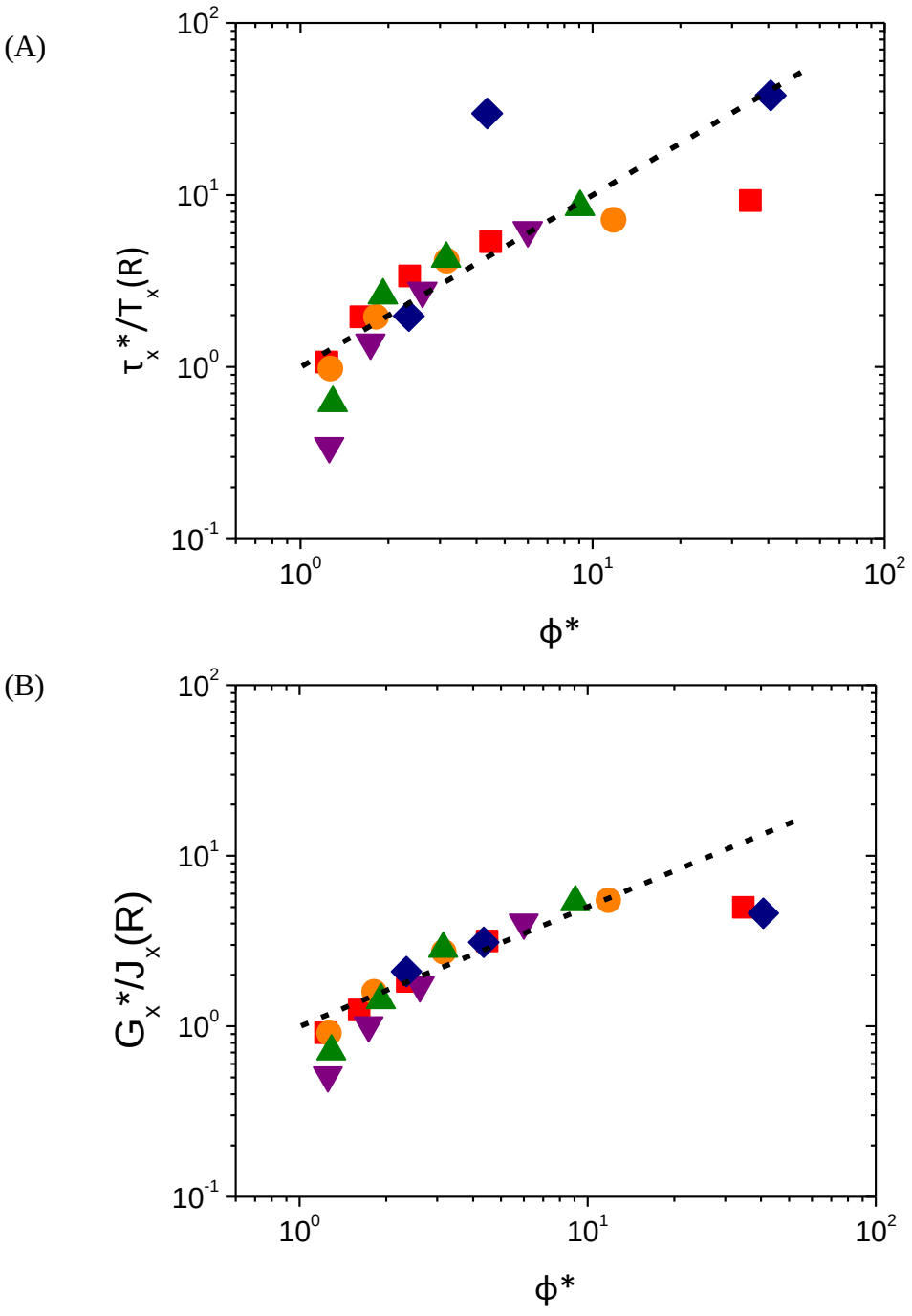

Figure 3.11 (A) Scaled dimensionless yield stress $\tau_x^*/T_x(R)$ and (B) scaled dimensionless frequency $G_x^*/J_x(R)$ as a function of ϕ^* for R=0 (■), R=0.29(●), R=0.5(▲), R=0.71 (▼) and R=1(◆). Dashed lines in (A) and (B) are fittings of power law $\tau_x^*/T_x(R) = \phi^*$ and $G_x^*/J_x(R) = \phi^{*0.7}$.

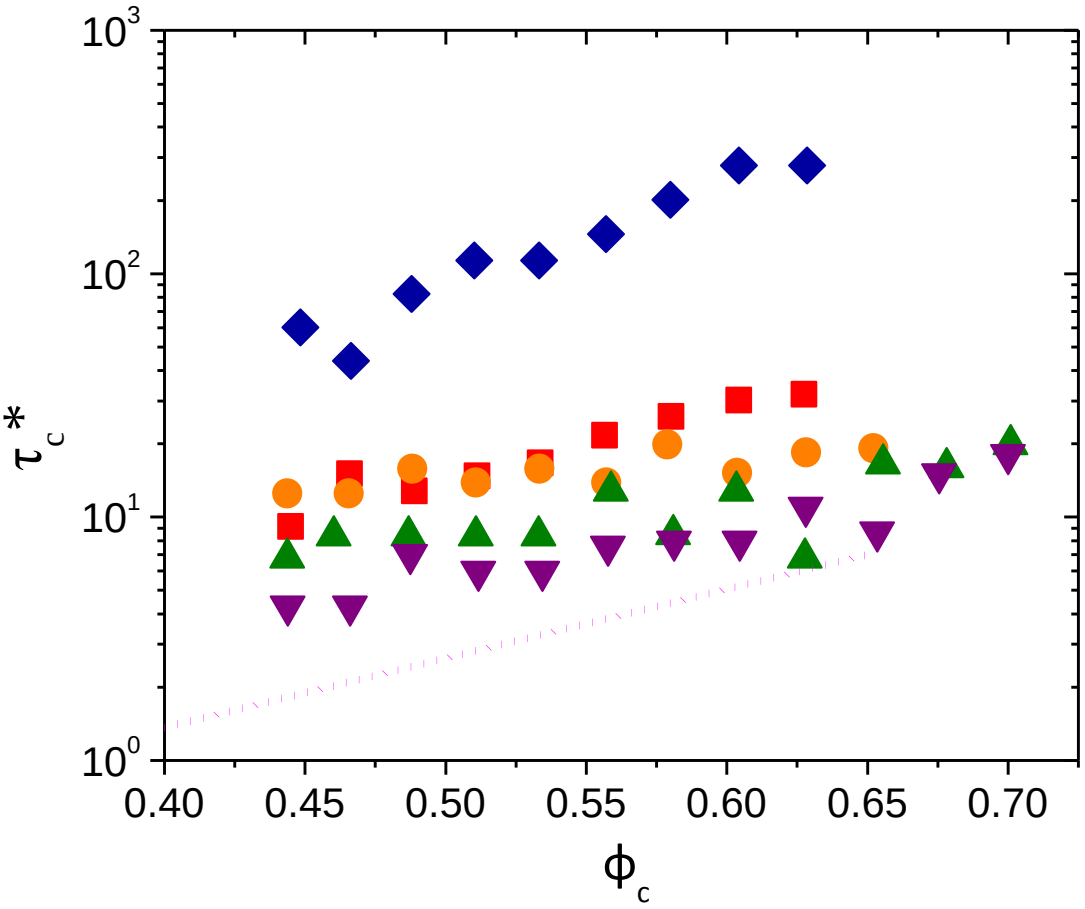

Figure 3.12 Dimensionless critical stressed τ_c* as a function of ϕ_c for R=0(■), R=0.29(●), R=0.5(▲), R=0.71 (▼) and R=1(◆).The dotted line is the correlation of hard sphere experiment experiencing Brownian force reported before.[56]

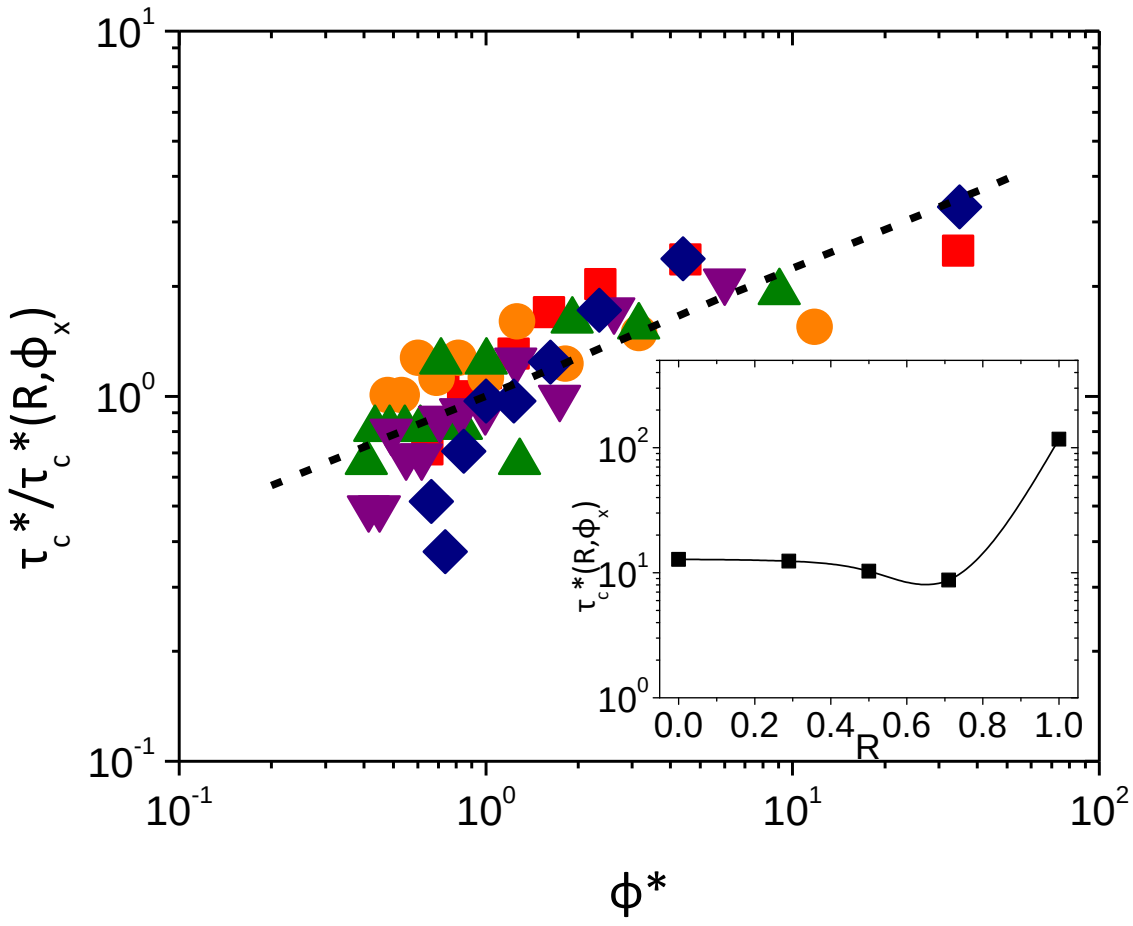

Figure 3.13 Scaled dimensionless stress $\tau_c^*/\tau_c(R, \phi_x)$ as a function of ϕ^* for R=0(■), R=0.29(●), R=0.5(▲), R=0.71 (▼) and R=1(◆). The dashed line is fitting of power law $\tau_c^*/\tau_c^*(R,\phi_x) = \phi^{*0.35}$. Inset: $\tau_c(R, \phi_x)$ is plotted as a function of R with the solid curve used to guide eyes.

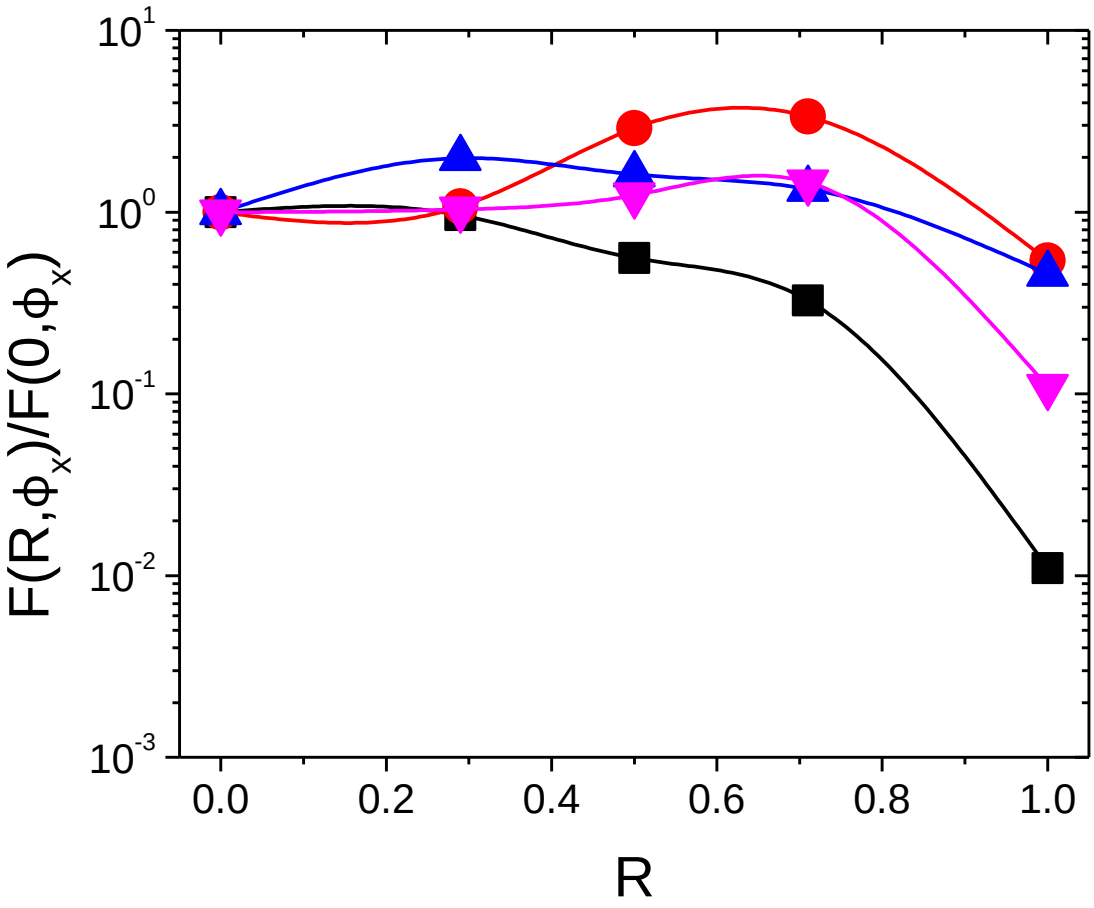

Figure 3.14 Plots of $F(R, \phi_x)/F(0, \phi_x)$ as a function of R, where $F(R, \phi_x)$ are $\eta_{r,\infty}(R, \phi_x)$ (■), $G_p'^*(R, \phi_x)$ (●), $\omega_{x2}^*(R, \phi_x)$ (▲) and $1/\tau_c^*(R, \phi_x)$ (▼).

3.6 References

1. L. M. Hall, B. J. Anderson, C. F. Zukoski and K. S. Shweizer, *Macromolecules*, 2009, **42**, 8435-8442.
2. W. B. Russel, D. A. Saville and W. R. Schowalter, *Colloidal Dispersions*, Cambridge University Press, Cambridge, 1989.
3. K. S. Schweizer and G. Yatsenko, *Journal of Chemical Physics*, 2007, **127**, 164505.
4. V. Kobelev and K. S. Schweizer, *Journal of Chemical Physics*, 2005, **123**, 164903.
5. B. E. Rodriguez, E. W. Kaler and M. S. Wolfe, *Langmuir*, 1992, **8**, 2382-2389.
6. C. G. Dekruif, E. M. F. Vanlersel, A. Vrij and W. B. Russel, *Journal of Chemical Physics*, 1985, **83**, 4717-4725.
7. M. Pishvaei, C. Graillat, P. Cassagnau and T. F. McKenna, *Chemical Engineering Science*, 2006, **61**, 5768-5780.

8. S. R. Williams and W. van Megen, *Physical Review E*, 2001, **64**, 041502.
9. T. Voigtmann, *Physical Review E*, 2003, **68**, 051401.
10. G. Brambilla, D. El Masri, M. Pierno, L. Berthier, L. Cipelletti, G. Petekidis and A. B. Schofield, *Physical Review Letters*, 2009, **102**, 085703.
11. W. Gotze, *Journal of Physics-Condensed Matter*, 1999, **11**, A1-A45.
12. M. Pishvaei, C. Graillat, T. F. McKenna and P. Cassagnau, *Polymer*, 2005, **46**, 1235-1244.
13. J. Mewis, W. J. Frith, T. A. Strivens and W. B. Russel, *Aiche Journal*, 1989, **35**, 415-422.
14. K. S. Schweizer, *Journal of Chemical Physics*, 2007, **127**, 164506.
15. A. Imhof and J. K. G. Dhont, *Physical Review Letters*, 1995, **75**, 1662-1665.
16. A. D. Dinsmore, A. G. Yodh and D. J. Pine, *Physical Review E*, 1995, **52**, 4045-4057.
17. T. Coussaert and M. Baus, *Physical Review Letters*, 1998, **80**, 4832-4833.
18. P. Germain and S. Amokrane, *Physical Review Letters*, 2009, **102**, 058301.
19. P. Germain and S. Amokrane, *Physical Review E*, 2010, **81**, 011407.
20. M. Dijkstra, R. van Roij and R. Evans, *Physical Review E*, 1999, **59**, 5744-5771.
21. W. Gotze and T. Voigtmann, *Physical Review E*, 2003, **67**, 021502.
22. G. Foffi, W. Gotze, F. Sciortino, P. Tartaglia and T. Voigtmann, *Physical Review Letters*, 2003, **91**, 085701.
23. T. Voigtmann, *Epl*, 2011, **96**, 36006.
24. M. Pishvaei, C. Graillat, T. F. McKenna and P. Cassagnau, *Journal of Rheology*, 2007, **51**, 51-69.
25. B. J. Maranzano and N. J. Wagner, *Journal of Chemical Physics*, 2001, **114**, 10514-10527.
26. B. J. Anderson and C. F. Zukoski, *Journal of Physics-Condensed Matter*, 2009, **21**, 285102.
27. L. M. Hall and K. S. Schweizer, *Journal of Chemical Physics*, 2008, **128**, 234901.
28. L. M. Hall and K. S. Schweizer, *Macromolecules*, 2011, **44**, 3149-3160.
29. B. J. Anderson and C. F. Zukoski, *Macromolecules*, 2009, **42**, 8370-8384.
30. V. Kobelev and K. S. Schweizer, *Physical Review E*, 2005, **71**, 021401.
31. T. Jiang and C. F. Zukoski, *Macromolecules*, 2012, **45**, 9791-9803.
32. W. Stober, A. Fink and E. Bohn, *Journal of Colloid and Interface Science*, 1968, **26**, 62-69.
33. G. H. Bogush, M. A. Tracy and C. F. Zukoski, *Journal of Non-Crystalline Solids*, 1988, **104**, 95-106.
34. J. Bender and N. J. Wagner, *Journal of Rheology*, 1996, **40**, 899-916.
35. T. G. Mason and D. A. Weitz, *Physical Review Letters*, 1995, **75**, 2770-2773.
36. B. J. Anderson and C. F. Zukoski, *Macromolecules*, 2008, **41**, 9326-9334.
37. C. J. Rueb and C. F. Zukoski, *Journal of Rheology*, 1998, **42**, 1451-1476.
38. R. A. Lionberger and W. B. Russel, *Journal of Rheology*, 1994, **38**, 1885-1908.
39. N. Koumakis, A. B. Schofield and G. Petekidis, *Soft Matter*, 2008, **4**, 2008-2018.
40. R. C. Kramb, R. Zhang, K. S. Schweizer and C. F. Zukoski, *Physical Review Letters*, 2010, **105**, 055702.
41. A. K. Doolittle, *J. Appl. Phys.*, 1951, **22**, 1471-1475.

42. J. Mewis and N. J. Wagner, *Colloidal Suspension Rheology*, Cambridge University Press, Cambridge, United Kingdom, 2012.
43. M. D. Rintoul and S. Torquato, *Physical Review Letters*, 1996, **77**, 4198-4201.
44. N. Ouchiyama and T. Tanaka, *Industrial & Engineering Chemistry Fundamentals*, 1984, **23**, 490-493.
45. D. Hajnal, J. M. Brader and R. Schilling, *Physical Review E*, 2009, **80**, 021503.
46. R. C. Kramb and C. F. Zukoski, *Journal of Rheology*, 2011, **55**, 1085-1101.
47. G. Yatsenko and K. S. Schweizer, *Journal of Chemical Physics*, 2007, **126**.
48. R. G. Larson, in *Topics in Chemical Engineering*, ed. K. Gubbins, Oxford University, New York, Editon edn., 1999, pp. 342-353.
49. T. G. Mason, J. Bibette and D. A. Weitz, *Journal of Colloid and Interface Science*, 1996, **179**, 439-448.
50. M. Laurati, S. U. Egelhaaf and G. Petekidis, *Journal of Rheology*, 2011, **55**, 673-706.
51. A. J. Giacomin, R. S. Jeyaseelan, T. Samurkas and J. M. Dealy, *Journal of Rheology*, 1993, **37**, 811-826.
52. R. H. Ewoldt, A. E. Hosoi and G. H. McKinley, *Journal of Rheology*, 2008, **52**, 1427-1458.
53. S. A. Rogers, *Journal of Rheology*, 2012, **56**, 1129–1151.
54. S. A. Rogers and M. P. Lettinga, *Journal of Rheology*, 2012, **56**, 1–25.
55. B. J. Maranzano and N. J. Wagner, *Journal of Rheology*, 2001, **45**, 1205-1222.
56. L. N. Krishnamurthy, N. J. Wagner and J. Mewis, *Journal of Rheology*, 2005, **49**, 1347-1360.

Chapter 4. The Effects of Polymer Induced Attraction on Dynamical Arrests of Polymer Composites with Bimodal Particle Size Distributions

4.1 Introduction

The impact of mixing particles of different size on suspension flow properties is both subtle and dramatic. In one sense little changes: as volume fraction increases the suspension viscosity increases,[1-3] gels and glasses are formed at high enough volume fraction,[4, 5] yield stresses develop and shear thickening[6] can be observed. When observed from a second perspective, however, introducing a second component with different size substantially alters the volume fraction where changes in state are observed. For example while numerous studies show that amorphous suspensions of hard spheres will not flow at a volume fractions above ~0.64,[7-10] the same state is not reached for mixtures of hard spheres with a size ratio of ~4 at a 1:1 mixing volume fraction ratio until the total particle volume fraction is ~0.70 as shown in experiment[3, 11] and theory.[12] This maximum packing fraction can be varied by changing the large particle volume fraction ratio or the size ratio. Viscosities, elasticities, relaxation times and yield stresses all change rapidly as maximum packing fraction is approached. As a result, at a total fixed solid loading, addition of a second component can dramatically alter suspension flow properties.

For particles experiencing repulsive interactions, the flow properties observed in suspensions of mixtures often appear as a delay in volume fraction where significant rheological transitions are observed. This is captured in scaling rheological parameters with the distance to maximum packing (i.e., as $1/(\phi_m-\phi_c)$, where ϕ_m is the maximum packing fractions of the mixture and ϕ_c is the total particle volume fraction in the suspension). In mixtures, ϕ_m is a function of the mixing ratio.[8]

In low molecular weight polymer melts where particles experience volume exclusion interactions,[11] flow properties tend to collapse onto similar curves when plotted as a function of $(\phi_m-\phi_x)/(\phi_m-\phi_c)$ for different ratios of large to small particles despite there being a variety of nearest neighbor environments in which particles may find themselves in a mixture. Here ϕ_x is the volume fraction at which onset of the glassy response occurs.[11] This observation leads to an attempt to develop pseudo one-component models for mixtures where the suspension is treated as being composed of particles with some average size that has a mixture specific maximum packing ratio. The pseudo-one component diameter, $<D>$, is often treated as lying between the D_s and D_l where D is the particle diameter and subscripts s and l correspond to the small and the large component of the binary mixture and to have a dependence on $R=\phi_l/\phi_c$ where ϕ_l is the volume fraction of the large particle in a binary mixture. In this approach, $<D>$ is independent of ϕ_c. The maximum packing fraction is a function of R and $\delta=D_l/D_s$ and is often found to be similar to that expected of granular or non-Brownian particles.[1, 3, 11] Given this pseudo one-component approach, the challenge to determining suspension flow properties lies in understanding the scaling relationships between relaxation times, viscosities, critical stresses and $<D>$, R, δ, and $(\phi_m-\phi_x)/(\phi_m-\phi_c)$ with the constraints that when R=0 or 1, and the suspension is reduced to a suspension of a single component, reduced flow properties are identical.

This picture is complicated by non-geometric factors when the particles do not experience volume exclusion interactions.[13-15] In particular, under conditions where the particles are attractive, substantial changes in flow properties arise and thus complicate the use of a pseudo-one component approach. Often the nature of the interactions

between the particles is poorly understood. Under these conditions, characterizing flow properties in terms of an R- and δ– dependent maximum packing fraction becomes difficult.

In this paper we explore the rheology of a binary mixture of spheres with δ=4.8 under the conditions where the particles experience short-range attractions. Previous studies characterized the flow properties of mixtures of the same particles under conditions where they experience near excluded volume interactions such that $\phi_m(R)$ is well characterized. For these excluded volume interactions, with increasing volume fraction, glassy behavior was observed. The onset of the glassy response occurred at a volume fraction $\phi_x(R)$ and we found that ϕ_x/ϕ_m =1.21 for all R. In addition, flow properties could be reduced in terms of a volume fraction averaged diameter (i.e., $< D >= [(1-R)/D_s^3 + R/D_l^3]^{-1/3}$ and a reduced volume fraction $\phi^* = (\phi_m - \phi_x)/(\phi_m - \phi_c)$ in the form of $F = F(\phi_x, R)\phi^{*a}$ where F is a rheological property such as plastic modulus, yield stress, or characteristic relaxation frequency, with $F(\phi_x, R)$ being the property at ϕ_x. The exponent a is independent of R, and $F(\phi_x, R)$ was found to have a weak dependence on R.

The experimental system displaying these characteristics was composed of D_s=127nm and D_l=612 nm diameter silica particles suspended in polyethylene glycol with a molecular weight of 400 (PEG400). The index of refraction of the silica and the PEG is nearly matched thus greatly reducing the van der Waals attractions. PEG is known to adsorb to the silica surface resulting in a repulsive potential of mean force resulting in the formation of colloidal glasses at elevated volume fractions.[16] Detailed studies indicate that there is agreement between the polymer reference interaction site

model (PRISM) of Schweizer and coworkers for the particle and polymer microstructure, indicating that the polymer is in equilibrium with the particle surface.[17] Agreement between theoretical and experimental particle and polymer structures degrades as polymer molecular weight increases.[18]

Introducing colloids into pure polymer melts often results in enhancement of mechanical properties.[19-22] For the PEG melt-silica particle system, this reinforcing is augmented when polymer length is increased such the suspensions pass from fluid-like to gel-like at a volume fraction well below that corresponding to localization associated with glass formation produced by excluded volume interactions.[18] Scattering studies suggest that this change in properties can be interpreted as resulting from the particles experiencing polymer induced attractions despite being coated with polymer layers with a thickness that grows with the polymer's radius of gyration.[18] The onset of attractions has been attributed to an increased number of segments on the same molecule binding to the particle surface resulting in slowed exchange kinetics such that the polymer at the surface cannot achieve equilibrium configurations with polymer segments in the bulk. One consequence of this slowed exchange dynamics is that the particle surface appears to polymer segments in the bulk as if they are composed of polymer segments such that the exchange enthalpy of a segment form the bulk to the particle surface is reduced. This reduced effective segmental enthalpy of attraction results in a weakly attractive potential of mean force.[17]

In this paper we exploit this weak attraction to investigate the flow properties of binary mixtures of spherical particles under conditions where, on increasing volume fraction, the particles form gels and attractive glasses.

Theoretical studies have been carried out to understand the glass transition and gelation in binary mixtures of hard spheres (.e., those experience only excluded volume interactions) and attractive spheres with comparable size.[23] For weak strengths of attraction between the attractive spheres, at sufficiently high total volume fraction, the system enters a glassy state. As the strength of attraction between the attractive particles is increased, gels are formed at lower total volume fraction. With even stronger attraction between the sticky spheres, a fluid-fluid phase separation is predicted. The phase boundary is only changed quantitatively as the relative concentration of hard spheres is altered.[13, 23] Experimentally, in this type of mixture the sticky particles form a homogeneous gel structure while the hard spheres either get trapped in the percolated network of sticky spheres or move freely.[15] The gel elasticity increases with the volume fraction of sticky particles where it is found that the elastic modulus grows as $G' \propto \phi_c^{5.6}$ suggesting the formation of strong gel rather than a glass transition where $G' \propto \phi_c^{14}$.[24] Because the parameter space is so large and characterizing the strength of attraction is difficult, there have been few experimental studies where particle size and strength of attraction have been varied.

We have previously studied binary mixtures of hard spheres (D_s=127nm and D_l=612nm) to characterize flow properties of binary mixtures in PEG400 at T=25 ℃ for the same particles studied in this paper. As mentioned above a variety of flow properties were found to diverge at a maximum packing fraction of ϕ_m and there was an onset of dynamic arrest at ϕ_x. In Table 4.1 we summarize the values of R, $\langle D \rangle$ used in the current paper and the values of ϕ_x and ϕ_m derived from these previous studies at these values of R for particles suspended in PEG400.[11] As mentioned, for these systems where

the particles feel excluded volume interactions, ϕ_m/ϕ_x~1.21 independent of R with ϕ_m passing through a maximum near R=0.8. As ϕ_m is determined by geometric effects, we anticipate that ϕ_m will not change when changing the medium to PEG2000; while if PEG2000 changes particle interactions, ϕ_x will be altered.

Previously we reported on the flow properties of suspensions of single sized particles of diameters D_s and D_l when suspended in PEG2000. At low volume fractions (ϕ_c<0.10) the relative zero shear viscosity of the composites can be expressed:[22]

$$\eta_{r,0} = 1 + 2.5k\phi_c + H(k\phi_c)^2 \tag{4.1}$$

Where, $k=\phi_{eff}/\phi_c$, defining ϕ_{eff} as the effective hard sphere volume fraction and the Huggins coefficient, H, is a measure of the strength of pair interactions. For hard spheres H = 5.9.[25] For the small particles suspended in PEG2000, k=1.09±0.08 and H=7.6±1.1 while for the large particles, k=1.02±0.04 and H=7.6±1.3. These results suggest that polymer binds to the particle surface, thus increasing their hydrodynamic diameter by a factor of approximately R_g, where R_g=1.9nm is the radius of gyration of PEG2000. Because the R_g/D_c <<1, the effects of the increased diameter on effective volume fraction are small. At the pair level, we conclude that the particles experience weak attractions giving rise to similar hydrodynamic effects. Bergenholtz and Wagner studied the Huggins coefficient of suspensions of particles experiencing a square well potential written:[26]

$$U(r) = \begin{cases} \infty, & 0 < r < D \\ -U_0, & D < r \le D + \Delta \\ 0, & D + \Delta < r \end{cases} \tag{4.2}$$

Due the very small values of $R_g/\langle D\rangle$ in our samples, we anticipate that the strength of attraction will be a weak function of particle size. If we use the results of Bergenholz and

Wagner and assume a square well depth $U_0 \sim 2k_BT$, we match the experimental Huggins coefficients with $\Delta = 3.8 \pm 1.3R_g$ ($\Delta/D_s = 0.057 \pm 0.019$) for small spheres and $\Delta = 12 \pm 6R_g$ ($\Delta/D_l = 0.032 \pm 0.016$) for large spheres. When ϕ_c is increased, these weak particle interactions alter the flow properties substantially from those observed for the same particles when suspended in PEG400 at T=25 ℃.[22] This attractive interaction in PEG2000 melts have also been reported in studies of the microstructure of D_c=44nm particles.[18]

With this background we report below on the flow properties of binary mixtures of particles with diameters D_s and D_l suspended in PEG2000 at T=75 ℃. We anticipate that there is a geometrical packing limit where all diffusion will stop at ϕ_m that will be the same as that seen when the particles are suspended in PEG400 and we anticipate that the attractions produced by the higher molecular weight will alter ϕ_x. Our studies show that for this system transitions in flow properties occur at nearly constant values of the average effective particle separation defined as in units of R_g which can be expressed as

$$h / R_g = \frac{< D >}{R_g}[(\phi_m / \phi_c)^{1/3} - 1] \tag{4.3}$$

While $<D>$ is used to value the effect of particle size distribution controlled by R.

Below we introduce the sample preparation procedure and measurement technique in Section 4.2. Results and discussions are presented in Section 4.3 with cross-over volume fraction characterized by changes in shear thinning behavior followed by an analysis of linear rheology and elasticities and yielding behavior. A summary of the results and conclusion are given in Section 4.4.

4.2 Experimental Methods

4.2.1 Sample Preparation

Monodispersed silica particles are synthesized by method that is developed by Stöber[27] and extended by Bogush et al.[28] Particles with two different submicron-sizes are prepared. For large particles, D_l=612±20nm and for small particles D_s=127±7nm. Binary mixtures will be made using these two different particles. The product particles are suspended in ethanol solution containing water and ammonia hydroxide. The resulting suspension is concentrated to a mass fraction ~0.20 by heating up the suspension to evaporate the solvent and drive off the ammonia. Following previous studies,[21] we chose to work with polyethylene glycol with MW~2000 (PEG2000, Sigma-Aldrich) at T=75°C as the polymer melts. PEG2000 is a Newtonian fluid with viscosity of 0.10 Pa·s at the condition where we study. The two concentrated silica particle suspensions with a fixed mass fraction ratio are mixed with PEG (with eventual large particle volume fraction ratio R=0, 0.29, 0.5, 0.71, 1) and the resulting suspension is placed into vacuum oven with temperature kept above T_m of PEG to remove ethanol.[22] History of cooling down to the room temperature which is below the melting point of PEG2000 has shown no effect on the rheology of binary mixtures.

4.2.2 Rheology

Rheology experiment is carried out at C-VOR Bolin rheometer where a cone and plate geometry is used. The cone diameter is 20mm with a 4° angle. Here the temperature is kept at 75°C for PEG2000 to behave as a Newtonian fluid in pure melts to make sure that solid-like behavior is only controlled by particle.

Oscillatory stress is used to measure elastic modulus *G'* and viscous modulus *G"* as a function of frequency *f* in the frequency sweep experiment with strain γ=0.01 held constant to make sure of searching in a linear region, and *G'* and *G"* are measured by varying shear stress/strain at fixed frequency *f*=1Hz and 0.1Hz to study the nonlinear rheology and yielding behavior. And continuous stress is applied in the viscometry measurement to study the viscosity as a function of applied shear stress or shear rate to understand the shear thinning behavior and the shear thickening behavior. These experiments demonstrate that the flow properties observed are independent of shear-history.

4.3 Results and Discussions

4.3.1 Continuous flow properties and the transition to dynamical arrest

In this subsection we study the flow properties of the suspensions when continuous shear is applied. In Figure 4.1, the flow curves are presented with shear stress τ (Pa) plotted as a function of shear rate $\dot{\gamma}$ (s^{-1}) for different *R* in panels (A)-(E) respectively. All these data sets display similar behavior for different *R*. At low volume fraction, the slope $d\log(\tau)/d\log(\dot{\gamma})$ is generally independent of $\dot{\gamma}$ with a constant value of unity. With ϕ_c increased, a dynamical shear stress plateau is gradually developed within the range of $\dot{\gamma}_1$~$\dot{\gamma}_2$. Below the point $\dot{\gamma}_1$ the slope $d\log(\tau)/d\log(\dot{\gamma})$ is about 1 which suggests a low shear rate plateau viscosity, η_0, is achieved. As a result we take $\dot{\gamma}_1$ as a measure of the rate of deformation comparable to the rate of long range diffusion. For shear rates less than $\dot{\gamma}_1$, the suspensions are in their equilibrium microstructures where diffusion and stress relaxation are governed by the equilibrium rate of long range diffusion. Within the context of the dynamical arrest theory of Schweizer and coworkers,[29] for shear rates

above $\dot{\gamma}_1$ the applied stress lowers the barrier to diffusion and particle diffusion is more rapid resulting in a lower viscosity. This is observed as shear thinning. Above $\dot{\gamma}_2$ a high shear rate region is entered, where $d\log(\tau)/d\log(\dot{\gamma})$ again approaches unity, indicating the approach of a high shear rate plateau viscosity, η_∞. In this region, stress transfer is dominated by hydrodynamic interactions where the effects of equilibrium caging are essentially eliminated. Between $\dot{\gamma}_1$ and $\dot{\gamma}_2$, the suspensions shear thin from η_0 to η_∞. With increasing ϕ_c, the window of shear thinning region opens with $\dot{\gamma}_1$ decreasing and $\dot{\gamma}_2$ increasing, and the value of $d\log(\tau)/d\log(\dot{\gamma})$ between $\dot{\gamma}_1$ and $\dot{\gamma}_2$ is decreased.

Despite the qualitative similarity in flow behavior for these five different data sets, there are special characteristics in the high shear region for all the high ϕ_c samples at R=0.71 and R=1. Rather than approaching a constant value above $\dot{\gamma}_2$, the slope $d\log(\tau)/d\log(\dot{\gamma})$ gradually increases and enters a region with the value larger than 1, which denotes the onset of continuous shear thickening as explained with a mechanism of hydrocluster formation.[30] However, for the samples with highest ϕ_c for R=0.29 (ϕ_c=0.571) and R=0.5 (ϕ_c=0.592), there are an abrupt increase of slope $d\log(\tau)/d\log(\dot{\gamma})$ in the high shear region which can be explained as jamming resulting from the shear bringing the particle surfaces into close proximity. Supporting the conclusion, double thickening behavior is observed for R=1 at ϕ_c=0.615 where the continuous thickening occurs due to hydrocluster formation and discontinuous thickening due to jamming at higher shear stresses.

We are interested in exploring how flow properties are altered as volume fractions are raised to the point where collective interactions begin to alter suspension dynamics. Within the frame work of dynamical arrest theory, this is not observed as a discontinuity

in flow properties. Instead it is observable in the rate of change in relaxation times with increasing volume fraction. In developing a measure of the onset of dynamical arrest, we focus on the shear thinning portion of the flow curves.

Schweizer and co-workers define the cross over volume fraction, ϕ_x, as demarking the onset of particle localization.[31] Experimentally, determining the location of ϕ_x is difficult. Often this is done with oscillatory shear experiments.[16, 32] This approach is compromised when working with large particles in relatively viscous suspending fluids as the measurement window often lies in the high frequency range rendering it difficult to ensure we are operating at low enough frequencies to characterize times for particles to diffuse out of cages of nearest neighbors.[10, 33] Here an alternative method is utilized motivated by empirical correlations developed for shear thinning suspensions containing Brownian fluids below the localization volume fraction, which has been used in previous studies in PEG400.[11] Experimentally it is observed that for ϕ_c<0.5, suspensions of Brownian particles experiencing a variety of pair potentials, shear thinned from a zero shear rate viscosity η_0 to a high shear rate viscosity of η_∞ as:

$$\frac{\eta - \eta_\infty}{\eta_0 - \eta_\infty} = \frac{1}{1 + \left(\tau / \tau_d\right)^d} \tag{4.4}$$

where τ is the applied stress and τ_d is the stress where the viscosity drops to half way between η_0 and η_∞. For hard particle, attractive and repulsive particles 1.4<d<1.8.[30] This expression correlates shear thinning for hard spheres when ϕ_c<0.5 and for attractive and repulsive particles below localization or disorder/order phase transition volume fractions.[34] Here we choose to characterize shear thinning through a shear thinning exponent as $p = d\log(\tau)/d\log(\dot{\gamma})$ evaluated at the shear rate where $d^2\log(\tau)/d\log(\dot{\gamma})^2 = 0$.

As the localization transition is approached, η_0/η_∞>>1, resulting in p=2/(2+d). From the observed values of d we find that for non-localized suspensions 0.53<p<0.59. At higher volume fractions the suspensions develop a dynamic yield stress plateau where p approaches zero. We locate ϕ_x as the volume fraction where p<0.56.[22] At volume fractions just below ϕ_x, $p \geq$~0.56, and above ϕ_x, p decreases sharply. This method yields ϕ_x=0.511 for D_s=127nm and ϕ_x=0.510 particles for D_s=612nm particles respectively when they are dispersed in PEG400. We note that this value is close to MCT predictions for hard spheres.[4] We choose this method of determining ϕ_x as we find that it is robust to changes in particle size, size distribution and pair potential.

In Figure 4.2 (A), we present the flow curves at ϕ=ϕ_x at different R. Also shown in the inset of Figure 4.2 (A) are the flow curves plotted as dimensionless parameters where $Pe = 3\pi\eta_p\dot{\gamma} < D >^3 / 4k_BT$ and τ^*=τ<D>^{3}/8k_BT. Here k_BT is the product of Botlzmann constant and absolute temperature.

As shown, at ϕ_x the suspensions display essentially the same flow properties over the entire shear thinning region. We emphasize that the superposition occurs for dimensional stress and shear rates; while if plotted in dimensionless terms (as in the insert), there is a much poorer superposition. When the same particles are suspended inPEG400 we find that ϕ_x defined in the same way displays similar superposition when plotting flow curves with dimensionless stress as a function of Pe.[11] The data presented in Figure 4.2(A) emphasizes that flow properties do not follow a hard sphere scaling as seen for the PEG400 mixtures. Here ϕ_x=0.330, 0.375, 0.438, 0.504 and 0.549 for R=0, 0.29, 0.5, 0.71 and 1 respectively. For R=0, 0.29, 0.5 and 0.71, ϕ_x is far below the values of those in

PEG400 systems where we expect for the glassy cage formation. We attribute this to gelation resulting from attractions.

In Figure 4.2(B) we present the slope p as a function of ϕ_c/ϕ_x. A good superposition of data is shown independent of R. Generally in the low volume fraction limit, the suspensions behave as Newtonian fluid with p~1 and at high volume fraction limit strongly arrested state approached with p~0.1, ϕ_x locates at the point when p decreases to the medium point of these two extreme values. Here we should emphasize that p≈0.53-0.59 is only observed over a narrow volume fraction range below ϕ_x. The estimates of p demarking the onset of localization derived from the empirical correlations for universal shear thinning behavior are based on the assumption that η_0/η_∞>>1. As volume fractions drop increasingly below ϕ_x, this condition is not matched such that there is not a step function from constant p to zero at ϕ_x. Instead a gradual transition is observed. Nevertheless, we find empirically that p changes rapidly over a narrow volume fraction range in a remarkably universal manner, indicating this approach is a useful way to characterize the onset of localization for both hard sphere and attractive suspensions.

For R=1, ϕ_x=0.547 which is above the value observed for the same particles suspended in PEG400 where we expect the particles to form volume exclusion glasses. The low volume fraction viscosity data suggests the particles experience attractions. Based on this observation, we suggest the elevated value of ϕ_x for R=1 arises from weak, short range attractions that push the suspensions into a reentrant glass region.[22] In Table 4.2 where we summarize ϕ_x and the surface separation h at ϕ_x based on Equation (4.2). While ϕ_x is a monotonically increasing function of R, $h/\langle D\rangle$ at the dynamical arrest transition, is nearly a constant.

Little theoretical understanding has been developed for predicting the potential of mean force, $U(r)$, for the silica particles suspended in a polymer melt when absorbed polymer is not in equilibrium with the polymer in the bulk. Here we apply a square well interacted system in form of Equation (4.2) to test our conclusions. For this system we assume the strength and range of the attraction are set by polymer binding density and that these are independent of $<D>$. We estimate $U_0 = 2k_BT$ as this value lies within the re-entrant glass transition boundary for many theoretical systems.[23, 35] We choose Δ=10.7nm=5.6R_g for the well width as this is the range of inter-particle attraction as this is the separation where substantial particle induced changes in polymer dynamics[36] and suspension flow properties have been reported.[18]

Bergenholz and Fuchs developed for predicting ϕ_x for gelling systems with $\Delta<0.2D_c$ yielding:[37]

$$\Gamma_c = 12(\Delta / D_c)\phi_x[\exp(U_0 / k_BT) - 1]^2 / \pi^2 \qquad (4.5)$$

where $\Gamma_c \sim 1.42$ occurs at ϕ_x.

Based on these assumptions, we find that for the four gelled systems with ϕ_x in PE2000 where we are confident that changes in suspension dynamics are associated with bonding and not caging, (R=0, 0.29, 0.5, 0.71), ϕ_x=0.340, 0.380, 0.428, 0.508 (consistent with our experimental results in flow curves). For R=1, the calculated result exceeds unity indicating we are in the reentrant region. For square well systems where $\Delta/<D>$=0.017 for large spheres and U_0/k_BT=2, full MCT calculations suggest ϕ_x =0.510. In Table 4.2, we also present the results of ϕ_x based on calculation of Equation (4.5) together with values of $\Delta/<D>$.

Full MCT calculations predict that as $\Delta/\langle D\rangle$ is increased from 0.03 to 0.05 reentrant glasses are no longer formed.[38] Using a fixed value of Δ, we find that $\Delta/\langle D\rangle$ changes sharply from 0.017 for R=1 to 0.056 for R=0.71 suggesting, in agreement with our measurements, that gel volume fraction will drop from above that observed for the hard sphere system (0.51 for this set of particles) to well below this value.

These calculations thus support our notion that dynamical arrest properties of the binary mixtures are well described by an pseudo one-component system composed of particles with size $\langle D\rangle$ experiencing a short range attraction that with a strength and a range that are independent of $\langle D\rangle$. In the following subsections we will explore the consequence of these interactions in the viscoelastic response of the suspensions.

4.3.2 Linear Rheology

In order to characterize the mechanical properties of these suspensions above ϕ_x, we investigate the linear response using frequency sweep experiments. In Figure 4.3, we present the linear elastic modulus *G'* and linear viscous modulus *G"* as functions of strain frequency *f*. As with the continuous shear data, these five different data sets show very similar qualitative features. At high frequencies, a plateau in *G'* is developed and a minimum in *G"* is formed within the frequency range *f*=0.1-1Hz. In this frequency range, *G'*>*G"* denoting that the samples are more elastic than viscous. At low frequencies, a terminal region is entered as *G"* passes through a maximum and *G'* becomes smaller than *G"* as frequency is decreased. The crossing point generally moves to the lower frequencies with increasing ϕ_c.

We note that unlike relaxation of glasses formed by hard spheres,[16, 32] complex behavior is observed in the low frequency range where multiple shoulders are displayed

in G' and two maxima in G'' are observed with $G' \approx G''$. Similar phenomenon have been observed in mixtures of particles and hyper-branched polymers with the spectrum of relaxation times begin associated with relaxation of the polymer arms and particles within their cages.[39] In our system, we suggest that the presence of multiple characteristic relaxation times at low frequencies is associated with the strain frequency exceeding characteristic time for particle diffusion and characteristic time associated with bound polymer layers. We do not attribute these multiple relaxations to the presence of two particle sizes as they are also observed when R=0 and R=1. This behavior is only observed for samples in medium range of ϕ_c. At lower ϕ_c, the particles are sufficiently far apart that adsorbed polymer layers do not interact and a single relaxation at low frequencies is observed associated with particle diffusion. At high ϕ_c, particles are brought into close proximity confining the adsorbed polymer layers such that relaxations due to the polymer layer either occur at much lower frequencies or overlap with relaxations due to particle diffusion. The state diagram showing this behavior is presented in Figure 4.4. The lower volume fraction limit for this complex relaxation behavior shows the monotonic shape of dynamical arrest transition boundary and the upper volume fraction limit shows the non-monotonic shape of the R dependent maximum packing fraction.

In the high frequency range, as volume fraction is raised for all samples in Figure 4.3, a plateau elasticity is reached. With increasing R, there is an increasing dependence of this plateau elasticity on deformation frequency. Here we use the value of G' at the frequency f_m where a minimum of G'' is observed to characterize the plateau elastic modulus G_p'. The results of G_p' are plotted as a function of ϕ_c in Figure 4.5. For each R,

the data is well described by of $G_p' = A\phi_c^{\,b}$ where b increases with R. Based on our conclusions about the nature of the attraction experienced by the effective particles, we suggest that increasing the volume fraction ratio of spheres with a smaller attraction range results in a stronger volume fraction dependence of G_p'. This suggestion is consistent with the observation in the mixtures of repulsive and attractive particles, where increasing the volume fraction ratio of hard spheres can result in stronger volume fraction dependence of G_p'.[24]

In Figure 4.6, we show that for all of the mixtures studied, $G_p'h^2\langle D\rangle/k_BT$ has a value near unity independent of ϕ_c. This is a remarkable result.

In star polymer solutions, $G_p'\delta^2 D/k_BT$=constant above overlap concentration where δ is the long time limit displacement of caged particles physically representing the largest excursion distance within which a caged microgel particle can diffuse in the arrested state.[40] This result is consistent with the predictions of dynamical arrest theory where $\frac{G_p' D^3}{kT} \cong \frac{9}{5\pi}\frac{\phi_c D^2}{r_{loc}^{\,2}}$.[41] Here r_{loc} is a diffusion distance in the short time limit. In comparing the experimental observation on microgels with the prediction of caged particles, we note that ϕ_c can be approximately treated as a constant term with the value~0.5 thus we can suggest that for our systems the maximum diffusion distance in our gels occurs when r_{loc}/h~0.54. Accepting this conclusion suggests that G_p' is a correlated function of both $\langle D\rangle$ and h, where both parameters are sensitive to R. The volume fraction dependence of r_{loc} is then determined by h which is sensitive to both ϕ_m and $\langle D\rangle$. .

4.3.3 Nonlinear Rheology and Yielding Behaviors

To further investigate the nonlinear rheology and yielding behavior of the suspensions, we choose to apply dynamical stress sweeps at a fixed frequency f=1Hz which, except for the R=1 systems, lies close to f_m where, the minimum of G'' is formed, and below the crossing point of G' and G'', f_{x2}, in the high frequency region above which $G''>G'$. For the R=1 systems, f=1Hz lies near f_{x2}. This frequency is chosen so that we are deforming the suspensions at a time scale that is shorter than that where the particles can diffuse out of their nearest neighbor cages but still long enough for the particles to fully explore its nearest neighbor cage during a deformation cycle. To achieve similar conditions for the R=1 systems we also report data at f=0.1Hz.

With the strain frequency fixed, we increase the magnitude of the applied stress and determine G' and G''. In the low strain limit, G' and G'' exhibit a constant plateau value of G_0' and G_0'' respectively with $G_0'>G_0''$. Above some large strain ~0.1, G' starts to roll off the plateau and G'' develops a maximum and rolls off passing that peak with $G'<G''$ eventually. In Figure 4.7, we present dynamical stress sweep results in the panel of G'/G_0'-τ/G_0' (main panel) and G''/G_0''-τ/G_0' (inset) for three representative volume fractions at different R values. We summarize information from all samples in Table 4.3. The three volume fractions used in Figure 4.7 are chosen to give us comparable values of h/R_g at 14.4 ±1.8, 10.4 ±0.9 and 7.2 ±0.6 respectively. This ensures that at each value of h, $G_0'h^2<D>/k_BT$ and $G_0''h^2<D>/k_BT$ are similar, allowing us to focus on characterizing the differences in yielding as h is varied. There are small changes when R=1, but the absolute values of the R=1 sample become comparable to the lower values of R using f=0.1Hz.

In Figure 4.7, for all values of R, G'/G_0' rolls off with increasing applied stress to a power law decay form of $G'/G_0'' \propto (\tau/G_0')^{-\beta}$ and G''/G_0'' develops a peak above the point of $\tau/G_0' \sim 0.1$ with the peak of G''/G_0'' hard to observe for R=1 at both f=0.1Hz and f=1Hz. At a fixed value of R, when ϕ_c is increased (h is decreased), G'/G_0' decreases more slowly at large shear stress (i.e., β increases)ing and the peak in G''/G_0'' becomes sharper.

We present the results of dynamical stress sweeps at h/R_g=7.2 ±0.6 for different R in Figure 4.8. Below we make comparisons using the f=0.1Hz data for R=1 but include the f=1Hz data for comparison purposes. In the inset of Figure 4.8 (A), we present $G_0'h^2\langle D\rangle/k_BT$ as a function of stress demonstrating again the remarkable scaling seen in Figure 4.6. From Figure 4.8(A), the curves of G'/G_0'-τ/G_0' superimpose well with same functional form and magnitude with increasing stress. In Figure 4.8(B), the behavior is similar but the peak G''/G_0'' is a decreasing function of R. Significant differences are observed with R=1 at f=1Hz. We suggest that this behavior is a result of combined effects of shear thickening and that for this system f=1Hz approaches f_{x2}. From these results we conclude that the nonlinear rheology of these mixtures is very similar at a fixed value of h.

Yielding in colloidal glasses and gels at a particular deformation frequency is often associated with the stress τ_x (strain γ_x) required to make $G'=G''=G_x$, at which point the barrier of diffusion for breaking dynamical arrest states is driven to zero.[16, 42, 43] In Figure 4.9 we present the results of τ_x, G_x and γ_x as function of ϕ_c.

In Figure 4.9(A) and (B), similar increasing behavior of τ_x and G_x with increasing ϕ_c is observed as in G_p', where monotonic decreasing of τ_x and G_x are enhanced ϕ_c

dependence is attained with increasing R. In Figure 4.9(C), γ_x passes a maximum when increasing ϕ_c, the magnitude of which is decreased as R increased. The volume fraction where the maximum is observed is 0.432, 0.474, 0.524, 0.545 and 0.590 for R=0, 0.29, 0.5, 0.71 and 1 respectively, which we note is a monotonically increasing function of R.

Again we find that nonlinear properties (τ_x and G_x) of these suspensions scale on $h^2<D>/k_BT$ as shown in Figure 4.10 (A) and (B). The data for γ_x (Figure 4.10 (C)) displays a maximum in a narrow inter-particle surface separation range h/R_g=8-10 independent of R.

Continuous shear thickening is only present for the R=0.71 and R=1 samples. Again we seek to scale the critical stress on $k_BT/h^2<D>$ and find superposition of the data $\tau_c h^2<D>/k_BT$ is a linearly increasing function of h while $\tau_x h^2<D>/k_BT$ is generally constant. By extrapolating the data in Figure 4.11 to the point of overlap, we expect to reach a volume fraction where the suspensions will thicken before they yield will occur when $h/R_g \approx 2$.

4.4 Conclusion

Introducing colloidal particles into unentangled polymer melts results in enhancement of the mechanical properties and solid-like response at fixed shear strains and experimental time scales.[19-22] This reinforcement is augmented such that gelation is observed at substantially lower volume fractions as polymer molecular weight is increased.[18] For polymer molecular weights far below the condition for entanglement and under conditions where particle-polymer segment attraction produces sterically stabilized particles, the dynamical arrest transition occurs at a high volume fraction and the model of hard spheres with an effectively size augmented by the adsorbed polymer

layer can be used to describe crystallization,[44] or glass formation.[16] When the polymer molecular weight is increased, a variety of explanations for the increased attractions have been introduced including surface confined entanglements,[45, 46] polymer bridging between polymer stabilized particles,[20] and depletion effects of polymer matrix.[47]

Schweizer and coworkers have developed polymer reference interaction site model (PRISM) to explain the depletion effect in polymer-colloid suspension.[48] This model agrees with detailed studies of particle and polymer microstructure studies for low molecular weight polymers but agreement is increasingly poor as molecular weight is increased. Studies of flow properties and microstructure suggest that the increased molecular weight induces an attraction between the particles even though there is strong evidence that the polymer is adsorbed to the particle surface producing a layer with thickness that grows with the polymer molecular weight.[36] The attractions are thought to be a consequence of adsorption of multiple segments from the same polymer chain to the particle surface which results in sluggish approach to equilibrium between segments bound to the particle surface with those in the bulk. In the limit where the adsorbed polymer cannot exchange with polymer in the bulk, this phenomenon can be thought of as producing a particle surface that is composed of polymer segments with a result that the enthalpy gain of moving a segment from the bulk to the particle's effective surface is diminished. This in turn produces depletion attractions between the particles.

Here we exploit this attraction to investigate the flow properties of binary mixtures which have short-range inter-particle attractions. We find that the dynamical arrests of the mixtures can be understood in terms of an attraction with strength of $\sim 2k_BT$ and width of $\sim 5.6R_g$, which is independent of the large particle volume fraction ratio. As a

consequence, the polymer induced inter-particle attraction is the same between like-species and unlike-species. This short-range attraction is sufficiently weak that the particles respond very nearly like hard spheres at low volume fractions but gel and form glasses differently from hard spheres as volume fraction is raised. [22]

By studying the continuous flow properties the dynamical arrested transition boundaries are characterized for different R. The volume fractions at this boundary, ϕ_x, is found to locate far below glass transition point of spheres experiencing volume exclusion interactions for R=0, 0.29, 0.5 and 0.71 denoting the formation of gels, while for R=1, ϕ_x is higher than that for hard spheres suggesting a re-entrant phase behavior and formation of attractive glasses. This state transition occurs at the volume fraction where the effective single component particle surface separation is ~14R_g, which is larger than the distance within which the adsorbed polymer layer can interact. Therefore, this inter-particle attraction cannot be explained as a result of polymer entanglement and instead is associated with the attractions resulting from the nonequilibrium dynamics of the adsorbed polymer layers.[18]

The presence of the adsorbed polymer layers and their confinement upon gelation is observed in the linear response of the composite melts where for all R at low strain frequency a double relaxation is observed at medium $\phi_c > \phi_x$. The two relaxations are associated with particle diffusion and confined polymer layer relaxations. This phenomenon is shown in a wider volume fraction range for mixtures (R=0.29, R=0.5 and R=0.71) than single-component system.

The plateau elastic modulus G_p' monotonically increases with ϕ_c, and is found to scale as $k_BT/h^2\langle D\rangle$, denoting the localization length in the dynamical arrested state is

proportional to the inter-particle separation independent of R. This dependence of properties on average surface to surface separation is also observed for the yield stress and elastic modulus at the yield stress measured in stress sweep experiments. Finally the scaled critical stress for thickening $\tau_c h^2 <D>/k_B T$ is a linear function of h for R=0.71 and R=1.

Our results suggest that the flow properties of these systems are controlled by a short range attractive pair potential that results in gelation and glass formation that is well described by the dynamic arrest theory and binary mixtures behave as if composed of particles with a uniform effective size $<D>$. Of significance to general studies of colloidal suspensions are our observations that the point of dynamic arrest is well characterized through the slope p and that flow properties diverge near ϕ_m independent of the presence of attractions while attractions impact ϕ_x.

4.5 Tables and Figures

Table 4.1 Summary of $<D>$, ϕ_x and ϕ_m for different R in PEG400

R	$<D>$/nm	ϕ_x	ϕ_m
0	127	0.511	0.631
0.29	142	0.557	0.661
0.5	160	0.603	0.713
0.71	190	0.605	0.719
1	612	0.51	0.632

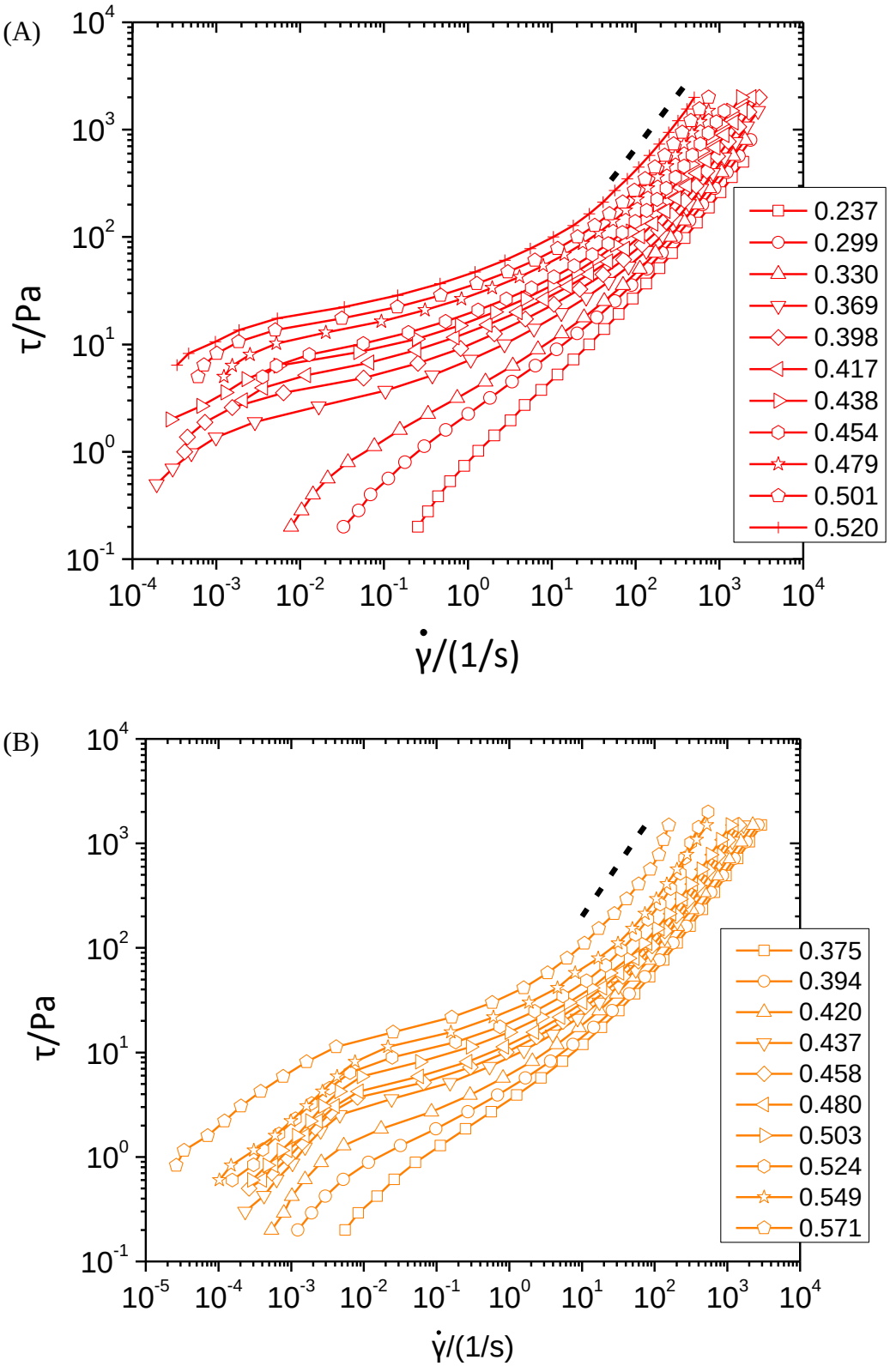

Figure 4.1 (continued on next page)

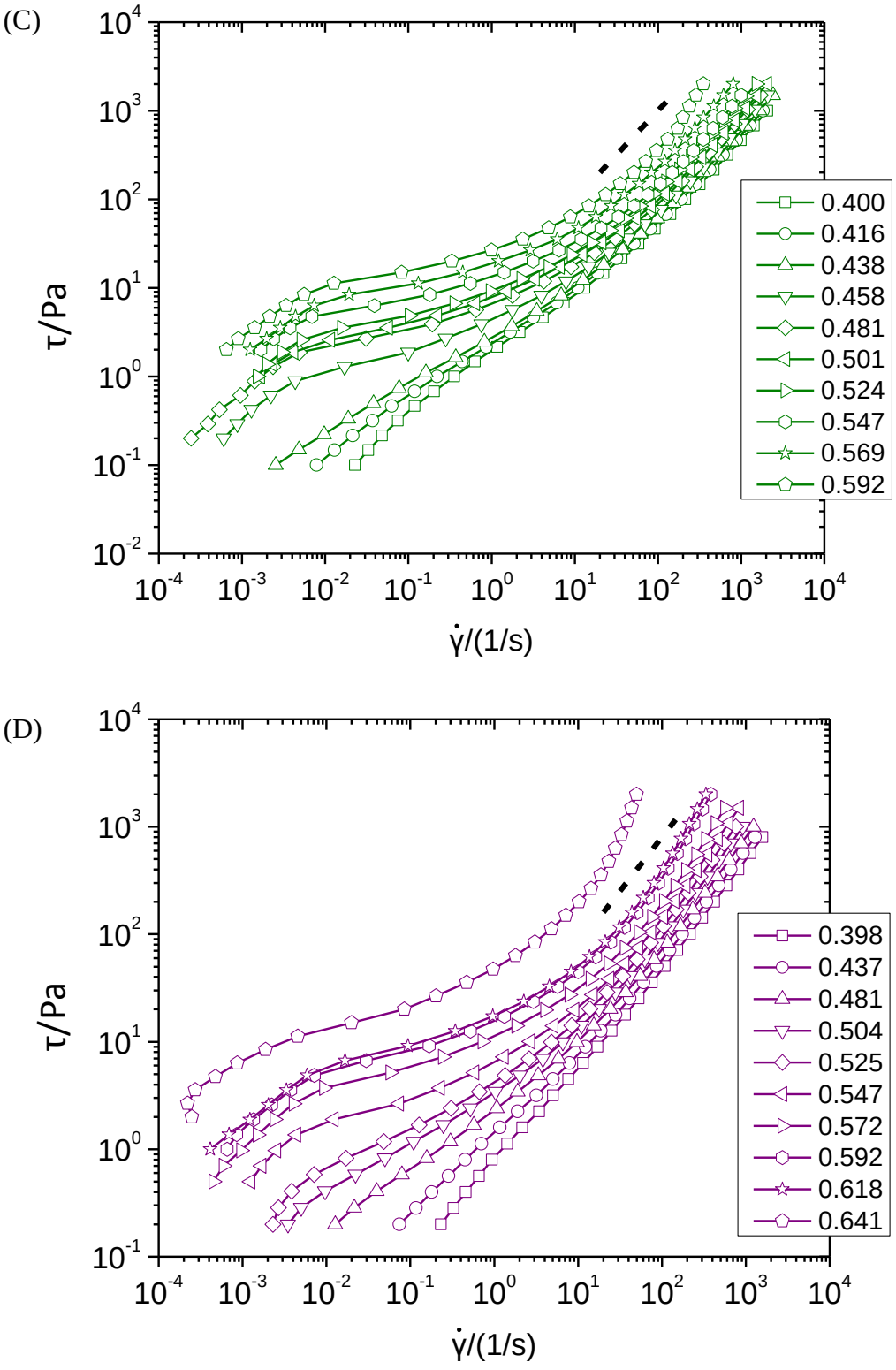

Figure 4.1 (continued on next page)

(E)

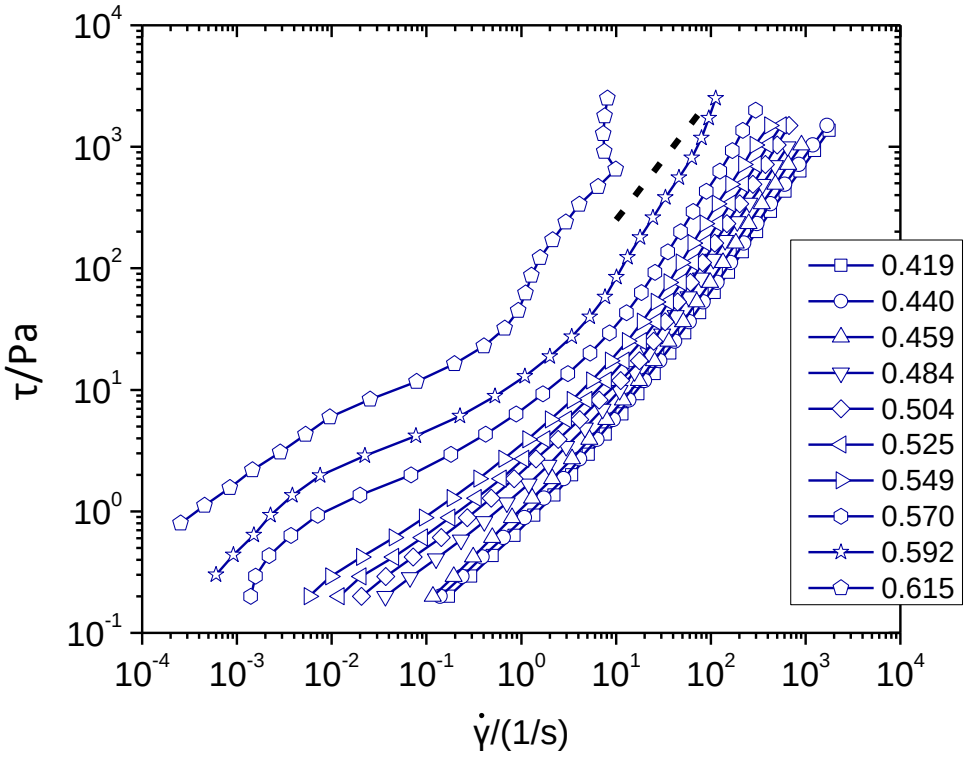

Figure 4.1 Flow curves for (A) *R*=0, (B) *R*=0.29, (C) *R*=0.5, (D) *R*=0.71, (E) *R*=1. The dashed lines represent a slope of 1.

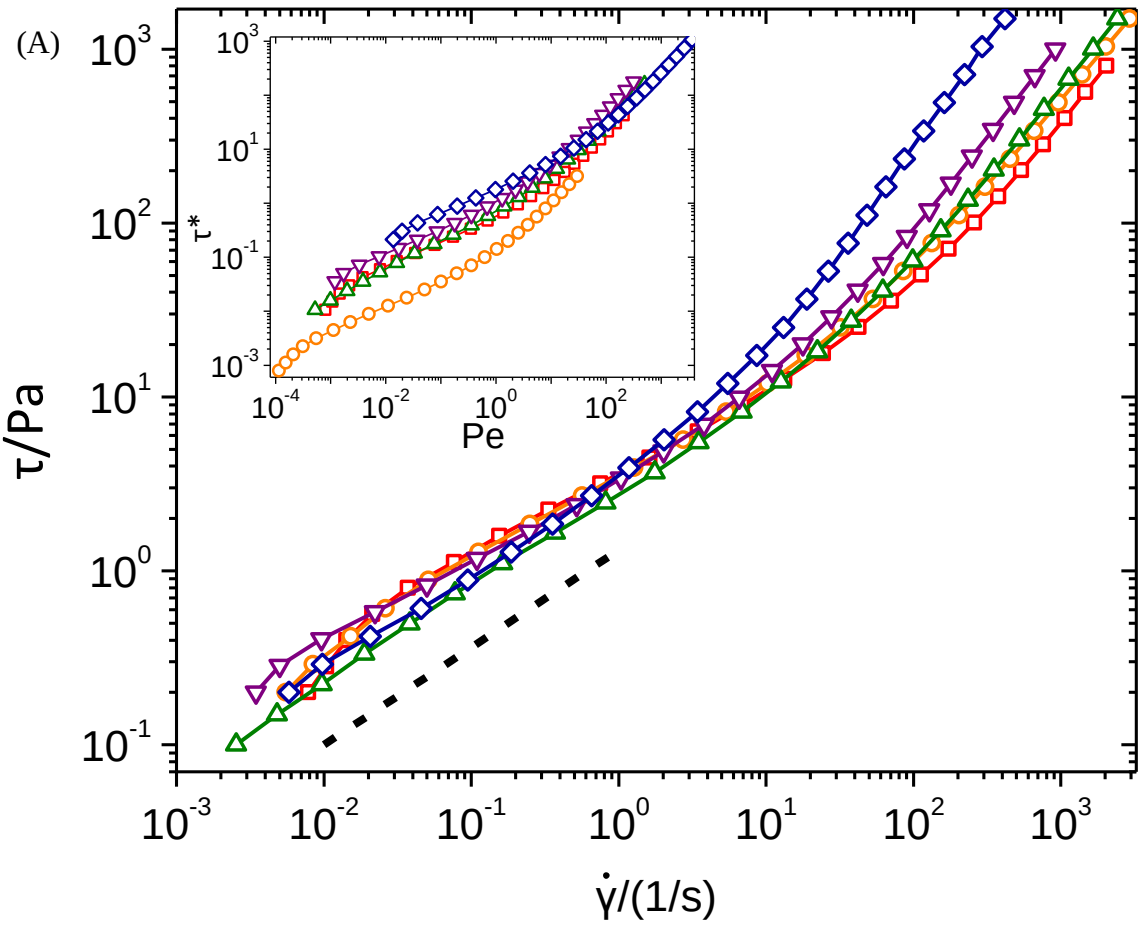

Figure 4.2 (continued on next page)

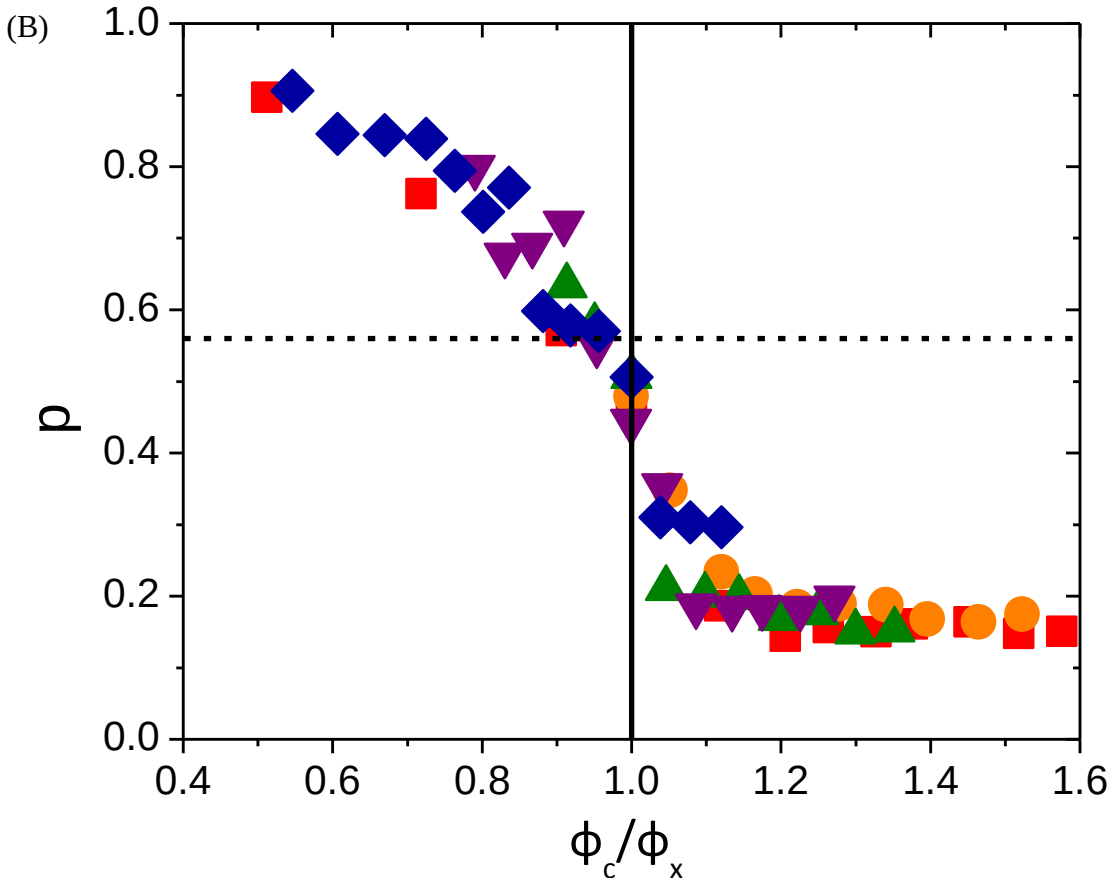

Figure 4.2 (A) Flow curves of R=0 at ϕ_c=0.330(□), R=0.29 at ϕ_c =0.375(○), R=0.5 at ϕ_c =0.438 (△), R=0.5 at ϕ_c=0.504(▽) and R=1 at ϕ_c =0.549(◇). The dashed line has a slope of p=0.56. Inset panel show the flow curves in the dimensionless panel. (B) The slope p as a function of ϕ_c for R=0(■), R=0.29(●), R=0.5(▲), R=0.71 (▼) and R=1(◆).Solid line represents ϕ_c/ϕ_x=1. Dashed line represents p=0.56.

Table 4.2 $\langle D \rangle$, experimental results of ϕ_x, average particle surface separation based on Equation (4.2), corresponding values of $\Delta/\langle D \rangle$ used in Equation (4.5) and theoretical prediction of ϕ_x based on Equation (4.5).

R	$\langle D \rangle$/nm	ϕ_x	h/R_g	$\Delta/\langle D \rangle$	ϕ_x (theory)
0	127	0.330	16.1	0.084	0.340
0.29	142	0.375	15.5	0.075	0.380
0.5	160	0.438	14.9	0.067	0.428
0.71	190	0.504	12.6	0.056	0.508
1	612	0.549	15.5	0.017	0.510[a]

[a] Obtained by extrapolating the plotted results of Ref [38] at U_0/k_BT=2 with increasing $\Delta/\langle D \rangle$.

(A)

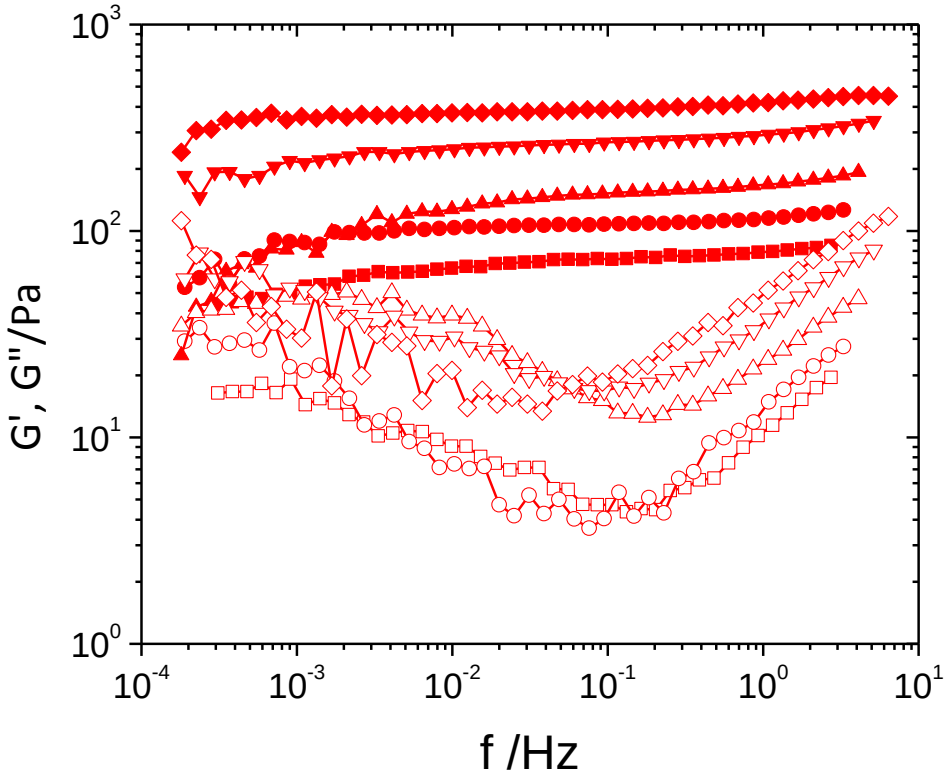

(B)

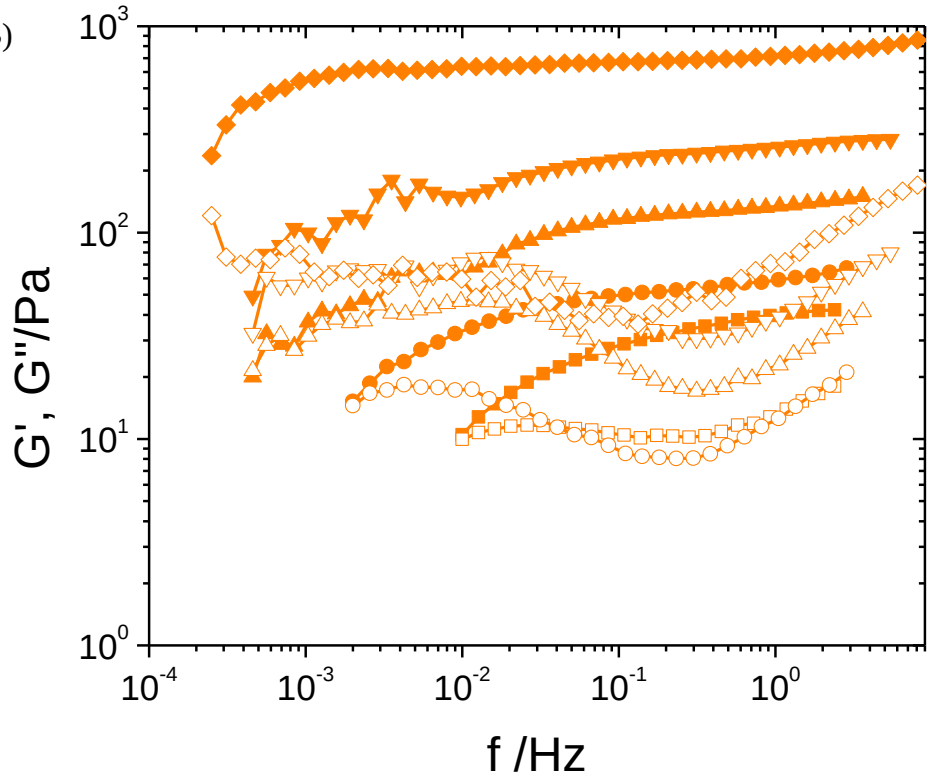

Figure 4.3 (continued on next page)

(C)

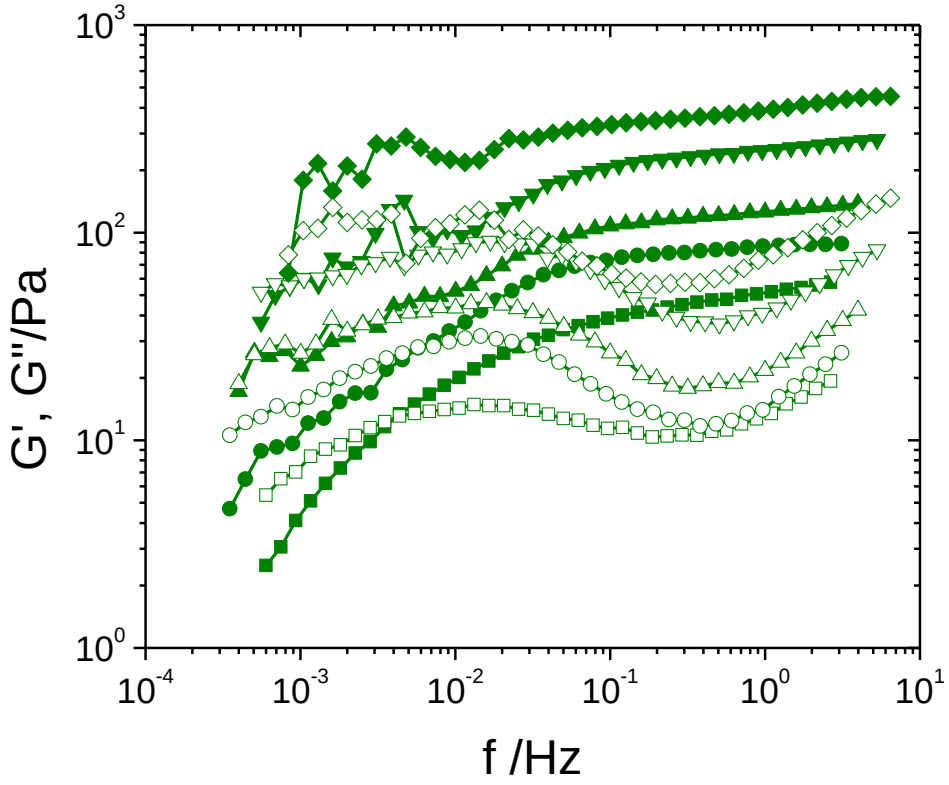

(D)

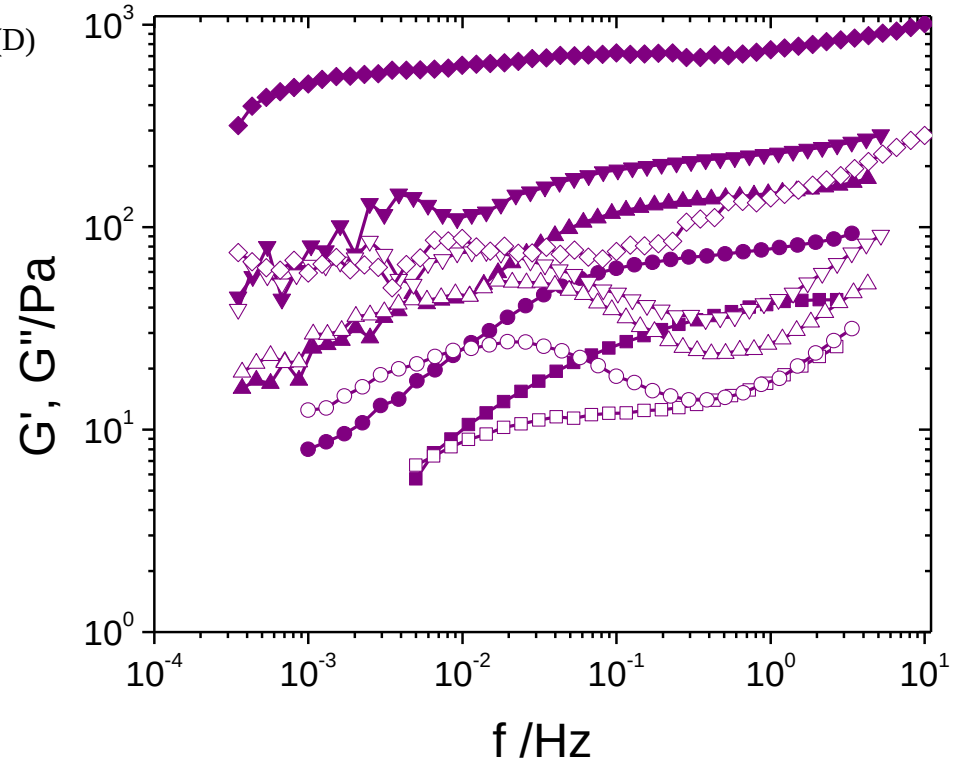

Figure 4.3 (continued on next page)

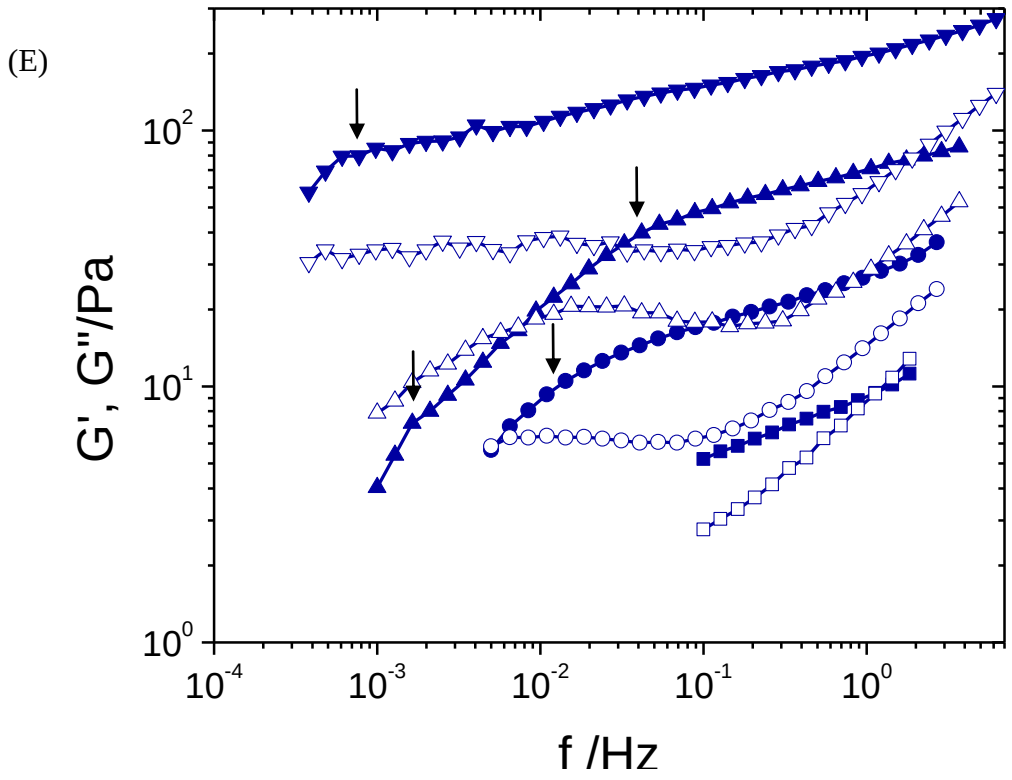

Figure 4.3 Linear G' (Close symbols) and G" (Open symbols) for (A) R=0 at ϕ_c=0.369(■, □), 0.398 (●,○) 0.438 (▲,△), 0.479 (▼, ▽) and 0.501 (◆,◇); (B) R=0.29 at ϕ_c=0.394(■, □), 0.420 (●, ○) 0.480 (▲,△), 0.524 (▼, ▽) and 0.571 (◆,◇); (C)R=0.5 at ϕ_c=0.458(■, □), 0.481 (●,○) 0.524 (▲,△) and 0.569 (▼, ▽) and 0.592 (◆,◇); (D)R=0.71 at ϕ_c=0.525(■, □), 0.547 (●,○) 0.572 (▲,△), 0.618 (▼, ▽) and 0.641 ((◆,◇); (E) R=1 at ϕ_c=0.549(■, □), 0.570 (●,○), 0.592 (▲,△) and 0.615 (▼, ▽). Arrows in (E) show single or double relaxation in low frequency limit.

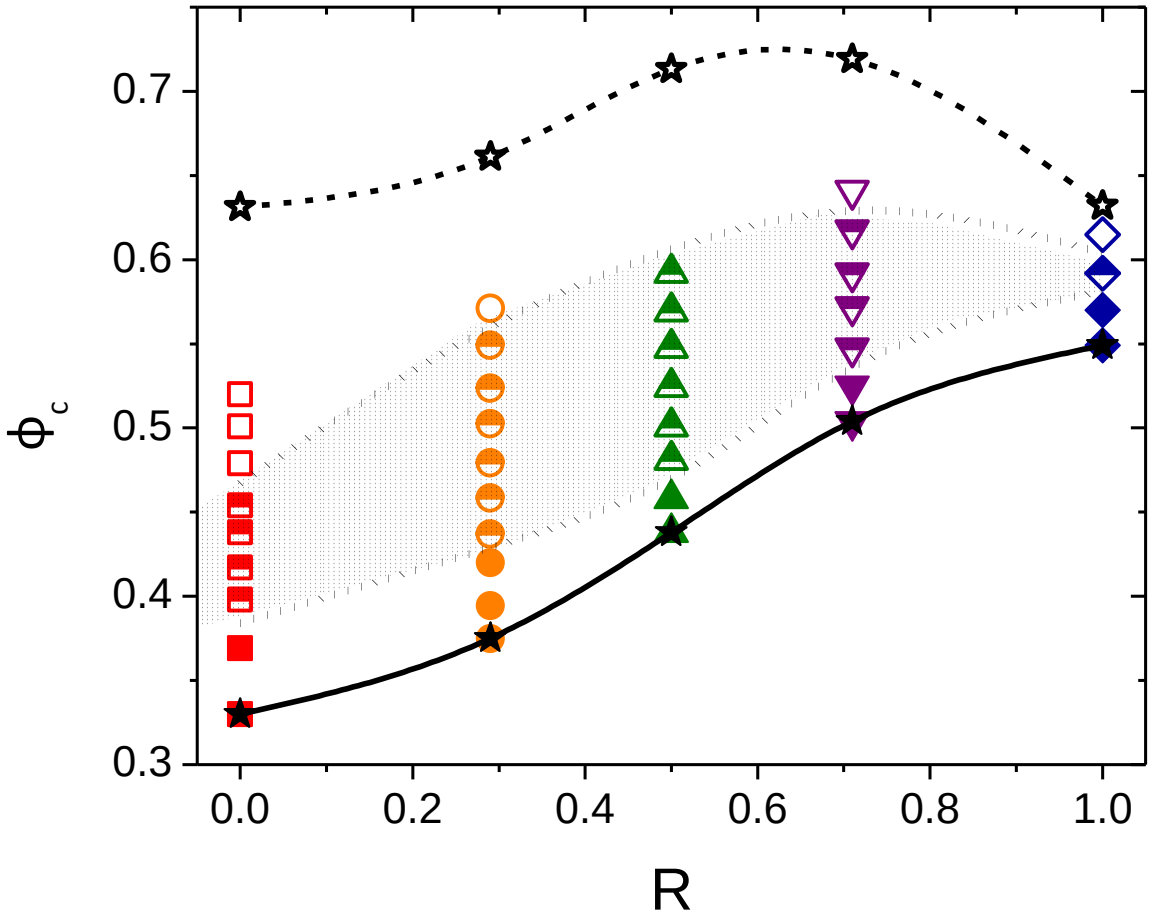

Figure 4.4 State diagram with close stars (solid curve used to guide eyes) for ϕ_x and open stars (dashed curve used to guide eyes) for ϕ_m (in low MW polymer). Closed color symbols stand for samples with single relaxation at low frequency , half open color symbols stand for samples with double relaxation (and marked with shadow), and open color symbols stand for samples with coupled relaxations.

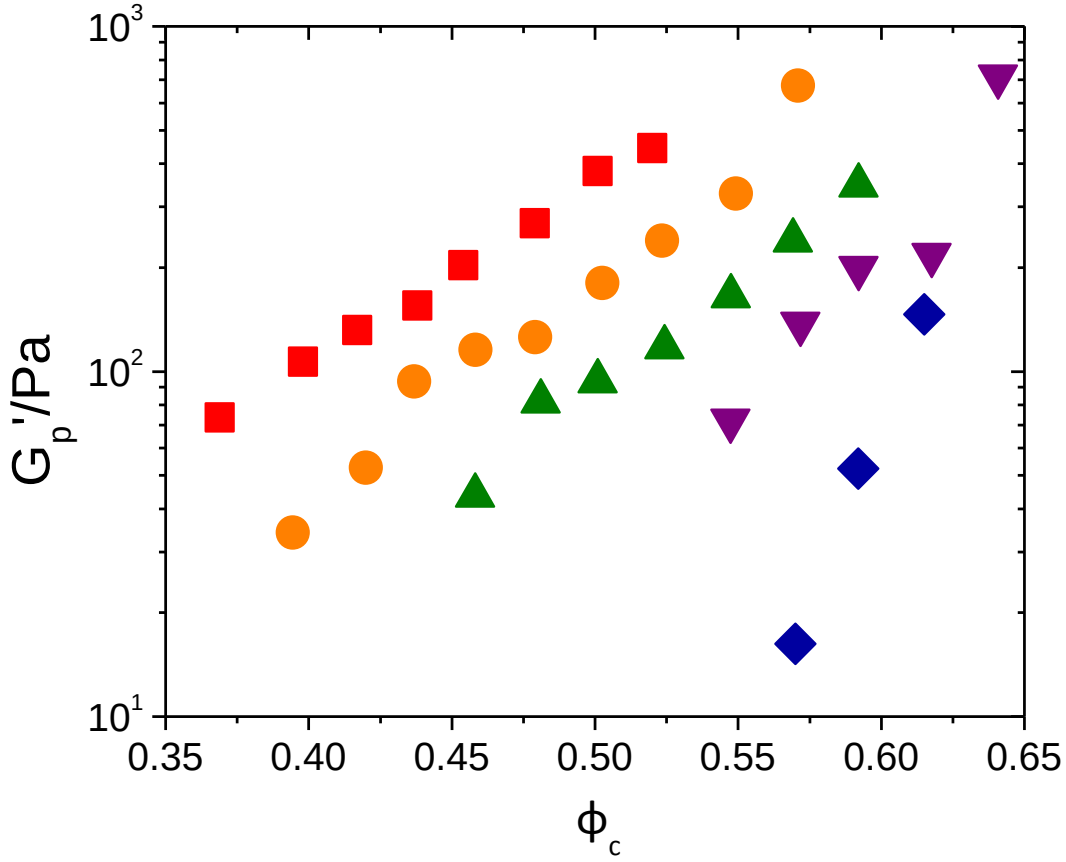

Figure 4.5 G_p' as function of ϕ_c for R=0(■), R=0.29(●), R=0.5(▲), R=0.71 (▼) and R=1(◆).

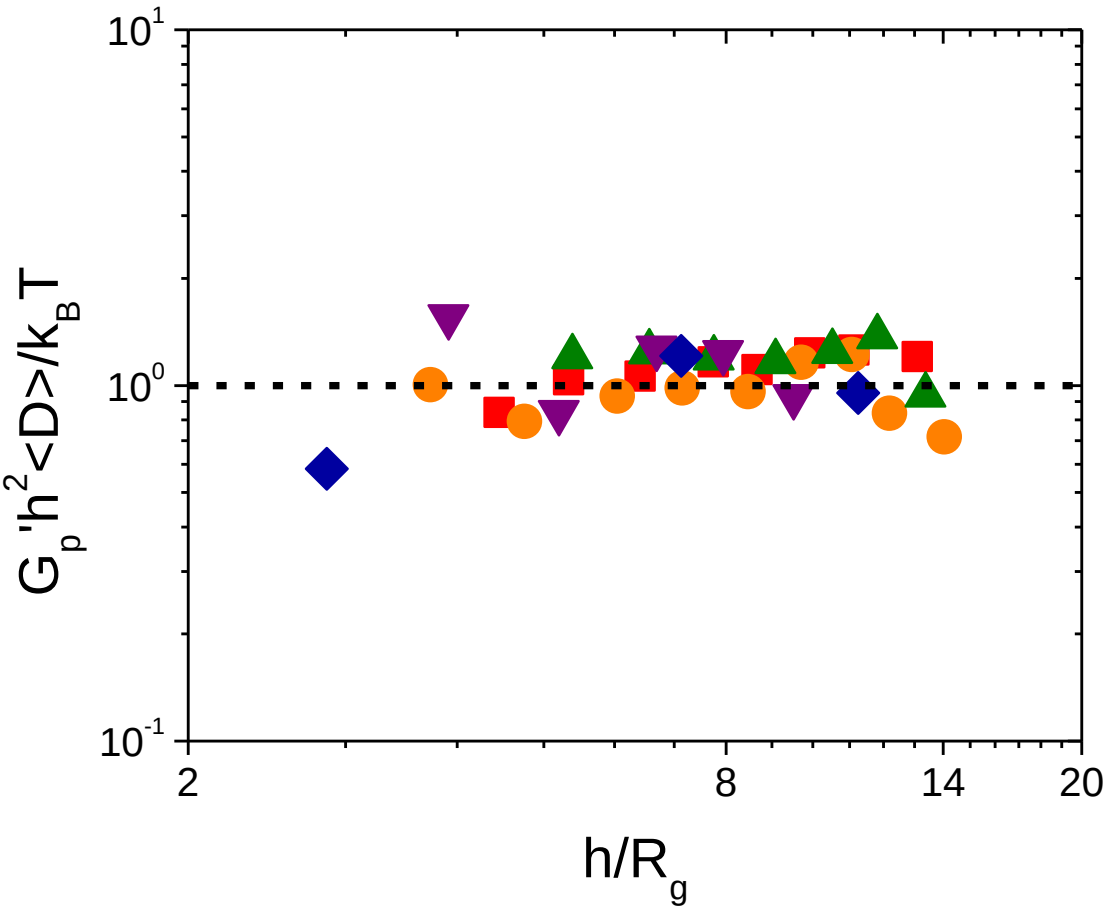

Figure 4.6 Scaled G_p' (with $h^2<D>/k_BT$) as function of h/R_g for R=0(■), R=0.29(●), R=0.5(▲), R=0.71 (▼) and R=1(◆). The dashed line shows a constant value of unity.

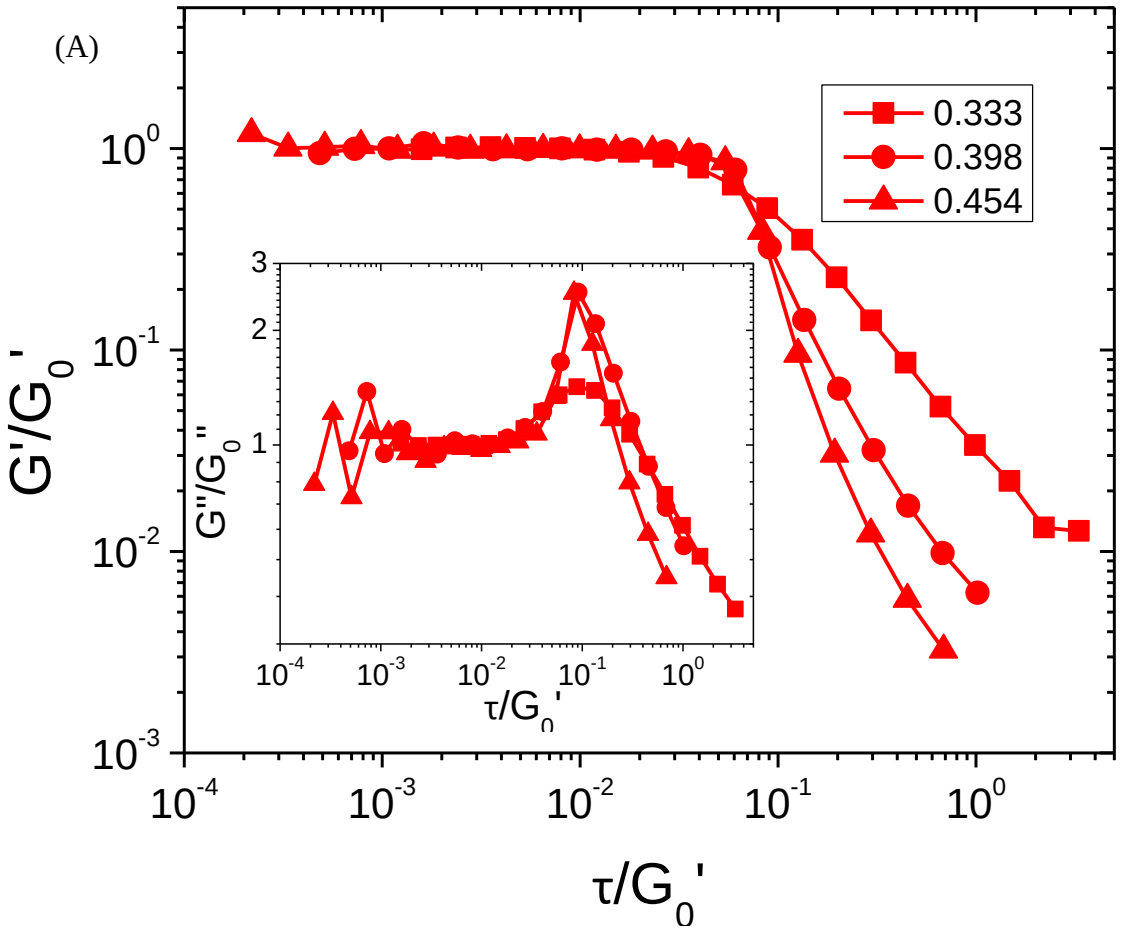

Figure 4.7 (continued on next page)

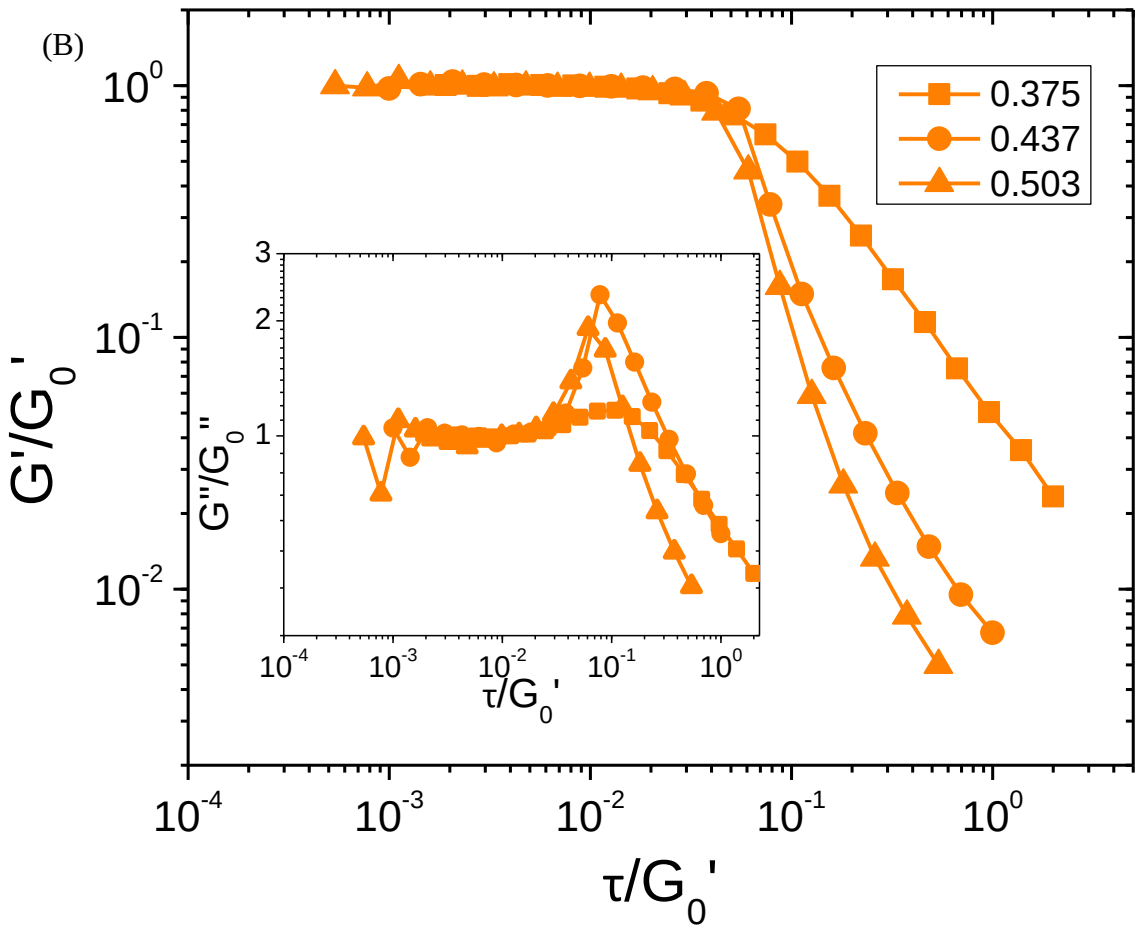

Figure 4.7 (continued on next page)

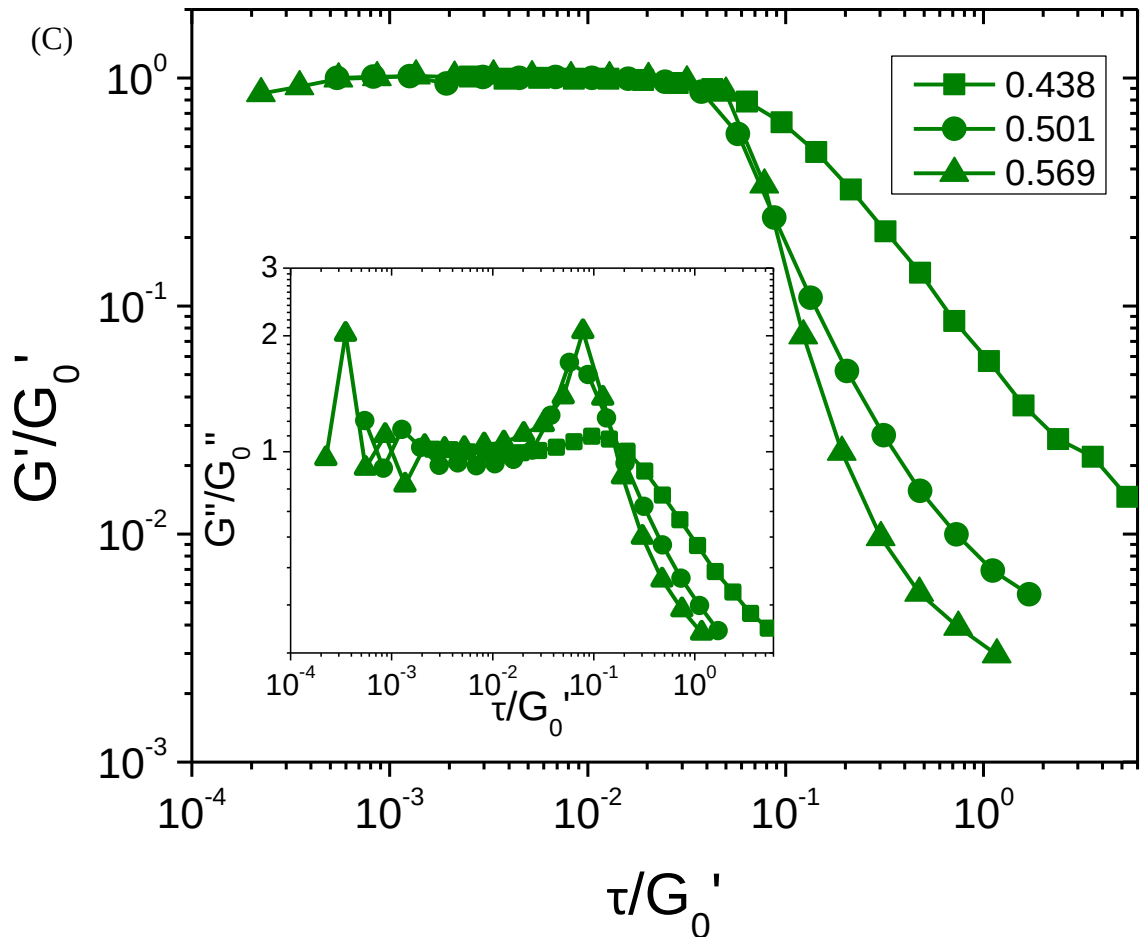

Figure 4.7 (continued on next page)

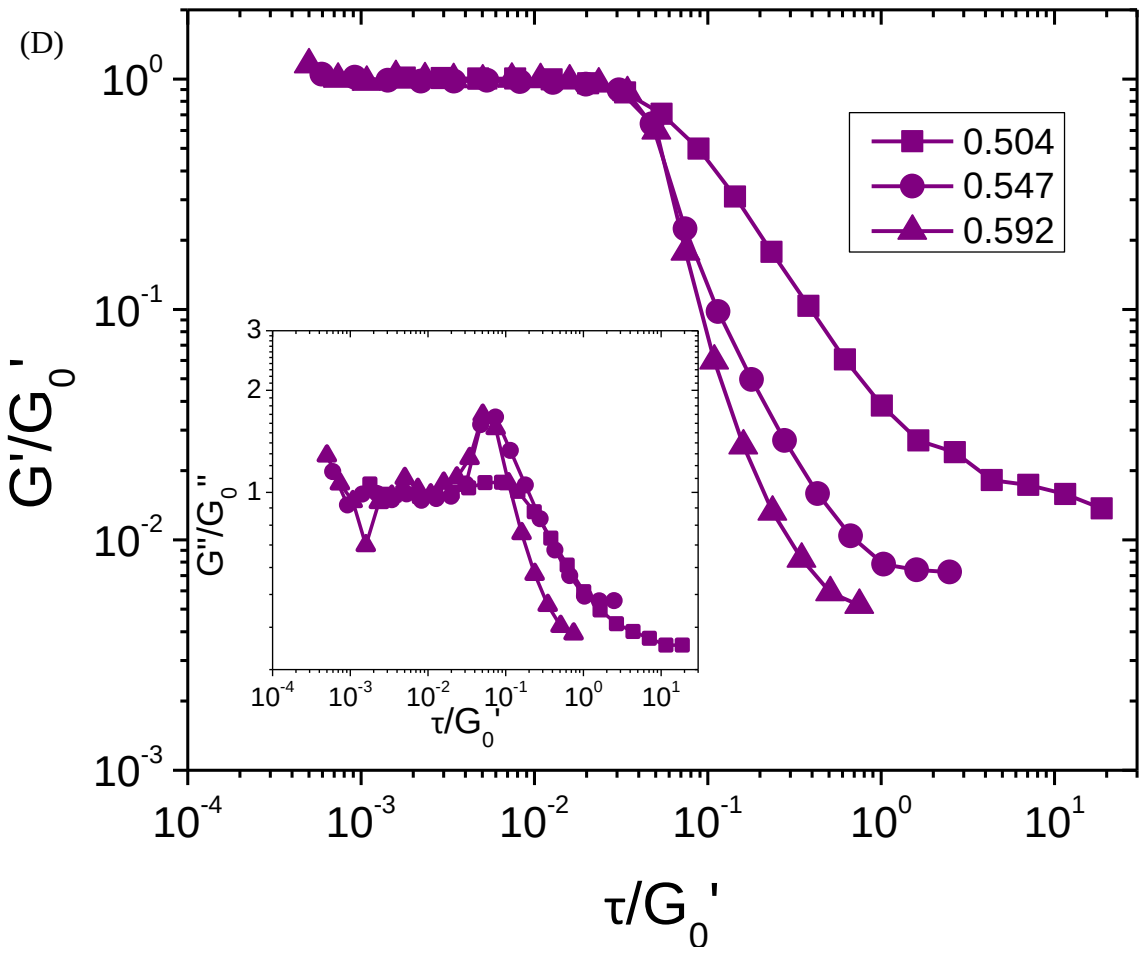

Figure 4.7 (continued on next page)

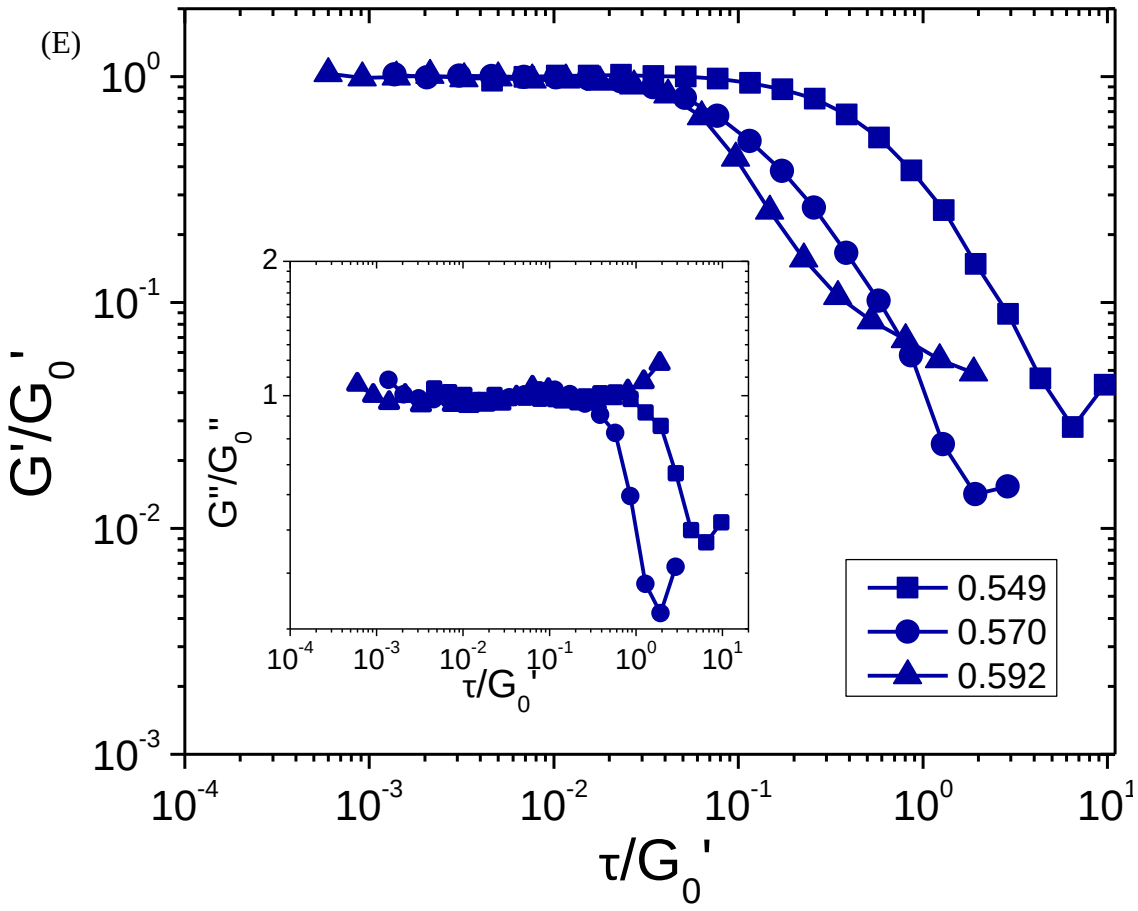

Figure 4.7 (continued on next page)

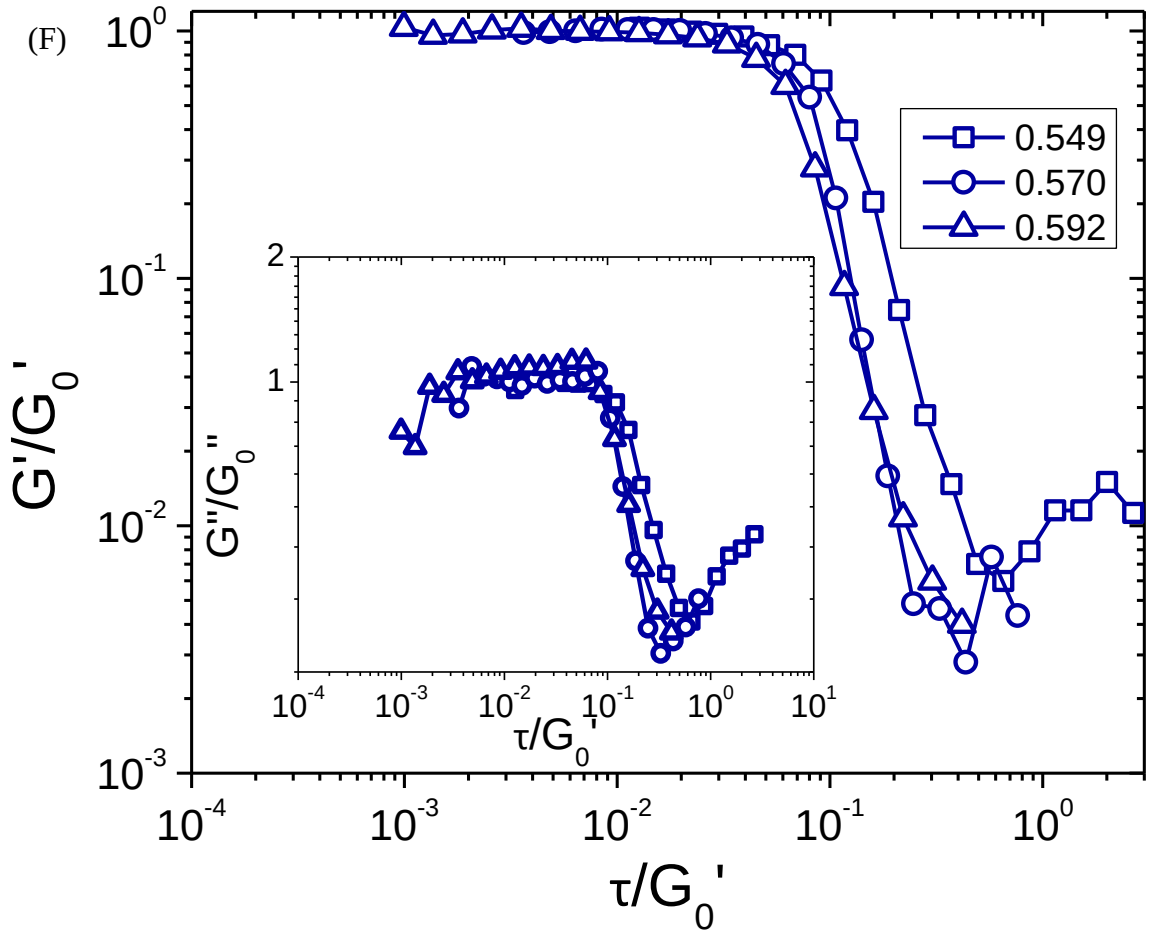

Figure 4.7 Dynamics stress sweeps at *f*=1Hz for (A) *R*=0, (B)*R*=0.29, (C)*R*=0.5, (D) *R*=0.71, (E) *R*=1 and (F) at *f*=0.1Hz for *R*=1 with G'/G_0' plotted with τ/G_0' (main panel) and G''/G_0'' plotted with τ/G_0' (inset). The information of samples is summarized in Table 4.3.

Table 4.3. Information of samples in Figure 4.7.

R=0				
ϕ_c	h/R_g	$h(\phi_x)/h$	G_0'/Pa ($G_0'h^2<D>/k_BT$)	G_0''/Pa ($G_0''h^2<D>/k_BT$)
0.330	16.1	1	30.2 (0.75)	13.2 (0.33)
0.398	11.1	1.45	98.2 (1.16)	16.9 (0.20)
0.454	7.7	2.08	218.1 (1.23)	31.9 (0.18)
R=0.29				
ϕ_c	h/R_g	$h(\phi_x)/h$	G_0'/Pa ($G_0'h^2<D>/k_BT$)	G_0''/Pa ($G_0''h^2<D>/k_BT$)
0.375	15.6	1	25.0 (0.64)	14.6 (0.37)
0.437	11.0	1.41	100.1 (1.29)	17.2 (0.22)
0.503	7.1	2.18	185.5 (1.00)	37.4 (0.20)
R=0.5				
ϕ_c	h/R_g	$h(\phi_x)/h$	G_0'/Pa ($G_0'h^2<D>/k_BT$)	G_0''/Pa ($G_0''h^2<D>/k_BT$)
0.438	14.9	1	18.7 (0.50)	14.6 (0.39)
0.501	10.5	1.41	87.9 (1.17)	23.9 (0.32)
0.569	7.8	2.26	213.5 (1.56)	43.0 (0.31)
R=0.71				
ϕ_c	h/R_g	$h(\phi_x)/h$	G_0'/Pa ($G_0'h^2<D>/k_BT$)	G_0''/Pa ($G_0''h^2<D>/k_BT$)
0.504	12.6	1	26.6 (0.60)	16.3 (0.37)
0.547	9.5	1.32	80.3 (1.04)	18.1 (0.23)
0.592	6.7	1.88	199.5 (1.28)	44.2 (0.28)
R=1 (f=1Hz)				
ϕ_c	h/R_g	$h(\phi_x)/h$	G_0'/Pa ($G_0'h^2<D>/k_BT$)	G_0''/Pa ($G_0''h^2<D>/k_BT$)
0.549	15.5	1	10.3 (1.14)	9.3 (1.03)
0.57	11.3	1.37	34.7 (2.04)	18.5 (1.09)
0.592	7.1	2.18	79.7 (1.85)	35.1 (0.81)
R=1 (f=0.1Hz)				
ϕ_c	h/R_g	$h(\phi_x)/h$	G_0'/Pa ($G_0'h^2<D>/k_BT$)	G_0''/Pa ($G_0''h^2<D>/k_BT$)
0.549	15.5	1	3.8 (0.42)	2.3 (0.26)
0.57	11.3	1.37	13.1 (0.76)	5.7 (0.33)
0.592	7.1	2.18	48.0 (1.12)	17.9 (0.42)

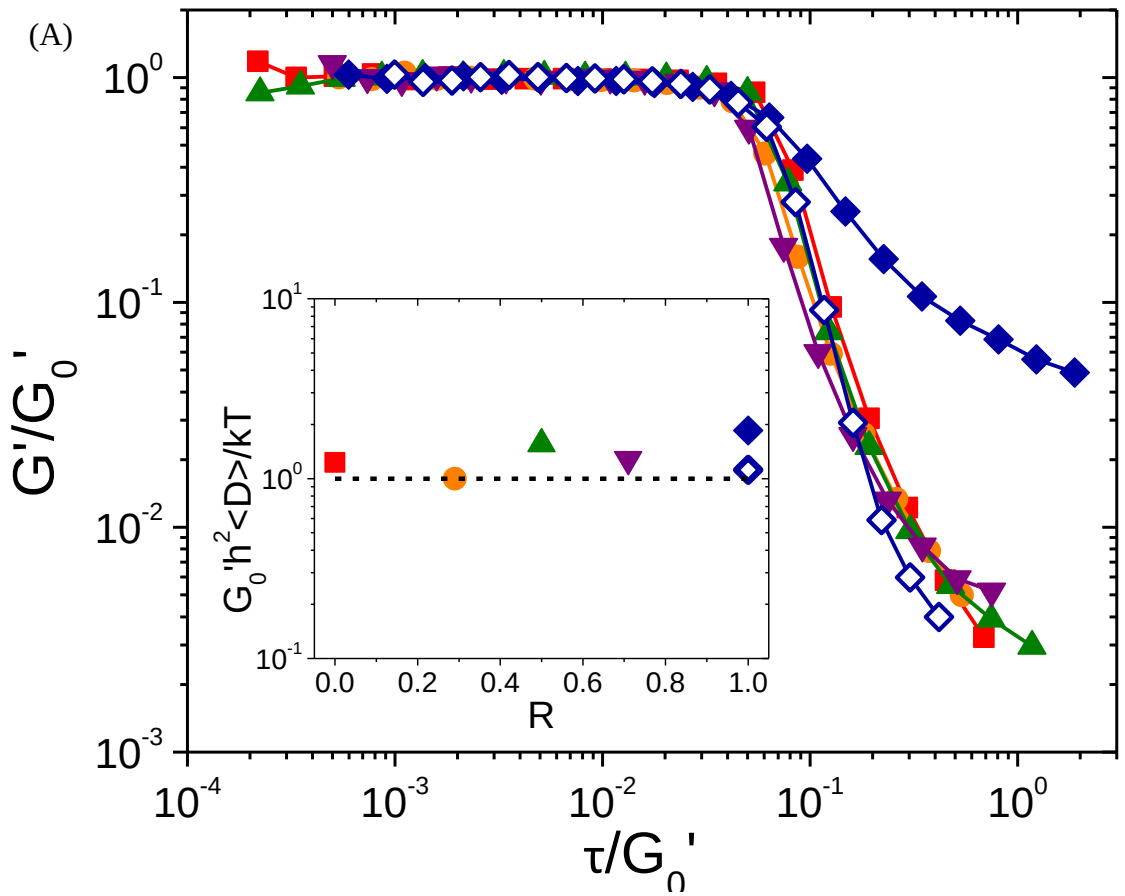

Figure 4.8 (continued on next page)

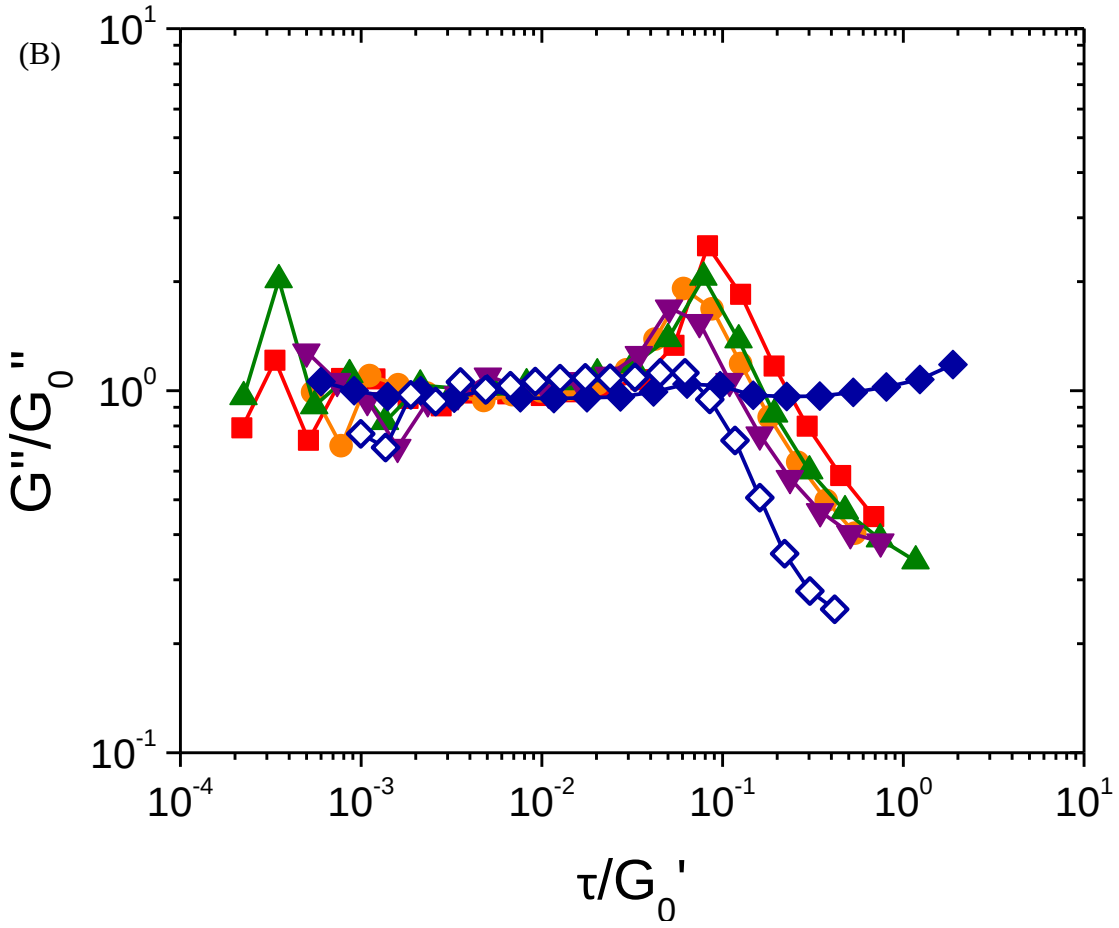

Figure 4.8 Dynamics stress sweeps at for at f=1Hz for R=0, ϕ_c=0.454(■), R=0.29, ϕ_c=0.503(●), R=0.5, ϕ_c=0.569 (▲), R=0.71, ϕ_c=0.592 (▼) and R=1, ϕ_c=0.592(◆) and at f=0.1Hz for R=1, ϕ_c=0.592(◇). with (A) G'/G_0' plotted with τ/G_0' and (B) G''/G_0'' plotted with τ/G_0'. The inset of (A) is scaled G_0' as a function of R with dashed line represents a constant with value of unity.

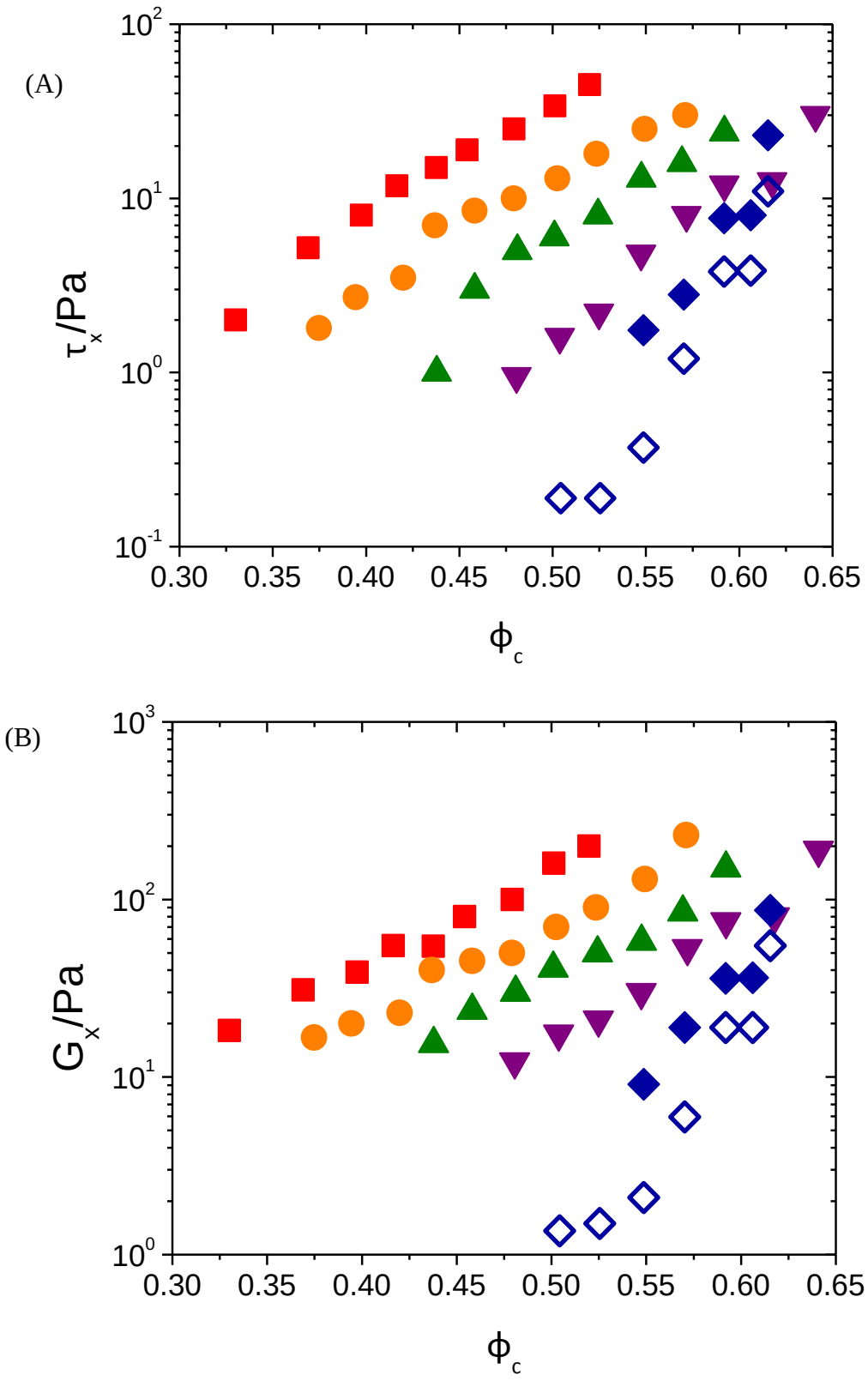

Figure 4.9 (continued on next page)

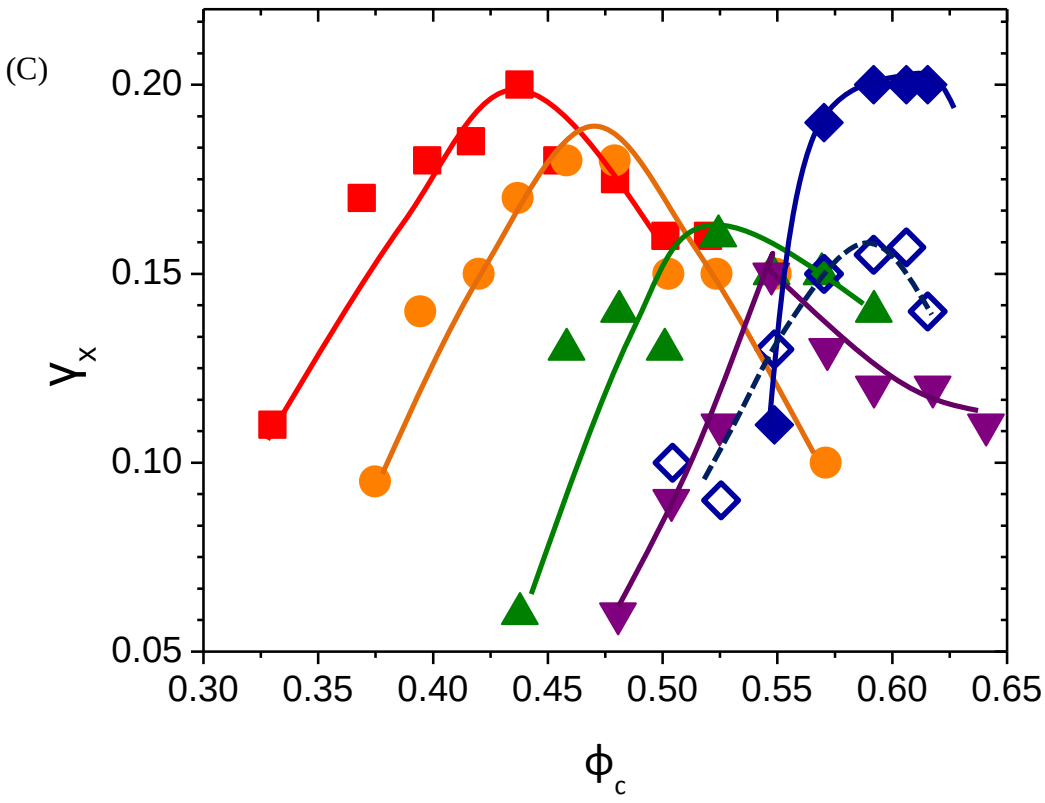

Figure 4.9 (A) τ_x (B) G_x (C) γ_x at the cross point where $G'=G''=G_x$ plot with volume fraction at f=1Hz for R=0(■), R=0.29(●), R=0.5(▲), R=0.71 (▼) and R=1(◆) and at f=0.1Hz for R=1(◇). The curves (red for R=0, orange for R=0.29, green for R=0.5, purple for R=0.71, solid blue for R=1 at f=1Hz, and dashed blue for R=1 at f=0.1Hz) in (C) are used to guide eyes for the peak in γ_x.

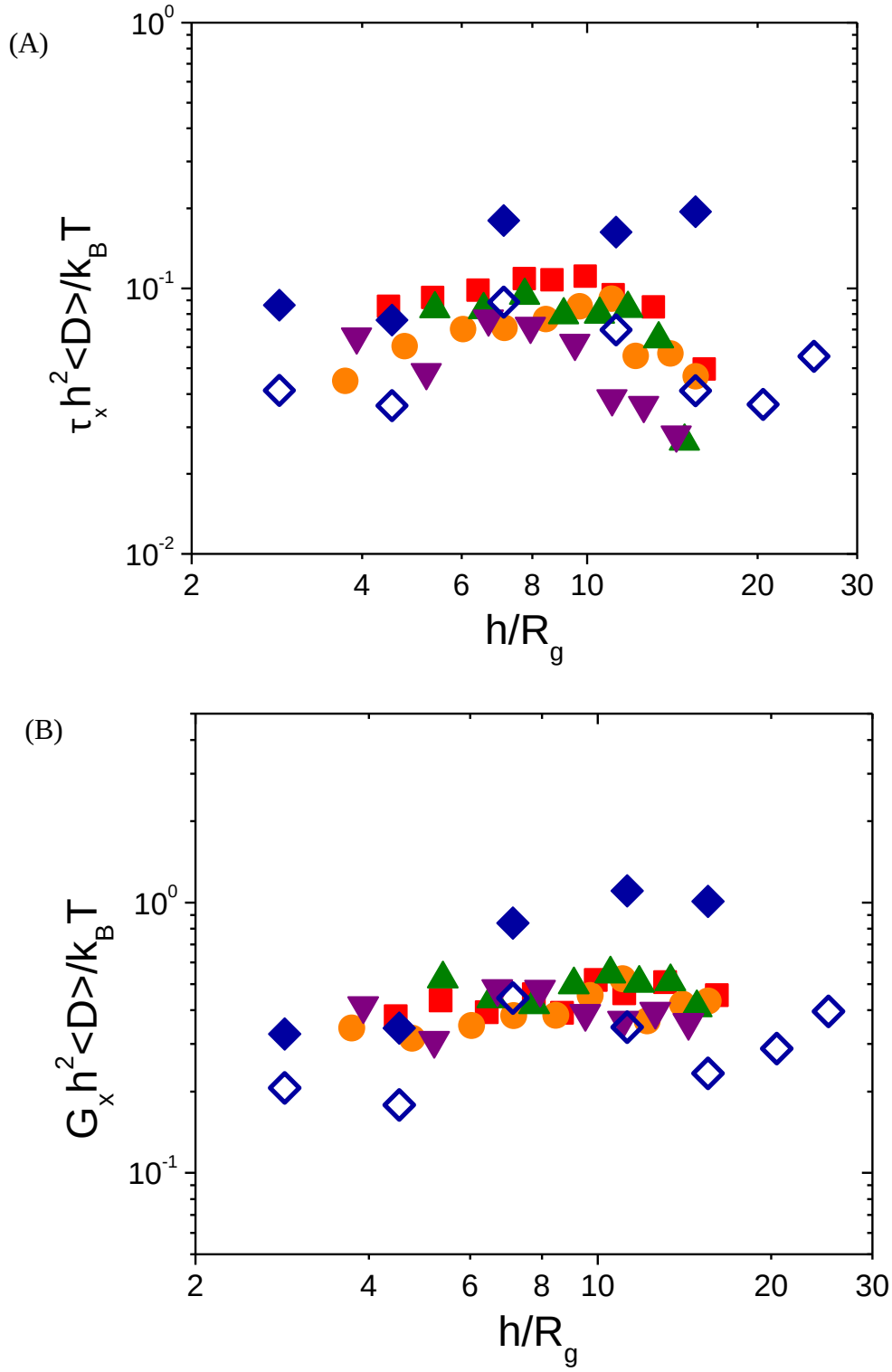

Figure 4.10 (continued on next page)

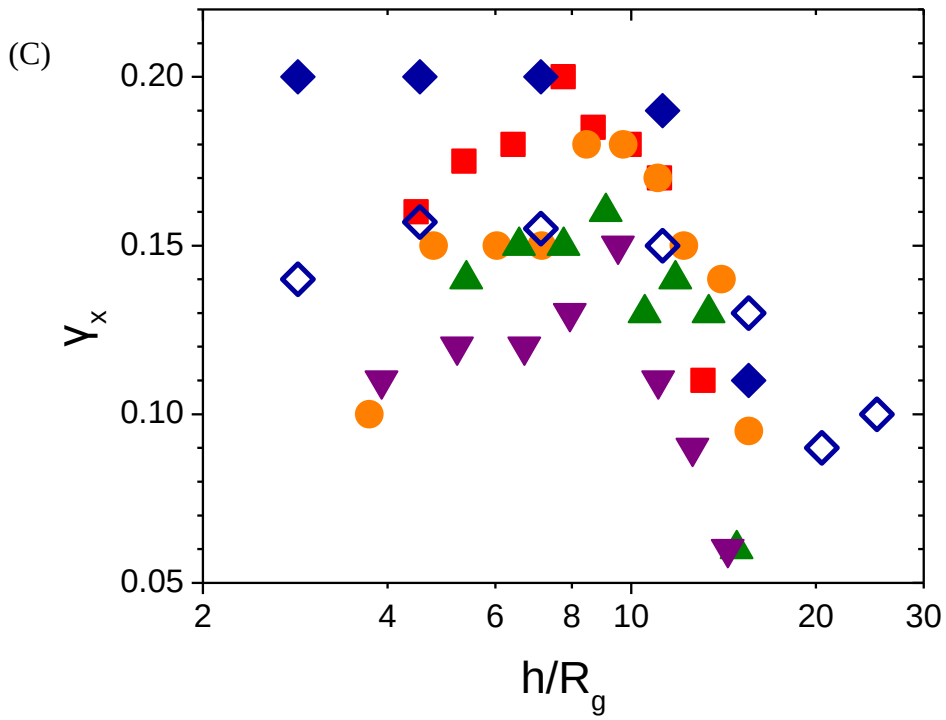

Figure 4.10 (A) Scaled τ_x and (B) scaled G_x (with $h^2<D>/k_BT$) as function of h/R_g at f=1Hz for R=0(■), R=0.29(●), R=0.5(▲), R=0.71 (▼) and R=1(◆), and at f=0.1Hz for R=1 (◇).

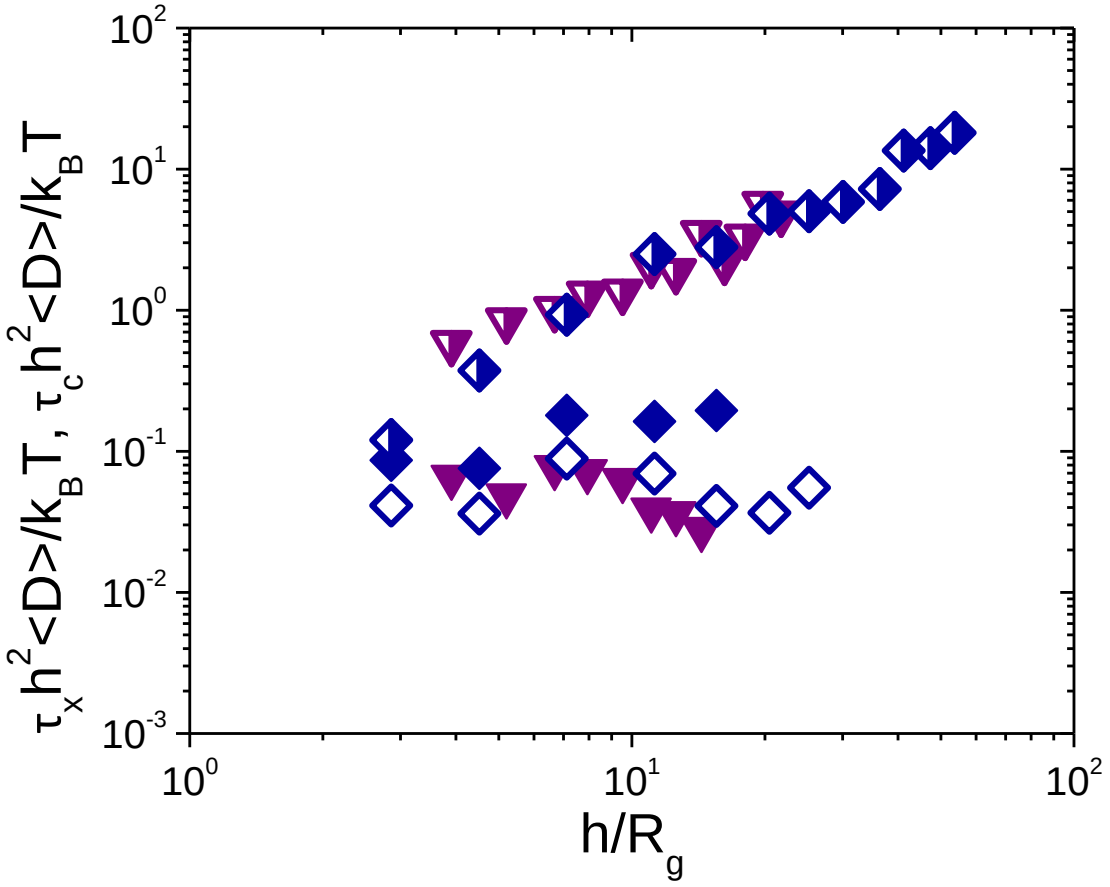

Figure 4.11 Scaled τ_x (with $h^2<D>/k_BT$) as function of h/R_g at f=1Hz for R=0.71 (▼) and R=1(◆), and at f=0.1Hz for R=1 (◇), and scaled τ_c (with $h^2<D>/k_BT$) as function of h/R_g for R=0.71 (▽) and R=1 (◈).

4.6 References

1. B. E. Rodriguez, E. W. Kaler and M. S. Wolfe, *Langmuir*, 1992, **8**, 2382-2389.
2. W. J. Hunt and C. F. Zukoski, *Journal of Colloid and Interface Science*, 1999, **210**, 343-351.
3. M. Pishvaei, C. Graillat, P. Cassagnau and T. F. McKenna, *Chemical Engineering Science*, 2006, **61**, 5768-5780.
4. W. Gotze and T. Voigtmann, *Physical Review E*, 2003, **67**, 021502.
5. A. Imhof and J. K. G. Dhont, *Physical Review Letters*, 1995, **75**, 1662-1665.
6. J. Bender and N. J. Wagner, *Journal of Rheology*, 1996, **40**, 899-916.
7. C. G. Dekruif, E. M. F. Vanlersel, A. Vrij and W. B. Russel, *Journal of Chemical Physics*, 1985, **83**, 4717-4725.
8. R. C. Kramb, R. Zhang, K. S. Schweizer and C. F. Zukoski, *Physical Review Letters*, 2010, **105**, 055702.

9. D. A. R. Jones, B. Leary and D. V. Boger, *Journal of Colloid and Interface Science*, 1992, **150**, 84-96.
10. R. A. Lionberger and W. B. Russel, *Journal of Rheology*, 1994, **38**, 1885-1908.
11. T. Jiang and C. F. Zukoski, *Soft Matter*, 2012, **9**, 3117-3130.
12. Yerazuni.S, S. W. Cornell and B. Wintner, *Nature*, 1965, **207**, 835-837.
13. D. C. Viehman and K. S. Schweizer, *Journal of Chemical Physics*, 2008, **128**, 084509.
14. D. C. Viehman and K. S. Schweizer, *Journal of Physical Chemistry B*, 2008, **112**, 16110-16114.
15. A. Mohraz, E. R. Weeks and J. A. Lewis, *Physical Review E*, 2008, **77**, 060403.
16. B. J. Anderson and C. F. Zukoski, *Journal of Physics-Condensed Matter*, 2009, **21**, 285102.
17. S. Y. Kim, University of Illinois Urbana-Champaign, 2011.
18. B. J. Anderson and C. F. Zukoski, *Macromolecules*, 2009, **42**, 8370-8384.
19. R. Buscall and R. Ettelaie, *Industrial & Engineering Chemistry Research*, 2006, **45**, 6915-6922.
20. Q. Zhang and L. A. Archer, *Langmuir*, 2002, **18**, 10435-10442.
21. B. J. Anderson and C. F. Zukoski, *Macromolecules*, 2008, **41**, 9326-9334.
22. T. Jiang and C. F. Zukoski, *Macromolecules*, 2012, **45**, 9791-9803.
23. D. C. Viehman and K. S. Schweizer, *Physical Review E*, 2008, **78**, 051404.
24. J. C. Conrad, S. R. Ferreira, J. Yoshikawa, R. F. Shepherd, B. Y. Ahn and J. A. Lewis, *Current Opinion in Colloid & Interface Science*, 2011, **16**, 71-79.
25. G. K. Batchelor, *Journal of Fluid Mechanics*, 1977, **83**, 97-117.
26. J. Bergenholtz and N. J. Wagner, *Industrial & Engineering Chemistry Research*, 1994, **33**, 2391-2397.
27. W. Stober, A. Fink and E. Bohn, *Journal of Colloid and Interface Science*, 1968, **26**, 62-69.
28. G. H. Bogush, M. A. Tracy and C. F. Zukoski, *Journal of Non-Crystalline Solids*, 1988, **104**, 95-106.
29. V. Kobelev and K. S. Schweizer, *Physical Review E*, 2005, **71**, 021401.
30. J. Mewis and N. J. Wagner, *Colloidal Suspension Rheology*, Cambridge University Press, Cambridge, United Kingdom, 2012.
31. K. S. Schweizer, *Journal of Chemical Physics*, 2007, **127**, 164506.
32. T. G. Mason and D. A. Weitz, *Physical Review Letters*, 1995, **75**, 2770-2773.
33. T. Shikata and D. S. Pearson, *Journal of Rheology*, 1994, **38**, 601-616.
34. C. J. Rueb and C. F. Zukoski, *Journal of Rheology*, 1998, **42**, 1451-1476.
35. M. Tripathy and K. S. Schweizer, *Physical Review E*, 2011, **83**, 041406.
36. S. Y. Kim, H. W. Meyer, K. Saalwachter and C. F. Zukoski, *Macromolecules*, 2012, **45**, 4225-4237.
37. J. Bergenholtz, M. Fuchs and T. Voigtmann, *Journal of Physics-Condensed Matter*, 2000, **12**, 6575-6583.
38. K. Dawson, G. Foffi, M. Fuchs, W. Gotze, F. Sciortino, M. Sperl, P. Tartaglia, T. Voigtmann and E. Zaccarelli, *Physical Review E*, 2001, **63**, 17.
39. M. Kapnistos, A. N. Semenov, D. Vlassopoulos and J. Roovers, *Journal of Chemical Physics*, 1999, **111**, 1753-1759.

40. M. Cloitre, R. Borrega, F. Monti and L. Leibler, *Physical Review Letters*, 2003, **90**, 068303.
41. K. S. Schweizer and G. Yatsenko, *Journal of Chemical Physics*, 2007, **127**, 164505.
42. T. G. Mason, J. Bibette and D. A. Weitz, *Journal of Colloid and Interface Science*, 1996, **179**, 439-448.
43. M. Laurati, S. U. Egelhaaf and G. Petekidis, *Journal of Rheology*, 2011, **55**, 673-706.
44. D. P. Kalman and N. J. Wagner, *Rheologica Acta*, 2009, **48**, 897-908.
45. S. Granick and H. W. Hu, *Langmuir*, 1994, **10**, 3857-3866.
46. S. Granick, H. W. Hu and G. A. Carson, *Langmuir*, 1994, **10**, 3867-3873.
47. D. L. Green and J. Mewis, *Langmuir*, 2006, **22**, 9546-9553.
48. K. S. Schweizer and J. G. Curro, *Atomistic Modeling of Physical Properties*, 1994, **116**, 319-377.

Chapter 5. The Effect of Shape Anisotropy on Dynamics of Dense Binary Colloidal Mixtures

5.1 Introduction

Mixing particles with different sizes will result in different flow properties as shown in many colloidal dispersion systems.[1-4] Specifically mixing spheres experiencing volume exclusion interactions results in smaller shear viscosity at a given total volume fraction, and larger glass transition volume fractions[2, 5-7]. These phenomena can be explained as a resulting from the mixture inducing more free space in the dense packed systems as reflected in increased maximum packing fraction. When particle-particle interactions are varied, binary spherical mixtures display complicated dynamics. Experimental studies of structure for biphasic colloidal mixtures composed of attractive and repulsive spheres shows that attractive spheres form space-filling gel matrix and repulsive particles show heterogeneous dynamics with some particles trapped in the gel matrix while others diffuse freely.[8]

Here we are interested in understanding changes to particle dynamics in suspensions when shape anisotropy is introduced to a binary mixture. In the past, experiments have been carried out to explore and suggest the principles of optimizing and controlling flow properties of colloidal mixtures when shape anisotropy is introduced.[9-13] Small angle neutron scattering has been used to study the depletion effects in sphere-plate mixtures with large size asymmetry, where the sphere have diameter d=30±5nm and the plate has thickness L=5±1nm and diameter D=203±40nm.[11] This work indicates that depletion interactions give rise to phase separations at elevated total volume fraction. Depletion effects have also been observed in mixtures of charged platelets (L=10.6±3.7nm and D=95.0±16.0 nm) and spheres (d=16.8nm), where the spheres act as depletants and locate

between the columnar stacks formed by the platelets in the equilibrium phase.[12] Some other report has shown that spheres form boundaries of the arrested phase of rods.[14] In addition to experimental characterization of microstructure of colloidal mixtures with variable shape, theoretical work has also opened up fundamental understanding of the dynamics of binary mixtures. These studies have been applied to gain understanding of colloid-polymer mixtures and binary mixtures of molecules.[15, 16] Simulation studies[17] suggest very similar liquid-crystal phase separation observed in experiment as discussed above.[14] In all of these systems, either the size ratio or the shape anisotropy is large with a key focus on the observed phase separation systems. However, it is necessary to systematically understand the dynamics in this nonergodic region when elevating the volume fractions results in glass transition or gelation and explain the different enhancement effects of varied shape on rheology of binary mixtures which has been suggested by previous experimental results. [10, 18] Therefore, here we investigate systems containing binary mixtures with small particles experiencing volume exclusive interactions and large particles experiencing weak attractions, where small shape anisotropy and modest size disparity are introduced to guarantee that no phase separation is observed due to strong depletion attraction.

Recently, Zhang and Schweizer have studied the effects of shear stress on the rheology of hard uniaxial particles by generalizing the naïve Mode Coupling Theory (nMCT) and nonlinear Langevin equation to couple rotational and translational dynamics.[19, 20] They demonstrate that for hard dicolloids composed of two fused spheres with a small aspect ratio, plastic glasses are formed within a wide volume fraction range with rotational and translational relaxation decoupled when elevating shear stress for

small aspect ratio. When the aspect ratio is increased above 1.4, only double glasses are formed upon raising volume fraction predicting the loss of double yielding phenomena as shear stress is increased.[19] Experimentally, Kramb et al. observed such double-yielding behavior where the elastic modulus *G'* shows two shoulders and viscous modulus *G"* shows two maxima by increasing shear stress τ at a fixed deformation frequency for hard dicolloids with aspect ratio L/D~1.3. Under similar volume fraction and pair interaction conditions, spheres display only single-yielding phenomenon where *G'* shows one shoulder and *G"* shows one maximum when increasing shear stress τ at a fixed stress frequency).[21]

Complexity is introduced when tuning interaction among particles.[22-24] When weak attraction is introduced into suspensions of spheres, attractive glasses are formed at high concentrations with yielding occurring in two steps. Here, the first yielding event is associated with bond breaking between particles while the second yielding event is associated with cage breaking and the exchanges of nearest neighbors.[23] While one might imagine that dense suspensions of weakly attractive anisotropic particles could yield with bond breaking, rotational relaxation, and cage deformation, yielding occurs in one or two steps in suspensions of weakly attractive anisotropic particles, suggesting that rotational and center of mass relaxations are tightly coupled in attractive systems.[25] Recent experimental reports in dilute gel formed from introducing strong depletion attraction show double yielding representing rigid bond rotation and breakage in sequence, which is a mechanism than that observed in dense suspensions of particles experiencing weak attractions.[26]

Here we present a systematic study of colloidal mixtures to explore the effects of shape anisotropy on the rheological properties of binary mixtures with particular focus on constrains on particle relaxation in dense suspension. Two different binary mixtures of negatively charged polystyrene particles with size disparity δ~3 ($\delta=D_l/D_s$) are studied. One is composed of small spheres (SSP) with D_s=330nm and large dumbbells (LDB) with Diameter D_l=845nm and length L_l=1131nm. To compare with this system, the analogue system is used composed of small spheres with D_s=330nm and large spheres (LSP) with diameter D_l=1097nm. Our goal is to investigate suspension properties at high volume fractions where nearest neighbors form cages and constrain rotational and center of mass (CM) relaxations. As large particles have a smaller self-diffusivity and dominate the dynamical arrest transitions with increasing total particle concentrations, we do not change the shape of the small particles. The particles are dispersed in an aqueous e solution with ionic strength I=0.01M which establishes a weak attraction between large particles (LSP and LDB) independent of shape and volume exclusion interactions between small particles (SSP). To characterize the arrest and relaxation processes of dense suspension as a function of volume fraction ϕ_c and shear stress τ, continuous shear and oscillatory shear have been applied. For the continuous shear, we focus on investigating the discontinuous shear thickening phenomenon at high shear stress. For oscillatory shear, the results of frequency sweep experiment have been first presented to clarify the motivation of stress sweep experiment on mixtures at f=1Hz.

Below we introduce the procedure of sample preparation and rheological measurement in Section 5.2. Then results and discussions with a focus on nonlinear oscillatory rheology and underlying explanation of particle relaxation dynamics are

covered in Section 5.3. Finally we summarize the systems and give the main conclusions in Section 5.4.

5.2 Experimental Approaches

To obtain similar surface chemistry for small particles and large particles, a similar seeded emulsion polymerization synthesis technique which can produce shape anisotropy and has been pioneered by Sheu and coworkers[27] is used to make all of the three particles.

To make LDB, negatively charge polystyrene seeds cross-linked by 2wt% divinyl benzene (DVB) with diameter ~800nm were made first before the seeded emulsion polymerization using a soap-free emulsion polymerization recipe.[28] The details have been introduced in previous literature.[29] After the reaction have been completed, the volume fraction of the seed suspension was determined, by placing ~0.5mL suspension into 20mL glass vial, drying the suspension in ~110℃ oven and calculating the volume loss with measured weight loss based on a polystyrene density of 1.055g·cm^{-3}. Then the seed particle suspension was diluted to a volume fraction ~0.08 with deionized water (DIW) according to the measured volume fraction. To make LDB with seeded emulsion polymerization afterwards, 150mL diluted seed dispersion was discharged into a 500mL round-bottom glass flask which was fitted with a glass impeller carrying a PTFE blade and immersed into a water bath at room temperature. The impeller was connected to a Glas-Col 099D G31 stirring system which would operate at ~220rpm during the reaction. After everything has been set up, 0.64g 2,2′-Azobisisobutyronitrile (AIBN) was solved into 28mL styrene, and the mixture was added into the reactor. The stirring was kept throughout the process of swelling and secondary polymerization. After the swelling step proceeding for 24h, including 2.5h to allow the temperature to increase to 75 ℃, 6.0g

sodium dodecyl sulfate dissolved into 60mL DIW and 5.8g hydroquinone dissolved into 100mL DIW were added into the reactor. The reaction proceeded for 24h.

To make LSP, negatively charge polystyrene seeds cross-linked by 0wt% DVB with diameter ~800nm were made first before the seeded emulsion polymerization using a soap-free emulsion polymerization recipe which was similar to the recipe used to make LDB with no DVB added in the reaction. After the seeds were made, all the procedures of swelling and secondary polymerization in making LDB were followed to make LSP.

To make SSP, first small negatively charged polystyrene seeds were made using a similar recipe as used in previous studies.[30] A 1000mL round-bottom glass flask which was fitted with a glass impeller carrying a PTFE blade and immersed into a water bath at temperature about 75℃. The impeller was connected to a Glas-Col 099D G31 stirring system which would operate at ~300rpm during the reaction. 400mL DIW, 46.6mL styrene and 0.50g SDS dissolved into 50mL DIW were discharged into the reactor. The container used to dissolve SDS was rinsed with 50mL DIW which was added into the the reactor afterwards. After 1h to allow the reaction system to reach the temperature, 1.55g potassium persulfate dissolved into 75mL DIW was added into the reactor to initiate the emulsion polymerization. The reaction was allowed to proceed for about 24h. Then the volume fraction of the seed suspension was determined, by placing ~0.5mL suspension into 20mL glass vial, drying the suspension in ~110℃ oven and calculating the volume loss with measured weight loss based on a polystyrene density of 1.055g·cm^{-3}. To make SSP with seeded emulsion polymerization afterwards, 200mL seed dispersion with volume fraction about 0.07 was discharged into a 500mL round-bottom glass flask which was fitted with a glass impeller carrying a PTFE blade and immersed into a water bath at

room temperature. The impeller was connected to a Glas-Col 099D G31 stirring system which would operate at ~220rpm during the reaction. After everything has been set up, 0.64g 2,2′-Azobisisobutyronitrile (AIBN) was dissolved into styrene to make sure the swelling ratio is 2:1, and the mixture was added into the reactor. The stirring rate was held constant throughout the process of swelling and secondary polymerization. After the swelling step proceeding for 24h, including 2.5h to allow the temperature to increase to 75 ℃, 6.0g sodium dodecyl sulfate dissolved into 60mL DIW and 4g hydroquinone dissolved into 100mL DIW were added into the reactor. The reaction proceeded for 24h.

The sizes of the resulting particles are measured with Scanning Electron Microscopy (SEM) with the pictures shown in Figure 5.1. SSP has a diameter D_s=330±5nm, LSP has diameter D_l=1097±9nm, LDB has length L_l=1131±30nm and diameter D_l=845±25nm (The aspect ratio is L/D=1.3). Basically these three sets of particles have narrow size distribution below 5%.

The resulting particles were cleaned by dialysis. The suspensions were placed into a SpetroPor Dialysis tubing (molecular weight cutoff 12000-14000) and dialyzed against DIW for about 2-3 days with DIW outside the tubing being replaced for about 5-6 times until the conductivity outside the tubing reached constant. This will eliminate hydroquinone, oligomers and other species resulting from the reaction. Then about 200g polyethylene glycol with Mn~20000 (PEG20000, Sigma-Aldrich) was dissolved into the DIW out of the dialysis tubing to concentrate the suspension to a volume fraction ~0.30. This process was continued for about 2 days. PEG 20000 here was used to increase the osmotic pressure of the dialysate and raise the flow rate of the water which flew out of the tubing.

Then the resulting particles were coating with a monolayer of non-ionic surfactant n-dodecyl-hexaethylene-glycol $C_{12}E_6$ based on adsorption isotherm results in previous study.[29] The critical micelle concentration in pure DIW is about $C_{cmc}=8\times10^{-5}$M with saturated surface coverage for polystyrene is $\Gamma=1.5$ molecules·nm^{-2}. The amount of $C_{12}E_6$ necessary for monolayer coverage was calculated as follows:

$$m(C_{12}E_6) = M_s V_t (1-\phi_c) C_{cmc} + M_s V_t \phi_c \Gamma A_p/(V_p A_v) \quad (5.1)$$

where the molar weight for $C_{12}E_6$ is M_s=450g/mol, V_t and ϕ_c are the total volume and volume fraction of the suspension respectively, $A_v=6.02\times10^{23}$ molecules/mol is Avogadro constant and A_p and V_p are surface area and volume of a single particle. The suspensions were placed in an oven with the temperature set at ~35 ℃ after the surfactant was added for about 1h. Sodium chloride solution containing $C_{12}E_6$ with C_{cmc} was used to tune the ionic strength to [I]=0.01M. Zeta-potential of the resulting particles were measured in the solution containing [NaCl]=0.01M and $[C_{12}E_6]=8\times10^{-5}$M. For SSP, the zeta-potential is about -28mV; for LSP and LDB, the zeta-potential is about -45mV.

The resulting large particles and small particles were mixed afterwards according to desired large particle volume fraction ratio R which we would introduce below. The suspension was then discharged into a dialysis tubing which was placed in a ~1000mL container containing about 800mL solution with [NaCl]=0.01M and $[C_{12}E_6]=8\times10^{-5}$M and 60g PEG20000 for ~1 day. The resulting suspension has a volume fraction ~0.6-0.70 with volume ~30mL, which was placed into a 50mL centrifuge tube.

Rheological measurements were carried out on a Bohlin C-VOR rheometer with a cup and bob geometry, with ~3 ml samples loaded each time. The bob is made of roughened titanium with a diameter of ~14 mm and a ~0.7 mm gap remained when fitted

into the cup. The temperature was kept constant at ~25±0.2℃. To guarantee uniform mixing, samples were pre-sheared by rotating the bob carefully by hand to avoid shear thickening. A solvent trap was placed to minimize the evaporation during the experiment, but the time for each running was still controlled within 20 min to guarantee no obvious change in volume fraction. After each measurement, ~0.5mL sample was taken from the cup and placed into a 20mL vial; the vial was kept in an oven with temperature ~110 ℃ for ~20mL to evaporate the solvent and measure the mass loss during the evaporation. Then the volume fraction of the sample was calculated based on a polystyrene density ~1.055g·cm^{-3}. Then residual suspension in the cup was placed back into the centrifuge tube and diluted with solution containing [NaCl]=0.01M and [$C_{12}E_6$]=8×10^{-5}M. The cup and bob were cleaned with toluene and rinsed with DIW before the next experiment on the diluted suspension.

For rheology measurement, we apply both continuous shear and oscillatory shear. In the oscillatory shear, we mainly focused on stress sweep experiment with elastic modulus G'(Pa) and viscous modulus G''(Pa) measured as a function of shear stress τ(Pa) at a fixed frequency f=1Hz, with linear elastic modulus G_0'(Pa) and linear viscous modulus G_0''(Pa) measured below a shear strain γ~0.001. In the continuous shear, dynamic shear was applied to increase shear stress τ (Pa) with resulting viscosity η(Pa·s) and shear rate $\dot{\gamma}$ (s^{-1}) measured.

Here for further characterization purpose in understanding the rheology results by studying the dimensionless parameters, we introduce the concept of effective diameter for LDB, which characterizes the length scale for studying the dimensionless parameters in the rheology as following:

$$D_{eff}^3 = L_l^2 D_l \tag{5.2}$$

Therefore we have D_{eff}=1026nm for LDB, which is close to the diameter value of LSP. In order to study the flow properties in mixtures, we introduce the volume average diameter <*D*> which is the value for single-component suspension containing the same volume fraction and density fraction as the binary mixtures; therefore it can be expressed as following:

$$< D >= (\frac{R}{D_l^3} + \frac{1-R}{D_s^3})^{-1/3} \tag{5.3}$$

where we use D_{eff} as the value of D_l for LDB, and *R* is the large particle volume fraction ratio. We studied six different values of *R* for both mixtures (0, 0.29 0.5, 0.71, 0.85 and 1), SSP/LSP and SSP/LDB, with the volume average diameter <*D*> summarized in Table 5.1.

Below we use these average particle sizes as the characteristic length scale for each value of *R*.

5.3 Results and Discussions

5.3.1 Surface Potential and Interaction Energy

After truncating the van der Waals attraction using the non-ionic surfactant $C_{12}E_6$ as in previous studies by producing a steric layer with length ~4nm. We expect that the interaction energy between different sets of particles can be expressed as composed of three parts according to Equation (5.4), electrostatic repulsion (U_E), van der Waals attraction (U_V), and steric interaction (U_S):

$$U = U_E + U_V + U_S \tag{5.4}$$

where

$$U_E = \frac{\pi\varepsilon_0\varepsilon D_1 D_2}{4(D_1+D_2)}\left\{(\Psi_1+\Psi_1)^2\ln[1+\exp(-\kappa h+\kappa\delta)]+(\Psi_1-\Psi_1)^2\ln[1-\exp(-\kappa h+\kappa\delta)]\right\} \quad (5.5)$$

$$U_V = -\frac{A_H}{12}\left[\frac{D_1 D_2}{h^2+h(D_1+D_2)}+\frac{D_1 D_2}{h^2+h(D_1+D_2)+D_1 D_2}+2\ln\frac{h^2+h(D_1+D_2)}{h^2+h(D_1+D_2)+D_1 D_2}\right] \quad (5.6)$$

$$U_s = \begin{cases}\infty, & h<\delta \\ 0, & h>\delta\end{cases} \quad (5.7)$$

Here, the relative dielectric constant ε is 80 for water, the dielectric constant for vacuum ε_0 is 8.854×10^{-12} $C^2/N\cdot m^2$. The diameter of the i^{th} kind of sphere is D_i (i stands for s or l), and the closest surface separation between two spheres δ is 8 nm, which is twice the surfactant length.[31] The surface potential of the i^{th} sphere is ψ_i (i stands for s or l), h is the surface distance between two particles, and κ^{-1} is the Debye thickness in nanometers, which is determined from $0.304/[I]^{0.5}$, which is 3.0nm here. The Boltzmann constant k_B=1.38$m^2\cdot kg\cdot s^{-2}\cdot K^{-1}$, and the absolute temperature is T=298K. The Hamaker constant is A_H=1 $\times10^{-20}$J.[31]

As LSP and LDB have similar surface potential and effective diameter, here we just use the value of LSP to estimate different pair interaction in binary mixtures. Therefore the interaction energy is calculated as varying particle-particle separation h, with the result plotted in Figure 5.2.

The interaction between SSP with either SSP or LSP is relatively small with a minimum larger than -1k_BT. Therefore we treat SSP-SSP and SSP-LSP as experiencing volume exclusion interactions. However, LSP-LSP interaction energy has a minimum on the order ~-2k_BT which is sufficient to later the dynamics of these particles and to observe re-entrant effect on dynamic arrest trasnition.[32] These calculations suggest that we have mixtures of large and small particles where the small/mall and small/large interactions are

short ranged and harshly repulsive near contact while large/large interactions show a weak attraction followed by a harsh repulsion at smaller particle separations.

5.3.2 Linear Shear Elasticity

The frequency (ω) dependence of the elastic moduli are explored by carefully tuning the shear strain $\gamma<\sim10^{-3}$ for a series of samples to ensure that the measurements lie in the linear response region. The frequency sweep experiment results are presented in Figure 5.3 for the two extreme single-component cases R=0 and R=1 for SSP/LSP system.

The data shown in Figure 5.3 indicate that as the volume fraction, ϕ_c, is raised, the characteristic relaxation time denoting where terminal low frequency behavior is reached shifts to lower frequencies. In the volume fraction range studied, at high frequencies (f>1Hz), the plateau elastic modulus is approached. With ϕ_c kept high enough, f=1Hz is guaranteed to be located in the range of plateau. The f dependence of G'' is different from that of G', with a minimum observed when ϕ_c is large, and when ϕ_c is small, a plateau developed and terminal behavior reached at low frequencies. We note here that there was no obvious minimum point observed in the curve of G'' at high ϕ_c as reported in previous study in systems containing silica particles dispersed in PEG.[33] Often the elastic modulus at the frequency of the minimum in G'' is taken as a measure of the plateau elastic modulus G_p'.[33, 34] For these systems, the lack of a minimum in G" presents an uncertainty in how to estimate G_p'. However, as the point of f=1Hz is located in the basin developed in the frequency sweep experiment, denoting that f=1Hz sets an observation time scale $\sim1/2\pi$ s which is short enough to detect dynamic arrested states without letting the particles diffuse out of the nearest neighbor cages, and long enough to make sure the particle can respond to the applied shear. Nevertheless, the f dependence of G' and G''

are weak around the point f=1Hz which sets the time scale to observe the characteristics of dynamic arrested state. Therefore we chose this frequency to study both linear moduli (G_0' and G_0'') and yielding in the stress (τ) sweep experiments.

In Figure 5.4, we show an example of dynamic stress sweep experiment results, where dimensionless elastic modulus $G_0'^*$ and dimensionless viscous modulus $G_0''^*$ are plotted as a function of dimensionless stress τ^*, where $G'^* = G' < D >^3 / k_B T$, $G''^* = G'' < D >^3 / k_B T$ and $\tau^* = \tau < D >^3 / k_B T$.

In low stress limit, both G'^* and G''^* develop plateau values which were dimensionless linear elastic modulus $G_0'^*$ and linear dimensionless viscous modulus $G_0''^*$ respectively. Also the method of determining yielding point is also illustrated in Figure 5.4, which we would discuss in details below.

In Figure 5.5, the results of linear elasticity $G_0'^*$ are plotted as a function of ϕ_c based on different large particle volume fraction ratio R for both systems SSP/LSP and SSP/LDB.

For both SSP/LSP and SSP/LDB mixtures, we can note two characteristics in common. First, $G_0'^*$ increases as an exponential function of ϕ_c which has the form $G_0'^* \propto \exp(b\phi_c)$. Second, in single-component systems (R=0 and R=1), $G_0'^*$ has a stronger dependence on ϕ_c compared to binary mixtures (R=0.29, R=0.5, R=0.71 and R=0.85), meaning that the parameter b is larger for binary mixtures than for suspensions of single-sized particles. However, a substantial difference is observed in the two systems in that the magnitude of $G_0'^*$ at a fixed ϕ_c is non-monotonic function of R for SSP/LSP (reaching a minimum value for R=0.85), but is a monotonic function of R for SSP/LDB (reaching a minimum at R=1).

To understand this phenomenon, we discuss the results by introducing the concept of iso-elasticity line which is determined by the points with equal values of G_0'* in the panel of ϕ_c-R. As shown in Figure 5.5, with mixture type and large particle volume fraction ratio R varied, the G_0'* values are increased in the range of 10^3-10^4 by increasing ϕ_c, within this range we locate values ϕ_c when G_0'*=10^3, 3×10^3 and 10^4 for two binary mixture types for different values of R by interpolating the exponential fitting. The iso-elasticity lines set as these three G_0'* values are plotted for both SSP/LSP and SSP/LDB in the panel of ϕ_c-R in Figure 5.6.

Both systems display very similar behaviors for R=0, R=0.29 and R=0.5, where the volume fraction ratio of small particles are substantially dominant ($\phi_s/\phi_c \geq 0.50$). As a result, we conclude that the flow properties are controlled by SSP without obvious effects of large particle shape anisotropy for these conditions. Difference between SSP/LSP and SSP/LDB are apparent for R=0.71, R=0.85 and R=1, where SSP/LSP shows a maximum in the iso-elasticity lines at R=0.85, but iso-elasticity lines of SSP/LDB consistently increases with ϕ_c when increasing R. In another aspect, for R=0.71 and R=0.85, SSP/LSP at a given elastic modulus has a larger volume fractions than SSP/LDB. However, for R=1, SSP/LSP has a smaller volume fractions than SSP/LDB at a given elastic modulus.

NMCT has predicted that $G_0'^* \cong A\left(\frac{D_c}{r_{loc}}\right)^{2.2}$, where r_{loc} is the localization length and A is a constant weakly influenced by aspect ratio.[35] The localization length characterizes the diffusion length scale for short time self-diffusion of a caged particle. As volume fraction increases, the localization length decrease in size and the modulus increase. The localization length is calculated from equilibrium structure factors and, in principle, can

be determined for any pair potential. In naïve Mode Coupling Theory and in Dynamic Localization Theory,[36] $1/r_{loc}$ is infinite (indicating no caging) below dynamic arrest volume fraction ϕ_x and takes on a finite value at ϕ_x, demarking the onset of glassy behavior. r_{loc} is known to scale well on $(\phi_c-\phi_x)$ and on $\phi^*=(\phi_m-\phi_x)/(\phi_m-\phi_c)$ where ϕ_m/ϕ_x is found to be a constant for hard shape anisotropic particles[37] and binary mixtures of hard spheres.[38] By choosing to look at lines of constant dimensionless modulus we are choosing to look at lines where r_{loc}/D_c is a constant for different systems.

Previous theoretical studies have shown that dumbbell shaped particles show non-monotonic behavior in cross-over volume fraction ϕ_x with increasing aspect ratio L/D with a maximum achieved at L/D=1.4. Universal elasticity observed when scaling ϕ_c with ϕ_x, which suggests similar $G_0'^*$ (similar r_{loc}/D_c) are measured at substantially larger ϕ_c for weakly shape anisotropic particles (L/D=1.3) compared to spherical particles.[39] These phenomena are associated with the more efficient packing of the anisotropic particles as the dumbbell shaped particles can be viewed as two fused spheres. As has been shown theoretically and experimentally for hard particles[37] and weakly attractive particles.[40] We conclude that the differences seen in the moduli for these two different systems with similar weakly attractive interactions at R=1 can be attributed to increases in maximum packing fraction due to the minor increase in shape anisotropy in the LDB system.

As shown theoretically for hard sphere binary mixtures and observed in weakly attractive binary mixtures adding a small volume of SSP into LSP enhances the packing efficiency and correlated relaxations. This is evidenced in the larger value of ϕ_c required to achieve the same dimensionless modulus at R=0.71 and R=0.85.[2, 5] This enhanced relaxation has not been observed by adding a small amount of SSP into LDB as shown

from the iso-elasticity lines. We would expect, for example that if small spheres raise the dynamic arrest volume fractions in the same way for the LDB suspensions as for LSP systems, the line of constant elasticity would have negative slopes near R=1 and pass through a maximum above those of the SSP/LSP systems in the region of R=0.71 and R=0.85. Rather than increasing ϕ_x and thus increase r_{loc}, addition of small spheres to large dumbbells decreases fm and r_{loc}.

Zhang and Schweizer recently generalized the nMCT and nonlinear Langevin equation theories of coupled rotational-translational dynamics of dumbbell shaped particles to predict linear elasticity and yielding behaviors in dense suspensions.[20] They predict for weakly shape anisotropic particles (L/D=1.15 and 1.3) that linear elasticity is a function of both r_{loc} and θ_{loc}, where θ_{loc} is the localization angle and changes from infinity to a finite value through a plastic glass-double glass transition when increasing ϕ_c. Based on this observation we suggest that the deceased value of ϕ_c to reach a particular elasticity in the SSP/LDB system results from a complicated localization mechanism with the cooperative relaxation of SSP and LDB due to shape anisotropy when SSP are added to suspensions of LDB. From SEM pictures in Figure 5.1, LDB particles clearly possess girdles in the middle, which can produce a source of cooperative localization in the suspensions. We expect the existence of this girdle to further alter the relaxation properties of mixtures of dumbbells and spheres that can be taped in the girdles.

To further investigate this shape anisotropy effect in the rheology of dense suspension for binary mixtures, we will study the nonlinear rheology and yielding behaviors below.

5.3.3 Yielding Behaviors and Nonlinear Rheology

In Figure 5.4, we have shown the method of determining the yield stress τ_x^* which is determined as the point where $G'^*=G''^*=G_x^*$ in the dynamic stress sweep experiment. At lower shear stresses $\tau^*<\tau_x^*$, $G'^*>G''^*$ with the suspension responding in a more elastic manner than as a viscous liquid, while for $\tau^*>\tau_x^*$, $G'^*<G''^*$ where the suspension response is dominated by loss. At the yielding point, we also define the yield strain γ_x as the strain at τ_x^*. In Figure 5.7, γ_x, τ_x^* and G_x^* are plotted as functions of ϕ_c for SSP/LSP and SSP/LDB. Again we see similar behaviors between SSP/LSP and SSP/LDB for R=0, R=0.29 and R=0.5, with differences observed for R=0.71, R=0.85 and R=1.

For γ_x, other than R=0 where a maximum is observed similarly as reportedly previously for hard sphere systems,[33, 41, 42] and R=0.85 for SSP/LDB where γ_x is independent of ϕ_c, other systems show that γ_x is an exponential function of ϕ_c, with the magnitude of γ_x larger for single-component systems than binary mixtures. Indeed the mixtures have yield strains that are much smaller than for homogeneous suspensions. We note that under the framework of nMCT, the yield strain is the ratio of stress and modulus, where the stress is determined by the barrier height of the dynamic potential and the modulus is determined by the curvature of the dynamic potential at the minimum. Therefore, we would expect a significant change in the volume fraction dependence of γ_x when small changes are made to the barrier-controlled yielding. We note significant changes to the yield strains when adding small spheres to large spheres compared to adding small spheres to large dumbbells as seen in comparing the volume fraction dependence of yield strains at R=0.85.

τ_x* and G_x* are both exponential functions of ϕ_c for various systems. τ_x* data can be differentiated easily for different R in the SSP/LSP system. However, τ_x* data cannot be differentiated for different R in the SSP/LDB system where we see very similar magnitudes for R=0.71, R=0.85 and R=1. We again conclude that introducing SSP into LDB does not change suspension flow properties through the mechanism of increasing the maximum packing fraction as expected if these systems behave in a manner similar to the SSP/LSP systems. The G_x* data are very similar to G_0'* data regarding the difference between single-component systems and binary mixtures and the difference between SSP/LSP and SSP/LDB, however we note here that the data are superimposed well for binary mixtures for both systems which is different from G_0'*.

How can we understand the complicated cooperative localization produced by weak shape anisotropy in these weakly attractive systems? As substantial difference introduced by shape anisotropy is only observed for R=0.71, R=0.85 and R=1, we compare SSP/LSP and SSP/LDB by focusing on the nonlinear rheology for these three R values.

In Figure 5.8(A)-(F), the results of dynamic stress sweeps are plotted in the panel of G'*/G_0'*-τ*/G_0'* and G''*/G_0''*-τ*/G_0'* (insets) for representative volume fractions. For the two different single-component systems (R=1), double yielding has been observed for both systems at all the volume fractions studied here as characterized by two shoulders in G'*/G_0'* and two maxima in G''*/G_0''* with increasing τ*/G_0'*. For LSP suspensions as shown in Figure 5.8(E), the first yielding step is located in the region τ*/G_0'*~10^{-3}-10^{-2}, with this location weakly influenced by ϕ_c, and the second yielding is located in the region τ*/G_0'*~5×10^{-2}-5, moving to larger values of τ*/G_0'* with decreasing ϕ_c. In addition, we note that the peak in G''*/G_0''* of the first yielding event is larger than in

the second yielding event as shown in the inset plot of Figure 5.8(E). We attribute this to a stronger first constraint in the yielding process. For LDB suspensions as shown in Figure 5.8(F), the location of the first yielding step is $\tau^*/G_0'^*$~5×10^{-3}-5×10^{-2} and the location of the second yielding is $\tau^*/G_0'^*$~5×10^{-1}-5, both moving to higher values of $\tau^*/G_0'^*$ with decreasing ϕ_c. Significantly different from LSP suspensions, LDB suspensions display a "stronger" second yielding than first yielding which is reflected in the small first peak ($G''^*/G_0''^*$~1) and substantial second peak ($G''^*/G_0''^*$>1) in the $G''^*/G_0''^*$-$\tau^*/G_0'^*$ plot. In addition, in the main panel of Figure 5.8(F) is evidence of weak shear thickening in the second yielding step as $G'^*/G_0'^*$ is increased with $\tau^*/G_0'^*$. All these phenomena convince us that the LDB particles encounter a much stronger second constraint to yielding than the LSP suspensions. To understand the difference between the yielding mechanism of LSP and LDB, we explore the source of the double yielding phenomenon displayed by both large particles.

The estimates shown in Figure 5.2, suggest that there is a weak attraction introduced between large particles due to van der Waals interactions, with a minimum in the interaction energy ~$-2k_BT$. Following other studies,[22, 43] we treat the first yielding in LSP as a consequence of overcoming the inter-particle bonding produced by this weak attraction, and the second yielding in LSP suspensions as an indication of particle escaping from the cage formed by nearest neighbors. The second yielding in the suspension becomes less obvious when decreasing ϕ_c, which is shown for the sample with ϕ_c~0.600. Similar double yielding events have been reported for weakly attractive systems of spheres.[22, 43] For LDB suspensions, particles escape from the attractive potential well in the first yielding step, and overcome the combined rotational and

translational constrains in the second yielding step.[25] For these systems we conclude that the second yielding event requires larger stresses and involves a greater loss of energy as measured by the value of $G_0''^*$. This double yielding due to bonds breaking and coupled translational-rotational dynamics for dumbbell shaped particles have also been reported for homogenous suspensions of weakly anisotropic particles.[25]

Double yielding behavior is greatly weakened in the mixtures even when the large particle volume fraction ratio is as high as 0.85. For SSP/LSP mixtures at R=0.85, double yielding is still observed at high ϕ_c (ϕ_c >0.671) as shown in the main panel of Figure 5.8(C) with two shoulders observed in the $G'^*/G_0'^*$-$\tau^*/G_0'^*$ plot. This phenomenon is still weakened as shown in the inset of Figure 5.8(C) where only the sample with ϕ_c =0.729 displays two shoulders in the $G''^*/G_0''^*$-$\tau^*/G_0'^*$ plot, but no maxima are seen in $G'^*/G_0''^*$ ($G''^*/G_0''^*$<1 throughout the whole stress range). We attribute the loss of double yielding to the destruction of the attractive glass formed by LSP when adding SSP, as reported in theoretical prediction that addition of hard spheres in the suspension of sticky spheres will suppress the re-entrant behavior.[44] For R=0.85 in the mixtures with size ratio used here (δ~3), the large particle number density fraction is only 0.17. However, for this value of R, when $\phi_c \geq 0.684$, the volume fraction of large spheres lies in the glassy region ($\phi_l \geq 0.581$). Thus the presence of small spheres is not sufficient to disrupt the attractive large sphere glass and double yielding is observed. However, no double yielding observed for R=0.71 for all the volume fractions studied here (($\phi_c \leq 0.665$, $\phi_l \leq 0.472$), with the yielding only controlled by center of mass relaxation. Thus for all the volume fractions studied at R=0.71, the large particles are unable to form an attractive glass.

LDB's are arrested at much lower volume fractions than suspensions of spheres. This can be understood as increased constraints to relaxation arising from changes to packing introduced by the geometry of large particles. The attractive glasses formed by LDB are disrupted at all the volume fractions ($\phi_c \leq 0.679$, $\phi_l \leq 0.577$) studied here even for R=0.85. For R=0.71, single yielding is still observed for SSP/LDB, suggesting that the small particles drive the larger particles into a glass at lower volume fraction but eliminate a mechanism for constraints release in a decoupled manner.

5.3.4 Shear-Thickening

Continuous shear has been applied to a different set of samples (with different ϕ_c range) in order to study the shear thickening phenomenon for SSP/LSP and SSP/LDB mixtures. In Figure 5.9, relative viscosity η_r is plotted as a function of dimensionless shear stress τ^* at elevated ϕ_c for different sets of samples, where $\eta_r = \eta / \eta_w$ with viscosity of water η_w=9.1 ×10^{-4}Pa·s and $\tau^* = \tau < D >^3 / k_B T$.

At low ϕ_c, only shear thinning is detected with η_r decreasing to an apparent high shear stress plateau with increasing τ^*. We note here that zero-shear viscosity plateau was not observed due to long relaxation time making the zero-shear viscosity plateau out of the measurement range. For higher ϕ_c, shear thinning is interrupted at a certain shear stress τ_c^*, with discontinuous shear thickening occurring when $\tau^* > \tau_c^*$. This discontinuous thickening suggests that jamming occurs when applied shear rate is relatively large compared to the rate of particle diffusion. Increasing R in either SSP/LSP or SSP/LDB mixtures results in stronger shear thickening at the same total volume fraction. In addition, introducing small particles increases the volume fraction above which shear thickening is observed. We define ϕ_t as this transition point below which no shear-

thickening is observed and calculate this as the average of the two volume fractions bracketing the first observation of shear-thickening. Values are tabulated in Table 5.2.

ϕ_t is increased with R decreased for both SSP/LSP and SSP/LDB, suggesting increased jamming volume fractions. The onset of shear thickening is expected to be purely hydrodynamic and as such is expected to track increases in ϕ_m. For R=1, ϕ_t for LDB is larger than for LSP indicating increased maximum packing fraction for the dumbbells with L/D~1.3. In mixtures for R=0.71 and R=0.85, SSP/LDB have smaller ϕ_t than SSP/LSP, indicating that SSP/LSP mixtures have more efficient packing than SSP/LDB.

5.4 Conclusion

In this study, we explore the effects of shape anisotropy on dynamics of binary colloidal mixtures by studying linear rheology and yielding behavior of binary mixtures which are composed of small spherical particles (SSP) and large particles with shape varied. Two large particles are explored. One set of samples are spheres (LSP) while the second set of particle are weakly anisotropic particles with a length to diameter ratio of ~1.3 (LDB). Pair potentials are tuned by truncating the van der Waals attraction through coating the particles with a nonionic surfactant $C_{12}E_6$ and tuning the ionic strength to [I]=0.01M. Under these conditions, the large particles have weakly attractive interactions with a minimum ~-2k_BT in the potential energy while the interactions between small particles or unlike species are essentially those with excluded volume. Six different large particle volume fraction ratio, R, are studied for both types of mixtures. We find that the effects of shape anisotropy are observed only for R=0.71, R=0.85 and R=1.

Iso-elasticity curves generated from linear elastic moduli are plotted to compare the volume fractions at equal dimensionless elastic modulus. When R=1, at a fixed elastic

modulus, the volume fractions of the SSP/LDB occur at a higher ϕ_c than SSP/LSP. However, for R=0.71 and R=0.85, SSP/LDB reach the probe modulus at smaller ϕ_c than SSP/LSP. This phenomenon is explained as a consequence of small spheres hindering rotational relaxations of LDB. This phenomenon is absent when SSP is added into suspensions of LSP.

The yielding behaviors confirms our argument about rotational constrain of shape anisotropic particles, with enhanced second yielding observed in attractive glass formed by LDB than that in the attractive glass formed by LSP. Upon adding SSP (R=0.71 and R=0.85), these attractive glasses are destroyed more quickly for SSP/LDB than SSP/LSP which can be viewed as a consequence of the spheres changing rotational constrain.

When studying the discontinuous shear thickening behavior, for R=1, LDB has larger transition volume fraction for thickening than LSP, indicating larger maximum packing fractions of dumbbells over spheres. However, in mixtures with R=0.71 and R=0.85, the suspensions containing dumbbells have smaller ϕ_t than the suspensions containing spheres. This indicates that the mixtures of spheres have a larger maximum packing fraction than do mixtures of small spheres and large dumbbells.

5.5 Tables and Figures

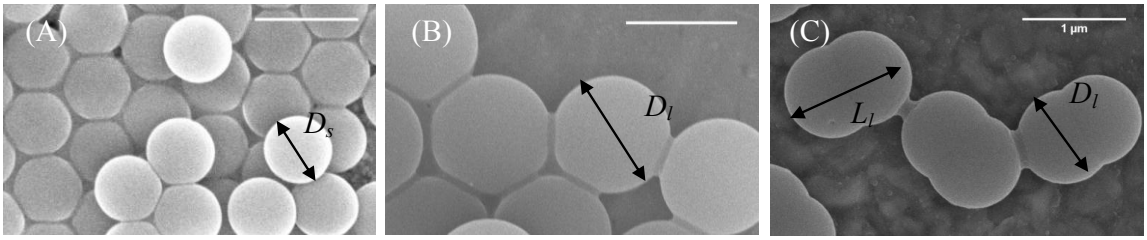

Figure 5.1 SEM pictures of (A) SSP, (B) LSP and (C) LDB. The scale bar has the length ~500nm in (A) and ~1μm in (B,C). The important size parameters are labelled in the pictures.

Table 5.1 Summary of volume average diameter <*D*>

R	0	0.29	0.5	0.71	0.85	1
SSP/LSP <*D*>/nm	330	369	412	488	592	1097
SSP/LDB <*D*>/nm	330	368	411	486	586	1026

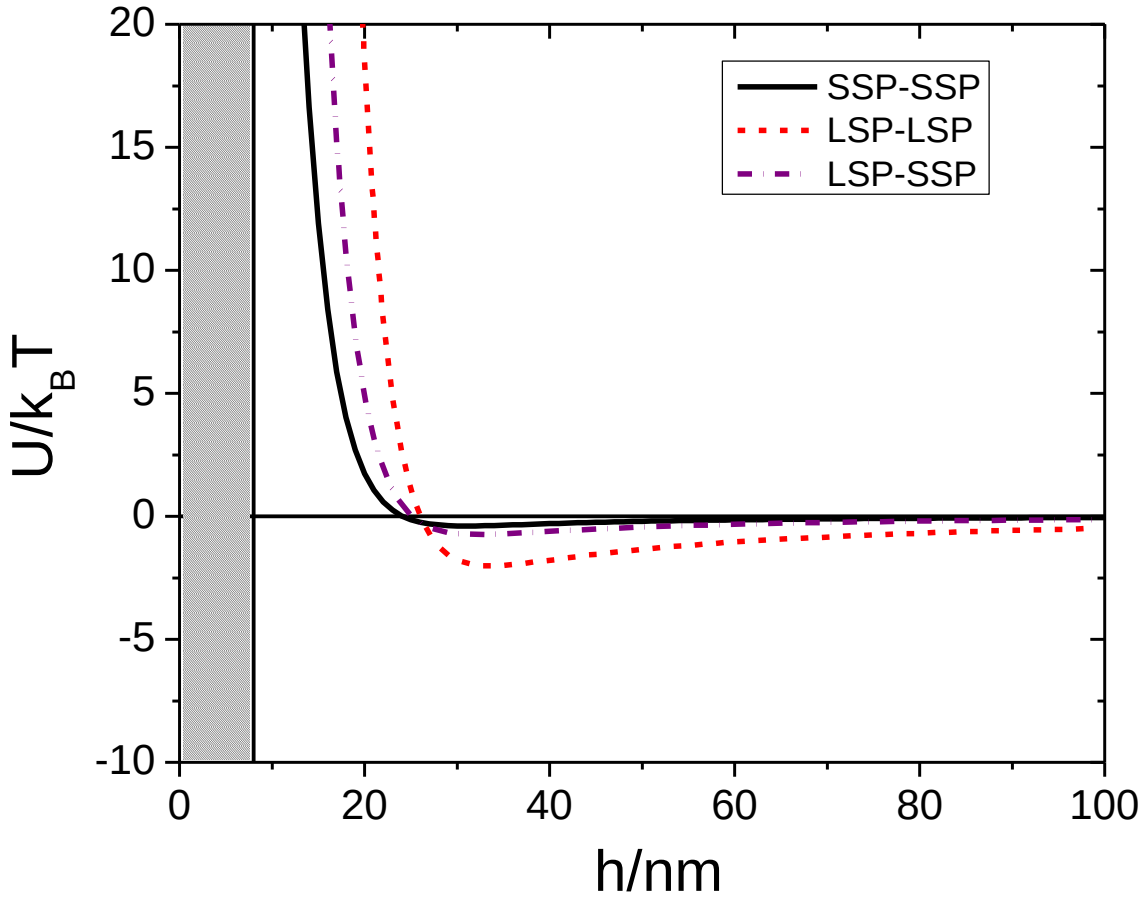

Figure 5.2 Interaction energy between SSP and SSP (solid curve), LSP and LSP (dashed curve), LSP and SSP (dash-dot curve), shaded area dotes steric interaction induced by non-ionic surfactant.

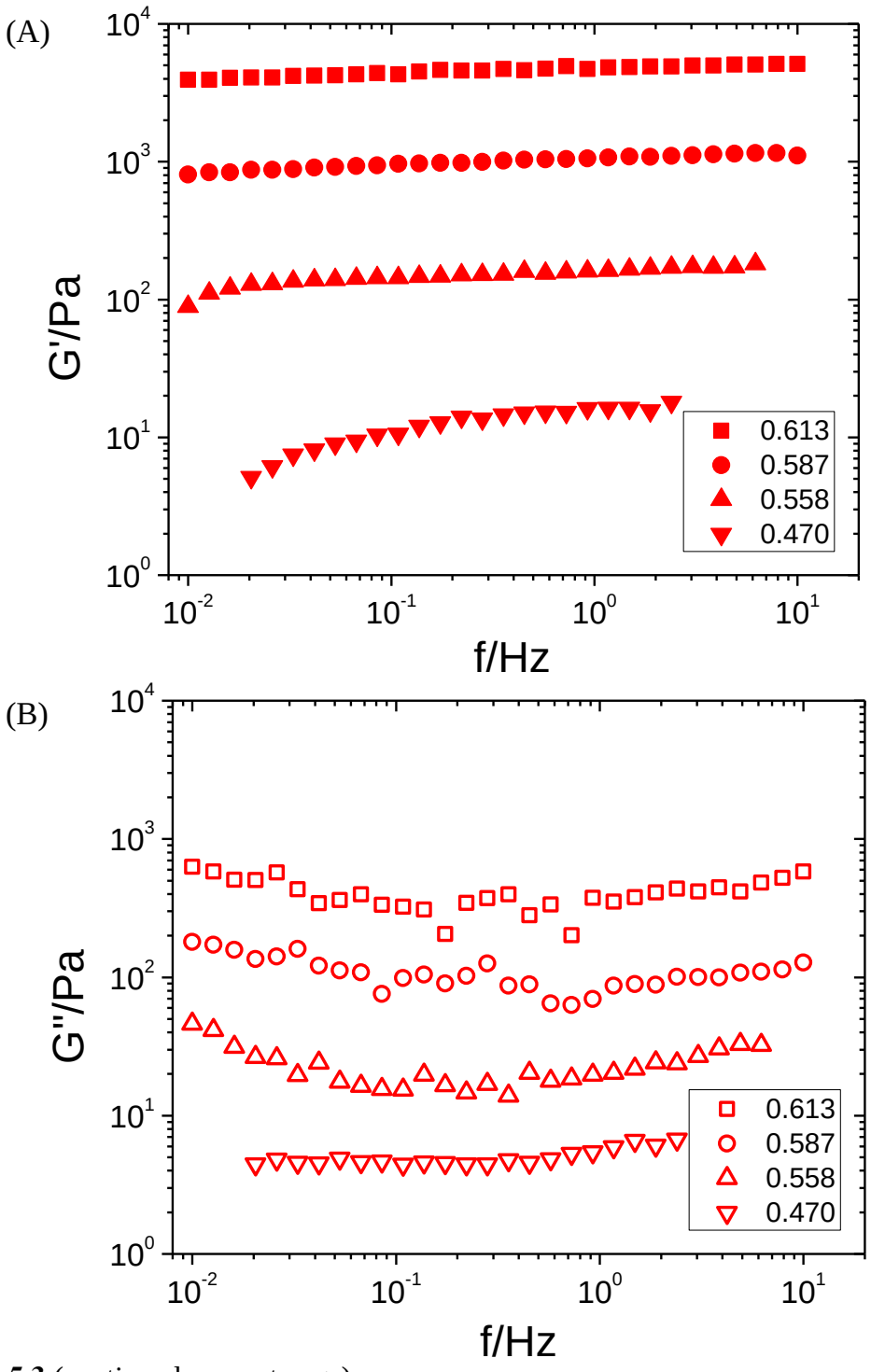

Figure 5.3 (continued on next page)

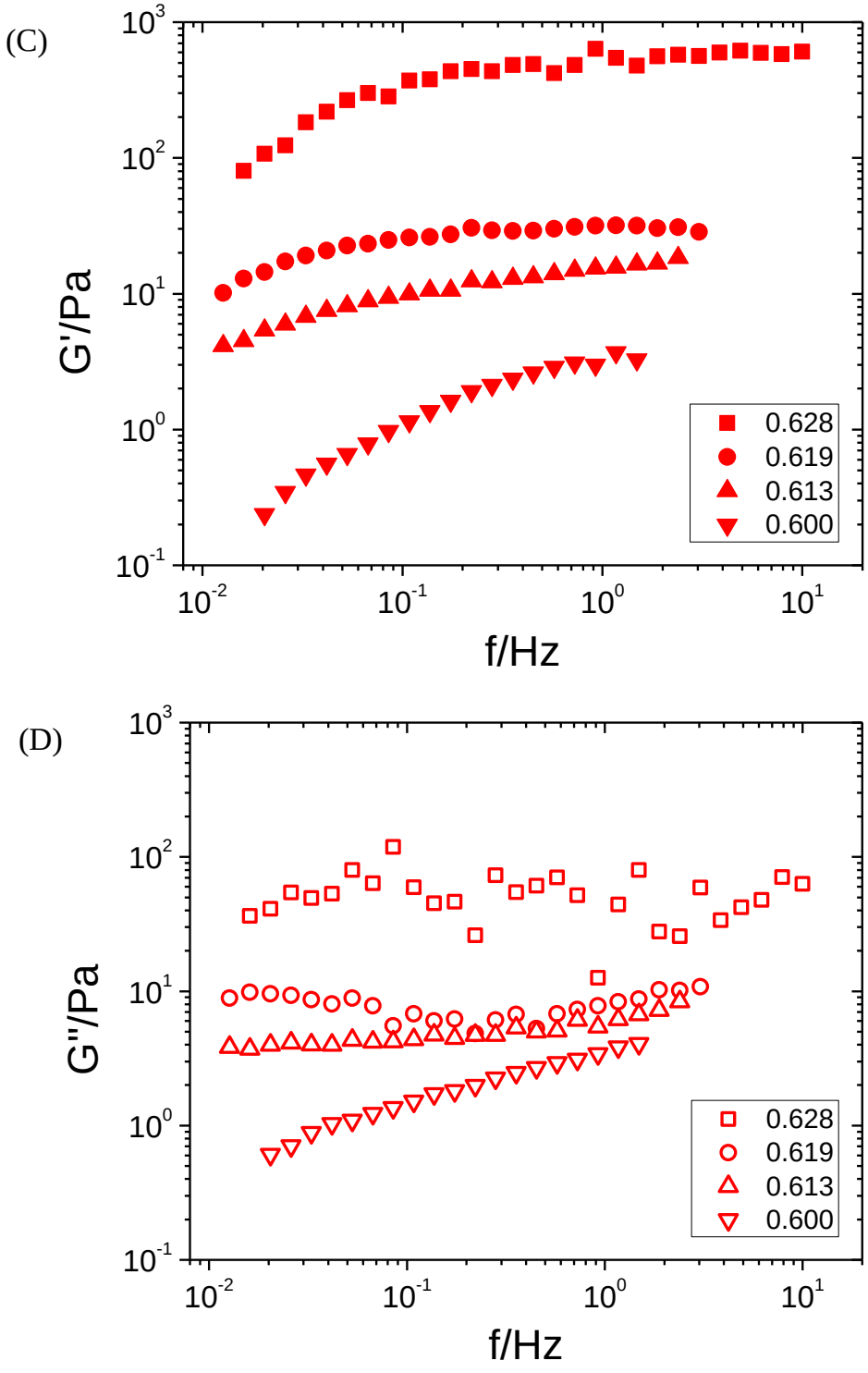

Figure 5.3 Elastic modulus *G'* (A, C) and viscous modulus *G"*(B, D) as a function of frequency *f* at different volume fractions for *R*=0 (A, B) and *R*=1(C, D) in SSP/LSP systems.

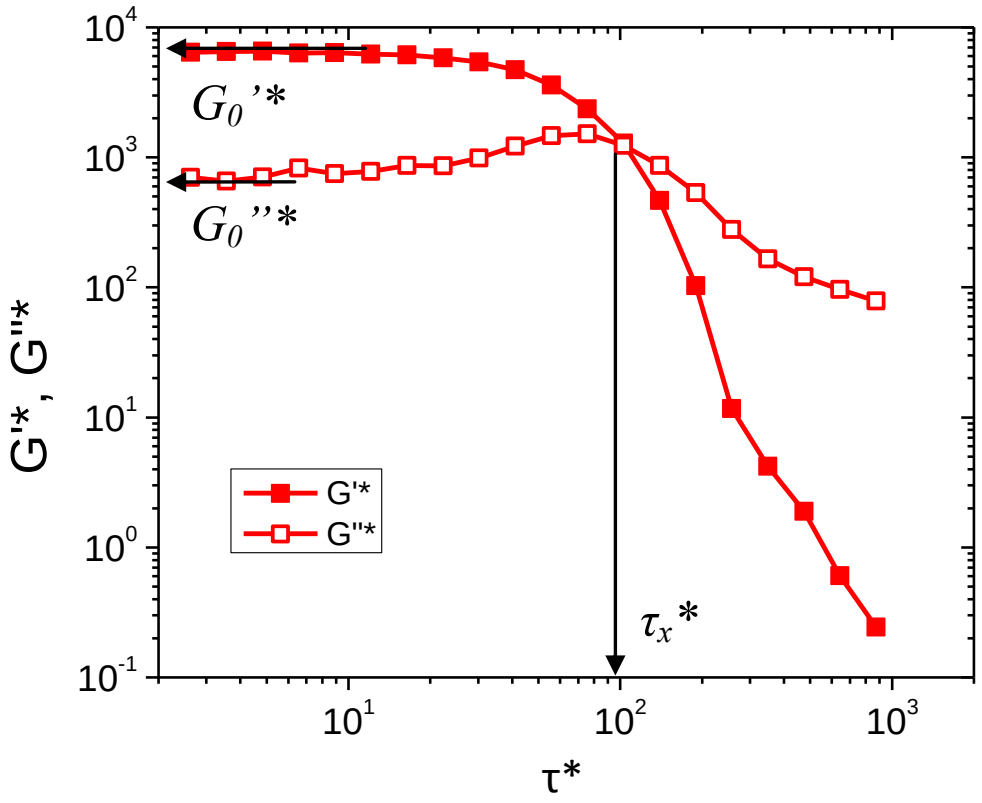

Figure 5.4 Dynamic stress sweep for SSP at ϕ_c=0.582 in the dimensionless parameter panel. The arrows illustrate the methods of determining linear elastic modulus G_0'*, linear viscous modulus G_0''* and yield stress τ_x*.

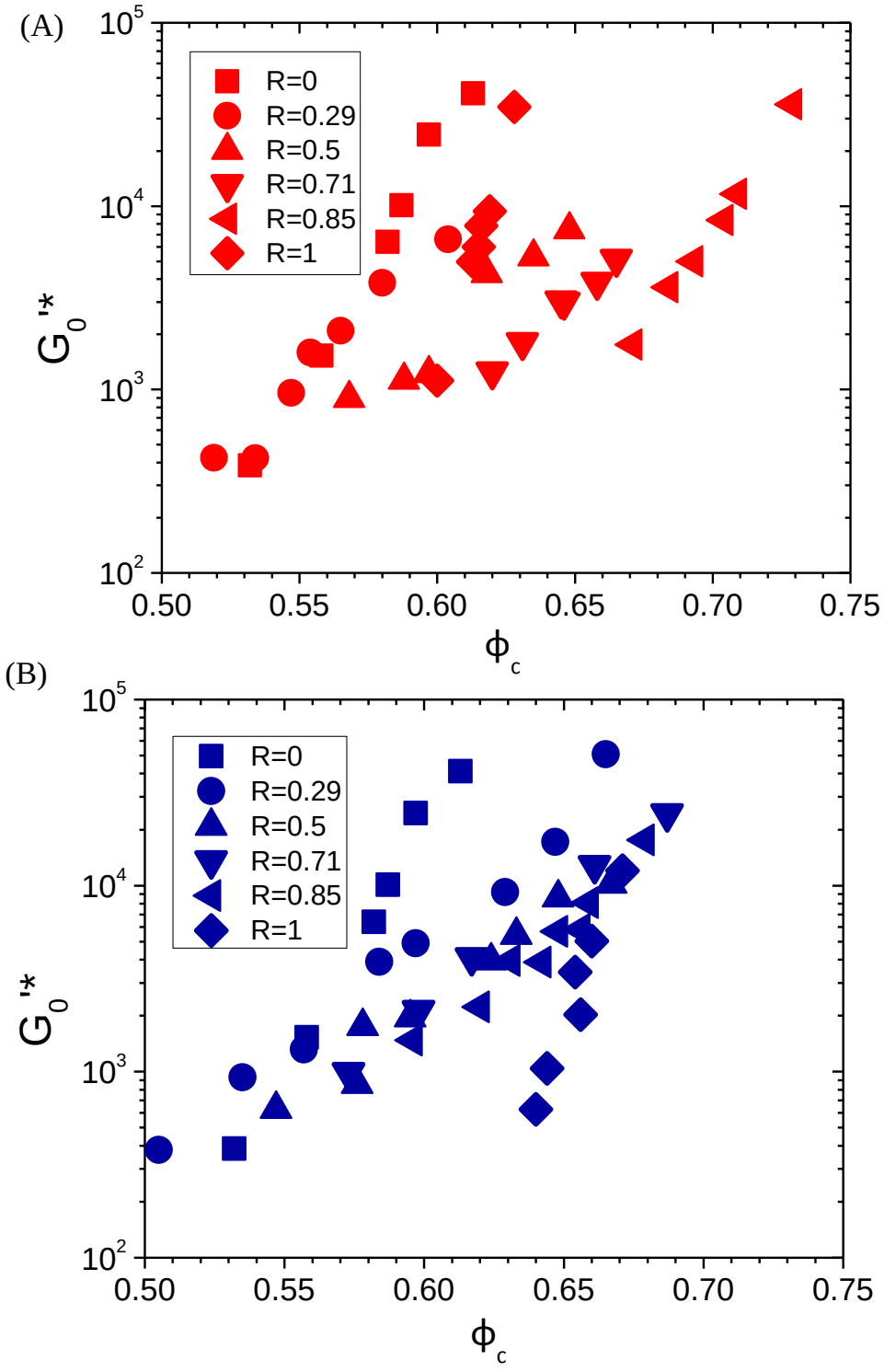

Figure 5.5 $G_0'^*$ plotted as a function of ϕ_c based on different large particle volume fraction ratio R for both binary systems (A) SSP/LSP and (B) SSP/LDB.

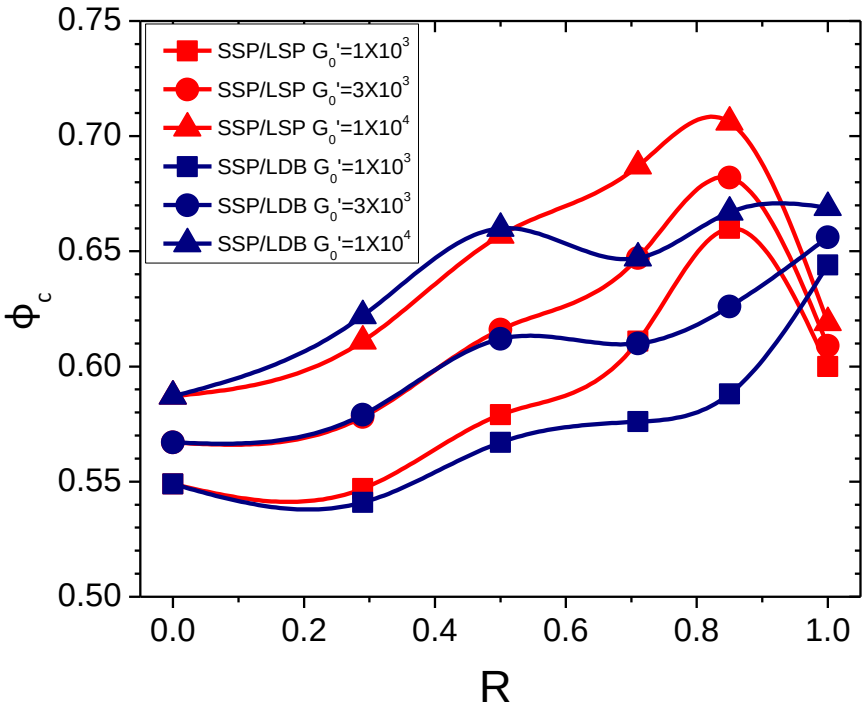

Figure 5.6 Iso-elasticity lines for SSP/LSP (red) and SSP/LDB (blue) based on three different G_0'* values.

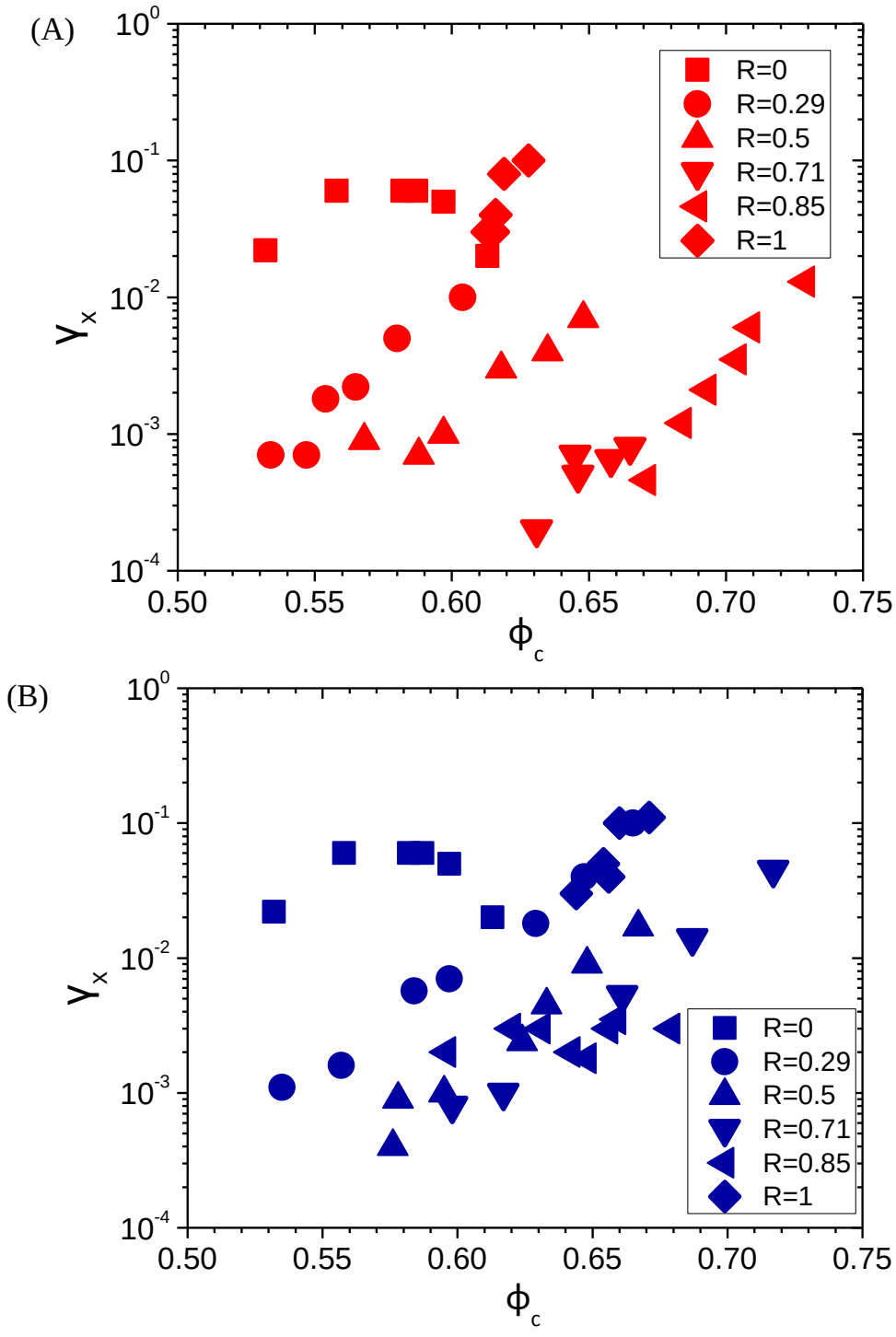

Figure 5.7 (continued on next page)

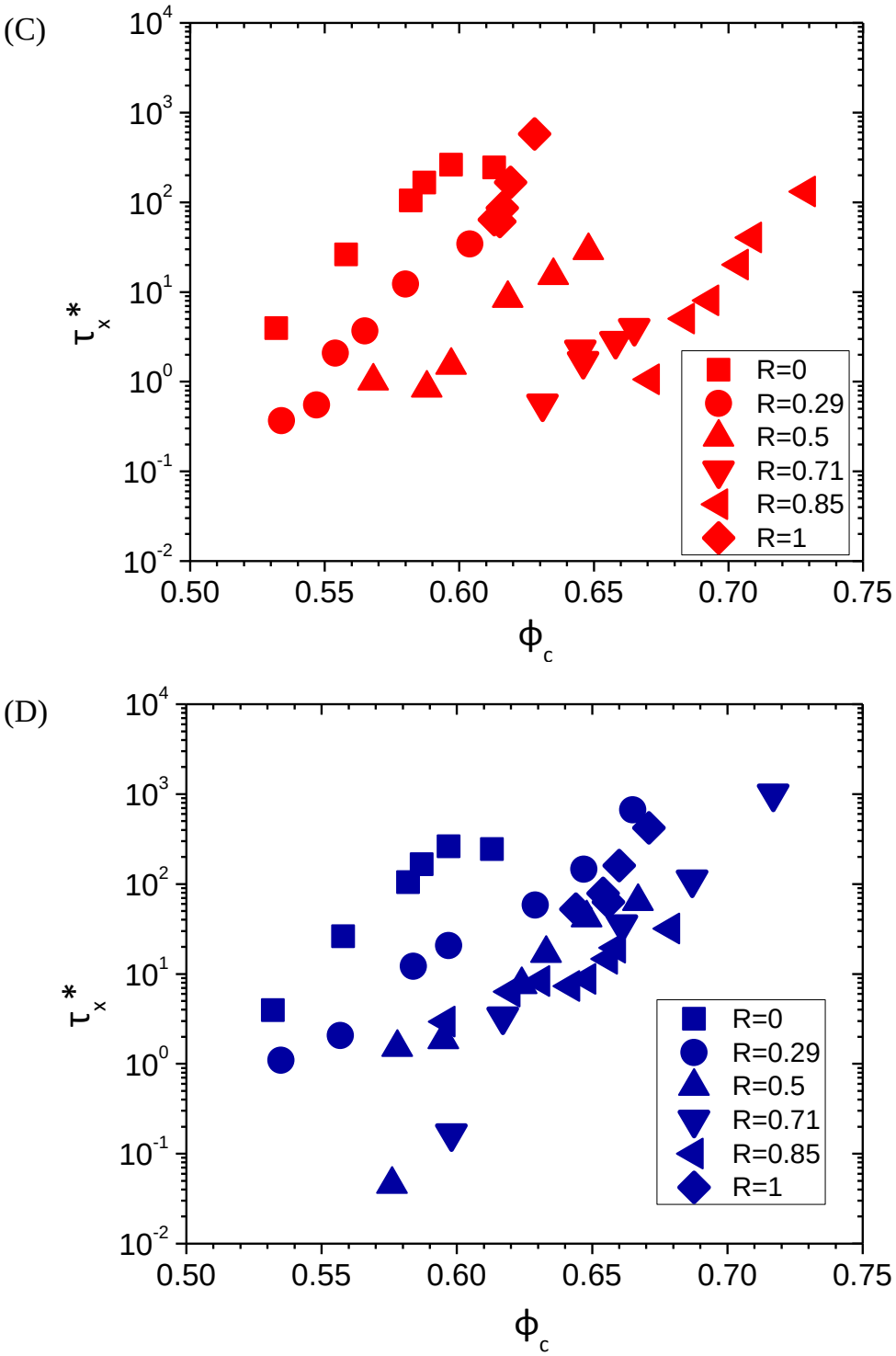

Figure 5.7 (continued on next page)

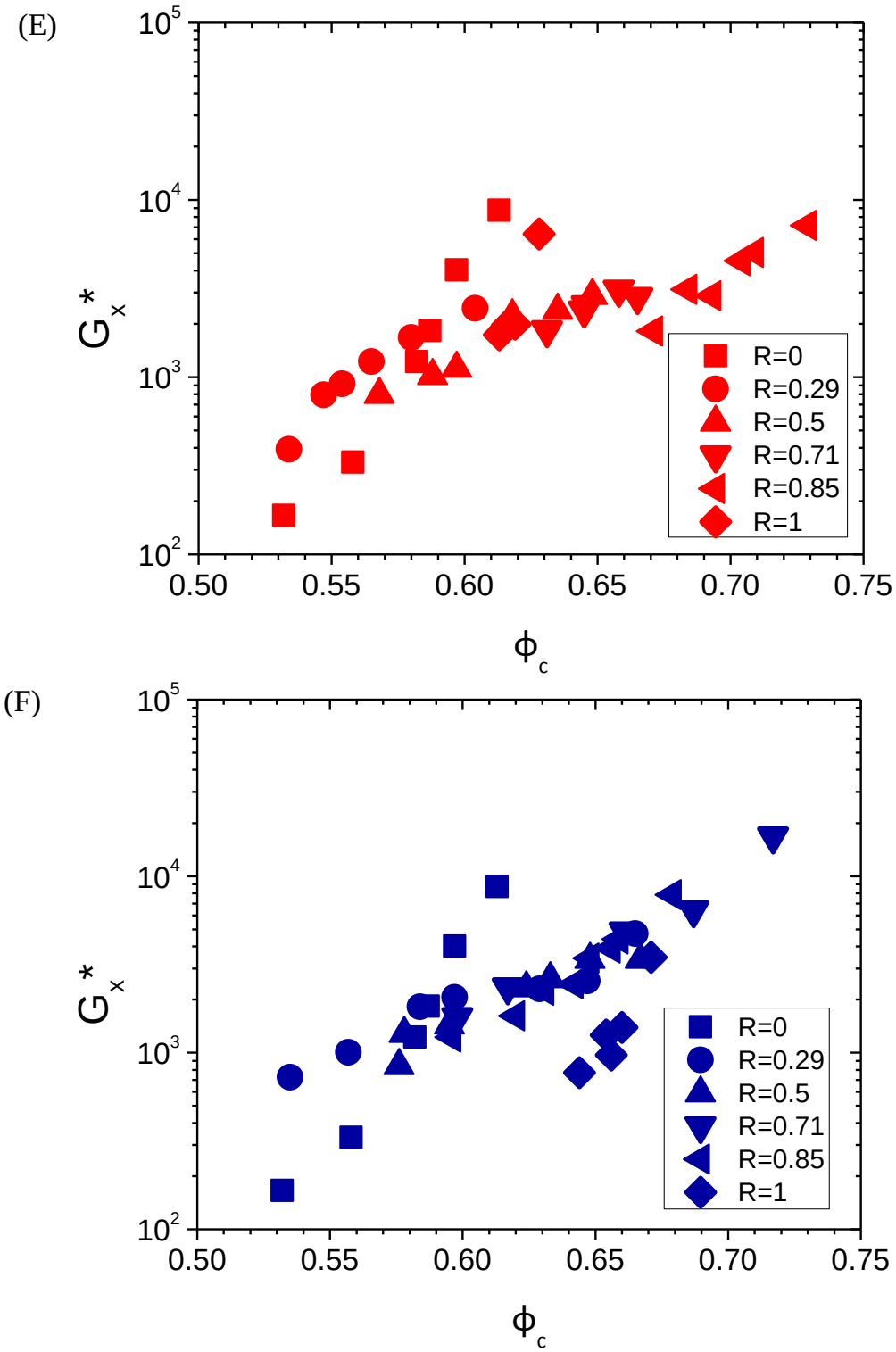

Figure 5.7 γ_x (A, B), τ_x^* (*C, D*) and G_x^* (E, F) are plotted as functions of ϕ_c for SSP/LSP (A, C, E) and SSP/LDB (B, D, F).

(A)

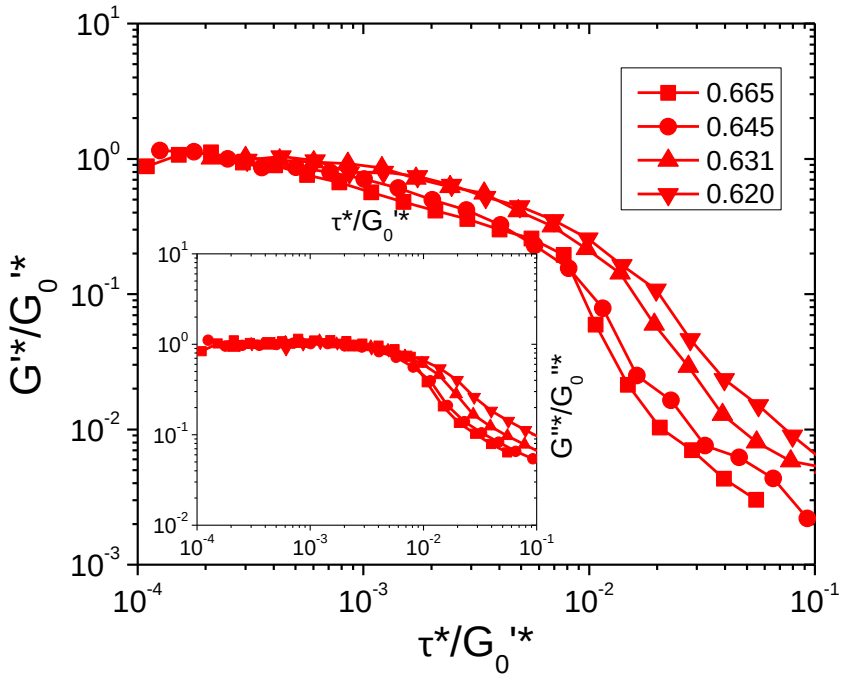

(B)

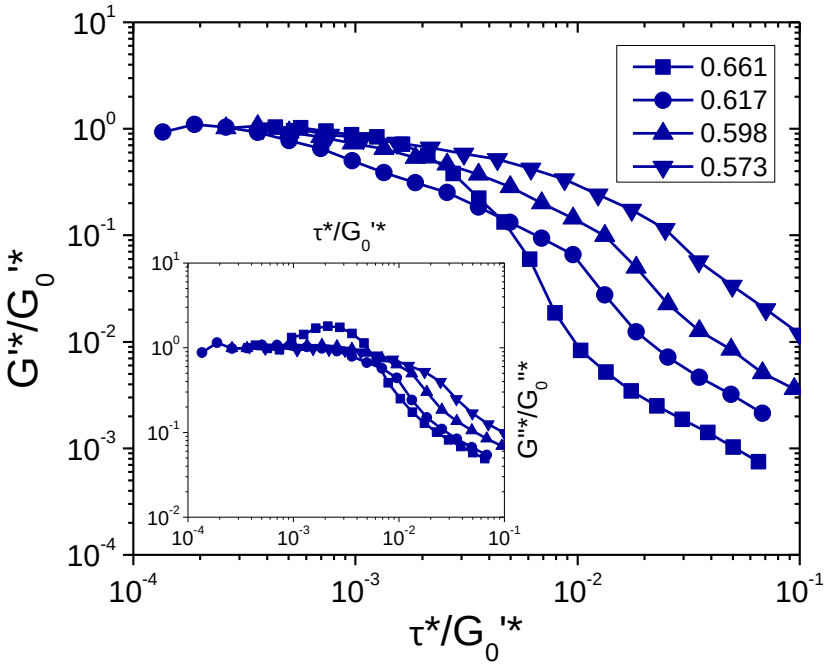

Figure 5.8 (continued on next page)

(C)

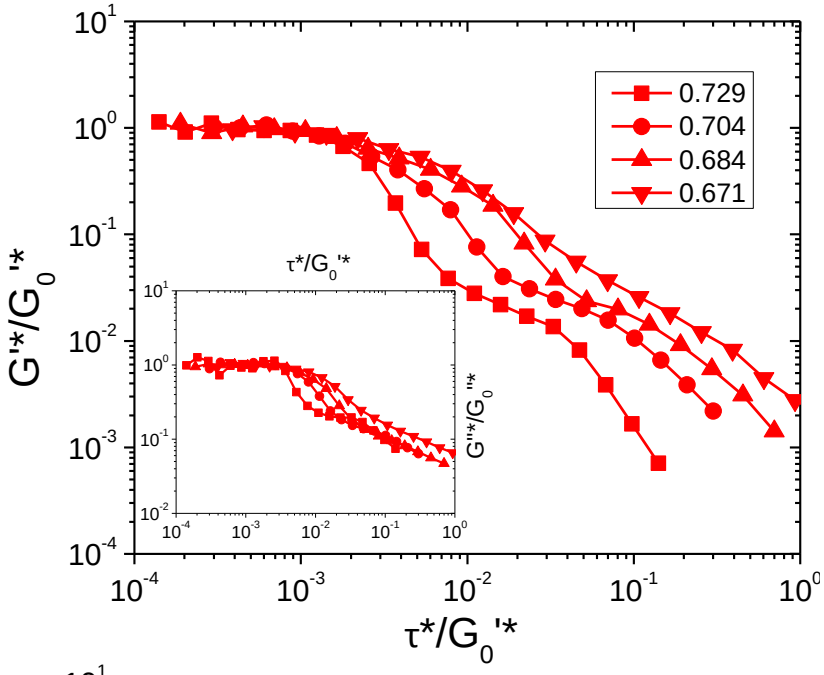

(D)

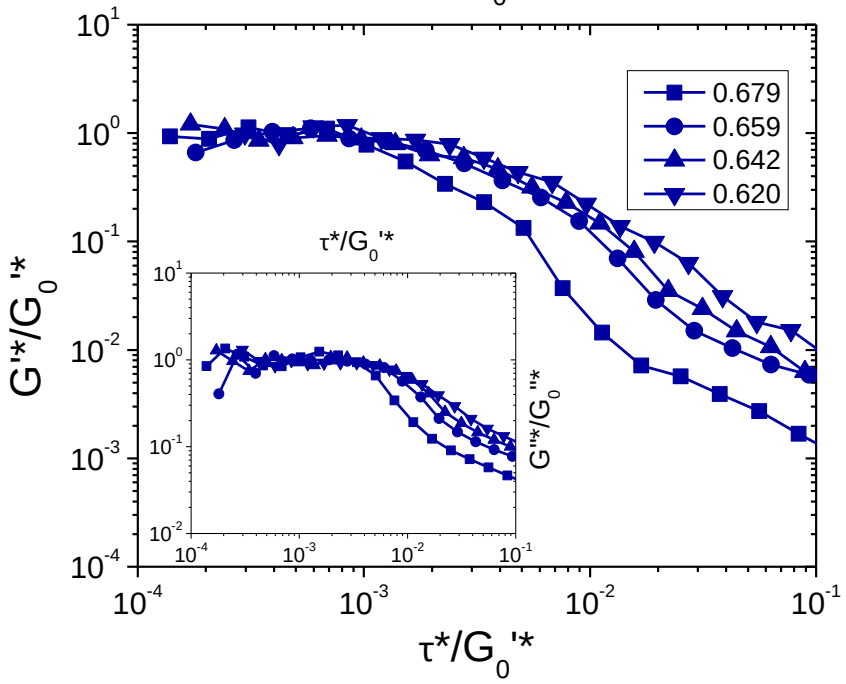

Figure 5.8 (continued on next page)

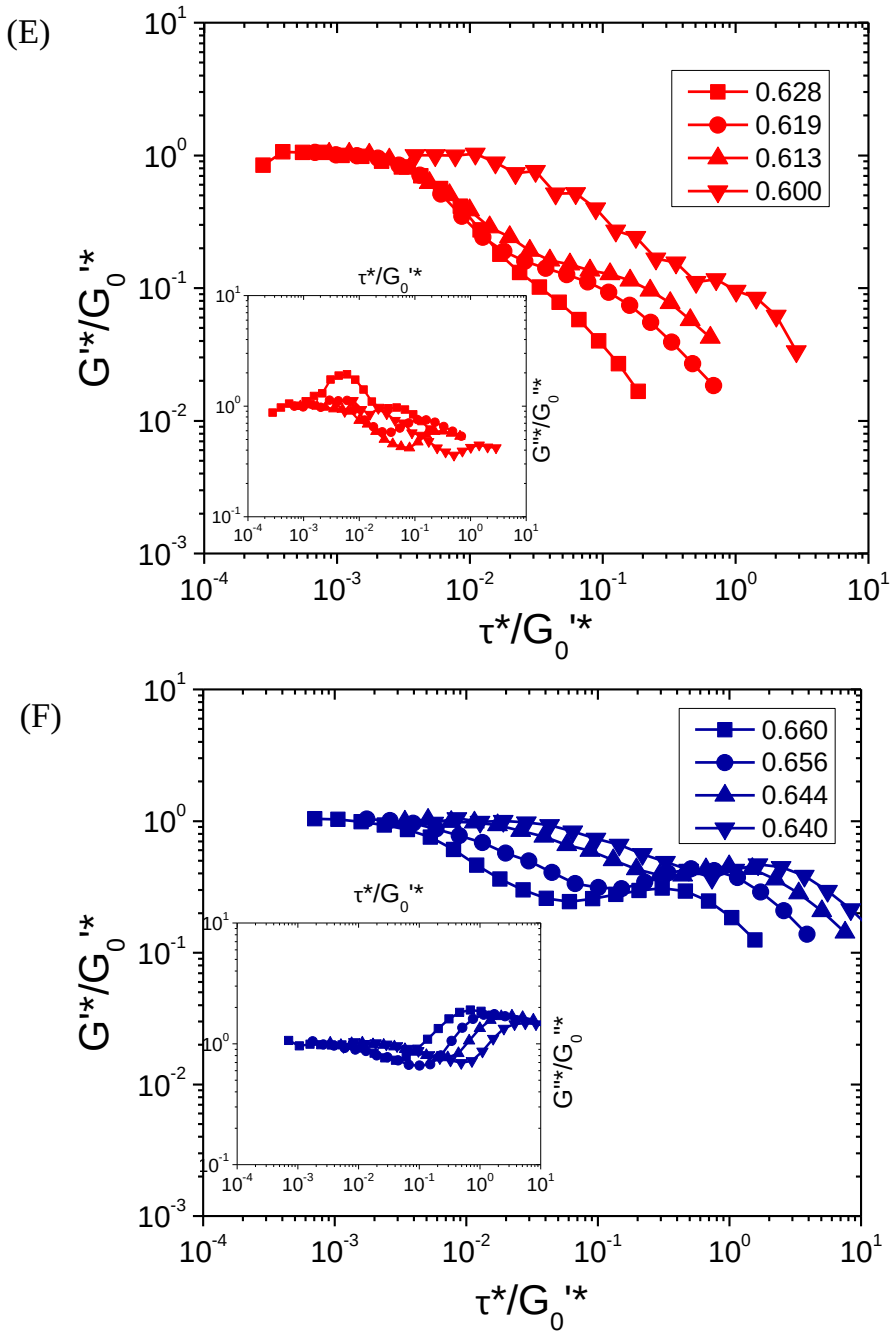

Figure 5.8 Dynamic stress sweeps at four representative volume fractions for SSP/LSP (A, C, E) and SSP/LDB (B, D, F) at R=0.71(A, B), R=0.85 (C, D) and R=1 (E, F). The main panels show $G'^*/G_0'^*$ as a function of $\tau^*/G_0'^*$ and the insets show $G''^*/G_0''^*$ as a function of $\tau^*/G_0'^*$.

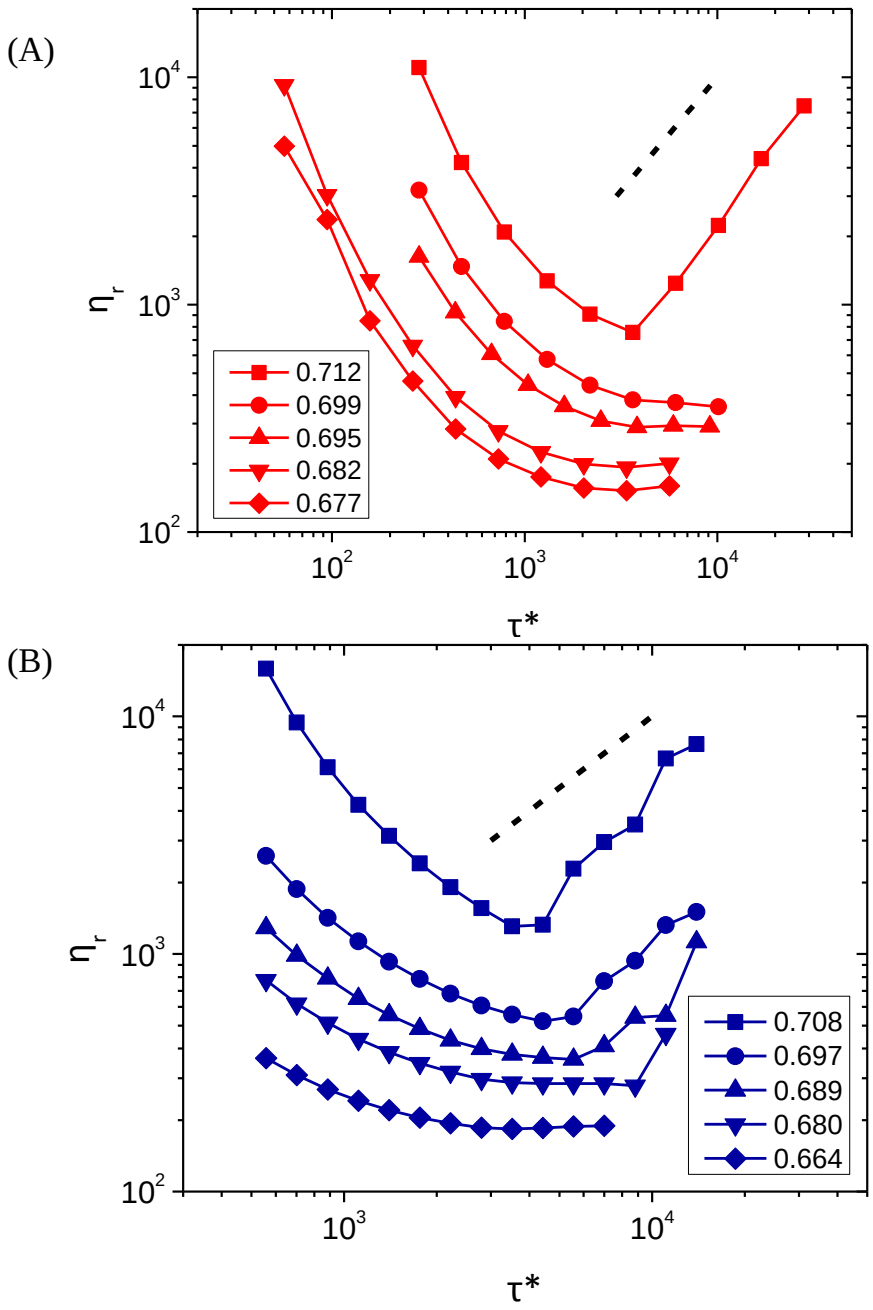

Figure 5.9 (continued on next page)

(C)

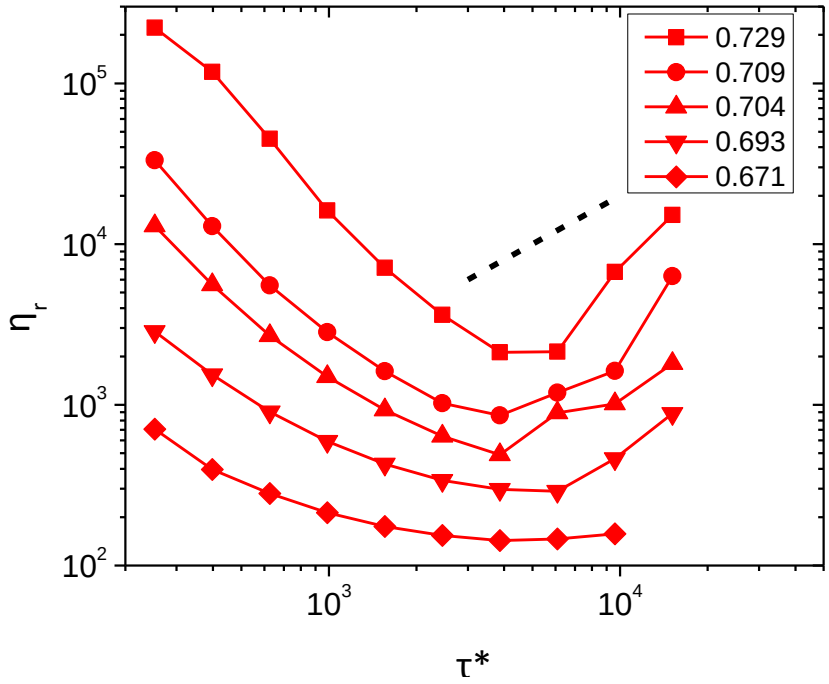

(D)

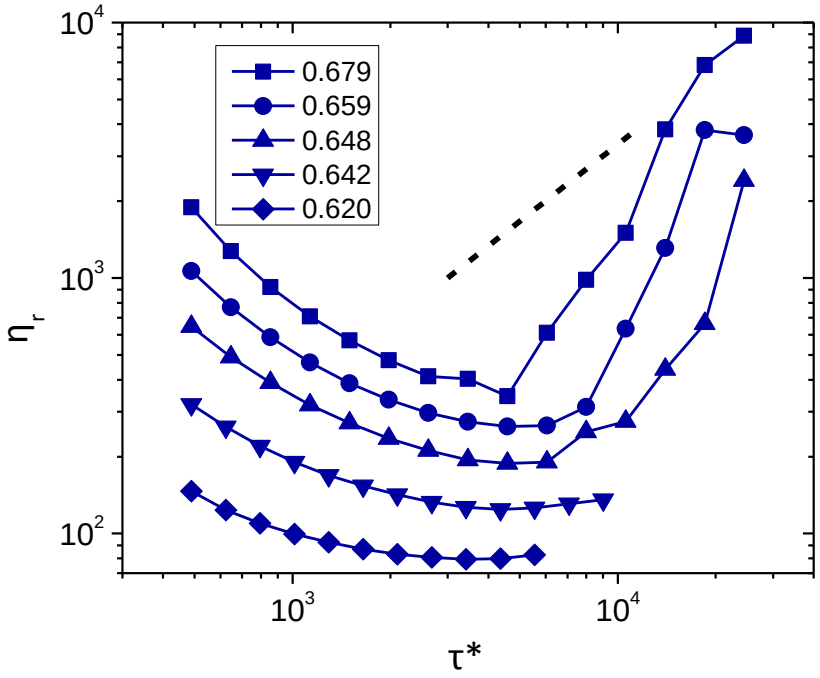

Figure 5.9 (continued on next page)

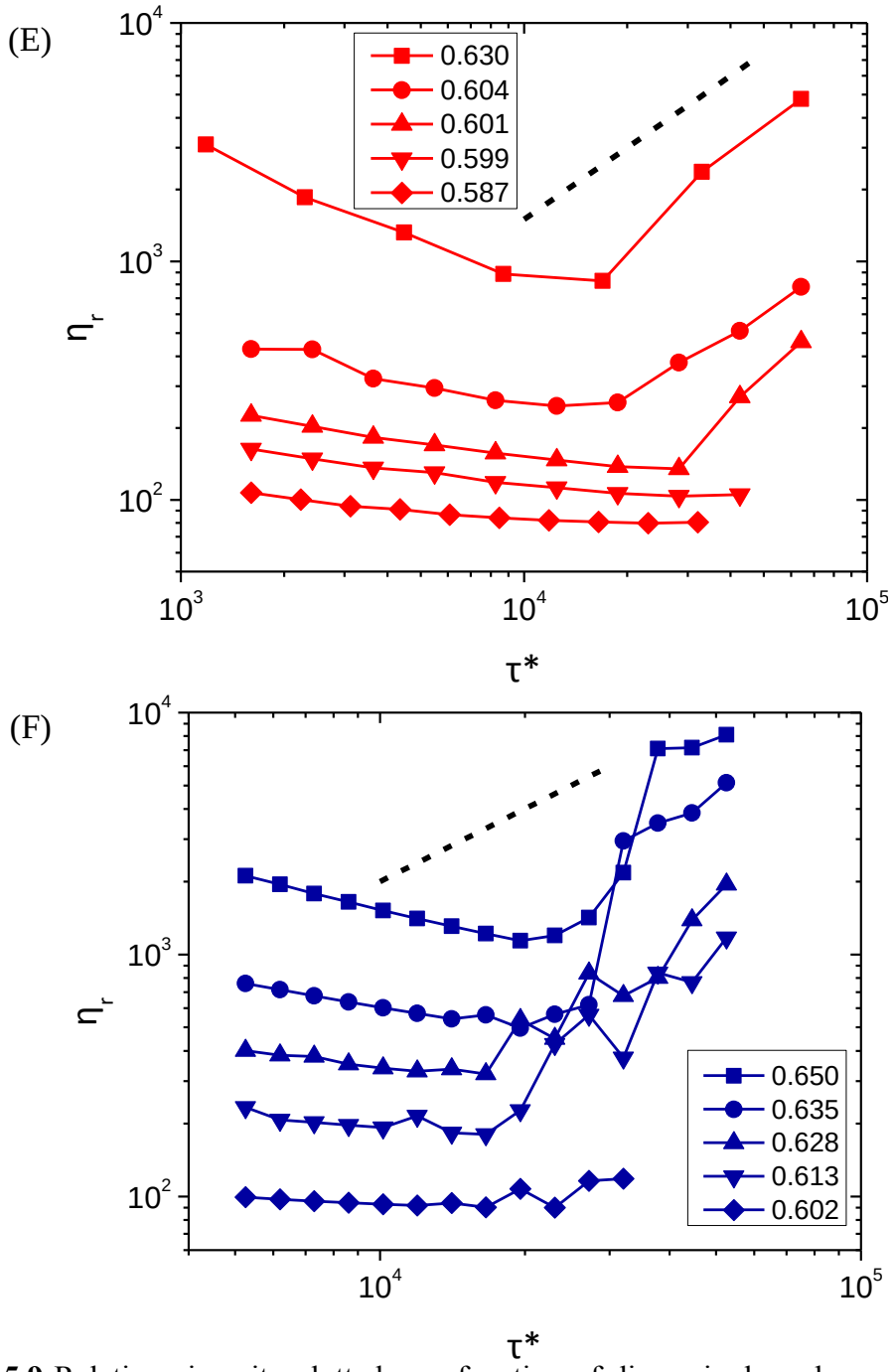

Figure 5.9 Relative viscosity plotted as a function of dimensionless shear stress at five representative volume fractions for SSP/LSP(A, C, E) and SSP/LDB(B, D, F) at R=0.71(A, B), R=0.85(C, D) and R=1(E, F). The dashed lines in different panels have a slope ~1.

Table 5.2 ϕ_t at different R for SSP/LSP and SSP/LDB

R	0.71	0.85	1
SSP/LSP ϕ_t	0.706	0.689	0.600
SSP/LDB ϕ_t	0.675	0.645	0.608

5.6 References

1. W. J. Hunt and C. F. Zukoski, *Journal of Colloid and Interface Science*, 1999, **210**, 343-351.
2. B. E. Rodriguez, E. W. Kaler and M. S. Wolfe, *Langmuir*, 1992, **8**, 2382-2389.
3. E. Stiakakis, B. M. Erwin, D. Vlassopoulos, M. Cloitre, A. Munam, M. Gauthier, H. Iatrou and N. Hadjichristidis, *Journal of Physics-Condensed Matter*, 2011, **23**, 234116.
4. S. K. Rhodes and J. A. Lewis, *Journal of the American Ceramic Society*, 2006, **89**, 1840-1846.
5. M. Pishvaei, C. Graillat, P. Cassagnau and T. F. McKenna, *Chemical Engineering Science*, 2006, **61**, 5768-5780.
6. M. Pishvaei, C. Graillat, T. F. McKenna and P. Cassagnau, *Journal of Rheology*, 2007, **51**, 51-69.
7. W. Gotze and T. Voigtmann, *Physical Review E*, 2003, **67**, 021502.
8. A. Mohraz, E. R. Weeks and J. A. Lewis, *Physical Review E*, 2008, **77**, 060403.
9. A. J. W. ten Brinke, L. Bailey, H. N. W. Lekkerkerker and G. C. Maitland, *Soft Matter*, 2007, **3**, 1145-1162.
10. A. J. W. ten Brinke, L. Bailey, H. N. W. Lekkerkerker and G. C. Maitland, *Soft Matter*, 2008, **4**, 337-348.
11. N. Doshi, G. Cinacchi, J. S. van Duijneveldt, T. Cosgrove, S. W. Prescott, I. Grillo, J. Phipps and D. I. Gittins, *Journal of Physics-Condensed Matter*, 2011, **23**, 194109.
12. D. Kleshchanok, A. V. Petukhov, P. Holmqvist, D. V. Byelov and H. N. W. Lekkerkerker, *Langmuir*, 2010, **26**, 13614–13621.
13. F. M. van der Kooij and H. N. W. Lekkerkerker, *Langmuir*, 2000, **16**, 10144-10149.
14. N. Yasarawan and J. S. van Duijneveldt, *Soft Matter*, 2010, **6**, 353-362.
15. R. Jadrich and K. S. Schweizer, *Journal of Chemical Physics*, 2011, **135**, 234902.
16. A. Galindo, A. J. Haslam, S. Varga, G. Jackson, A. G. Vanakaras, D. J. Photinos and D. A. Dunmur, *Journal of Chemical Physics*, 2003, **119**, 5216-5225.
17. S. D. Peroukidis, A. G. Vanakaras and D. J. Photinos, *Journal of Materials Chemistry*, 2010, **20**, 10495-10502.
18. J. C. Baird and J. Y. Walz, *Journal of Colloid and Interface Science*, 2007, **306**, 411-420.
19. R. Zhang and K. S. Schweizer, *Physical Review E*, 2009, **80**, 011502.
20. R. Zhang and K. S. Schweizer, *Journal of Chemical Physics*, 2012, **136**, 154902.

21. R. C. Kramb and C. F. Zukoski, *Journal of Rheology*, 2011, **55**, 1069-1084.
22. K. N. Pham, G. Petekidis, D. Vlassopoulos, S. U. Egelhaaf, W. C. K. Poon and P. N. Pusey, *Journal of Rheology*, 2008, **52**, 649-676.
23. G. Petekidis, D. Vlassopoulos and P. N. Pusey, *Faraday Discussions*, 2003, **123**, 287-302.
24. G. Petekidis, D. Vlassopoulos and P. N. Pusey, *Journal of Physics-Condensed Matter*, 2004, **16**, S3955-S3963.
25. R. C. Kramb and C. F. Zukoski, *Journal of Physics-Condensed Matter*, 2011, **23**, 035102.
26. H. K. Chan and A. Mohraz, *Physical Review E*, 2012, **85**, 041403.
27. H. R. Sheu, M. S. Elaasser and J. W. Vanderhoff, *Journal of Polymer Science Part a-Polymer Chemistry*, 1990, **28**, 629-651.
28. A. M. Homola, M. Inoue and A. A. Robertson, *Journal of Applied Polymer Science*, 1975, **19**, 3077-3086.
29. T. Y. Jiang and C. F. Zukoski, *Langmuir*, 2012, **28**, 6760-6768.
30. E. B. Mock, H. De Bruyn, B. S. Hawkett, R. G. Gilbert and C. F. Zukoski, *Langmuir*, 2006, **22**, 4037-4043.
31. W. B. Russel, D. A. Saville and W. R. Schowalter, *Colloidal Dispersions*, Cambridge University Press, Cambridge, 1989.
32. M. Tripathy and K. S. Schweizer, *Physical Review E*, 2011, **83**, 041406.
33. T. Y. Jiang and C. F. Zukoski, *Macromolecules*, 2012, **45**, 9791-9803.
34. B. J. Anderson and C. F. Zukoski, *Macromolecules*, 2008, **41**, 9326-9334.
35. G. Yatsenko and K. S. Schweizer, *Journal of Chemical Physics*, 2007, **126**.
36. T. R. Kirkpatrick and P. G. Wolynes, *Physical Review A*, 1987, **35**, 3072-3080.
37. R. C. Kramb, R. Zhang, K. S. Schweizer and C. F. Zukoski, *Physical Review Letters*, 2010, **105**, 055702.
38. T. Jiang and C. F. Zukoski, *Soft Matter*, 2012, **9**, 3117-3130.
39. G. Yatsenko and K. S. Schweizer, *Physical Review E*, 2007, **76**, 041506.
40. R. C. Kramb, R. Zhang, K. S. Schweizer and C. F. Zukoski, *Journal of Chemical Physics*, 2011, **134**, 014503.
41. B. J. Anderson and C. F. Zukoski, *Journal of Physics-Condensed Matter*, 2009, **21**, 285102.
42. N. Koumakis, A. B. Schofield and G. Petekidis, *Soft Matter*, 2008, **4**, 2008-2018.
43. M. Laurati, S. U. Egelhaaf and G. Petekidis, *Journal of Rheology*, 2011, **55**, 673-706.
44. D. C. Viehman and K. S. Schweizer, *Journal of Chemical Physics*, 2008, **128**, 084509.

Chapter 6. Dynamic Localization and Shear Induced-Hopping of Particles: a Way to Understand the Rheology of Dense Colloidal Dispersions

6.1 Introduction

There are many strategies to tune the mechanics and state behaviors of dense colloidal dispersions including varying the particle softness,[1] shape,[2] strength of particle interactions[3] and varying particle size distribution.[4] Despite these many variables, the flow properties of the resulting suspensions often show similarities. These include liquid-like behavior at low volume fractions and the development of dynamic yield stresses at high volume fractions. In detail, these suspensions show storage moduli, G', that are lower than loss moduli, G'' at low volume fractions while $G'>G''$ at high volume fractions. Often when the suspensions take on solid like behavior ($G'>G''$), loss moduli show a characteristic separation of time scales indicating that self diffusion occurs rapidly for small distances but becomes sluggish for long diffusion distances. The transition volume fraction characterizing a transition from liquid-like behavior to solid-like behavior can be tuned with particle variables from very low (<0.01) to values in excess of 0.58.[5] Developing an understanding of the physical processes that underlie the commonality of suspension flow behavior remains a challenge.

The ability to drive Brownian particles to aggregate has historically been a subject of intense study leading theory of colloidal stability in the years preceding and after the development of Derjaguin, Landau, Verwey and Overbeek (DLVO) theory.[6] This theory balances van der Waals attractions with electrostatic repulsions and predicts the ionic strength where attractions overwhelm repulsions and make particles rapidly aggregate. Under conditions where particles aggregate, suspensions develop elastic plateaus and shear thinning properties and other characteristic of gels. These observations led to the

development of heuristic models for characterizing shear properties of a suspension with a Bingham constitutive equation where stress, τ, is related to shear rate, $\dot{\gamma}$, through $\tau = \tau_B + \eta_{PL}\dot{\gamma}$ where the high shear rate behavior is viscous characterized by a viscosity η_{PL}, and the suspensions show a Bingham yield stress τ_B in the limit as $\dot{\gamma}$ goes to zero. The Bingham yield stress is characterized by the stress required to overcome the maximum restore force in pair potential and rupture the bonds which hold aggregates together. In the elastic floc model developed originally by Hunter an colleagues[7, 8] τ_B is linked to the volume fraction and pair potential based on the DLVO theory through:[9, 10]

$$\tau_y = \frac{\phi_c K(\phi_c)}{24\pi D_c}\left(\frac{A}{H^2} - \frac{24\pi\varepsilon_0\varepsilon\kappa\zeta^2}{1+e^{\kappa H}}\right) \tag{6.1}$$

Here ϕ_c is the volume fraction, $K(\phi_c)$ is the mean coordination number determined by volume fraction, D_c is the particle diameter. A is the Hamaker constant, H is the particle surface separation, ε is relative dielectric constant, ε_0 is the dielectric constant for vacuum, κ is the Debye parameter and ζ is the surface potential of particle. Of significance this theory describes yielding in term of a structural parameter $K(\phi_c)$ that links the yield stress to suspension microstructure and particle properties of Hamaker coefficient, the distance of closest approach, particle surface potential, and through the Debye parameter, the suspending fluid ionic strength. Experimental tests of Equation (6.1) show remarkable success when normalized by the maximum value of the yield stress with the zeta-potential varied systematically by changing pH for amphoteric mineral particles.[9] As originally developed, this theory also relates the elastic modulus of the suspension of the second derivative of the pair potential when the particles are held at a distance H.

While successful for aqueous mineral suspensions, this approach fails to capture the absolute magnitude of the yield stress and its volume fraction dependence and holds little useful information for systems where the suspensions experience non DLVO pair potentials. Numerous studies have been done to relate volume fractions dependencies of yield stress and elastic modulus to microstructure. In particular, following the observation that aggregated suspensions take on fractal microstructures and the fractal dimension of the suspension varies depending on the mechanism of aggregation, numerous models were developed linking volume fraction dependence to the fractal dimension of the suspension.[11-13] These approaches link mechanics to mesoscopic structures relating elasticity to bending elasticities of aggregates. The elemental spring unit remains that of a pair but the volume fraction dependency of the modulus changes with the number of pairs per unit volume which is altered by the way particles are arranged in flocs and in the suspension. Again these models have limited success but fail to capture the point where suspensions take on solid-like properties and fail as the volume fraction at the gel point approaches close packing- i.e., when the suspensions experience largely excluded volume interactions.

A separate approach to understanding gelled suspension mehcanics approaches gelation from the perspective of equilibrium dynamics where particles are assumed to be trapped in a pair potential well and the time constant for rearrangement of nearest neighbors is governed by diffusion out of the potential energy landscape in which the particles are trapped.[14] If a suspension is driven by a stress to deform in a steady state manner, these models predict that the potential energy barrier is lowered as described by Eyring for the viscosity of liquids.[15] In this model, the pair potentials set the potential

energy landscape and establish barriers over which particles must diffuse to for the suspension to undergo steady deformation. The viscosity is related to properties as $t_{hop}G'$ where G' is typically taken as the elastic modulus at rest and t_{hop} is the time required for particles to diffuse our of a potential energy minimum. The hopping time is related to a barrier height which in turn is modified by an external stress. As stress is increased, the diffusion barrier and hopping time is decreased resulting in shear thinning behavior. If the barrier height for diffusion is not sensitive to the applied stress, the stress becomes independent of shear rate, giving rise to a dynamic yield stress plateau. At a sufficiently large stress, the viscous dissipation of the liquid destroys the structure and the suspension develops a high shear rate Newtonian viscosity.

In this approach, there is thus a low shear rate viscosity governed by the rate of self diffusion over the potential energy barrier that exists at rest. Shear thinning occurs when the stress drives the suspension at a rate faster than it can hop ($\dot{\gamma}_1 t_{hop}(0) \sim 1$, where $t_{hop}(0)$ is determined by the barrier height at zero shear rate) a plateau stress, τ_y, and finally a second characteristic shear rate where $\tau_y \sim \dot{\gamma}_2 \eta_\infty$ where η_∞ is the high shear rate plateau viscosity. If the applied stress lowers the potential barrier, the stress increases proportionally to $\dot{\gamma}^p$. Here the shear-thinning exponent, p, characterizes the ability of the applied stress to alter hopping rate of particles which are trapped in the pair potential wells. The deeper the potential well is, the closer p is to zero. This model establishes that $t_{hop} \sim K(\phi_c)\exp(-U_{\min}/k_B T)$, where $K(\phi_c)$ is related to the number of nearest neighbors and saturates at high volume fraction and U_{min} is the minimum value of the pair potential. When applied to electro-rheological fluids where particles experience dipolar attractions, the concepts of this model were shown to largely capture the electric field dependence of

the flow properties of Brownian electrorheological suspensions.[16] This model is important because it provides a natural link from the characteristics of Brownian hard sphere suspensions that set the viscosity of the suspension at high shear rates or low strength of attraction to a yield stress through increases in the absolute value of U_{min}. Of interest is the work of Baxter-Drayton and Brady, $K(\phi_c)$ is linked to the value of the pair distribution function which is seen to be a saturating but monotonically increasing function of the strength of attraction for particles experiencing highly anisotropic interactions.[14]

These approaches then link elasticity, yield stress and characteristic shear rates to pair potential, continuous phase viscosity, volume fraction, and particle diffusivity. The Bingham model is applicable for strongly interacting particles (high volume fraction and or large strengths of attraction) under conditions where $\dot{\gamma}_1 t_{hop}(0) > 1$. In applying these approaches, there has been an unambiguous link established between the strength of inter-particle attractions and the magnitude of the yield stress and gel elasticity. The models often fail at high volume fraction or low strength of attractions and are not designed to predict the onset of gel-like flow properties. In particular the models fail to capture the onset of solid-like flow characteristics in suspensions of hard spheres where particles experience only volume exclusion interactions and yet display flow properties very similar to gels of Brownian particle produced with attractions. When attractive interactions are thought to be required for elasticity and yielding, hard spheres represent a pathological end point. Nevertheless, by associating mechanical properties of gels with the Brownian nature of the particles, the models establish that, given enough time systems can approach equilibrium. Thus for large absolute values of U_{min}, $\dot{\gamma}_1$ may not be

measurable and p will approach 0. However, elasticity and shear thinning are associated with particles being localized by deformation with diffusion over localization barriers.

The mechanical properties of hard sphere systems have been investigated for many years with particular attention to behavior at the approach to random close packing and the origin of a glass transition in molecular systems. Molecular glasses are distinguished from colloidal glasses because they are typically formed by lowering temperature which simultaneously extracts thermal energy out of the system and thus lowers hopping rates and typically increases the systems density of volume fraction. In colloidal systems, altering the pair potential independent of the number density of particles in the suspension is routinely achieved. Only relatively recently has the understanding of colloidal systems been used to explore glass formation in molecular systems. Nevertheless, one of the first theories of the divergence of the molecular liquid viscosity on approach to a glass transition was that involving loss of free volume resulting in the increase in the viscosity to be written:

$$\Delta\eta_0 = C\exp\left(\frac{\gamma\phi_c\phi_m}{\phi_m - \phi_c}\right) \tag{6.2}$$

where C and γ are constants, and ϕ_m is maximum volume fraction. This concept has been applied to explain the hard sphere rheology in experiments.[17, 18] The free volume model suggests that the divergence of zero shear rate viscosity is associated with approaching maximum packing fraction for hard sphere suspension. However, it was not constructed to describe the shear-thinning behavior above glass transition volume fraction and does not capture the effects of the attractions.

More recent theoretical progress has been made by looking at force correlations between particles and recognizing the system dynamics is modified at high volume

fraction by correlated forces. These ideas are central to the development of idealized[19] and naive mode coupling theories[20] and have been extended to descriptions of flow in the development of dynamic localization theory (DLT) which rewrites force correlations that control particle diffusion in terms of a dynamical potential barrier that particles must cross to experience long range diffusion.[21] DLT is based on equilibrium descriptions of suspension microstructure arguing that the suspension remains at equilibrium approaching random close packing. The relaxation times required for a disturbed system to achieve equilibrium after being disturbed become longer as volume fraction is raised and diverge at random close packing. Nevertheless, the theory is based on suspensions always remaining at equilibrium up to the point where long range diffusion ceases due to geometric constraints imposed by hard core particles. This condition is set as the volume fraction where the pair distribution at contact diverges.

The power of this theory comes in its predictions of the onset the rapid rise in zero-shear viscosity at elevated volume fraction, the absolute viscosity as a function of volume fraction, the long range diffusion time and the dependence of the modulus on volume fraction for experimental hard sphere suspensions.[22] The theory predicts that the glass transition depends of the deformation time scale used to probe the system and that when attractions are turned on between hard particles in a state above ϕ_x, initially diffusivity increases and viscosity decreases while at stronger attractions the systems become re-localized and form gels. This re-entrant behavior is observed experimentally.[23, 24] Of critical interest here is that DLT predicts the onset of a shear stress plateau where stress depends in a power law manner of shear rate with exponent p, where p moves towards zero as volume fraction or strength of attraction are raised.

Predictions of transport properties in dynamic localization theory are based on equilibrium pair distribution functions (or the corresponding structure factors) and are thus calculable from the knowledge of particle volume fraction and pair potential. A key feature of DLT is the prediction of a localization length, r_L, which describes the extent of motion of a particle due to self diffusion when time scales is shorter than t_{hop}. The prediction of r_L is based on force correlations. At all volume fractions below the cross-over volume fraction, particles are free to diffuse throughout the volume of the suspension. Above critical volume fractions, force correlations alter the dynamics of particle diffusion such that there is a separation of time scales. At short times particles become localized and diffuse within a distance r_L at a rate that is much larger than the rate of diffusion over distances larger than the particle size. By rewriting these fluctuating forces in terms of a dynamical potential, $F(r)$, an intuitive picture emerges where particles become localized within a dynamical potential well where they diffuse freely but long-range diffusion requires activated transport over a dynamical potential barrier. The barrier height is termed F_B and this barrier appears at ϕ_x and diverges at ϕ_m, the maximum volume fraction for the suspension. A self-consistent set of equations can be written allowing calculation of r_L, ϕ_x, $F(r)$, and transport properties in terms of the suspensions equilibrium structure factor. Being based on pair correlations, the dynamical localization theory contains no information about the fractal dimension of aggregated systems. The integrals over structure factor which determine r_L and F_B are heavily weighted to large wave vector or, in real space, to small pair separations suggesting that transport properties of glasses and gels can be understood without resorting to fractal descriptions of aggregate and suspension structures.

In summary, DLT provides a consistent picture of suspension dynamics capturing the role of hard cores, longer range pair potentials, and volume fraction on the dynamics of suspensions. There are many emerging studies testing these ideas using well defined suspensions of spheres with well understood pair potentials. Here we are interested in exploring the ability of this theory to provide a framework for understanding the flow properties of more complicated compositions where the pair potential is not well understood and the particle size distribution is not monodisperse. In developing an understanding of DLT to predict the properties of complicated suspensions, we note that this theory defines critical volume fractions of ϕ_x, and ϕ_m and a critical stress τ_{abs} which is the stress required to eliminate the dynamical potential barrier allowing free diffusion. DLT relates properties to the localization length which is directly measurable with the plateau elastic modulus:

$$\frac{G_p' D_c^3}{k_B T} = A\phi_c \left(\frac{D_c}{r_L} \right)^2 \tag{6.3}$$

where A is an order 1 constant. Our goal is to take this understanding and develop methods for characterizing the flow properties of dense suspensions experiencing excluded volume and attractive interactions where we argue that from flow properties far from the zero shear rate limit we can extract ϕ_x, and the zero shear rate viscosity.

Experimentally we work with a system containing silica particles dispersed in low molecular weight polyethylene glycol melts where particle interactions are poorly understood. As a result, we seek methods of gaining understanding of flow properties and pair interactions from generalization of DLT. Specifically, we search the origin of shear stress plateau and use the magnitude of absolute yield stress and shear elasticity to predict the entropic barrier height, F_B. By studying the volume fraction dependence of barrier

height in different systems with varying pair interactions and size disparity conditions, we build relations between F_B and rheological properties including but not limited to the absolute yield stress. We also demonstrate the effects of F_B and t_{hop} on yielding investigated in oscillatory stress sweep experiments. We compare our results with other experimental systems to prove the wide applicability of the method.

In Section 6.2, we introduce the experimental method of sample preparation and rheology measurement. In Section 6.3, we introduce the basic information of DLT with our strategy in data analysis. In section 6.4, we present and discuss the main results, which are compared with theoretical predictions and other experimental systems. In section 6.5, we draw conclusions.

6.2 Experimental Methods

6.2.1 Sample Preparation

Monodispersed silica particles are synthesized by method that is developed by Stöber[25] and extended by Bogush et al.[26] Two different sizes are prepared with d_l=612±20nm (referred to as large particles) and d_s=127±7nm (referred to as small particles) with which binary mixtures will be made. The product particles are suspended in ethanol solution containing water and ammonia hydroxide. The resulting suspension is concentrated to a mass fraction ~0.20 by heating up the suspension to evaporate the solvent and drive off the ammonia. Following previous studies,[27] we chose to work with polyethylene glycol with MW~400 (PEG400, Sigma-Aldrich) at T=25℃ and polyethylene glycol with MW~2000 (PEG2000, Sigma-Aldrich) at T=75℃ as the polymer melts. Both polymer are Newtonian fluid at the condition where we study with viscosity of 0.10 Pa s. The two concentrated silica particle suspensions with a fixed mass

fraction ratio are mixed with PEG (with eventual large particle volume fraction ratio R=0, 0.29, 0.5 for PEG400 and R=0, 0.29, 0.5, 0.71 for PEG2000 which guarantee observation of shear stress plateau and high-shear viscosity) and the resulting suspension is placed into vacuum oven with temperature kept above T_m of PEG to remove ethanol.[27]

6.2.2 Rheology

Flow measurements were carried out on a C-VOR Bolin rheometer with a cone and plate geometry. The cone diameter was 20mm with a 4 ° angle.

Continuous stresses are applied to study the viscosity as a function of applied shear stress. Oscillatory stresses are applied to measure elastic modulus G' and viscous modulus G'' as functions of frequency ω in the frequency sweep experiments. In this work, the maximum strain was held at $\gamma \leq 0.01$ to ensure that only linear properties are reported. The samples are well behaved showing no thixotropy and the properties reported are independent of shear-history.

Volume average diameter $\langle D \rangle$ is used for obtaining dimensionless parameters as introduced in previous study. [28] Also according to previous study, here we note that silica particles are essentially hard spheres in PEG400 and attractive in PEG2000 with the interaction energy captured by square well potential which has well depth ~$2k_BT$ and well width ~$6R_g$.[29]

6.3 Dynamic Barriers and Activated Hopping

In DLT, the nonlinear response of colloidal dispersion is a consequence of changes to single-particle dynamics when a suspension is exposed to an external constant deformation force f. Therefore the non-equilibrium dynamic energy is modified as following:[21, 30]

$$F(r) = F(r;\tau = 0) - fr \tag{6.4}$$

Here the microscopic force on a single tagged particle f is transferred from the macroscopic shear stress τ as

$$f = D_c^2 \frac{\tau}{\phi_c^{2/3}} \tag{6.5}$$

When τ=0, the non-equilibrium energy $F(r; \tau=0)$ is composed of two parts as

$$F(r) = F_0 + F_I \tag{6.6}$$

The first term F_0 favors the fluidity and the second term F_I denotes the contribution of particle interactions. When the particles are localized, at small displacement r, the approximations can be made:

$$\partial F_0 / \partial r = -3/r, \qquad \partial F_I / \partial r \propto r \tag{6.7}$$

From this three characteristic lengths are expected in the effective energy as a function of displacement: $r_L < R^* < r_B$. At r_L, a local minimum develops in $F(r)$ and a maximum is developed at r_B. As a result, $\frac{\partial F(r)}{\partial r}\Big|_{r=r_L, r_B} = 0$. In addition there is an inflection at R^* where $\frac{\partial^2 F(r)}{\partial r^2}\Big|_{r=R^*} = 0$.

The barrier height F_B is defined as the energy required for particles hopping out of the dynamic energy local minimum such that $F_B = F(r_B) - F(r_L)$. Assuming r/D_c<<1, we make the assumption here that

$$F_B = (r_B - r_L)\frac{\partial F(r)}{\partial r}\Big|_{r=R^*} \tag{6.8}$$

When applying an external shear stress, the $F(r)$ changes according to Equation (6.4) with the R^* unchanged and r_L and r_B moving towards R^*. With increasing stress $F(r_B)$

becomes smaller and $F(r_L)$ becomes larger such that the barrier which controls the rate of long distance diffusion decreases in magnitude. When an absolute yield stress τ_{abs} is achieved with $f=f_{abs}$, both r_L and r_B merge into the inflection point and trapping barrier disappears, so $\frac{\partial^2 F(r;\tau=\tau_{abs})}{\partial r^2}\Big|_{r=R^*}=0$ and $\frac{\partial F(r;\tau=\tau_{abs})}{\partial r}\Big|_{r=R^*}=0$. At this point, with the external force unapplied, we expect that

$$\frac{\partial F(r)}{\partial r}\Big|_{r=R^*} = f_{abs} = D_c^2\frac{\tau_{abs}}{\phi_c^{2/3}} \tag{6.9}$$

Assuming that $r_L < R^* < r_B < 0.5D_c$, the approximation in Equation (6.7) such that $r_B r_L = R^{*2}$ demonstrating that R^* is correlated with r_L in a consistent manner. For hard spheres, $R^* = r_L + 0.18\gamma_{abs}D_c$ with $\gamma_{abs} \approx 0.25$ for volume fractions substantially larger than ϕ_x (γ_{abs}=0 at ϕ_x and quickly increases to a value near 0.25 when increasing ϕ_c further).[30] For systems experiencing short range attractions $r_L / D_c << 1$ and γ_{abs} may be a function of pair potential. Estimates of the yield strain can be derived from measurements of the strain where *G'=G"* in strain sweep experiments. These strains are often seen to pass through a maximum and are measured in the range of 0.05-0.2 for both volume exclusion and attractive systems. As a result, we expect $R^* = r_L + AD_c$ where A is a weak function of volume fraction and pair potential as predicted for hard spheres. It has been predicted in many systems where particle shape and strength of pair attractions are varied that γ_{abs}=0 is a good approximation for $\phi_c > \phi_x + 0.04$.[31] Combining these assumptions with Equation (6.3), we can estimate the barrier height F_B when τ=0 when obtaining macroscopic rheology $G_p'^*$ and τ_{abs}^* as following

$$\frac{F_B}{k_B T} = \frac{\tau_{abs}^*}{\phi_c^{2/3}}\left[0.09 + 0.00266\left(\frac{G_p'^*}{\phi_c}\right)^{1/2}\right] \tag{6.10}$$

In ultra-local limit development for hard spheres, when no external shear stress is applied, the barrier height is strongly correlated to D_c / r_L as[32]

$$F_B / k_B T = (3/\pi)^{2/3}(D_c / r_L) \tag{6.11}$$

Here, r_L is for the zero shear stress. Thus when the external shear stress is zero, we expect that F_B is correlated with G_p' when we combine Equation (6.11) with Equation (6.3) according to

$$F_B / k_B T = (G_p'^* / 0.58\phi_c)^{1/2}(3/\pi)^{2/3} \tag{6.12}$$

Thus a correlation between τ_{abs}^* and $G_p'^*$ is also derived as

$$\tau_{abs}^* = \phi_c^{2/3} / [0.0707(\phi_c / G_p'^*)^{1/2} + 0.00209] \tag{6.13}$$

The mean barrier hopping time for a single particle is correlated with the barrier height according to Kramer's theory as[22]

$$\frac{t_{hop}}{t_0} = \frac{2\pi g(D_c)}{\sqrt{K_0 K_B}} \exp(F_B / k_B T) \tag{6.14}$$

Here, t_0 is elementary Brownian diffusion time. K_0 and K_B are the absolute magnitudes of the harmonic curvatures of the minimum and barrier of $F(r)$.[30]

The analysis above summarizes conclusions drawn from DLT showing the effects of applied shear on the ability of particles to hop the dynamical energy barrier. At an applied stress of zero the hopping time is controlled by F_B and the system has a zero shear rate viscosity determined from Green-Kubo approach that $\eta_0 - \eta_\infty \cong G'\tau_{hop}$. With increasing

stress, F_B decreases, the hopping time is decreased and the viscosity is lower. At the absolute yield stress F_B decreases to zero and the suspension viscosity is η_∞.

In this study, we work with colloidal mixtures where the pair interactions are varied and the ratio of large and small particle volume fractions are changed. Our goal is to test concepts developed for systems of uniform particles on suspensions with less well defined characteristics. We expect ϕ_x to remain sensitive to pair interactions as well as particle size distribution. We introduce the scaled volume fraction $\phi^*=(\phi_m-\phi_x)/(\phi_m-\phi_c)$ to capture changes in flow properties as volume fraction is varied. This variable is designed to diverge as ϕ_c approaches ϕ_m and thus we expect transport properties to diverge as ϕ^{*d}, where d depends of the rheological parameter investigated. For example, for spheres and weakly anisotropic particles, the plateau modulus G_p^* diverges as ϕ^{*4} while for hard spheres F_B diverges as ϕ^{*2}, which is stronger than Doolittle or free volume model.[2, 32] In addition we find that ϕ_m/ϕ_x is nearly constant for a variety of systems with volume exclusive interactions when the size distribution is varied.[28] In previous studies we have developed method of determining ϕ_x and ϕ_m. ϕ_x is determined by determining p in the relationship of $\tau \propto \dot{\gamma}^p$ in the yield stress plateau region of suspensions. We find that p starts close to unity at low volume fraction and drops to close to zero at high volume fractions and that there is a universal curve when p is plotted as a function of ϕ_c/ϕ_x where p has a value ~0.5 when ϕ_c/ϕ_x=1. Maximum packing fractions are determined as extrapolations to the point where high frequency viscosities $\eta_{r,\infty}'$ diverge. We expect $\eta_{r,\infty}'\sim\phi^*$ and ϕ_m is chosen to achieve this result. For the systems studied here, a summary of volume average diameter $\langle D\rangle$, ϕ_m and ϕ_x is presented in the Table 6.1.

To understand the absolute yield stress, a continuous shear is applied on the colloidal dispersion to obtain flow curves (τ vs. $\dot{\gamma}$) with an example showing in the Figure 6.1. When increasing volume fraction to a sufficiently high value, a stress plateau is develop between two characteristic shear rates $\dot{\gamma}_1$ and $\dot{\gamma}_2$. Below $\dot{\gamma}_1$, a zero shear viscosity plateau is achieved thus $\tau \propto \dot{\gamma}$ indicating applied shear rate is smaller than inverse of relaxation time. Above $\dot{\gamma}_2$, a high shear viscosity plateau is achieved thus $\tau \propto \dot{\gamma}$ again indicating applied shear rate is larger than inverse of the characteristic time for Brownian diffusion. Between $\dot{\gamma}_1$ and $\dot{\gamma}_2$, a stress plateau has a slope ~p with $p = \frac{d\log_{10}(\tau)}{d\log_{10}(\dot{\gamma})}$ where $0<p<1$. In a finite shear rate window p is estimated as the value at the inflection point with $\frac{d^2(\log_{10}(\tau))}{d(\log_{10}(\dot{\gamma}))^2} = 0$. Thus viscosity η is also a power law function of shear rate $\dot{\gamma}$ according to $\eta \propto \dot{\gamma}^{p-1}$. In this region, $1/\dot{\gamma}$ is large enough to have particles respond to applied shear and smaller than the characteristic time for particle relaxation. We use the cross point of tangent lines of the shear plateau and high shear region τ_2 as the surrogate of absolute yield stress τ_{abs}. Therefore we have the dimensionless absolute yield stress $\tau_{abs}^* = \tau_{abs} < D >^3 / k_B T$. Based on Equation (6.14) and assuming that $1/\dot{\gamma}$ is a good estimation of t_{hop} which is varied by shear stress and that $F_B / k_B T = (F_B(\tau = 0)) / k_B T (1 - \tau / \tau_{abs})^{1.75}$ as predicted by Kobelev et al for hard sphere systems can be universally applied to other systems, it is easily to obtain for localized conditions that $p = 1.888(F_B / k_B T)^{-1}$ as an approximation for the inflection point. However, we note here that details of interaction and complexity of the suspensions will vary the dependence of shear stress of the barrier height with the resulting slope of shear

stress plateau and that it is difficult to define a development of shear stress plateau based on the view of DLT. Nevertheless, the decreasing tendency of shear-thinning exponent p with increasing F_B/k_BT is noticeable here which is different from the prediction in the original form of MCT.

The plateau elastic modulus $G_p'^*$ is the defined as the value of G'^* at the local minimum of G''^* in the frequency sweep experiment, with the details introduced in previous study.[27]

To explore links between the dynamic yield stress and the hopping time, we use the results of dynamic stress sweep experiment at a fixed frequency ω. An example of dynamic stress sweep experiment result is shown in Figure 6.2. We make the assumption that the dynamic yield, τ_x, is characterized by the stress required to drive the storage modulus to equal the loss modulus ($G'=G''=G_x$) when the suspension is driven at a frequency ω ($\omega=2\pi f$). This dynamic yield stress probes the ability of the particles to rearrange nearest neighbors in a time frame of an oscillation. As a result we suggest that at τ_x, we are probing the point where the deformation time is approximately the hopping time such that at τ_x, $t_{hop}/t_0 = 1/\omega^* = D_0/(\omega < D >^2)$ with the diffusivity $D_0 = k_BT/3\pi < D > \eta_m$ (η_m is the medium viscosity). Here we are arguing that for $\tau << \tau_x$, F_B remains sufficiently high that in a time scale of $1/\omega$, particles cannot diffuse over the dynamical barrier and exchange nearest neighbors. However, with increasing stress, the barrier is lowered and particles can diffuse over the barrier in a shorter time scale. For higher values of ω particles have less time to diffuse. As a result we expect τ_x to increase with ω.

Below we will discuss our experimental results and compare these results with literature report and theoretical predictions.

6.4 Results and Discussions

6.4.1 Particle Localization and Development of Dynamic Stress Plateau

As we discussed above, when increasing volume fraction in colloidal dispersions, a barrier will be developed in the effective energy when it is plotted as a function of particle displacement. This microscopic phenomenon is reflected as development of shear stress plateau when the suspensions are subjected to a steady shear. While the elastic floc model[7] and hopping model of Braxter-Drayton and Brady[14] estimate the magnitude of the yield stress plateau for attractive systems, the DLT predicts that flow curves will be similar at the same value of r_L and r_B independent of the nature of the attraction between hard core particles. In its original form, MCT predicts that, p>0 for all the liquid-like states decreasing with increasing ε ($\varepsilon = (\phi_c - \phi_x)/\phi_x$) to p=0 when ϕ_c=ϕ_x. Idealized mode coupling theory thus predicts that glasses will display a finite yield stress (i.e., there is no long range diffusion for volume fractions above the glass transition volume fraction.).[33] There is considerable evidence that zero shear rate viscosities and activated diffusion can be measured at volume fractions above the idealized mode coupling theory glass transition.[34-37] As a result, we anticipate that p>0 even above glass-transition volume fraction. Accepting that activated transport can still occur after particles are localized by nearest neighbors, the schematic p-spin model theory predicts that the shear-thinning exponent p~1/3 for ideal glass transition and approaches 0 when deep in the glassy slates.[38] Our experimental results and the prediction of DLT for hard sphere systems by Kobelev and coworkers[30] are similar and close to this prediction, as shown in Figure 6.3

(A). In Figure 6.3(A) we also contain the data of Zhou and coworkers for weakly attractive metal oxide particle suspensions.[9] We can see that from Figure 6.3(A) that volume fraction dependence of p for those single-component systems with weak interaction are very similar.

There is no sophisticated description of the shear-thinning exponent p. It is expected to start at a value close to unity for liquid like systems and decrease to a low value approaching zero deep into the glassy or gelled state. However, dynamic localization theory connects the shear-thinning exponent to distortion to the dynamic potential. The more easily the dynamic potential is flattened by the applied stresses, the closer p is to unity. If we assume the ability of the applied stress to distort the pair potential is a function of the magnitude of dynamic potential barrier, we would expect p to correlate with the onset of localization and as shown in Figure 6.3(B), we find universal behavior when p is plotted as a function of ϕ_c/ϕ_x. For the data reported by Zhou et al, ϕ_x=0.53 is used, and for the prediction by Kobelev et al, ϕ_x=0.51 is used to correlate the data. The data clearly show that there is a universal transition in flow behavior as the volume fraction passes through a characteristic volume fraction. We have chosen to define ϕ_x as the cross-over volume fraction where particles become localized and that this occurs when p=0.5. In the following discussion about particle localization, we consider particles localized only if p is substantially smaller that 0.5 to ensure particle localization as reflected in the development of dynamic yield stress plateau. The remarkable collapse of data for all of these systems suggests that shear thinning depends only on how far the solids volume fraction is from the cross over volume fraction. Thus from a single flow curve where ϕ_c is known, one can predict ϕ_x and the shear thinning exponent for all other

volume fractions. Thus when investigating the degree of shear thinning in a suspension, the information about pair potentials and particle size distributions is controlled by ϕ_x.

6.4.2 Barrier Height

Following the methods introduced in section 6.3 we have extracted F_B from the steady shear curves and the elasticity of the suspensions. These value are shown in Figure 6.3 (A), with a comparison with the theoretical prediction based on the Percus-Yevick hard sphere fluid structural input, which concludes that $r_L / D_c \cong 30\exp(-12.2\phi_c)$ and $F_B \cong 0.077/S_0 - 3.51$ (where $S_0 = (1-\phi_c)^4/(1+2\phi_c)^2$)).[30] These results show that F_B can be captured with the exponential fitting with $F_B / k_B T = A\exp(b\phi_c)$ for all the systems as shown in the inset of Figure 6.4(A). The slope *b* is nearly constant ~17 for all the experimental systems except for *R*=0 in PEG2000 in which *b* is smaller. For the samples resembling hard sphere single-component systems (*R*=0 in PEG400), the experimental results are smaller than theoretical predictions. We can understand this as resulting from our using τ_2 as a measure of τ_{abs} which incorporate the influence of shear thickening in this stress region as volume fraction is increased. Due to these concerns, those systems with strong shear thickening behavior are not reported here (*R*=0.71 for PEG400 and *R*=1 for PEG400 and PEG2000). The exponential dependence does not capture divergence of elasticity and viscosity when approaching maximum packing fraction and the universal effects of entropic barrier on rheology when pair interactions are varied.

The ultra-local approximation establishes that the divergence of elasticity approaching maximum packing is an immediate consequence of the correlation $F_B \propto r_L^{-1} \to \infty$.[32] In Figure 6.3(B), F_B/k_BT is plotted as a function of $r_L / < D >$. The

solid line is the prediction of the ultra-local theory for hard sphere Percus-Yevick structural input. We note that experimental curves converge to the theoretical values as r_L decreases (ϕ_c approaches ϕ_m) but the data do not collapse for large values of r_L.

We expect flow properties to correlate with F_B for $\phi_x<\phi_c<\phi_m$. Figure 6.4(B) does not show the expected correlation. We argue that while hard cores dominate behavior as ϕ_c approaches ϕ_m, pair potentials are much more important as ϕ_c approaches ϕ_x. We find that a correlation between flow properties over the entire range of $\phi_x<\phi_c<\phi_m$, occurs if we characterize particle volume fraction with $\phi^*=(\phi_m-\phi_x)/(\phi_m-\phi_c)$. This is shown in Figure 6.4(C). All the data collapse well at both extreme conditions: $\phi^*\rightarrow 1$ and $\phi^*\rightarrow\infty$ for hard sphere systems (PEG400). When initially entering the localization states, F_B increases quickly from 0 and shows slower increase as the jamming condition is approached. We note here that there is increased scattering of data for the attractive systems (in PEG2000) at large ϕ^* limit. We attribute this difference to the effect of attractions which will alter the contact value of the pair distribution function thus alter the correlation with hard sphere predictions.[28] However, further development is necessary to build a better universal volume fraction scaling for F_B when particle interactions are dominant (and $\phi_x << 0.3$).

DLT suggests that the entropic barrier, F_B/k_BT, for a single particle to overcome to achieve steady long time diffusion gives rise to macroscopic rheological properties of colloidal gels/glasses. To emphasize on this point, $G_p'^*$ and τ_{abs}^* are plotted as a function of F_B/k_BT, as shown in Figure 6.5, with universal behavior clarified.

6.4.3 Zero-Shear Viscosity

As we discussed above, the zero-shear viscosity plateau reflects the long-time relaxation behavior when the suspension is exposed to no external shear and approximately we assume the relaxation is equal to hopping time and thus to derive

$$\eta_0 \cong G_p' t_{hop} \tag{6.15}$$

According to Equation (6.12) and Equation (6.14), we anticipate a correlation between $\eta_{r,0}$ and $F_B(\tau=0)/k_BT$. In the limit of large barriers this can be written:

$$\eta_{r,0} = A(F_B / k_BT)^2 \exp(F_B / k_BT) + B \tag{6.16}$$

Here the prefactor A is assumed to be a function of interaction and weakly influenced by concentration. And the constant B is a function of interaction and concentration, which reflects the value of zero shear viscosity at ϕ_x and is not as dominant as the first term when particles are deeply into the arrested state. When the suspension is exposed to a small external shear stress τ ($\tau << \tau_{abs}$), the effective energy for particle hopping is not distorted in a large extent with F_B/k_BT is essentially kept high, we assume Equation (6.16) can also be applied to the viscosity in the shear thinning region where the prefactor is influenced by particle concentration and interaction and the constant term reflects all the effects other than the particle localization.

For hard spheres, F_B/k_BT is predicted to decay in a universal manner with increasing τ/τ_{abs} which can be captured with $F_B(\phi_c, \tau)/k_BT = (F_B(\phi_c, \tau = 0)/k_BT)(1-\tau/\tau_{abs})^{1.75}$.[30] With this approach, we can extract the information of correlation between η_r and F_B/k_BT in the shear thinning region, with an example shown in Figure 6.6 which plots η_r as a function of $(F_B/k_BT)^2\exp(F_B/k_BT)$ for D_c=127nm silica particles dispersed in PEG400. In the inset of Figure 6.6, η_r is plotted as a function of F_B/k_BT. As shown in the large barrier

height region, the data increase according to a linear function of $(F_B/k_BT)^2\exp(F_B/k_BT)$. Therefore we extract the information of zero shear viscosity according to the relevant fitting with $F_B=F_B(\tau=0)$. The results of $\eta_{r,0}$ is plotted as a function of $(F_B/k_BT)^2\exp(F_B/k_BT)$ in Figure 6.7 (main panel) and as a function of F_B/k_BT in the inset.

From Figure 6.7, the universal dependence of barrier height for zero shear viscosity is proved, as predicted by Equation (6.16). But we note that the constant term B reflects the important information of viscosity where the localization state is not achieved yet, which is varied by tuning interaction and size distribution and reaches minimum for single-component hard sphere system (R=0 for silica particle dispersed into PEG400). When approaching the large value of F_B, Equation (6.16) can capture the tendency well and uniformly.

6.4.4 Dynamic Yield Stress and Barrier Hopping

As discussed above, the application of an external shear stress will distort the dynamic potential energy curve, resulting in a decrease of the entropic barrier height and favoring delocalization of a particle. When $\tau=\tau_{abs}$, the barrier height completely disappears, with $F_B(r;\tau=\tau_{abs})=0$ and the particle hopping time is reduced to zero: t_{hop}=0. When $\tau<\tau_{abs}$, $F_B(r;\tau)>0$, and $t_{hop}>0$. When τ=0, the hopping time is correlated with α-relaxation time. Therefore, dynamic yield stress τ_y can be varied based on different desired hopping time through Equation (6.14).

As a result, yielding, as defined as *G'=G"* in a stress sweep, will depend on the probing frequency. With increased frequency, we anticipate larger yield stresses.

In dynamic stress sweep experiment at a desired frequency *f*, yielding is expected when we match the experimental time scale to the hoping time scale: $t_{exp}=t_{hop}$. Here

$t_{exp}=1/(2\pi f)=1/\omega$. As a result in a stress sweep experiment at yielding, we expect $t_{hop}/t_0=1/\omega^*$. Experimentally we have investigated the yield stress at two frequencies f=0.1Hz (t_{hop}/t_0=3.3) and f=1Hz (t_{hop}/t_0=0.33) for single-component hard sphere suspensions(R=0 for PEG400). For this system t_0=0.48s. The dynamic yield stress τ_x^* again defined as the point where $G'=G''=G_x$, are plotted in Figure 6.8 where we also show the predictions of Kobelev et al[30] for τ_{abs}^* and τ_y^* for three different hopping times. For the experimental systems we have used τ_2^* an estimate of τ_{abs}^*.

From Figure 6.8, decreased dynamic stress is observed for increased hopping time, as predicted in theory, and the magnitude of τ_y^* is essentially smaller than the theory prediction. These observations are consistent with previous experimental observation for D_c=44nm silica particles in PEG400.[39] Figure 6.5 also shows the yield stress of D_c=270nm polystyrene particles suspended in an aqueous electrolyte where conditions have been tuned to render the particle interactions weakly attractive. For this system τ_y^* was measured at f=1Hz (t_{hop}/t_0=3.94). We note a stronger dependence on volume fraction than is observed for the silica particles. We attribute this to differences in pair potential. In particular we note that the conditions probed by Kramb et al may place the particles in an attractive glass regime where particles are localized both by hard core nearest neighbor interactions and attractions. Nevertheless, the data is consistent showing that as volume fraction increases, the yield stress approaches the absolute value τ_{abs}^* while as the probing frequency increases, the yield stress increases.

In Figure 6.9, we compare the volume fraction dependence of the yield stress for the D_c=127nm silica particles in PEG400 where they interact as hard spheres and for the same particles suspended in PEG2000 where they experience an attraction. Obviously,

when attractions are introduced, at a fixed experimental probing frequency, τ_x^* increases. However, we note that the increases in attraction also increase F_B and thus increase t_{hop}/t_0. We expect a universal scaling of yield stress at a fixed experimental strain frequency if we compare systems at the same value of F_B.

In Figure 6.10, dynamic yield stress τ_x^* is plotted as a function of F_B/k_BT (τ=0) at both f=1Hz and f=0.1Hz for all the systems. It is again confirmed that decreased shear frequency results in decreased dynamic yield stress τ_x^* when entropic barrier height is fixed. Here we note that for hard sphere systems (PEG400), when R is increased at fixed frequency f, the dynamic yield stress magnitude of τ_x^* is slightly increased, which can be attributed to a slight decrease in t_{hop}/t_0 as t_{hop}/t_0=0.33 (3.3), 0.24 (2.4) and 0.17 (1.7) for R=0, 0.29 and 0.5 respectively at f=1Hz (0.1Hz). This weak influence of t_{hop}/t_0 on τ_x^* is not obvious for attractive systems. We attribute this effect as a consequence of long α-relaxation time for attractive systems making $t_{hop}>t_\alpha$, therefore the yield stress is not strongly influenced at this condition, consistent with the result in Figure 6.9.

6.5 Conclusion

Here we use dynamic localization theory to explore the properties of particles interacting with volume exclusion pair potentials and weak attractions. In addition we look at the flow properties of suspensions composed of particles of two distinct sizes and compare with literature values of flow properties for different systems. In the framework of DLT, particle interactions result in a dynamic potential barrier that limits the system dynamics but does not alter the equilibrium particle microstructure. The theory relates suspension dynamics in systems rendered dense by increased volume fraction or by increased attractions to the time it take a particle to diffuse out of a minimum in the

dynamic potential. This minimum traps particles in a local minimum of size $r = r_L$ and requires particles to diffuse a distance $r = r_B$ to experience the maximum in the dynamic potential. Long-range diffusion is limited by the ability of particles to diffuse over this dynamic potential barrier. DLT predicts properties of the dynamic potential from equilibrium suspension microstructure. Particle localization occurs for $\phi_c > \phi_x$, and the dynamic potential barrier height, F_B, grows with volume fraction above ϕ_x. Transport occurs through an activated process where the rate of diffusion is dominated by the time it takes particles to hop out of the local minimum in the dynamic potential. With increasing volume fraction or increased inter-particle attractions F_B is increased, the hoping time decreases, and r_L decreases resulting in increased suspension elasticity. When an external stress is applied, DLT uses an Eyring type analysis to distort the dynamic potential barrier, lowering F_B and increasing r_L. At the absolute yield stress τ_{abs}*, F_B drops to zero and particles exchange nearest neighbors without being hindered by the dynamic potential barrier.

Applying these basic concepts, F_B is extracted from experimental results for different systems where ϕ_x and the maximum packing fraction ϕ_m are varied by changes to particle size distribution and pair potential. We find that F_B/k_BT is essentially a universal function of dimensionless volume fraction $\phi^* = (\phi_m - \phi_x)/(\phi_m - \phi_c)$, showing a universal behavior when exceeding dynamic arrest transition and approaching jamming condition. This behavior is consistent with previous studies on hard sphere systems showing scaling of elasticity and diffusivity with $1/(\phi_m - \phi_c)$ as ϕ_m/ϕ_x is found to be nearly constant for systems studied where ϕ_m is varied but particles interact with volume exclusion potentials. Linear plateau elasticity G_p'*, absolute yield stress τ_{abs}* and the extrapolated value of zero shear

viscosity $\eta_{r,0}$ are shown to have universal dependencies on F_B. With this basic knowledge, the dynamic yield stress is studied as a function of strain frequency. DLT predicts that the dynamic yield stress will increase with increased strain frequency- an effect that is confirmed experimentally.

Historically the commonality of flow behavior seen in suspensions as volume fraction has been tied to the pair potentials that cause Brownian particles to aggregate. Descriptions of yield stresses and elasticities have been developed based on pair potentials that do not vary with volume fraction and microstructures that are linked to fractal properties of aggregates. In DLT, the characteristic length giving rise to elasticity is controlled by both pair potential and volume fraction. As a result, DLT characterizes suspension flow properties in terms of equilibrium pair distribution functions with no reference to the fractal nature of the aggregates suspension. Application of DLT to a variety of suspensions suggests that the values of ϕ_c/ϕ_x and F_B can be estimated from steady shear experiments and a measure of the suspension elasticity. While the power of the elastic floc model originally developed by Hunter[7] and later carefully demonstrated by Scales et al. [10] lies in linking yield stresses to details of the colloidal pair potentials, the results presented here suggest F_B and ϕ_x can be extracted from steady shear curves when the pair potential is unknown while at the same time allowing for a connection between flow properties observed for hard sphere suspensions and the flow properties of suspensions where particles with hard cores experience strong attractions.

6.6 Tables and Figures

Table 6.1 Summary of ϕ_x and ϕ_m for different systems

R	$<D>$/nm	ϕ_x (PEG400)	ϕ_x (PEG2000)	ϕ_m
0	127	0.511	0.330	0.631
0.29	140	0.557	0.375	0.661
0.5	160	0.603	0.438	0.713
0.71	190	0.605	0.504	0.719
1	612	0.510	0.549	0.632

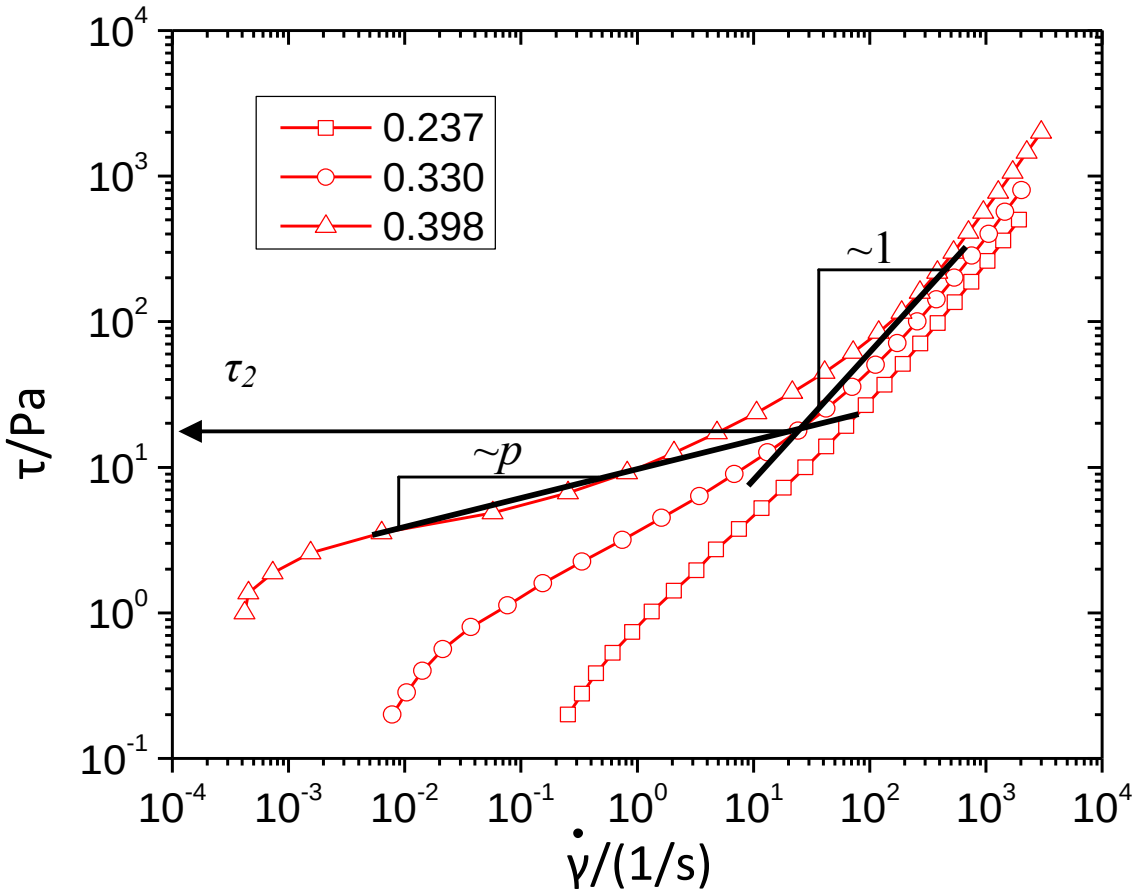

Figure 6.1 Examples of flow curves for D_c=127nm particles dispersed into PEG2000 at three different volume fractions. The method of determining τ_2 (τ_{abs}) is denoted in the plot.

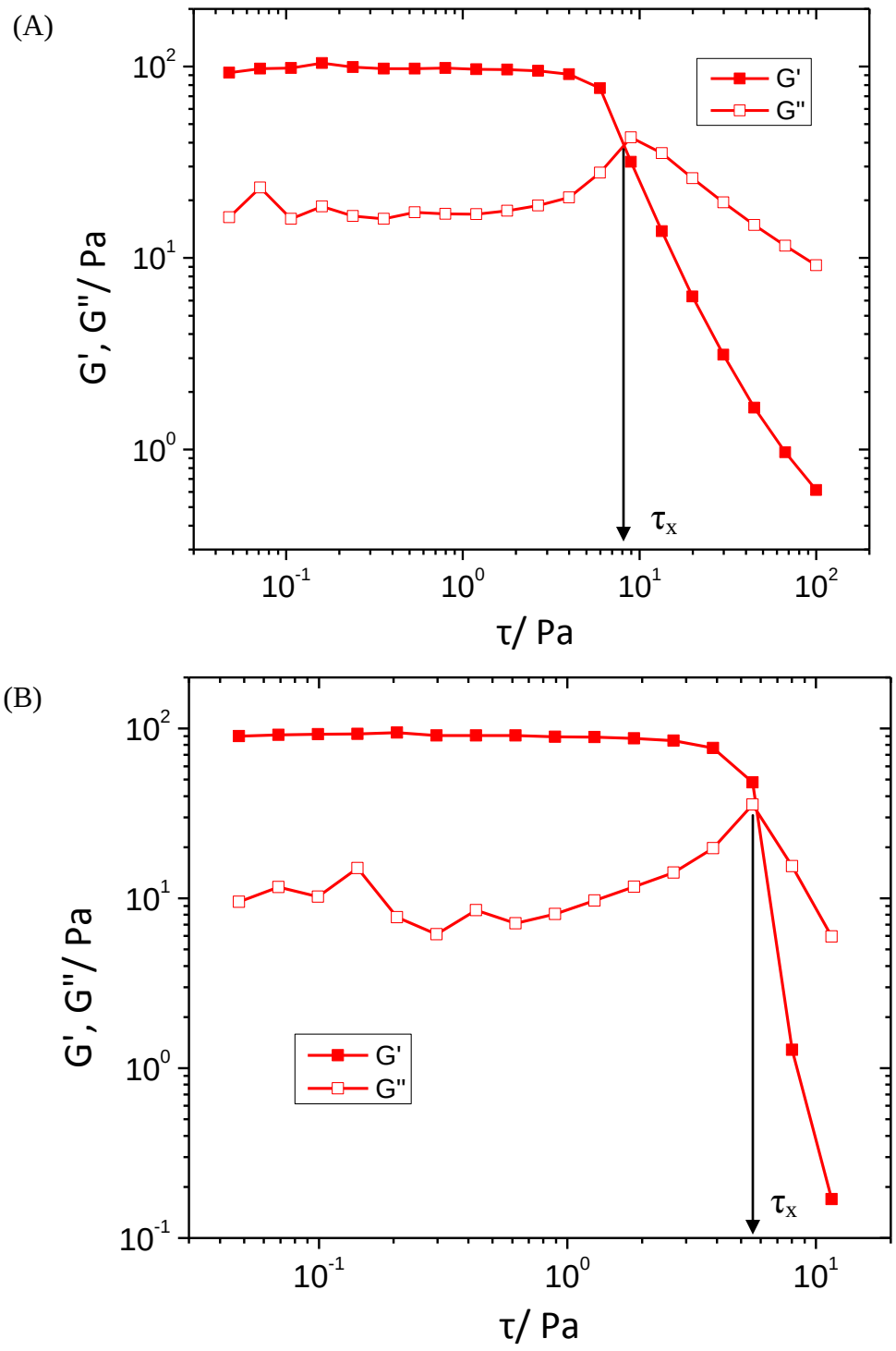

Figure 6.2 (continued on next page)

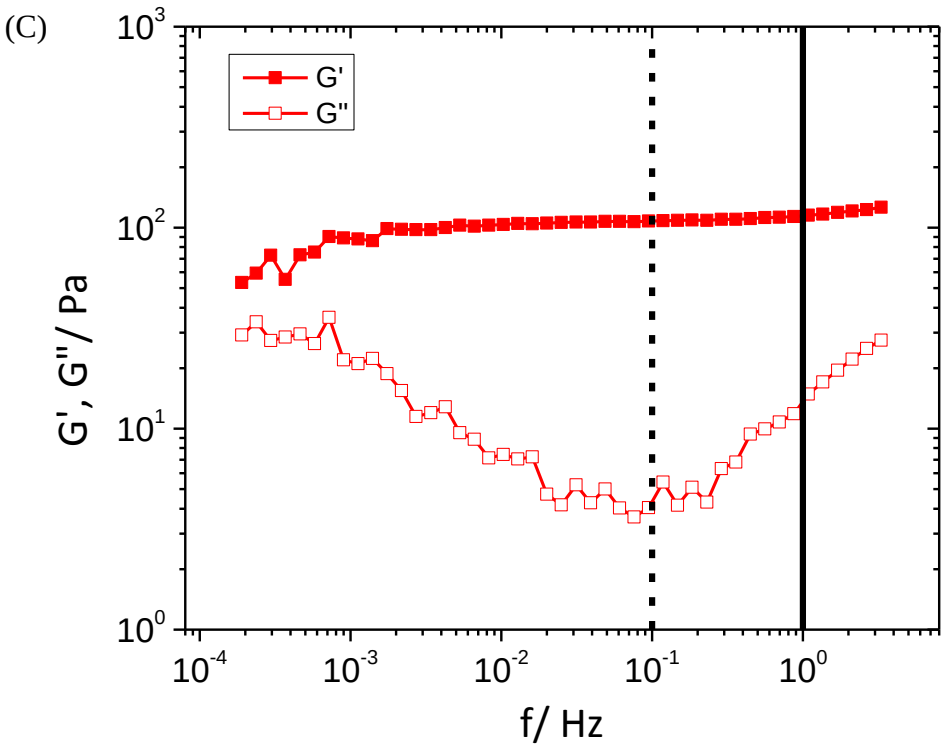

Figure 6.2 Example of dynamic stress sweep result (D_s=127nm silica particles dispersed into PEG2000 at ϕ_c=0.398) with dynamic stress applied at (A) f=1Hz and (B) f=0.1Hz. The method of determining τ_x is denoted in (A) and (B). (C) shows the frequency sweep experiment result for this sample, f=1Hz and f=0.1Hz are plotted with solid line and dashed line respectively.

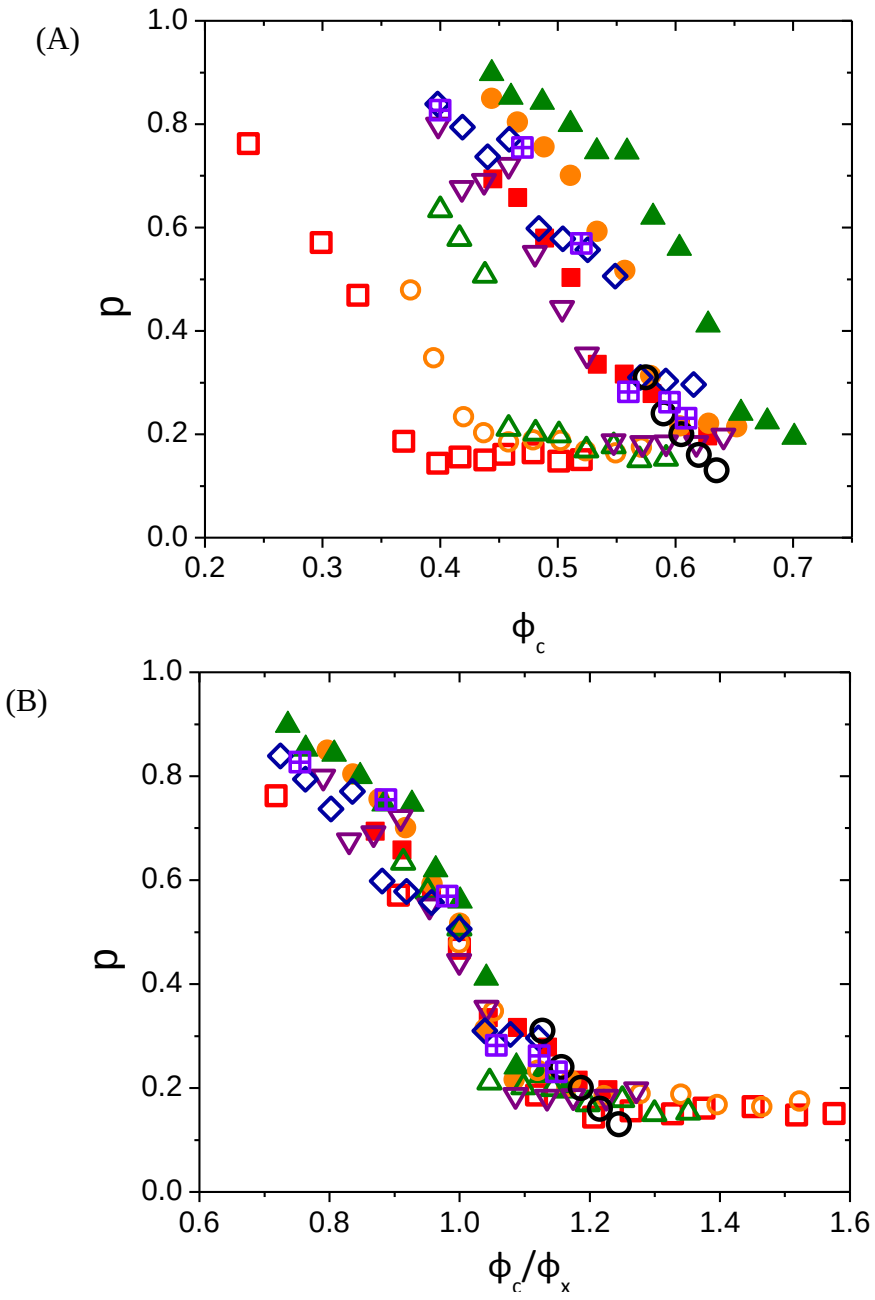

Figure 6.3 Shear-thinning exponent p as a function of (A) ϕ_c and (B) ϕ_c/ϕ_x for silica particles in PEG400: (■, R=0), (●, R=0.29), (▲, R=0.5) and silica particles in PEG2000: (□, R=0) (○, R=0.29) (△, R=0.5) (▽, R=0.71),(◇, R=1). Prediction of DLT (○) by Kobelev et al[30] and the experimental data of metal oxide suspensions (⊞) by Zhou et al[9] are also presented.

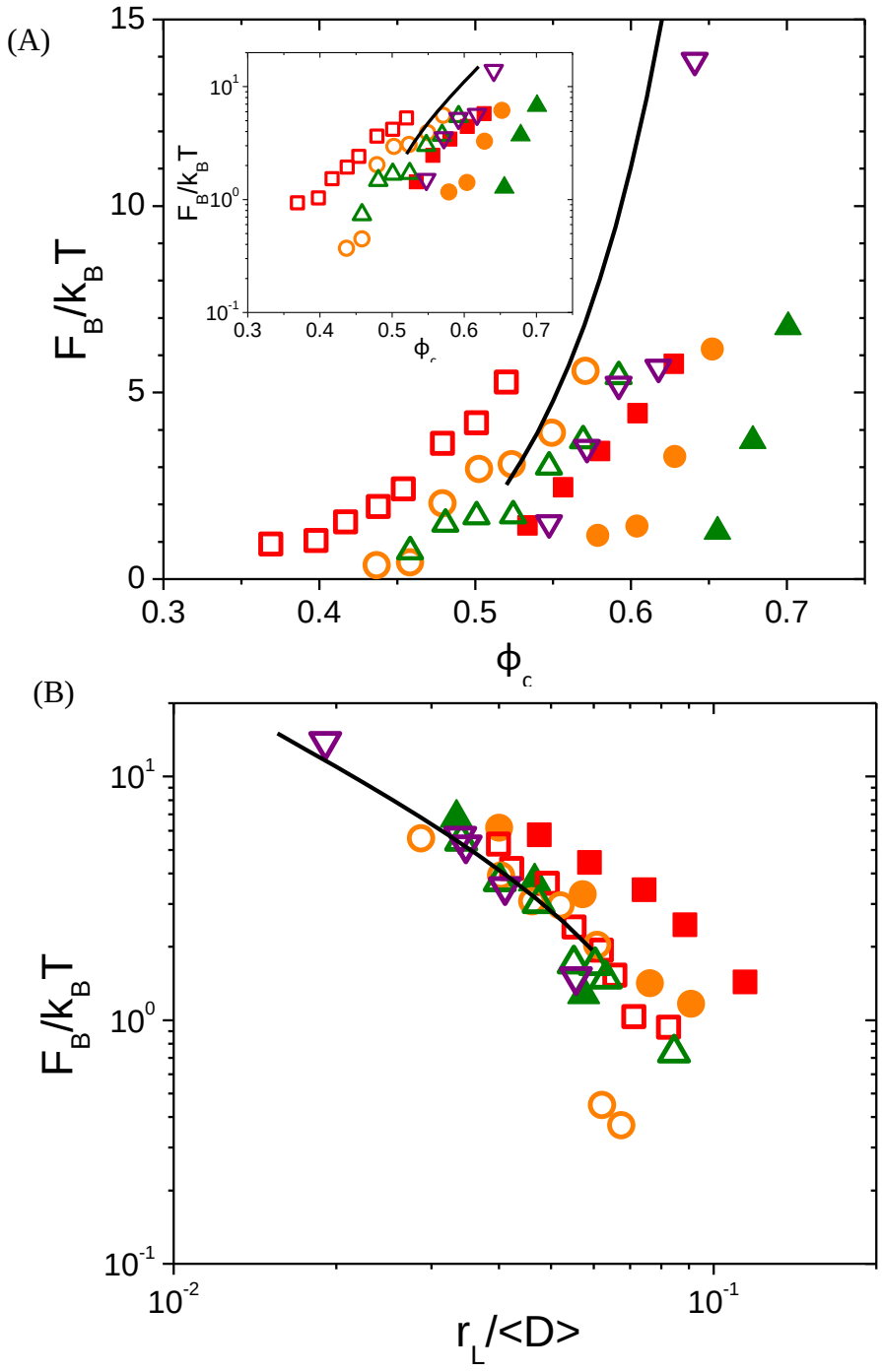

Figure 6.4 (continued on next page)

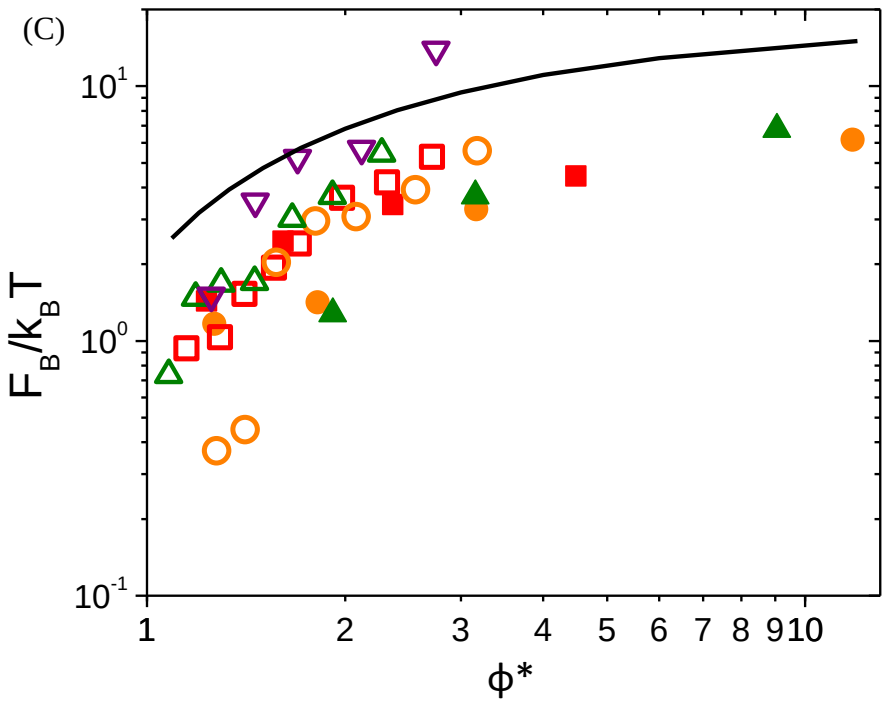

Figure 6.4 Entropic barrier height (τ=0) as a function of (A) ϕ_c (B) $r_L / < D >$ and (C) ϕ^* for silica particles in PEG400: (■, R=0), (●, R=0.29), (▲, R=0.5) and silica particles in PEG2000: (□, R=0), (○, R=0.29), (△, R=0.5), (▽, R=0.71). The solid curves are predictions based on Percus-Yevick structure input. The inset of (A) shows F_B/k_BT vs. ϕ_c in the log-liner scale.

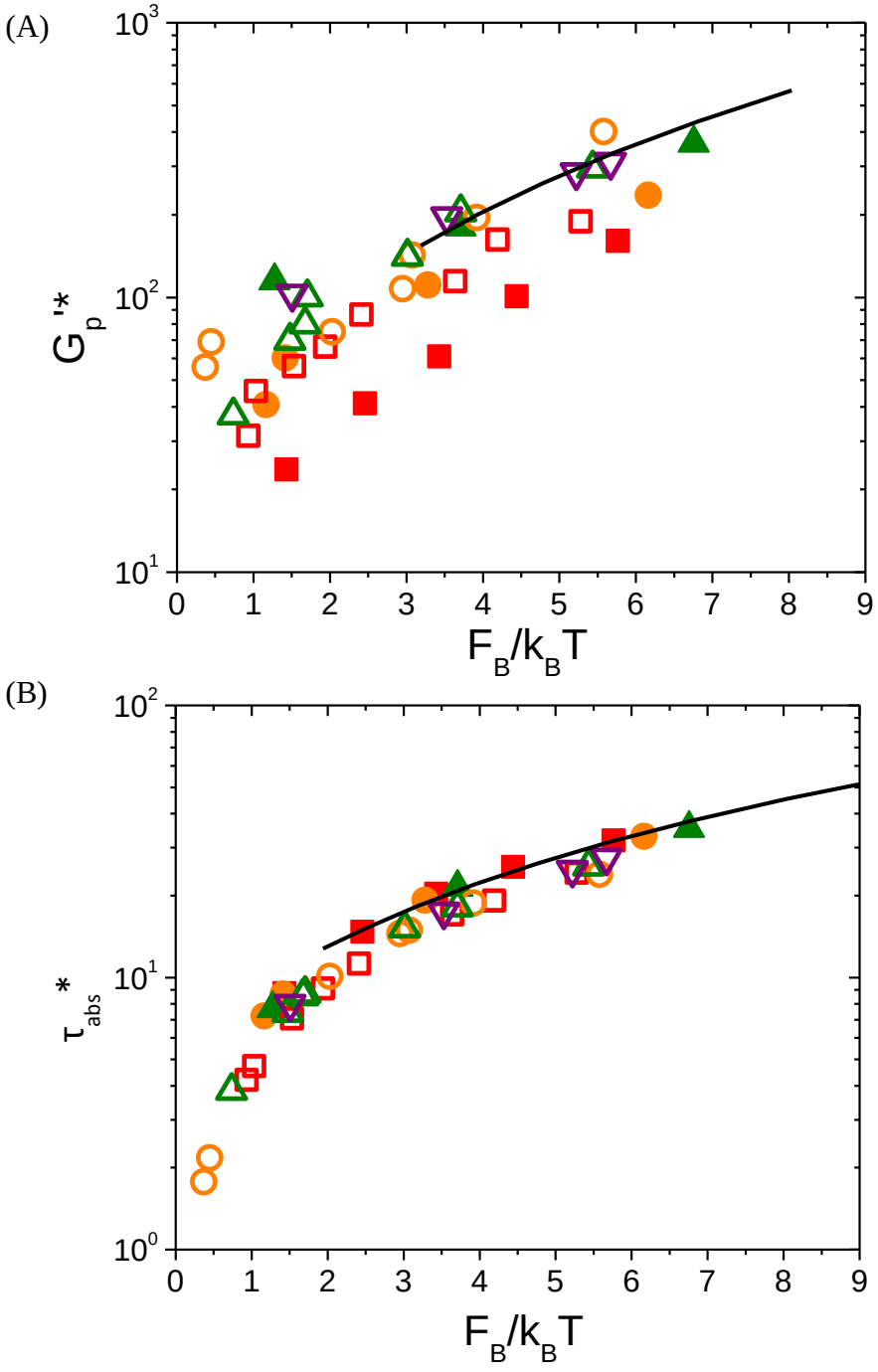

Figure 6.5 (A) G_p'* and (B) τ_{abs}* as a function of F_B/k_BT for silica particles in PEG400: (■, R=0), (●, R=0.29), (▲, R=0.5) and silica particles in PEG2000: (□, R=0), (○, R=0.29), (△, R=0.5), (▽, R=0.71). The solid curves are predictions based on Percus-Yevick structure input.

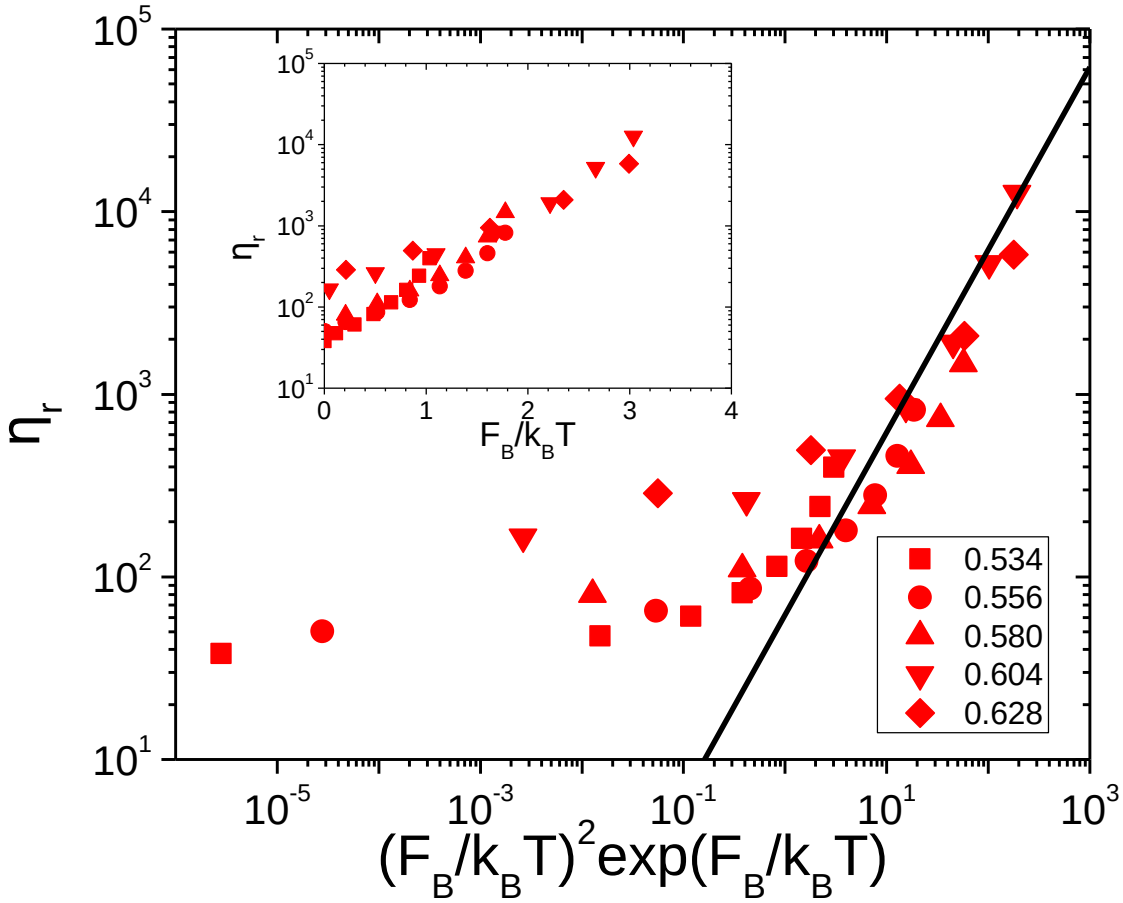

Figure 6.6 η_r as a function of $(F_B/k_BT)^2\exp(F_B/k_BT)$ for D_c=127nm silica particles dispersed in PEG400 at different volume fractions. The solid line has a slope ~1 showing the liner increasing tendency of η_r when F_B is large. The inset plots η_r as a function of F_B/k_BT.

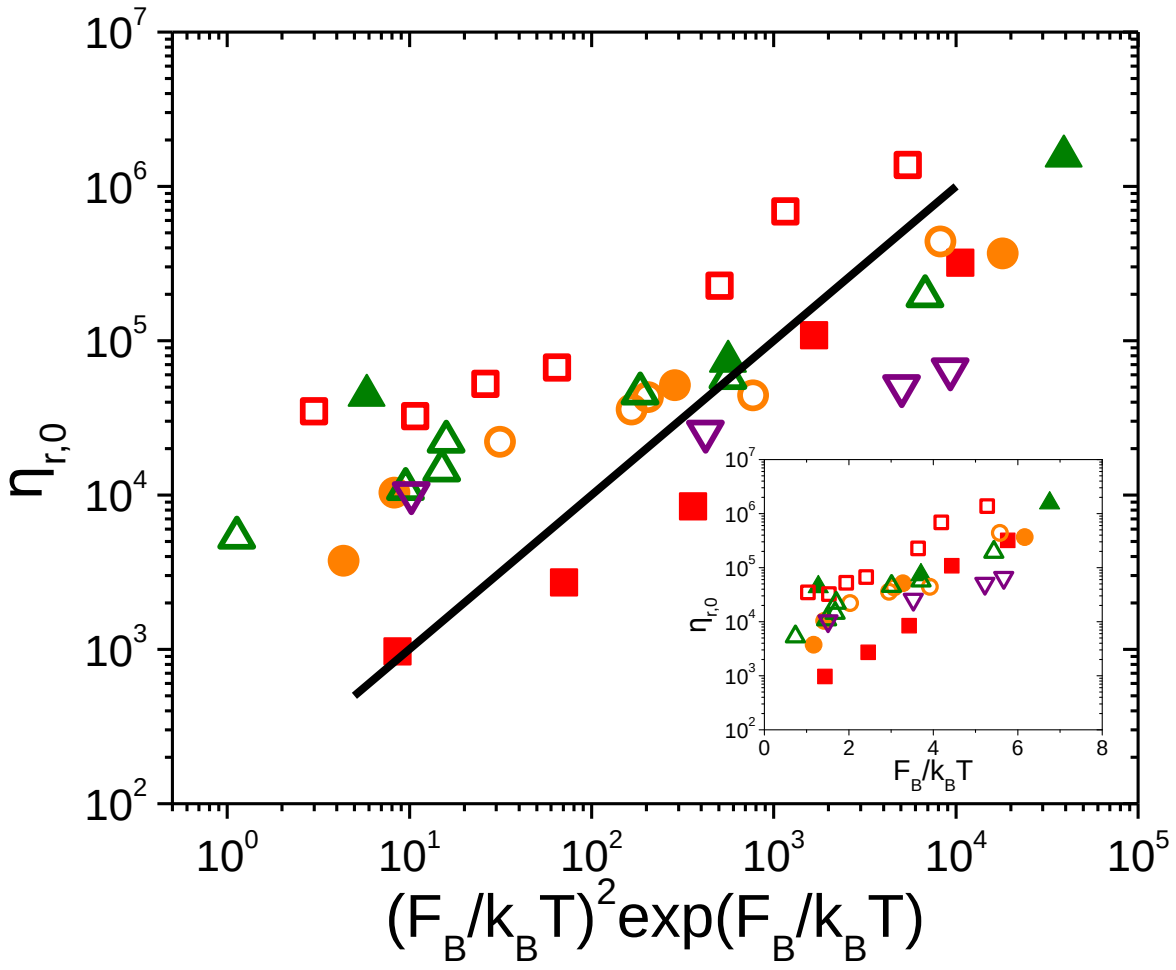

Figure 6.7 $\eta_{r,0}$ is plotted as a function of $(F_B/k_BT)^2\exp(F_B/k_BT)$ for silica particles in PEG400: (■, R=0), (●, R=0.29), (▲, R=0.5) and silica particles in PEG2000: (□, R=0), (○, R=0.29), (△, R=0.5), (▽, R=0.71). The solid line has a slope ~1 showing the liner increasing tendency of $\eta_{r,0}$. The inset plots $\eta_{r,0}$ as a function of F_B/k_BT.

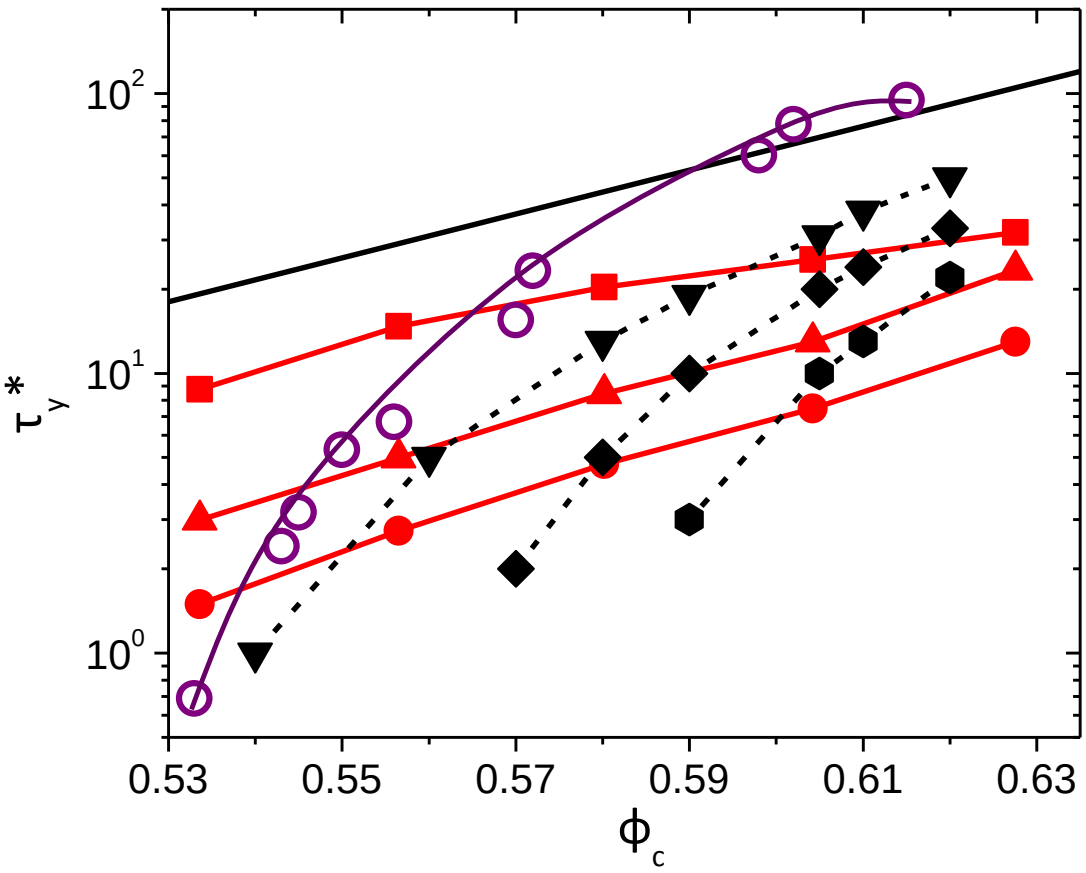

Figure 6.8 Experimental results (D_c=127nm spheres in PEG400) of τ_2* (■) and τ_x* for t_{hop}/t_0=0.33 (▲) and t_{hop}/t_0=3.3 (●). Theoretical predictions for τ_{abs}* (black solid curve at the top) and τ_y* for t_{hop}/t_0=10 (▼) and t_{hop}/t_0=100 (◆) and t_{hop}/t_0=1000 (⬢). The experimental data τ_x* for hard sphere reported by Kramb et al is also presented for t_{hop}/t_0=3.94 (○).The curves are used to guide eyes.

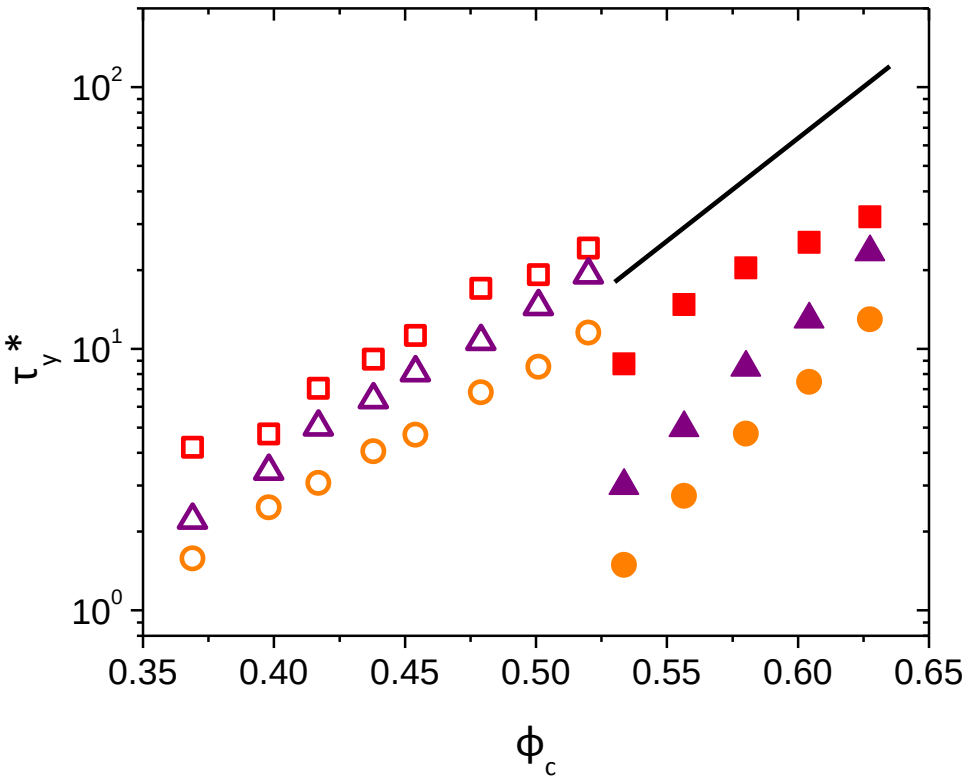

Figure 6.9 Experimental results of τ_2^* (■) and τ_x^* for f=1Hz (▲) and f=0.1Hz (●) (D_c=127nm silica particles in PEG400). The corresponding open symbols represent the data for D_c=127nm silica particles in PEG2000. The solid curves are predictions for τ_{abs}^* based on Percus-Yevick structure input.

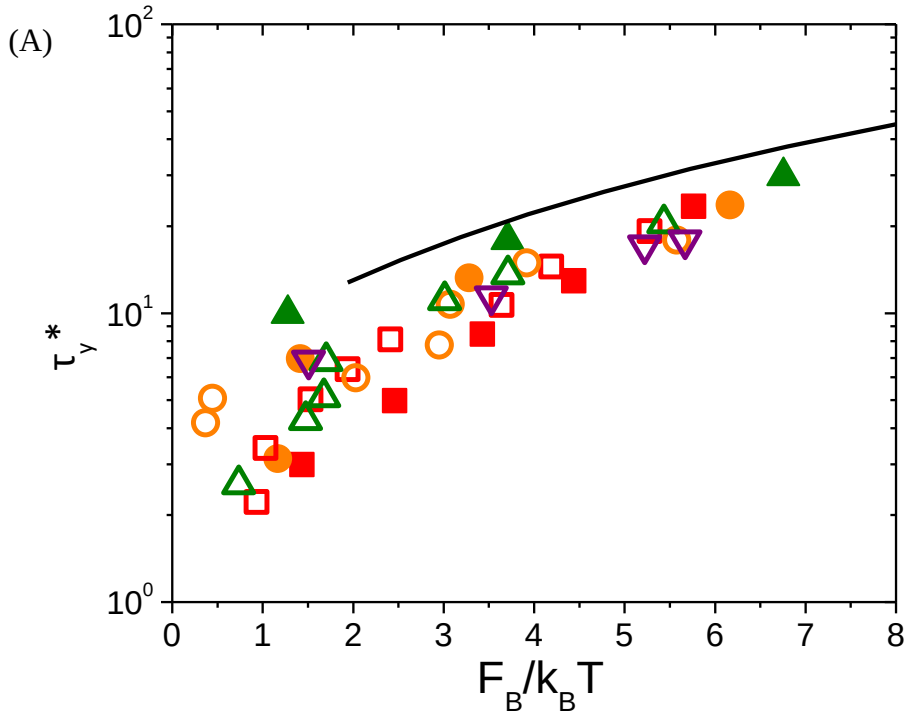

Figure 6.10 (continued on next page)

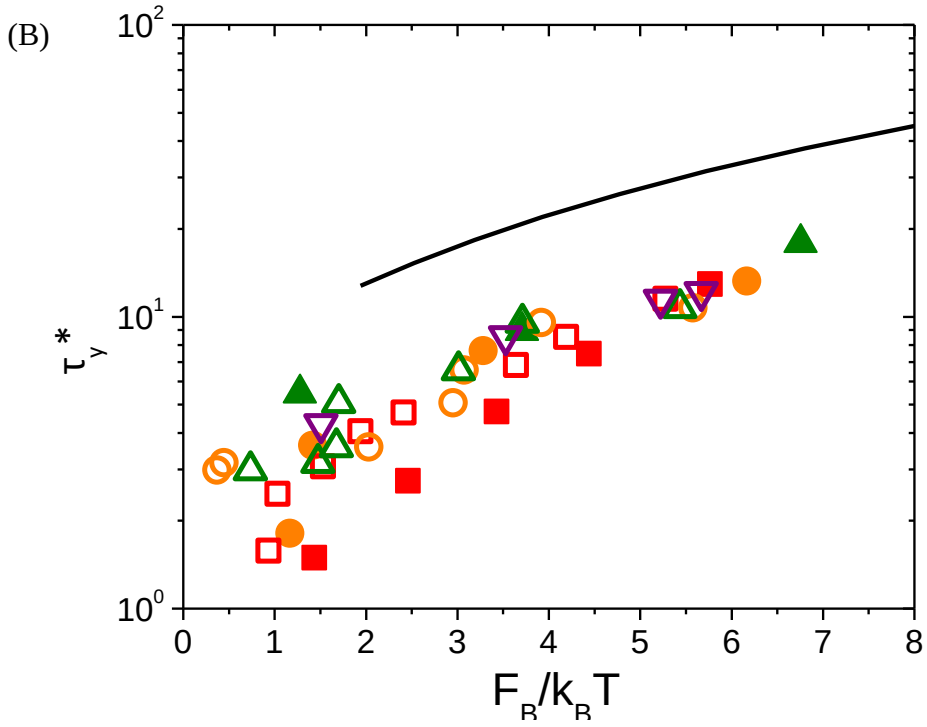

Figure 6.10 τ_x^* at (A) f=1Hz and (B) f=0.1Hz as a function of F_B/k_BT for silica particles in PEG400: (■, R=0, t_{hop}/t_0=0.33 for f=1Hz and t_{hop}/t_0=3.3 for f=0.1Hz), (●, R=0.29, t_{hop}/t_0=0.24 for f=1Hz and t_{hop}/t_0=2.4 for f=0.1Hz), (▲, R=0.5, t_{hop}/t_0=0.17 for f=1Hz and t_{hop}/t_0=1.7 for f=0.1Hz) and silica particles in PEG2000: (□, R=0, t_{hop}/t_0=0.39 for f=1Hz and t_{hop}/t_0=3.9 for f=0.1Hz), (○, R=0.29, t_{hop}/t_0=0.28 for f=1Hz and t_{hop}/t_0=2.8 for f=0.1Hz), (△, R=0.5, t_{hop}/t_0=0.19 for f=1Hz and t_{hop}/t_0=1.9 for f=0.1Hz), (▽, R=0.71, t_{hop}/t_0=0.12 for f=1Hz and t_{hop}/t_0=1.2 for f=0.1Hz). The solid curves are predictions for τ_{abs}* based on Percus-Yevick structure input.

6.7 References

1. N. Koumakis, A. Pamvouxoglou, A. S. Poulos and G. Petekidis, *Soft Matter*, 2012, **8**, 4271-4284, 4271-4284.
2. R. C. Kramb, R. Zhang, K. S. Schweizer and C. F. Zukoski, *Physical Review Letters*, 2010, **105**, 055702.
3. S. Ramakrishnan, V. Gopalakrishnan and C. F. Zukoski, *Langmuir*, 2005, **21**, 9917-9925.
4. M. Pishvaei, C. Graillat, T. F. McKenna and P. Cassagnau, *Journal of Rheology*, 2007, **51**, 51-69.
5. E. Zaccarelli, *Journal of Physics-Condensed Matter*, 2007, **19**, 323101.
6. J. N. Israelachvili, *Intermolecular and surface forces: with applications to colloidal and biological systems*, Academic press, London, 1985.
7. B. A. Firth and R. J. Hunter, *Journal of Colloid and Interface Science*, 1976, **57**, 266-275.
8. T. G. M. Vandeven and R. J. Hunter, *Rheologica Acta*, 1977, **16**, 534-543.
9. Z. W. Zhou, P. J. Scales and D. V. Boger, *Chemical Engineering Science*, 2001, **56**, 2901-2920.
10. P. J. Scales, S. B. Johnson, T. W. Healy and P. C. Kapur, *Aiche Journal*, 1998, **44**, 538-544.
11. D. A. Weitz, J. S. Huang, M. Y. Lin and J. Sung, *Physical Review Letters*, 1985, **54**, 1416-1419.
12. A. A. Potanin, R. Derooij, D. Vandenende and J. Mellema, *Journal of Chemical Physics*, 1995, **102**, 5845-5853.
13. P. Snabre and P. Mills, *Journal De Physique Iii*, 1996, **6**, 1811-1834.
14. Y. BaxterDrayton and J. F. Brady, *Journal of Rheology*, 1996, **40**, 1027-1056.
15. H. Eyring, *J. Chem. Phys.*, 1936, **4**, 283-291.
16. R. T. Bonnecaze and J. F. Brady, *Journal of Rheology*, 1992, **36**, 73-115.
17. Z. D. Cheng, J. X. Zhu, P. M. Chaikin, S. E. Phan and W. B. Russel, *Physical Review E*, 2002, **65**, 041405.
18. L. Marshall and C. F. Zukoski, *Journal of Physical Chemistry*, 1990, **94**, 1164-1171.
19. W. Gotze, *Journal of Physics-Condensed Matter*, 1999, **11**, A1-A45.
20. T. R. Kirkpatrick and P. G. Wolynes, *Physical Review A*, 1987, **35**, 3072-3080.
21. E. J. Saltzman and K. S. Schweizer, *Journal of Chemical Physics*, 2003, **119**, 1197-1203.
22. K. S. Schweizer and E. J. Saltzman, *Journal of Chemical Physics*, 2003, **119**, 1181-1196.
23. R. C. Kramb, R. Zhang, K. S. Schweizer and C. F. Zukoski, *Journal of Chemical Physics*, 2011, **134**, 014503.
24. A. K. Atmuri, G. A. Peklaris, S. Kishore and S. R. Bhatia, *Soft Matter*, 2012, **8**, 8965-8971.
25. W. Stober, A. Fink and E. Bohn, *Journal of Colloid and Interface Science*, 1968, **26**, 62-69.
26. G. H. Bogush, M. A. Tracy and C. F. Zukoski, *Journal of Non-Crystalline Solids*, 1988, **104**, 95-106.

27. T. Y. Jiang and C. F. Zukoski, *Macromolecules*, 2012, **45**, 9791-9803.
28. T. Jiang and C. F. Zukoski, *Soft Matter*, 2012, **9**, 3117-3130.
29. Chapter 4.
30. V. Kobelev and K. S. Schweizer, *Physical Review E*, 2005, **71**, 021401.
31. R. Zhang and K. S. Schweizer, *Journal of Chemical Physics*, 2012, **136**, 154902.
32. K. S. Schweizer and G. Yatsenko, *Journal of Chemical Physics*, 2007, **127**, 164505.
33. D. Hajnal and M. Fuchs, *European Physical Journal E*, 2009, **28**, 125-138.
34. M. Pishvaei, C. Graillat, T. F. McKenna and P. Cassagnau, *Polymer*, 2005, **46**, 1235-1244.
35. M. Pishvaei, C. Graillat, P. Cassagnau and T. F. McKenna, *Chemical Engineering Science*, 2006, **61**, 5768-5780.
36. C. G. Dekruif, E. M. F. Vanlersel, A. Vrij and W. B. Russel, *Journal of Chemical Physics*, 1985, **83**, 4717-4725.
37. J. Mewis, W. J. Frith, T. A. Strivens and W. B. Russel, *Aiche Journal*, 1989, **35**, 415-422.
38. L. Berthier, *Journal of Physics-Condensed Matter*, 2003, **15**, S933-S943.
39. B. J. Anderson and C. F. Zukoski, *Journal of Physics-Condensed Matter*, 2009, **21**, 285102.

Chapter 7. Conclusions

In this thesis, the phase behavior and rheological properties of dense colloidal mixtures dispersed in different continuous phases are studied to explore the effects of interaction, concentration, size distribution, and shape anisotropy. For single-component hard sphere suspensions, dynamic localization theory predicts that with increasing colloid volume fraction, ϕ_c, dynamical localization of single particles results in the onset of glassy properties when the volume fraction crosses the dynamic arrest volume fraction ϕ_x. Above ϕ_x, particle delocalization and the resulting relaxation of stress are accomplished by applying an external stress or increasing the observation time scale to above the time required for particles to exchange nearest neighbors. When the maximum volume fraction, ϕ_m, is approached, stress relaxation by long range diffusion ceases. Varying particle interactions alter ϕ_x, while the maximum packing fraction ϕ_m can only be varied by tuning the particle geometry or the particle size distribution.

Here we study, the universal rheology of dense colloidal dispersions when crossing ϕ_x and approaching ϕ_m, in different continuous media with binary particle size distributions. Different parameters are studied to systematically manipulate ϕ_x including variable particle interactions, variable volume fraction ratios of large and small particles and variable shape anisotropy. For hard sphere interactions, ϕ_x is correlated with ϕ_m ..

In Chapter 2, suspensions containing silica particles with variable sizes (D_c=127nm, 213nm, 612nm, 730nm) suspended in polyethylene glycol (PEG) with two different molecular weights below entanglement condition (PEG400 and PEG2000) are designed to investigate the effects of particle size and polymer molecular weight in terms of particle interaction potentials. It is concluded that particles with different sizes suspended in PEG400 are well represented as particles experiencing volume exclusion interactions.

Differences are only observed in shear thickening where details of soft repulsion result in different onset of thickening. In PEG2000, large colloids with D_c=612nm interact with weak attractions which still undergo dynamic arrest transitions at a high volume fractions and show a weakened shear thickening, while small colloids with D_c=127nm are strongly attractive which gel at a much lower dynamic arrest volume fraction and show no shear thickening.

In Chapter 3, the effects of mixing different sized particles (d_s=127nm and d_l=612nm) under hard sphere conditions are explored by varying the large particle volume fraction ratio R systematically in PEG400 from 0 to 1. With medium values of R, both ϕ_x and ϕ_m are larger than single component systems (R=0 and 1). ϕ_x and ϕ_m are correlated for excluded volume interactions with a constant ratio ϕ_m/ϕ_x~1.2. The flow properties including elastic modulus, shear thickening stress and high frequency viscosity can be expressed as products of the values at ϕ_x and power law functions of a rescaled volume fraction as $\phi^* = (\phi_m - \phi_x)/(\phi_m - \phi_c)$, and diverge at ϕ_m.

In Chapter 4, when suspending the colloidal mixtures with same size distributions in PEG2000, polymer induced attraction is incorporated into the dense binary colloidal mixtures. Considering the small size of polymer compared to the particle sizes, an assumption is made here that ϕ_m is not varied compared to the systems in PEG400. However, the influence of attraction dominates for suspension containing sufficient small strongly attractive particles, thus ϕ_x is no strongly correlated with ϕ_m as in PEG400 which is a monotonic increasing function of large particle volume fraction ratio R. The rheological properties of colloidal dispersions diverge at ϕ_m in a different manner which become constant when scaled with $k_BT/<D>h^2$, where k_BT is the product of Boltzmann

constant and absolute temperature, $<D>$ is the volume average diameter and h is average particle-particle surface separation.

In Chapter 5, to investigate the effects of particle shape on binary mixtures, a very different experimental system is designed containing polystyrene colloids with both shape anisotropy and size asymmetry which are dispersed into aqueous phase. Two different kinds of binary mixtures are studied here with similar size disparity ~3: small spheres (SSP) mixed with large spheres (LSP) and small spheres mixed with large dumbbells (LDB which has aspect ratio~1.3). With ionic strength carefully tuned to 0.01M, small particles interact with large particles or small particles very weakly, while there is an attraction between two large particles with a minimum ~-2k_BT. The interaction strength is essentially independent of particle shape. For single-component large particles, elasticity is consistently smaller for LDB than LSP at the same volume fraction, and the critical volume fraction for discontinuous shear thickening ϕ_t is larger for LDB. These phenomena denote increased ϕ_x and ϕ_m when introducing weak shape anisotropy in the single-component system. But when smaller particles are added into the suspensions, opposite changing tendencies for replacing LSP with LDB denote decreased ϕ_x and ϕ_m when introducing weak shape anisotropy in the binary mixtures.

In Chapter 6, to understand the dynamic arrest transitions and resulting rheological properties when crossing ϕ_x and approaching ϕ_m, the results of silica particles where the discontinuous shear thickening is absent are understood in terms of dynamic localization of single particle in dense suspension. The power law dependence of the stress on shear rate is found to be a universal function of volume fraction normalized by the cross-over volume fraction, ϕ_c/ϕ_x. When $\phi_c>\phi_x$ the barrier height out of which the particles must

diffuse to delocalize, F_B, grows. When size distributions and interactions are varied, F_B is a universal function of rescaled volume fraction as $\phi^* = (\phi_m - \phi_x)/(\phi_m - \phi_c)$ which shows both the appearance of localization when crossing ϕ_x and complete divergence of relaxation times when approaching ϕ_m. Experimentally, the dynamic yield stress measured in dynamic stress sweeps decreases with decreasing frequency. The frequency is taken as a surrogate for inverse of t_{hop}, the time for a particle to hop out of the dynamic potential well. At longer times for the same system, the barrier height at hopping will be larger thus a smaller yield stress is required to lowering the barrier height.

This thesis focuses on exploration of dynamic arrest transitions and maximum packing fractions of dense colloidal dispersions by systematically varying particle interaction, size distribution and shape anisotropy. These studies confirm major predictions of dynamic localization theory linking the dynamic potential to macroscopic mechanical responses.

Appendix A. Composites Density and Volume Fraction

The volume fractions of composites (silica particles dispersed into PEG) are determined by the equation $\phi_c = \left(\frac{\rho_T}{\rho_c} \right) X_c$, where X_c is the mass fraction of particles, ρ_c is the density of silica particle which is 1.6g/cm^3 and ρ_T is the density of composites which is measured by Mettler/KEM DA-100 density meter for low molecular weight polymer (PEG400) when ϕ_c<~0.50 at temperature (T≤40 ℃). It is assumed that the silica particle size does not vary the particle density ρ_c=1.6g/cm^3 with which very consistent calculated results of ϕ_c are obtained independent of particles sizes as summarized in Figure A.1 when T=25 ℃ for four different sized particles (SEM pictures are presented in Figure A.2). Therefore, to determine the volume fractions of other samples (more concentrated samples with which measuring density is difficult and those binary mixtures), the smaller particle data in Figure A.1 are interpolated or extrapolated as a reasonably approximate method.

To determine the composite density at higher temperature (T>40 ℃), the densities for the same sets of composites are measured for T=25 ℃, 30 ℃, 35 ℃, 40 ℃ and the data are extrapolated to a higher temperature. And the volume fraction at this higher temperature is determined in the same way as T=25 ℃. It has been determined that the polymer molecular has little influence on the composites density, so the volume fraction for composites containing higher molecular weight PEG is assumed to be the same as those containing PEG400 at the same conditions.

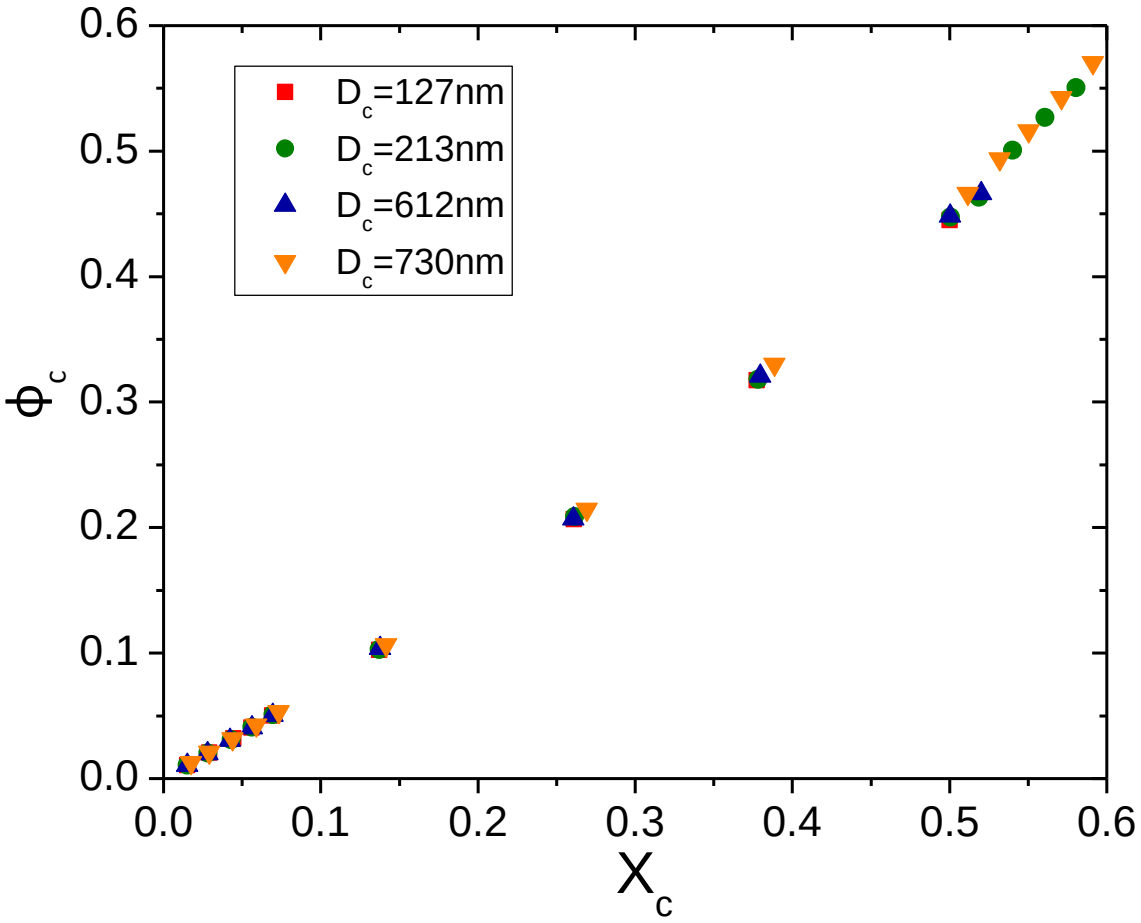

Figure A.1 ϕ_c (calculated based on ρ_c=1.6g/cm^3) as a function of X_c for silica particles with different sizes.

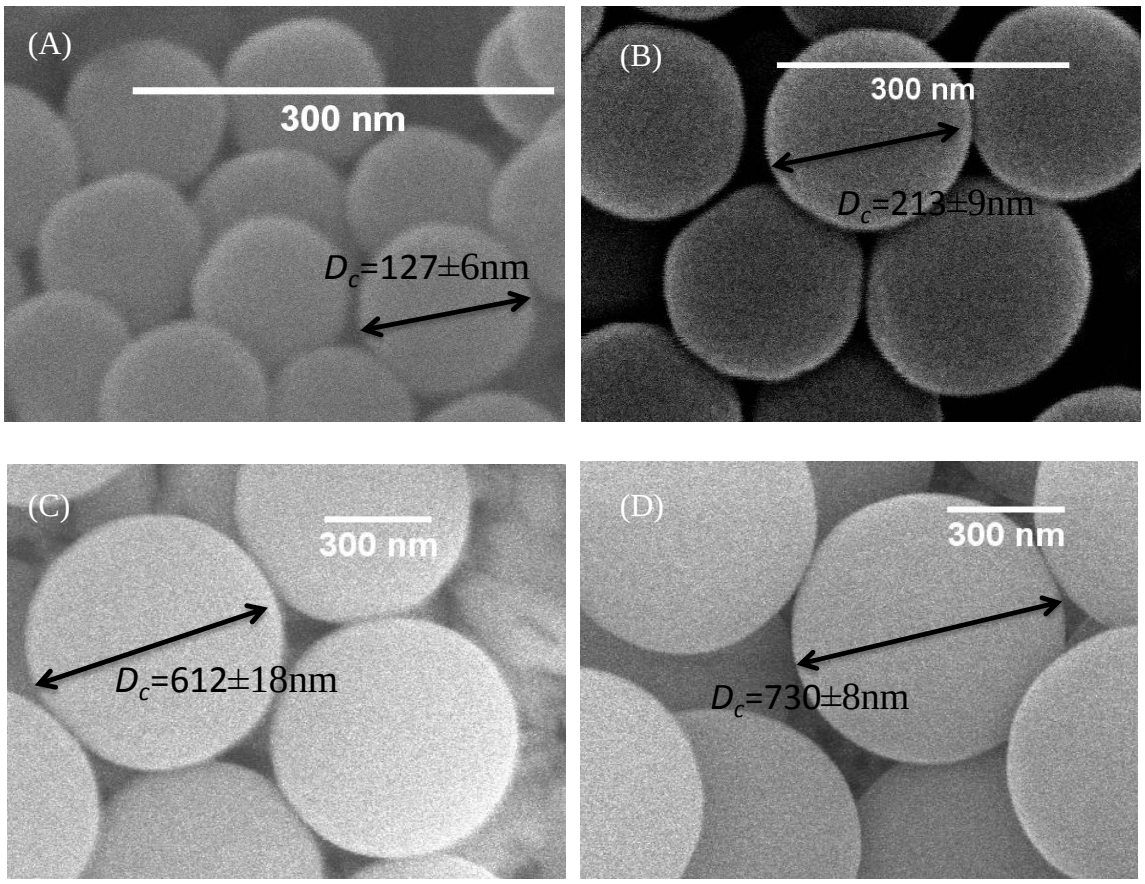

Figure A.2 SEM pictures for silica particles with four different sizes: (A) D_c=127±6nm, (B) D_c=213±9nm, (C) D_c=612±18nm, (D) D_c=730±8nm.

Appendix B. Supporting Information of Chapter 2

Table B.1 Characteristic rheology parameters for different composites under continuous shear

Small particles in PEG 400			
ϕ_c	p	h/nm	τ_c*
0.445	0.694	16.4	9.14
0.466	0.658	14.2	15.06
0.489	0.579	11.9	12.78
0.511	0.503	9.9	14.76
0.534	0.335	7.9	16.71
0.557	0.316	6.1	21.69
0.580	0.278	4.2	25.90
0.604	0.215	2.5	30.27
0.628	0.196	0.8	31.97
Large particles in PEG 400			
ϕ_c	p	h/nm	τ_c*
0.448	-	77.1	60.25
0.466	-	68.1	43.89
0.488	-	58.0	82.70
0.510	-	48.0	113.51
0.533	-	38.4	113.51
0.557	-	29.0	145.20
0.580	-	20.5	201.16
0.604	-	11.8	278.69
0.629	-	3.7	278.69
Small particles in PEG 2000			
ϕ_c	p	h/nm	τ_c*
0.237	0.762	49.9	-
0.299	0.571	36.7	-
0.330	0.469	31.4	-
0.369	0.186	25.6	-
0.398	0.144	21.8	-
0.417	0.156	19.5	-
0.438	0.150	17.1	-
0.454	0.161	15.4	-
0.479	0.164	12.9	-
0.501	0.148	10.8	-
0.520	0.151	9.1	-
Large particles in PEG 2000			
ϕ_c	p	h/nm	τ_c*
0.398	0.839	105.1	81.30
0.419	0.794	92.9	81.30
0.440	0.737	81.2	103.34
0.459	0.771	71.9	71.26
0.484	0.598	59.9	84.38
0.504	0.578	50.6	103.34
0.525	0.570	41.6	149.88
0.549	0.506	32.2	149.88
0.570	0.310	24.0	257.08
0.592	0.303	16.2	238.01
0.615	0.296	8.0	238.01

Appendix C. The Effect of Size Ratio on Glass Transition of Binary Hard Sphere Mixtures

The effects of size disparity ($\delta=d_l/d_s$ with d_l and d_s representing the diameters of large and small particles respectively) in colloidal mixtures with volume exclusive interactions are studied by dispersing silica particles in PEG400 at T=25 ℃. Using the same approach introduced in Chapter 3, the glass transition volume fraction ϕ_x is determined by locating the point where stress plateau develops. Two different diameter ratios are studied with δ=3.4 (d_l=730±8nm and d_s=213±9nm) and δ=4.8 (d_l=127±6nm and d_s=612±18nm), and both size ratios are large enough to increase ϕ_x which is correlated with maximum volume fraction ϕ_m and small enough to avoid depletion induced phase separation. In Figure C.1, the increased value of ϕ_x compare to single component system is plotted as a function of large particle volume fraction ratio R, which is calculated as $\Delta\phi_x = \phi_x - \phi_{x,s}$ with the glass transition volume fraction for single-component system $\phi_{x,s}$ estimated as $\phi_{x,s} = (1-R)\phi_x(R=0) + R\phi_x(R=1)$. $\Delta\phi_x$ is used here instead of ϕ_x to eliminate the effects of slight density variation, steric thickness difference and all the other systematic variation for particles with different sizes or from different batches, thus the results only reflect the effects of size disparity.

As shown in Figure C.1, with size disparity slightly decreased compared to the system we have focused on in Chapter 3, $\Delta\phi_x$ is slightly decreased for binary mixtures with the same large particle volume fraction ratios. This confirms again the correlation between ϕ_x and ϕ_m at this medium size disparity condition as ϕ_m is increased by increasing size disparity. The flow curves for binary mixtures at ϕ_x with δ=3.4 are plotted in Figure C.2. Considering no substantial difference reflected in glass transition brought by the size

disparity in this medium range, the studies of binary mixtures are focused on the fixed larger diameter ratio (δ=4.8) as shown in Chapter 3.

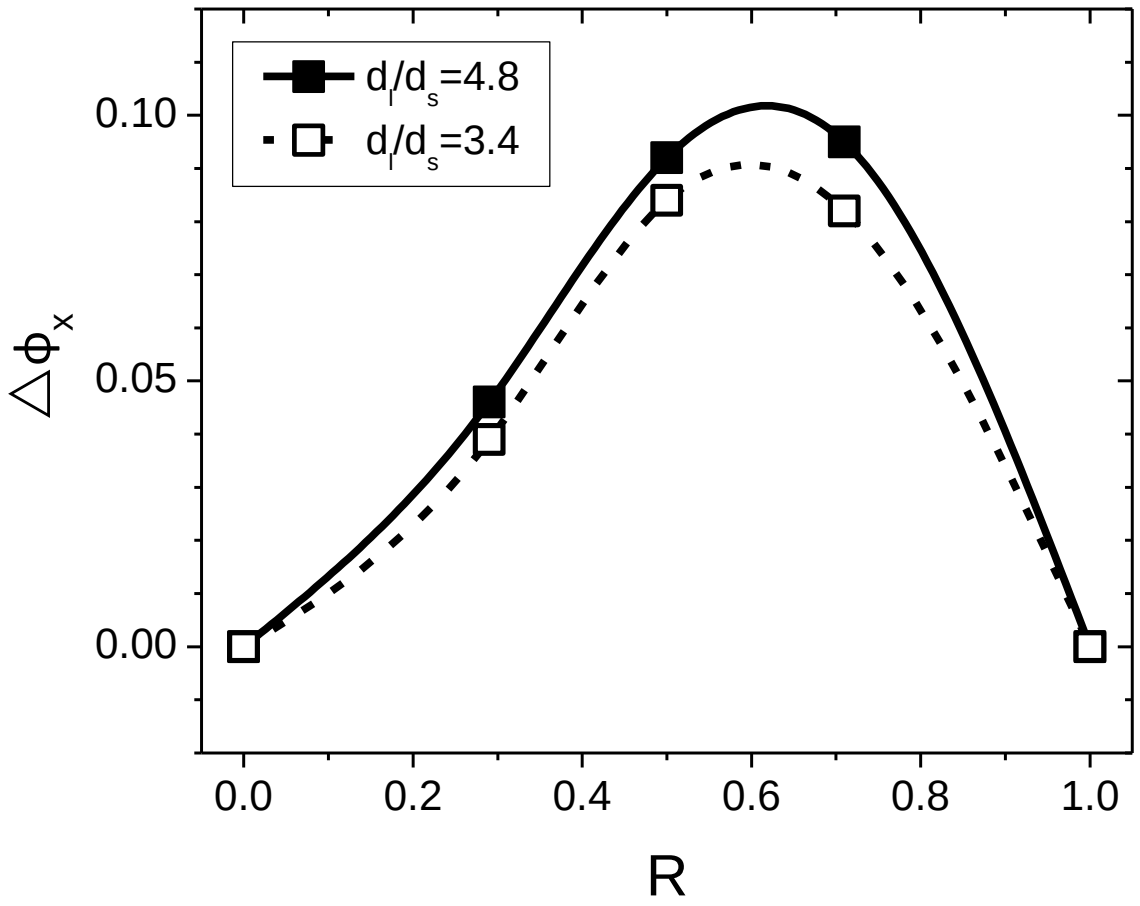

Figure C.1 $\Delta\phi_x$ as a function of R for two different particle diameter ratios for binary silica colloidal mixtures in PEG400 at T=25 ℃.

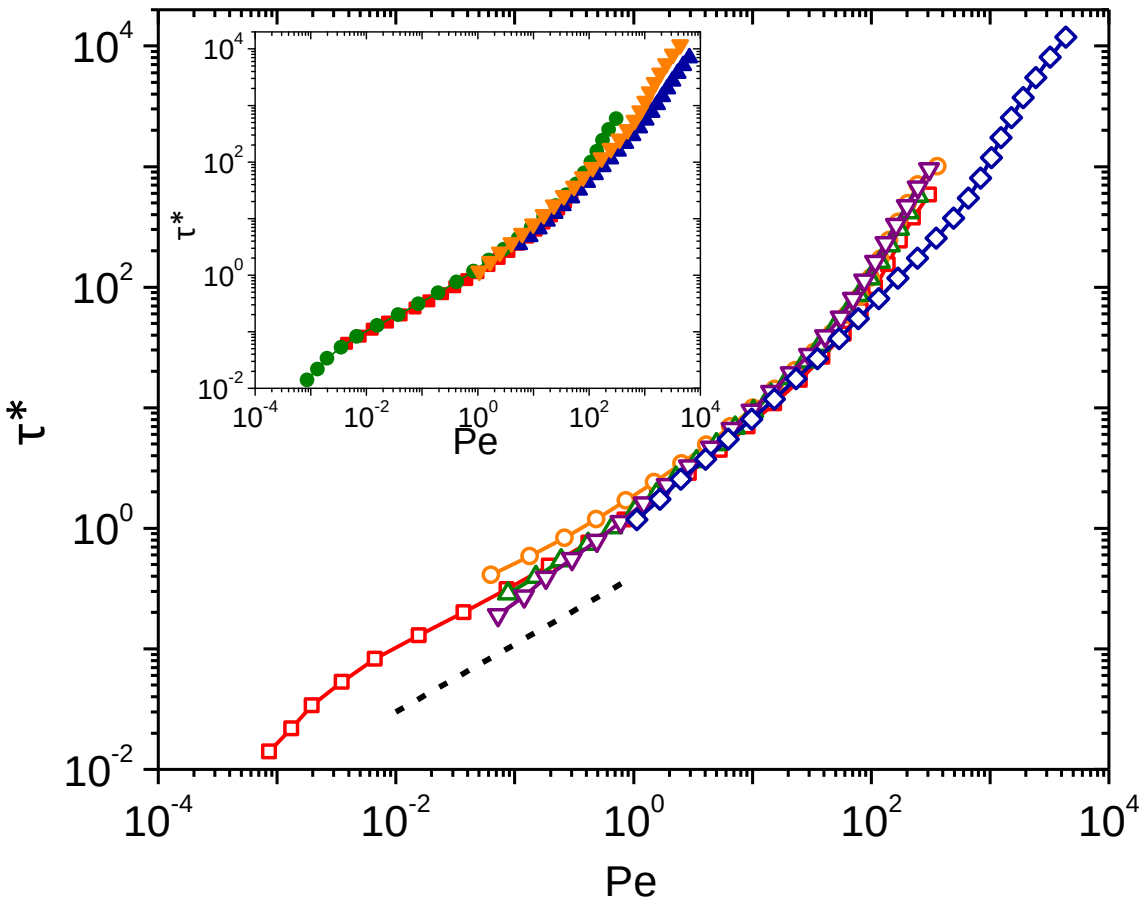

Figure C.2 Flow curves of binary mixture with δ=3.4 for R=0 at ϕ_c=0.527(▫), R=0.29 at ϕ_c =0.571(○), R=0.5 at ϕ_c =0.619(△), R=0.71 at ϕ_c=0.620(▽) and R=1 at ϕ_c =0.543(◇). The dashed line has a slope of 0.56. The superposition of flow curves at the shear thinning parts for the four single-component systems at ϕ_x is shown in the inset with D_c=127nm(■), D_c=213nm (●), D_c=612nm (▲) and D_c=730nm (▼).